CRANFIELD UNIVERSITY

J R FARMAN

DEVELOPMENT OF A PORT-HAMILTONIAN MODEL FOR USE IN OSCILLATING WATER COLUMN CONTROL SCHEME INVESTIGATIONS

SCHOOL OF ENGINEERING

PhD THESIS

CRANFIELD UNIVERSITY

SCHOOL OF ENGINEERING

PhD THESIS

Academic Year 2014-15

J R FARMAN

Development of a Port-Hamiltonian Model for use in Oscillating Water Column Control Scheme Investigations

Supervisors:
Dr J. A. Amaral-Teixeira
Dr J. F. Whidborne
Prof D. Mba

Dec 2014

Abstract

With global energy demand estimated to rise considerably and global warming accepted by the majority of scientists, the pressure to reduce fossil fuel usage is increasing. To this end, the UK government has set a target of generating 50% of electricity from renewable energy sources by 2050. It can therefore be deduced that decreasing the cost of renewable energy by increasing the energy capture is critical.

Oscillating Water Columns (OWCs) employing bidirectional turbines coupled with generators can be used to capture energy from oceanic waves and convert it to electrical energy. This thesis includes a study to quantify the potential power smoothing that can be achieved from a wave farm of ideal OWC devices and from auxiliary hardware such as flywheel energy storage systems. Also detailed are the upgrades to the OWC test facility at Cranfield University, including the world-first capability to simulate polychromatic waves. This test facility has been employed to validate turbine characteristics derived from Computational Fluid Dynamic (CFD) numerical results.

This thesis contains a literature review of the existing control strategies for OWCs that concludes that the optimization of power capture from individual components in the energy chain forces system-level compromises. This conclusion drove the development of an unique energy-based model of the complete wave-to-wire system utilizing port-Hamiltonian mechanics which mandated two modifications to the port-Hamiltonian framework. The first modification to the port-Hamiltonian framework resulted in a new generalized means of modeling systems where the potential energy is dependent on the momentum variables. The second modification expands the port-Hamiltonian framework to allow the modeling of flow source systems in addition to effort source systems. The port-Hamiltonian wave-to-wire OWC model enables the future development of a control approach that optimizes power capture at a system level. As a first step to achieving this goal an Injection Damping Assignment (IDA) Passivity Based Control (PBC) strategy was successfully applied to an OWC system and an energy storage flywheel system. These strategies pave the way for future developments utilizing optimization techniques, such as the use of cost functions to identify the peak efficiency operating condition.

Acknowledgements

Firstly I would like to thank my university supervisors Dr João Amaral-Teixeira, Dr James Whidborne and Prof David Mba for your advice, guidance, motivation, and teaching.

I would like to express my appreciation to Dresser-Rand Company Ltd for sponsoring my research and giving me the opportunity to design, build and commission an OWC turbine in the ocean as part of the HydroAir team. This gave me an insight into the practical as well as the more theoretical challenges in the marine energy field. I would like to add my thanks to all my colleagues at Dresser-Rand especially Gareth, Kevin, Geoff, Chris, Russell, George, Shahab and Andy.

An especially large thank you to my extended family for keeping me balanced and ensuring that I didn't work myself too hard, and for supporting me from the UK, America and Nepal. To my wonderful friends: Katie, Lindsay, Hannah, Anna, Steph D, Nicky, Mark, Annelies, Tom, Steph B and Andy for ensuring I continued to enjoy life, and afternoon coffee and cake.

And lastly but by no means least, thank you to my wonderful husband for your love and support, and for never doubting my ability to achieve my goals. None of this would be complete without you.

In memory of Mary D. Grimoldby née Stamps (1915 - 2014), an inspirational, strong and loving woman.

मेहनतको फल मिठो हुन्छ
Fruits of labor are always sweet

Contents

Abstract **i**

Acknowledgements **ii**

Contents **iii**

List of Figures **vii**

List of Tables **xii**

Acronyms **xiii**

Nomenclature **xvi**

1 Introduction **1**

1.1 Motivations 3

1.2 Objectives 4

1.3 Contributions 5

1.4 Thesis Layout 6

2 OWC Technology Overview **8**

2.1 Wave Devices 8

2.2 Oscillating Water Columns 9

2.3 OWC Turbines 14

2.3.1 Unidirectional Turbines 15

2.3.2 Bidirectional Turbines 15

2.3.3 Wells Turbine 16

2.3.4 Denniss-Auld Turbine 18

2.3.5 Savonius Turbine 19

2.3.6 Impulse Turbine 20

2.4 OWC Electrical PTO System 25
2.4.1 Generator Selection 26
2.4.2 Inverter Selection 27
2.4.3 Power Conditioning 29

3 Analytical Model of an OWC Wave-to-Wire System 31

3.1 Modeling Introduction 31
3.2 Energy Based Modeling 33
3.2.1 Euler-Lagrangian Mechanics 33
3.2.2 Port-Hamiltonian Mechanics 34
3.2.3 Port-Hamiltonian Mechanics and Momentum Dependent Potential Energy 36
3.2.4 Brayton-Moser Systems 39
3.2.5 Port-Hamiltonian Mechanics and a Change of Reference Frame 41
3.2.6 Bond Graphs 42
3.2.7 Energy-Based Modeling Summary 43
3.3 Incident Waves 44
3.3.1 Wave Spectra 44
3.3.2 Wave Time Series 50
3.4 Hydrodynamic OWC Modeling 52
3.4.1 OWC Model with Frequency Independent Added Mass 56
3.4.2 OWC Model with Frequency Dependent Added Mass 65
3.5 Pneumatic OWC Model 76
3.5.1 Inter-Component Volume Method 78
3.5.2 Turbine Mass Flow 82
3.5.3 Blow-Off Valve Mass Flow 85
3.5.4 Rate of Change of Mass within Air Chamber 86
3.5.5 Port-Hamiltonian Equations 86
3.6 Mechanical Drive-Train Model 90
3.6.1 Fixed Inertia Turbine Model 90
3.6.2 Variable Inertia Turbine Model 92
3.7 Electrical Generator Model 93
3.7.1 Induction Generator System Equations 94
3.7.2 Port-Hamiltonian Induction Generator Model 99

3.8 OWC System State Equations . . . 105
3.9 Summary of Contribution and Future Work . . . 111

4 Power Smoothing 114
4.1 Objectives . . . 114
4.2 Modeling . . . 116
4.2.1 Individual Chambers . . . 117
4.2.2 Energy Storage . . . 119
4.3 Simulation Results . . . 121
4.3.1 Power Output for Multiple Devices . . . 121
4.3.2 Energy Storage . . . 121
4.4 Physical System Design . . . 126
4.4.1 Baseline Design . . . 126
4.4.2 Multiple Units . . . 126
4.4.3 Energy Storage . . . 127
4.5 Summary of Contribution . . . 133

5 Power Shaping Control 135
5.1 Literature Review of Control Strategies for OWCs . . . 135
5.1.1 Speed Control . . . 136
5.1.2 Valve Control . . . 137
5.1.3 Latching and Unlatching . . . 139
5.1.4 Reactive and Complex Conjugate Control . . . 140
5.1.5 Balast Control . . . 140
5.1.6 Comparison of Control Strategies . . . 141
5.2 Control Restrictions . . . 142
5.3 Passivity Based Control . . . 144
5.4 DFIG Speed Control . . . 146
5.4.1 Simulation Results . . . 151
5.5 Power Control of an Energy Storage System . . . 153
5.5.1 Simulation Results . . . 157
5.6 Turbine Damping Control . . . 160
5.6.1 Simulation Results . . . 162

5.7 Summary of Contribution 162

6 Test Facility **165**

6.1 Literature Review of Test Facilities 166
6.2 Pneumatic Wave Generator Test Facility 170
6.2.1 PWG Hardware 170
6.2.2 Instrumentation 171
6.2.3 Test Rig Control Strategy 173
6.2.4 Generated Waves 181
6.3 Validation of Numerical CFD Results 184
6.4 Simulation Parameters 188
6.5 Summary of Contribution 192

7 Conclusions and Further Work **193**

7.1 Conclusion 193
7.2 Further Work 197

References **200**

A Wave Equations **218**

A.1 Linear Theory - Deep Water 218
A.2 Intermediate Water 219
A.3 Deep Water 220

B Wave Spectra **222**

B.1 Wave Spectra Equations 222

List of Figures

1.1 Oscillating Water Column (OWC) principle (Dresser-Rand Company Ltd 2015) 2

2.1 Buoy Shapes a) FFDB, b) Vertical draft c) BBDB 9

2.2 Limpet diagrammatic and side view (Folley & Whittaker 2002) . . . 10

2.3 Examples of near-shore installations: Oceanlinx prototype device at Port Kembla (Oceanlinx Ltd 2011b) and Ocean Energy prototype device at Galway Bay (Ocean Energy Ltd 2011) 10

2.4 Energetech prototype device with parabolic wall focusing the waves into the chamber (Alcorn & Finnigan 2004) 11

2.5 The Multi Resonant Chamber (MRC) OWC device (Renewable Energy Development 2009) 11

2.6 Mighty Whale (Washio et al. 2001) 13

2.7 Wave Energy Ireland (Kelly et al. 2013) 14

2.8 Different Wells turbine designs going from left to right, top to bottom: WTGV, BWGV, TSCB and lastly the CRWT (Setoguchi & Takao 2006) 17

2.9 Wells turbine characteristics (Setoguchi & Takao 2006) 18

2.10 Energetech turbine pitching mechanism (Alcorn & Finnigan 2004) . . 18

2.11 Blade pitching sequence in oscillating flow (Finnigan & Auld 2003) . 18

2.12 Efficiency and non-dimensional pressure drop against flow coefficient for the Denniss-Auld turbine (Curran & Folley 2008) 19

2.13 Savonius wind turbine (Dorrell et al. 2010a) 20

2.14 IFGV and ISGV turbines (Setoguchi & Takao 2006) 21

2.15 HydroAir prototype Variable Radius Turbine (VRT) (Dresser-Rand Company Ltd 2015) . . . 22

2.16 McCormick turbine design as shown in the patent (McCormick 1981a) 23

2.17 McCormick contra-rotating stator and rotor rows (Setoguchi & Takao 2006) . . . 23

2.18 Diagrammatic representation of a radial turbine (Setoguchi et al. 2002) 24

2.19 Diagrammatic representation of a biradial turbine with a) fixed guide vanes and b) moving guide vanes (Falcão & Nunes 2013a) . . . 25

2.20 Back-to-back rectifiers for generator power rectification for non-synchronous speeds (Ahmed & Zobaa 2009) . . . 28

3.1 DC motor and mechanical load (Banerjee 2005) . . . 37

3.2 Voltage source and current source electrical systems . . . 41

3.3 Bond Graph for Series and Parallel (Banerjee 2005) . . . 43

3.4 Common wave terminology (Pretor-Pinney 2010) . . . 44

3.5 Properties of waves under various depth conditions a) deep water; b) intermediate water; and c) shallow water (McCormick 1981b) . . . 45

3.6 Comparison of long term energy spectrum and real data collected by Mollison (McCormick 2010) . . . 47

3.7 JONSWAP spectra for three peak enhancement factors. . . . 48

3.8 Wave scatter diagram (Borgarino et al. 2011) . . . 49

3.9 Key OWC parameters . . . 57

3.10 Nemoh mesh for a 24m cylindrical OWC device . . . 66

3.11 BEM calculated coefficients for added mass, damping and excitation force for a cylindrical OWC with a 12m diameter for a range of panel densities . . . 68

3.12 Impulse response of a 24m cylindrical OWC . . . 72

3.13 Basic inter-component volume method for OWC air chamber and turbine . . . 79

3.14 Extended inter-component volume method for OWC air chamber and turbine . . . 79

3.15 Simulink model of the turbine (Anand et al. 2007) . . . 85

3.16 Per unit power for induction generator vs permanent magnet (Hodgins 2010) 94

4.1 Comparison of the device shapes under consideration 119

4.2 Energy storage decision matrix 120

4.3 Multiple 10 m OWCs spaced at 15 m intervals 122

4.4 Multiple OWCs with energy storage 124

4.5 Single OWC with energy storage 125

4.6 Electrical connection for a single OWC 126

4.7 Electrical connection for multiple OWCs 127

4.8 Fixed inertia flywheel on-shore with AC transmission lines to shore . 129

4.9 Fixed inertia flywheel on-shore with DC transmission lines to shore . 129

4.10 Fixed inertia flywheel off-shore with AC transmission lines to shore . 129

4.11 Off-shore variable inertia flywheel 131

4.12 Off-shore SC system 133

5.1 Average efficiency, η_t for irregular waves, with air flow control by a throttle-valve, a Blow-Off Valve (BOV), and no flow control (Falcão & Justino 1999) 139

5.2 DFIG speed control tuning J_m=5 a) over-damped b) under-damped . 152

5.3 DFIG speed control tuning J_m=10 a) over-damped b) under-damped 153

5.4 Energy storage system is electrically positioned between the OWC system and the national grid 154

5.5 DFIG FIF power flow control 159

5.6 DFIG FIF power flow control error 159

5.7 DFIG FIF power flow control transient error 159

5.8 Damping achieved with fixed speed control for a variety of turbine diameters and generators and the associated power extracted 163

5.9 DFIG damping control for a 1m turbine diameter in conjunction with a 1 pole-pair and 4 pole-pair generator 164

6.1 Test rig using bellows (Raghunathan & Ombaka 1985). 167

6.2 Test rig using a piston (Maeda, Takao, Setoguchi, Kaneko & Kim 2001). . . . 168

6.3 PWG test facility air chamber . . . 170

6.4 CAD drawing of PWG test facility (Dresser-Rand Company Ltd 2014) . . . 170

6.5 Test rig hardware diagram . . . 171

6.6 Total pressure probes embedded in turbine blades . . . 173

6.7 PID speed control loop . . . 174

6.8 Phase relationship between position and velocity . . . 175

6.9 a) Monochromatic wave with ramp duration not equal to an integer multiple of the period of the wave which produces no offset. b) Monochromatic wave with ramp duration not equal to an integer multiple of the period and, hence, produces an offset from the desired the position . . . 179

6.10 Time series generated for three different JONSWAP spectra with the same phase shifts . . . 180

6.11 Comparison of the desired and actual time series generated for the JONSWAP spectra with a peak enhancement factor of 1 . . . 180

6.12 Polychromatic wave position and velocity . . . 181

6.13 Dynamic pressure measurements for a wave of 12s period and $1.8m^3/s$ flow rate . . . 183

6.14 Standard deviation of the total pressure measurements divided by the RMS pressure for a wave of 12s period and 1.8 m^3/s flow rate . . . 183

6.15 Pressure plot for a scaled Pierson-Moskowitz derived irregular wave with a wind speed of 15.4 m/s . . . 185

6.16 Pressure plot for a scaled Bretschneider derived irregular wave with a significant wave height of 4.5m and and a peak period of 12 s . . . 185

6.17 Accuracy for a Pierson-Moskowitz wave . . . 186

6.18 Flow coefficient for turbine free-wheeling under a monochromatic wave (wave 17) which has a period of 12s, an amplitude of 114deg and a design flow rate of $1.2m^3/s$ subject to turbine running conditions . 187

6.19 Speed for numerical simulation tests . . . 188

6.20 Test results and numerical simulation results for non-dimensional pressure flow rate relationship using monochromatic waves . . . 188

6.21 Test results and numerical simulation results for non-dimensional pressure flow rate relationship using polychromatic waves 189

6.22 Plan view of PWG (Dresser-Rand Company Ltd 2014) 190

B.1 Variance spectral density for Pierson-Moskowitz spectrum in frequency and time domain 225

List of Tables

2.1 Generator selection advantages and disadvantages (O'Sullivan & Lewis 2008) 27

5.1 Turbine and generator efficiency vs pressure drop (Amundarain, Alberdi, Garrido & Garrido 2010) 141

6.1 Scaling of test rig waves for OWC simulation model 182

6.2 Simulation parameter settings 190

6.3 Air chamber volumes 191

Acronyms

ANN	Artificial Neural Networks.
BBDB	Backward Bent Duct Buoy.
BEM	Boundary Element Method.
BERR	Department for Business, Enterprise and Regulatory Reform.
BOV	Blow-Off Valve.
BWGV	Biplane Wells Turbine with Guide Vanes.
CFD	Computational Fluid Dynamics.
COB	Center Of Buoyancy.
COG	Center Of Gravity.
CRWT	Contra Rotating Wells Turbine.
CT	Current Transformer.
D-R	Dresser-Rand.
D.C.	Direct Current.
DFIG	Doubly Fed Induction Generator.
DNO	Distribution Network Operator.
DOF	Degree Of Freedom.
DTI	Department of Trade and Industry.
EMEC	European Marine Energy Center.
EMI	Electro-Magnetic Interference.
EMR	Electro-Magnetic Radiation.
ESR	Equivalent Series Resistance.
FFDB	Forward Facing Duct Buoy.
FIF	Fixed Inertia Flywheel.
GRP	Glass Reinforced Plastic.
GV	Guide Vane.

HMI	Human Machine Interface.
IDA	Interconnection and Damping Assignment.
IFFT	Inverse Fast Fourier Transform.
IFGV	Impulse turbine with Fixed Guide Vanes.
IGBT	Integrated Gate Bipolar Transistor.
IGV	Inlet Guide Vanes.
ISGV	Impulse turbine with Self-pitching linked Guide Vanes.
JAMSTEC	Japan Marine Science and Technology Center.
JONSWAP	Joint North Sea Wave Project.
LWT	Linear Wave Theory.
MPT	Marine Power Technologies.
MRC	Multi Resonant Chamber.
NG	National Grid.
OGV	Outlet Guide Vanes.
OWC	Oscillating Water Column.
PBC	Passivity Based Control.
PDE	Partial Differential Equation.
PF	Power Factor.
PID	Proportional Integral Derivative.
PLC	Programmable Logic Controller.
PMG	Permanent Magnet Generator.
PROFIBUS	PROcess FIeld BUS.
PTO	Power Take-Off.
PWG	Pneumatic Wave Generator.
RAO	Response Amplitude Operator.
RLC	Resistance Impedance Capacitance.
RMS	Root Mean Square.
ROCOF	Rate Of Change Of Frequency.
SC	Super-Capacitor.
SCADA	Supervisory Control And Data Acquisition.
SCIG	Squirrel Cage Induction Generator.
SFE	Sinusoidal Front End.
SG	Synchronous Generator.

SI	System International.
SOV	Shut-Off Valve.
SWL	Sea Water Level.
TSCB	Turbine Self-pitching Controlled Blades.
VI	Virtual Instrument.
VIF	Variable Inertia Flywheel.
VRT	Variable Radius Turbine.
VT	Voltage Transformer.
WEC	Wave Energy Converter.
WRIG	Wound Rotor Induction Generator.
WTGV	Wells Turbine with Guide Vanes.

Nomenclature

α_p	State variable constant used in the Prony method for approximating the convolutions of the impulse response function (s^{-1}).
β_p	State variable constant used in the Prony method (m^{-1}).
β_x	Relative electrical speed (rad/s).
χ	Additional state variables using the Prony method (N).
η_d	Incident wave elevation at the depth of the draft (m).
η_r	Incident wave elevation with ramp gain (m).
η_t	Turbine efficiency (%).
η	Incident free-surface elevation (m).
γ	Heat capacity ratio.
κ_e	Excitation force impulse response function.
κ_r	Radiation force impulse response function.
λ	Wave length (m).
μ_∞	Infinity added mass (kg).
ω_e	Generator electrical supply frequency (rad/s).
ω_m	Rotor mechanical frequency (rad/s).
ω_p	Peak wave frequency (rad/s).
ω_r	Rotor electrical frequency (rad/s).
ω_s	Stator electrical frequency (rad/s).
ω_w	Wave angular frequency (rad/s).
ω_x	Reference frequency for park transform (rad/s).
ϕ	Phase angle (rad).
ψ_{abcr}	Three phase rotor flux (Wb).
ψ_{abcs}	Three phase stator flux (Wb).
ψ_{dqr}	Rotor flux in the dq frame (Wb).
ψ_{dqs}	Stator flux in the dq frame (Wb).
ψ_f	Field flux (Wb).
ψ_{qd0r}	Quadrature-direct-zero-rotor flux (Wb).
ψ_{qd0s}	Quadrature-direct-zero-stator flux (Wb).
ψ_{qr}	Quadrature-rotor flux (Wb).
ψ_{qs}	Quadrature-stator flux (Wb).
ψ_w	Armature winding flux (Wb).
ψ	Flux (Wb).

ρ_{a0}	Initial density of air (i.e. at atmospheric pressure) (kg/m^3).
ρ_a	Density of air (kg/m^3).
ρ_w	Density of water (kg/m^3).
σ	JONSWAP spectral width parameter.
τ	Dummy variable.
θ_g	Generator rotary position (rad).
θ_l	Load rotary position (rad).
θ_m	Rotor mechanical position (rad).
θ_r	Rotor electrical position (rad).
θ_s	Stator electrical position (rad).
θ	Angular position (rad).
Δp	Pressure drop across turbine or orifice plate (Pa).
Γ	Peak enhancement factor.
Φ	Flow coefficient.
Θ	Angle of attack of waves (deg).
$\mathscr{A}$	Added mass coefficient (kg).
$\mathscr{B}$	Damping coefficient (kg s^{-1}).
$\mathscr{C}$	State error function.
$\mathscr{D}^d$	Desired dissipation matrix.
$\mathscr{D}$	Dissipation matrix.
$\mathscr{E}$	Effort.
$\mathscr{F}$	Force.
$\mathscr{G}$	Function.
$\mathscr{H}^d$	Desired Hamiltonian function (J).
$\mathscr{H}$	Hamiltonian function (J).
$\mathscr{J}^d$	Desired inertial matrix.
$\mathscr{J}$	Inertial matrix.
$\mathscr{L}$	Lagrangian function (J).
$\mathscr{N}$	Interconnection matrix.
$\mathscr{P}$	mixed potential function (W).
$\mathscr{R}^d$	Desired Rayleigh dissipation function (W).
$\mathscr{R}$	Rayleigh dissipation function (W).
$\mathscr{T}$	Potential energy (J).
$\mathscr{V}$	Kinetic energy (J).
a	Amplitude (m).
b	Device width (m).
c_s	Speed of sound in air (m/s).
c	Integral constant.
e	Position error.

f_e Electrical frequency (Hz).
f Wave frequency (Hz).
g_c Control input function.
g_d Disturbance input function.
g_s Input function.
g Gravity (m/s^2).
h_{a0} Air draft of the chamber (m).
h_a Air chamber height above the still water level in the chamber (m).
h_b Height of blade (m).
h_d Water draft of the chamber (m).
h_r Impulse response function.
h_w Water depth (m).
i_{0r} Zero-rotor current (A).
i_{0s} Zero-stator current (A).
i_{abcr} Rotor current in the abc frame (A).
i_{abcs} Stator current in the abc frame (A).
i_{dqr} Direct-quadrature-rotor current (A).
i_{dqs} Direct-quadrature-stator current (A).
i_{dr} Direct-rotor current (A).
i_{ds} Direct-stator current (A).
i_{qd0l} Quadrature-direct-zero-load current in the qd0 frame (A).
i_{qd0n} Quadrature-direct-zero-network current (A).
i_{qd0r} Quadrature-direct-zero-rotor current (A).
i_{qd0s} Quadrature-direct-zero-stator current (A).
i_{qd0t} Quadrature-direct-zero-turbine current (A).
i_{qr} Quadrature-rotor current (A).
i_{qs} Quadrature-stator current (A).
i Integer / ith frequency component of wave.
j Integer.
k_1 Total stiffness associated with body 1 (N/m).
k_2 Total stiffness associated with body 2 (N/m).
k_h Hydrostatic stiffness (N/m).
k_m Mooring stiffness (N/m).
k_s Shaft rotational stiffness (J).
k Wave number (m^{-1}).
l_b Blade chord length (m).
l_c OWC device length (m).
l Number of state variables to approximate using Prony method.
m_c Mass of air in the OWC air chamber (kg).
$\dot{m}_o$ Mass flow through the orifice (kg/s).
n Number of rotor blades.
n_p Number of poles.

p^*	Non-dimensional pressure.
p_{atm}	Atmospheric pressure (Pa).
p_c	Pressure within the air chamber (Pa).
p_d	Dynamic pressure (Pa).
p_s	Static pressure (Pa).
p_t	Total pressure (Pa).
p_w	Wave pressure (Pa).
p	Pressure (Pa).
q_1	Charge 1 (C).
q_d	Diffraction flow rate (m^3/s).
q_i	Generalized coordinate.
q_{qd0r}	Quadrature-direct-zero-rotor charge (C).
q_{qd0s}	Quadrature-direct-zero-stator charge (C).
q_r	Radiation flow rate (m^3/s).
q_v	Turbine flow rate (m^3/s).
q_v	Valve flow rate (m^3/s).
q_w	Armature winding charge (C).
r_c	Radius of the OWC (m).
r^d	Diagonal terms of the desired Rayleigh function (J).
r_m	Radius of the mid point of the turbine (m).
r	Ramp amplitude (m).
s_χ	Prony state variables.
s^d	desired state variables.
s_e	Electrical state variables.
s_x	Main OWC state variables.
s	State variables.
t_{DS}	Minimum duration for a wind to blow to generate a developed sea (s).
t_r	Ramp duration (s).
t	Time (s).
u_c	Control inputs.
u_d	Disturbance inputs.
u_{owc}	OWC inputs.
u_{pwg}	Paddle inputs.
u_s	Control inputs.
v_{0r}	Rotor-zero voltage (V).
v_0	Zero voltage (V).
v_{abcr}	Rotor three phase line voltage (V).
v_{abcs}	Stator three phase line voltage (V).
v_a	Three phase line voltage (V).
v_b	Three phase line voltage (V).
v_c	Three phase line voltage (V).

v_{dqr} Direct-quadrature-rotor voltage (V).
v_{dqs} Direct-quadrature-stator voltage (V).
v_{dr} Rotor-direct voltage (V).
v_{ds} Stator-direct voltage (V).
v_d Direct voltage (V).
v_{qd0r} Quadrature-direct-zero-rotor voltage (V).
v_{qd0s} Quadrature-direct-zero-stator voltage (V).
v_{qr} Rotor-quadrature voltage (V).
v_{qs} Stator-quadrature voltage (V).
v_q Quadrature voltage (V).
w_b Mass flow through blow-off valve (kg/s).
w_o Mass flow through orifice (kg/s).
w_t Mass flow through turbine (kg/s).
x Horizontal position (m).
y System output.
z_1 Vertical elevation of OWC device (m).
z_2 Vertical elevation of water column piston (m).
z_p PWG paddle position (deg).
z Vertical position of body (m).

A_R Cross section area of the annulus at the rotor blades (m^2).
A_b Area of the BOV (m^2).
A_c Area of water column (m^2).
A_o Area of orifice (m^2).
A_s Heave wetted surface area (m^2).
A_y JONSWAP constant.
B_b Bearing loss coefficient for the turbine/generator rotating assembly (kg/m^2).
B_g Generator resistance (kg m^2).
B_l Load resistance (kg m^2).
B_q Turbine resistance due to flow through turbine.
B_t Turbine windage loss coefficient (kg/m^2).
B Damping coefficient (kg s^{-1}).
C_a Power coefficient.
C_d Coefficient of discharge of the orifice.
C_t Torque coefficient.
C Spring coefficient.
D_o Orifice diameter (m).
D_t Turbine diameter (m).
E_r EMF across resistor (V).
E_s EMF source (V).
F_{DS} Minimum fetch distance for a developed sea (m).

F_{FK}	Froude-Krylov force (N).
F_P	PTO force (N).
F_a	Added mass force (N).
F_{di}	Diffraction force (N).
$F_{\Delta p}$	Force due to the air chamber (N).
F_{em}	Force due to the expelled mass (N).
F_e	Excitation force (N).
F_g	Gravitational force (N).
F_h	Hydrostatic force (N).
F_m	Mooring force (N).
F_n	Net force (N).
F_r	Wave radiation force (N).
G_b	BOV control gain.
G_k	Speed control gain.
G_{owc}	OWC transfer function.
G_{pwg}	PWG transfer function.
H_s	Significant wave height (m).
I_2	Identity matrix of dimension 2.
I_3	Identity matrix of dimension 3.
I_s	Current source (A).
J_2	Skew symmetric matrix of dimension 2.
J_d	Drive train moment of inertia (kgm^2).
J_g	Generator moment of inertia (kgm^2).
J_l	Load moment of inertia (kgm^2).
J_m	Mechanical moment of inertia (kgm^2).
J	Jacobian.
K_f	Field constant.
K_r	Rotor coordinate transform.
K_s	Stator coordinate transform.
K	Turbine damping ($\mathrm{Ns/m}^5$).
L_{lr}	Rotor leakage inductance (H).
L_{ls}	Stator leakage inductance (H).
L_l	Load inductance (H).
L_{mr}	Rotor magnetizing inductance (H).
L_{ms}	Stator magnetizing inductance (H).
L_m	Magnetizing inductance (H).
L_r	Rotor inductance (H).
L_{srx}	Rotor-stator inductance matrix (H).
L_{sr}	Mutual inductance (H).
L_s	Stator inductance (H).
L_w	Armature winding inductance (H).
L	Inductance (H).

M_1	Mass of body 1 (kg).
M_2	Mass of body 2 (kg).
M_a	Added mass (kg).
M_b	Mass of body (kg).
M_d	Displaced water mass (kg).
M_{wc}	Mass of water within column (kg).
N_t	Turbine gyrator ratio (m^{-3}).
N	Number of frequency components.
$P1$	Plane 1, chamber side of turbine.
$P2$	Plane 2, atmosphere side of turbine.
P_{BS}	Power in Brent-Schneider spectrum (W).
P_{PM}	Power in Pierson Moskowitz spectrum (W).
P_m	Mechanical/turbine power (W).
P_{nom}	Nominal power (W).
P_n	Real network power (W).
Q^*	Non-dimensional flow rate.
Q_n	Reactive network power (W).
Q_{tg}	Gyrator flow rate through the turbine (m^3/s).
Q_{tr}	Resistive flow rate through the turbine (m^3/s).
Q_t	Flow rate through the turbine (m^3/s).
R^2	Coefficient of determination.
R_1	Resistance 1 (Ω).
R_a	Specific gas constant for air (J kg^{-1} K^{-1}).
R_d	Applied damping.
R_l	Load resistance (Ω).
R_r	Rotor resistance (Ω).
R_s	Stator resistance (Ω).
R_w	Armature winding resistance (Ω).
S_D	Directional spectrum.
S_{JON}	JONSWAP spectrum (m^2/Hz).
S_{PM}	Pierson-Moskowitz spectrum (m^2/Hz).
S	Generic wave spectrum (m^2/Hz).
T^*	Non-dimensional torque.
T_{atm}	Atmospheric air temperature (K).
T_b	Torque due to bearing and other mechanical losses (Nm).
T_c	Air temperature within the OWC chamber (K).
T_e	Electrical torque (Nm).
T_l	Load torque (Nm).
T_m	Mechanical torque (Nm).
T_n	Net torque (Nm).
T_p	Peak wave period (s).
T_t	Turbine torque (Nm).

T	Wave period (s).
U_{10}	Wind speed at 10 meters above sea level (m/s).
$U_{19.5}$	Wind speed at nineteen 19.5 meters above sea level (m/s).
U	Rotational speed at mid point of blade (m/s).
V_a	Axial velocity (m/s).
V_{c0}	Initial volume of water column (m^3).
V_c	Volume of water column (m^3).
V_e	Effective volume (m^3).
V_p	Volume within the PWG (m^3).
X_a	Matrix variable.
X_b	Matrix variable.
X_c	Matrix variable.
X_d	Matrix variable.
X_e	Matrix variable.
X_f	Matrix variable.
X_m	Magnetizing reactance (XX).
Y_1	Momentum of OWC device (kg m s^{-1}).
Y_2	Momentum of water column piston (kg m s^{-1}).
Y_g	Generator momentum (kg m s^{-1}).
Y_i	Generalized momentum.
Y_l	Load momentum (kg m s^{-1}).
Y_m	Mechanical momentum (kg m^2 s^{-1}).
Y	Momentum (kg m s^{-1}).
Z_l	Load impedance (Ω).

Chapter 1

Introduction

The future and source of mankind's energy needs are the subject of much debate - both in relation to global warming and to the availability of fossil fuels. In parallel with these debates, renewable energy sources are being thoroughly investigated. Many different wave energy conversion devices have been designed, and prototypes built, to develop another potential energy source for the ever-growing demands of the world's population. It is a realistic possibility that wave energy devices will supplement the current energy portfolio (Brekken et al. 2009).

Oscillating Water Columns (OWCs), see Figure 1.1 for a schematic representation, are one of the most well-studied wave energy devices as there are no mechanical or electrical components under the water line. It could be argued that this significantly improves the potential reliability in comparison to over wave energy devices. OWCs can be built on-shore and off-shore e.g. the Ocean Energy off-shore device (O'Sullivan & Lewis 2011) and the Limpet breakwater power station on Islay (Heath 2007); one of the additional advantages of off-shore OWCs over other off-shore devices is that all Power Take-Off (PTO) components can be inspected and maintained at sea (Patel et al. 2011), rather than the costly alternative of towing the whole unit to a dry dock. A number of units have been grid connected proving the viability

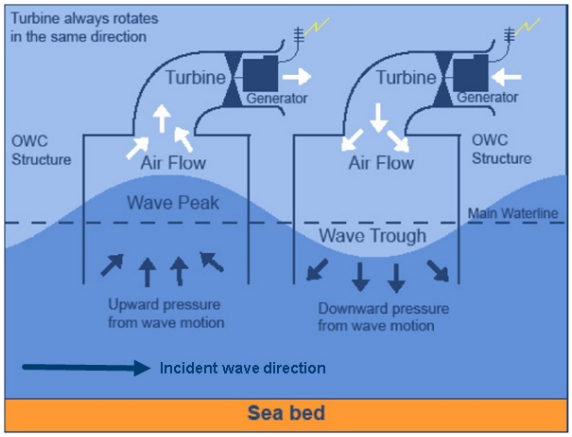

Figure 1.1: OWC principle (Dresser-Rand Company Ltd 2015)

of the design. The Oceanlinx OWC device was grid connected in Port Kembla, Australia (Oceanlinx Ltd 2010a). The Mutriku plant, in the Basque country, was constructed with multiple chambers and turbines within a breakwater, and was grid connected in 2009 (Torre-Enciso et al. 2009). The author proposes that there is the added bonus with OWCs that there is the ability to transfer knowledge from the off-shore oil and gas industry, particularly in the design of moorings and survivable structures as the device has similarities to existing floating platforms.

There are many different types of turbines that have been used on OWCs, however, this research will concentrate specifically on the unique HydroAir Variable Radius Turbine (VRT), which is an impulse type design. It is publicized (Dresser-Rand Company Ltd 2015) as having comparable peak efficiency to, and wider bandwidth than other OWC turbines in the field, and research and development is ongoing to develop this yet further. The main advantage of this turbine is that it has fixed geometry guide vanes and rotor blades, reducing the number of potential failure modes compared to turbines with additional moving components such as the Wells or Denniss Auld turbine (both of which will be discussed in greater detail in Chapter 2).

Significant resources have been expanded in designing optimized turbines, but until

very recently the strategies for controlling these turbines under highly dynamic conditions have largely been neglected. Some research has been completed into the control strategies that could be employed on OWCs in general but, as will be seen in the literature review in Chapter 5, very little has been conducted for impulse turbines specifically.

1.1 Motivations

Development work on the turbine that was to become HydroAir started in 2005, with a Department of Trade and Industry (DTI) funded project entitled "Air turbine development project". This encompassed the research completed by Stephen Herring as part of his PhD entitled "The design and evaluation of turbines for use in OWC power plants", Herring (2007). It was through this work that the variable radius turbine came into existence, and a patent application was made and granted to Freeman et al. (2008). The patent was held by Peter Brotherhood Ltd. The turbine was developed in conjunction with Banks (2009) who developed a code for optimizing the geometry of the VRT. A test facility, named the Pneumatic Wave Generator (PWG), was built to validate the Computational Fluid Dynamics (CFD) numerical results (obtained by Banks (2009), Natanzi (2010a), Tarver (2013) and the author of this thesis).

In the Summer of 2008, Dresser-Rand (D-R) purchased substantial assets from Peter Brotherhood including the HydroAir product and patent. Throughout, collaborative work to develop the turbine has continued between Cranfield University and Peter-Brotherhood/Dresser-Rand, resulting in the funding of two further PhD students. In 2008 work commenced on a Department for Business, Enterprise and Regulatory Reform (BERR) funded project. The project was a collaboration between the Peter Brotherhood Hydro-Air team, Orecon (an OWC device developer), Converteam

(an electrical package supplier) and Cranfield University. Entitled "Full scale design and concept verification of the Orecon Multi Resonant Chamber (MRC) wave energy device", the project involved the full scale design of three 500 kW turbines, a material study, and electrical package design. In 2009, D-R received an order for a prototype unit which was built at the Peterborough factory, and the author subsequently was part of the team that installed and commissioned the device on site in Australia in early 2010.

Also in 2010, an upgrade to the Hydro-Air test facility at Cranfield University was proposed by the author in order to reduce the mechanical losses in the drive train, to improve the instrumentation, to enable the validation of control strategies and to simplify the modeling of the turbine and associated components. The test-rig Supervisory Control And Data Acquisition (SCADA) system has subsequently been upgraded and the ability to generate polychromatic waves has been implemented.

Much research has been completed on optimizing the efficiency of the HydroAir turbine and other impulse turbines, but little research has been published in the area of power optimization control strategies for impulse turbine OWCs. The electrical system efficiency has often been considered only at full load. It is important to consider the issue of power smoothing as many sites suitable for the use of wave power farms have weak or island grid connections.

1.2 Objectives

The aim of this body of research is to take account of the full system when designing the control strategy and optimize accordingly, rather than concentrating on optimizing a single component. At a more specific level, the objectives of this research were as follows:

1. Derive a simulation model of the test facility
2. Develop a simulation model to represent the full wave-to-wire OWC system
3. Develop the PWG test facility to incorporate polychromatic waves
4. Derive an initial energy-based or power-based control strategy using the aforementioned simulation model with the view of power optimization and power smoothing

1.3 Contributions

- A generalization of the port-Hamiltonian framework for cases where the potential energy is dependent upon one or more of the momentum variables
- A further development in the field of the port-Hamiltonian framework whereby a change in reference frame allows the modeling of flow sources
- Development of a beyond state-of-the-art port-Hamiltonian model of the complete OWC wave-to-wire analytical model utilizing the aforementioned modifications to the port-Hamiltonian framework
- Development of a power-based control strategy for an energy storage system using a fixed inertia flywheel
- The development of a power-based control strategy for damping control of an OWC, using the port-Hamiltonian OWC system model
- An upgrade to the Cranfield University test facility to be the first in the world with bi-directional polychromatic wave capability
- Using the upgraded Cranfield facility, turbine CFD results were validated under bi-directional polychromatic flow conditions for the first time

1.4 Thesis Layout

The thesis is arranged in the following manner:

Chapter 2 gives a background to wave energy devices, in particular OWCs devices which are the focus of this study. It details the turbine choices for an OWC and the associated generators and inverters that enable the conversion of wave energy into electrical energy.

A simulation model for the full wave-to-wire model is presented in Chapter 3. It details the analytical and numerical modeling of each of the subsystems. First, energy-based modeling techniques such as Euler-Lagrangian mechanics, port-Hamiltonian systems and Brayton-Moser equations are reviewed as these methods have been applied to each of the subsystems. Two modifications to the port-Hamiltonian framework are introduced with the view to widening the range of systems they can be applied to. The chapter then progresses through each portion of the wave-to-wire model (e.g. hydrodynamic, pneumatic, and electrical). The discussion of each subsystem contains a literature review of the current modeling techniques before developing a new port-Hamiltonian model.

Chapter 4 first simulates a farm of "idealized" wave energy devices to assess the potential smoothing that can be achieved as a function of wave energy device spacing and size. It then progresses to present a simulation that enables an approximate calculation of the capacity required for an energy storage system in order to achieve a certain level of power smoothing.

Three different Passivity Based Control (PBC) strategies are introduced in Chapter 5, employing both a numerical and an analytical solver to find the desired operating condition for all state variables. The first control strategy is a speed controller for a multi-pole generic Doubly Fed Induction Generator (DFIG). This is followed with

a power-based control strategy for a fixed inertia flywheel energy storage system. The final control strategy introduced is applied to the full wave-to-wire model and controls the damping of the device within the constraints of the PTO system.

Validation of the control strategy proposed herein, although outside the scope of the present work, is possible using the PWG test facility at Cranfield due to its recent upgrade. This validation could take many forms, firstly providing a means of confirming the suitability of the modeling approach. Secondly, the effectiveness of the control strategy can be confirmed, since the PWG can accurately reproduce polychromatic waves. Finally, the confidence gained from these validations tests can be used to more accurately predict the system level efficiency of any proposed OWC installation.

A review of the variety of OWC turbine test facilities is presented in Chapter 6, which then details the development work that has been conducted on the Cranfield test facility, including the upgrade of instrumentation and the data acquisition system. The chapter then details the work involved in creating polychromatic waves. The ability to test turbine control strategies under more realistic sea conditions with the use of polychromatic waves, prior to deployment at sea, will reduce the risk and uncertainty that goes hand in hand with a first installation.

The final chapter, 7, concludes this report and reviews the findings of the subsequent chapters and details potential future development work.

Chapter 2

OWC Technology Overview

2.1 Wave Devices

Wave energy conversion is a relatively immature technology at present and, as a result, no single technical solution has yet become dominant. As a consequence, there is a plethora of types of wave energy devices. These have been categorized by the European Marine Energy Center (EMEC) under the following headings (EMEC Ltd 2009):

- Overtopping / terminator device
- Attenuator
- Point absorber
- Oscillating wave surge converter
- Submerged pressure differential
- Oscillating Water Columns (OWCs)

This body of research concentrates only on the last, OWCs.

2.2 Oscillating Water Columns

The basic principle of an OWC is that a volume of air is trapped within a hollow structure between a water surface and a turbine. As the water level rises and falls, air flows back and forth through the turbine(s), which is the mechanism for harnessing the wave power, see Figure 1.1. The design changes considerably from concept to concept. The main variables are the direction of entry of the waves (e.g. Backward Bent Duct Buoy (BBDB), Forward Facing Duct Buoy (FFDB) or vertical draft), see Figure 2.1, the device's geometry (e.g. circular or square), the number of chambers housed together, and the device's location: on-shore, near-shore, or off-shore. On-shore are those devices that are land-based, near-shore are those in water less than 40m deep and off-shore are those in water deeper than 40m (Thorpe 1999).

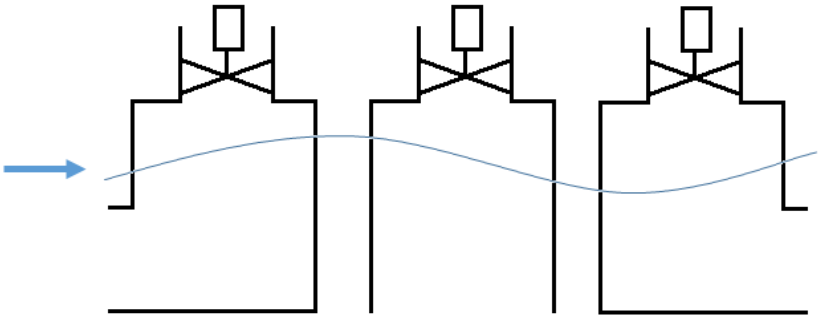

Figure 2.1: Buoy Shapes a) FFDB, b) Vertical draft c) BBDB

A number of on-shore devices have been commissioned such as Matriku, in the Basque country, (Amundarain, Alberdi, Garrido & Garrido 2010), Pico, in the Azores (Torre-Enciso et al. 2009) and the Limpet device on the Isle of Islay, in the Hebrides (Alcorn & Beattie 2001). The Limpet device is shown in Figure 2.2 this had a Wells turbine rated at 18kW.

Two very different installed near-shore OWCs are shown in Figure 2.3 by Ocean Energy and Oceanlinx respectively.

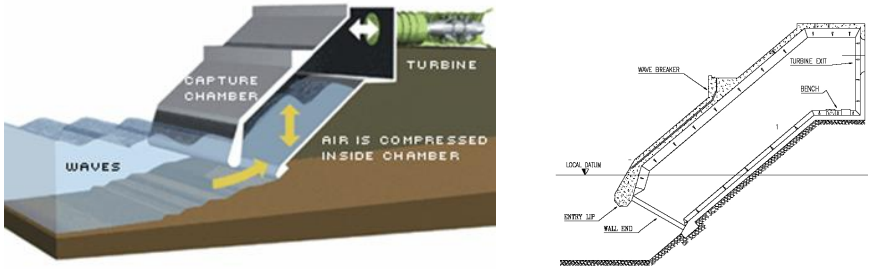

Figure 2.2: Limpet diagrammatic and side view (Folley & Whittaker 2002)

The Ocean Energy device is a BBDB (Ocean Energy Ltd 2011), suitable for deep water. The Ocean Energy prototype was installed at the Irish National Scale Test Site in Galway in December 2006 and has been through multiple stages of testing and development, O'Sullivan et al. (2011).

The Oceanlinx prototype device was commissioned in February 2010, grid connected and operated successfully over a three month period, Oceanlinx Ltd (2010a). Their full-scale designs, greenWAVE and blueWAVE, are designed for different water depths. The greenWAVE device is a single concrete chamber sitting on the ocean bed in a water depth of 10-15m, whereas the blueWAVE device has six chambers floating in deep water, Oceanlinx Ltd (2010b, 2011a). Oceanlinx were previously known as Energetech and their initial design, which preceded the greenWAVE and BlueWAVE concepts, incorporated the use of parabolic walls to concentrate the waves into the chamber. A schematic representation of this device can be seen in Figure 2.4.

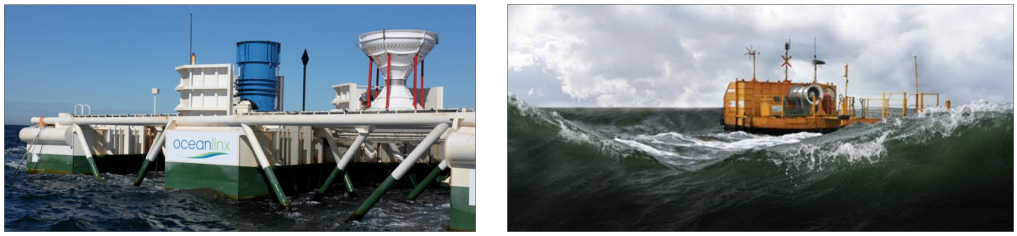

Figure 2.3: Examples of near-shore installations: Oceanlinx prototype device at Port Kembla (Oceanlinx Ltd 2011b) and Ocean Energy prototype device at Galway Bay (Ocean Energy Ltd 2011)

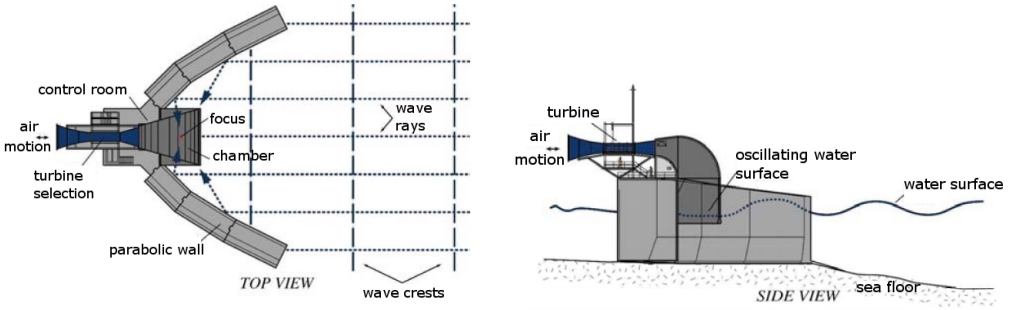

Figure 2.4: Energetech prototype device with parabolic wall focusing the waves into the chamber (Alcorn & Finnigan 2004)

Oceanlinx are not alone in designing multiple chambers in one platform. Orecon developed a device that was based on the Multi Resonant Chamber (MRC) concept, presented by (Johnson & Dai 2003), which employed multiple chambers of different lengths built into the same floating structure. Each chamber has a different draft length tuning it for a specific range of wave frequencies which theoretically widens the operating range of the device. A drawing of the MRC device for a 1.5MW system can be seen in Figure 2.5.

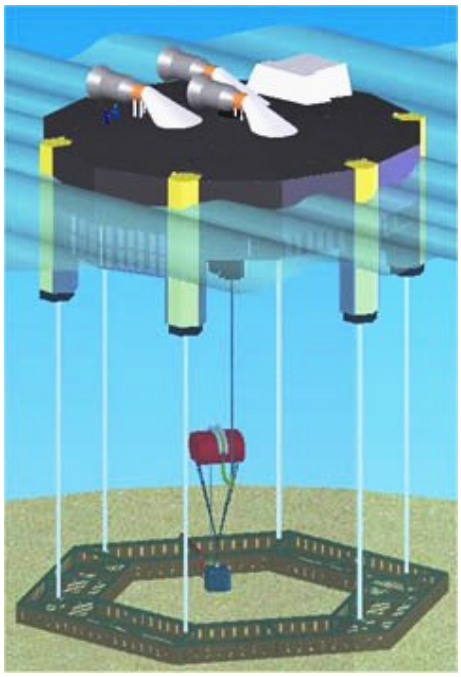

Figure 2.5: The MRC OWC device (Renewable Energy Development 2009)

One of the early OWC concepts was the floating wave power generator Kaimei

(Masuda et al. 2002), which was tested between 1976 and ∼1984 and developed by Japan Marine Science and Technology Center (JAMSTEC). It was installed in the sea near Yura in the Wakayama Prefecture of Japan. Kaimei was 80m long, 12m wide and used an impulse turbine with a valve. Masuda et al. (2002) also stated that the device survived a long time but the efficiency was insufficient to make it economically viable and testing against a BBDB showed that it had significantly poorer efficiency.

JAMSTEC started development on the Mighty Whale concept in 1987 and a prototype was installed in 1998, at the mouth of Gokasho Bay in Mie Prefecture (Washio et al. 2001). A schematic of the Might Whale device can be seen in Figure 2.6. The device had a power rating of 110kW and was tested for several years (Falcão 2010).

In order to increase power density, concepts have been developed that combine OWCs with alternative energy technology. One such device has been developed by Marine Power Technologies (MPT). It is a triangular-shaped "island" equipped with six OWCs submerged and a number of wind turbines above the waterline, rated at 10MW (Earth Techling 2010).

Wave Energy Ireland have developed a concept which employs two legs joined at 90 degrees with trusses between the two legs for structural strength (Kelly et al. 2013), see Figure 2.7. Each leg contains a number of OWC chambers which are connected to two plenums via air admittance valves. One plenum operates at a pressure higher than atmosphere and the other which operates at a pressure lower than atmosphere. The OWC and plenum arrangement has been tested at 1:50 scale and showed that the OWCs can be manifolded and rectified in an efficient manner (Kelly et al. 2013). It can be assumed that the resulting benefit would be the use of unidirectional turbines from the rectified air and a single air turbine per plenum chamber rather than per OWC chamber. It is stated by Kelly et al. (2013) that it

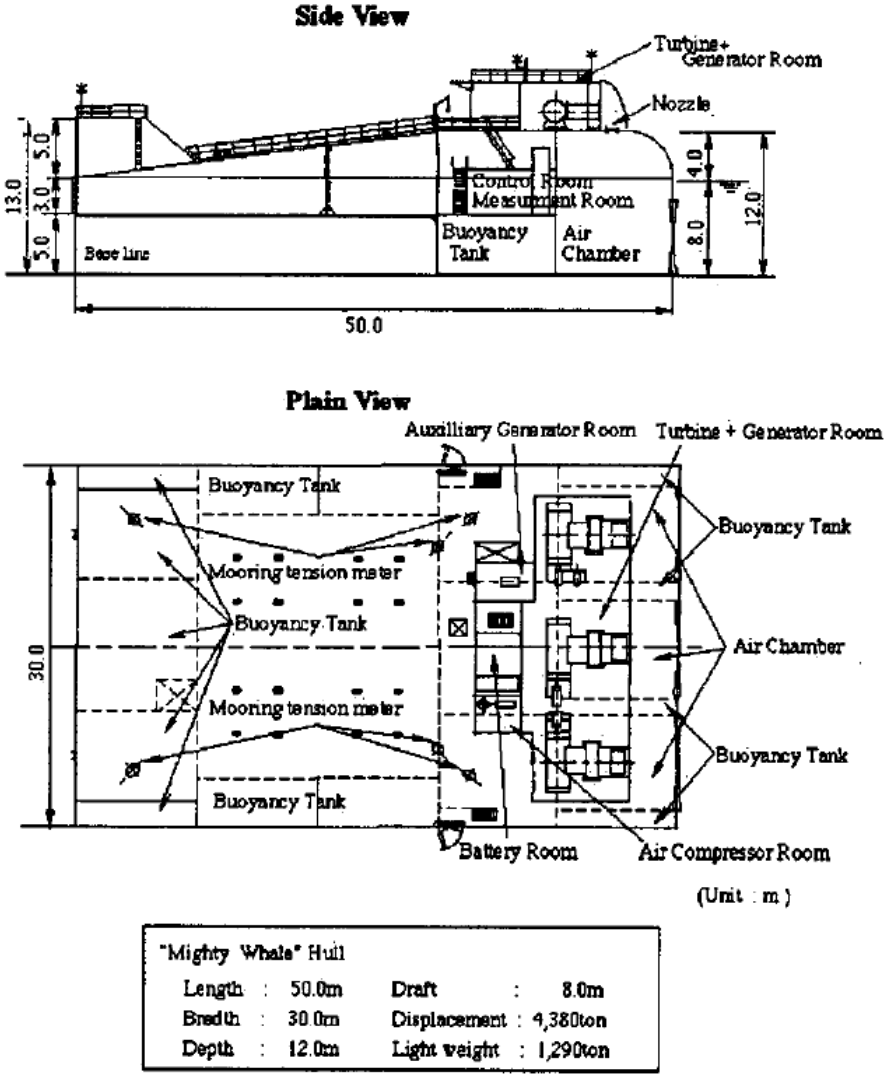

Figure 2.6: Mighty Whale (Washio et al. 2001)

is intended that wind turbines will also be placed on the structure.

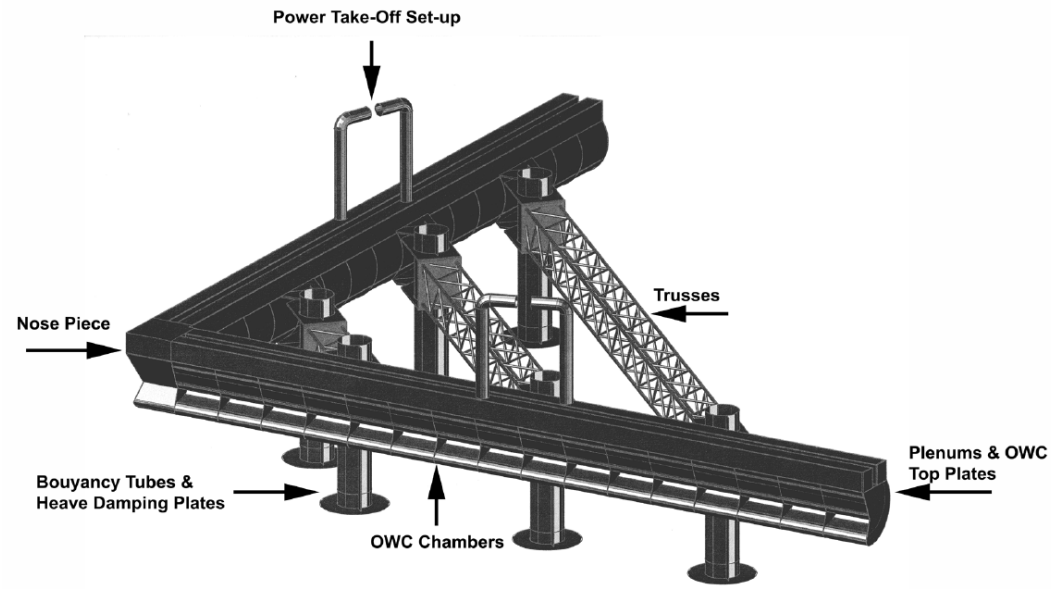

Figure 2.7: Wave Energy Ireland (Kelly et al. 2013)

As has been shown, the designs differ greatly and will therefore affect the system modeling. The motion of a floating device can have up to six degrees of freedom (surge, sway, heave, pitch, yaw and roll). A cylindrical device, with a bottom opening will mainly move with heave motion, however the BBDB and FFDB devices are designed to take advantage of the water movement from additional degrees of freedom such as pitch. This can potentially increase the power yield.

2.3 OWC Turbines

Since the OWC technology is still in its infancy, there are multiple technical solutions still under investigation particularly in the area of turbine design. The literature on OWC control is sparse, and due to the different control inputs, each is specific to the turbine in question. As a consequence, if a thorough knowledge of existing OWC control strategies is to be obtained, strategies for turbine designs other than the

impulse turbine must also be studied. The literature review in Section 5.1 expands upon the various control strategies.

The variety of turbines will be discussed in the following sections, they have different principles of operation and therefore a knowledge of their mechanism of operation is essential in understanding what information from each strategy can be carried across to the impulse turbine. The oscillating airflow produced by the oscillating column creates a need for specialized turbines. In conventional thermal gas and coal power generation the turbine is provided with unidirectional working fluid flow of a fairly constant flow rate. In OWCs the airflow is reciprocating and the air flow varies greatly with the incident wave elevation.

2.3.1 Unidirectional Turbines

According to McCormick et al. (1992), the earliest implementations of the OWCs used unidirectional turbines, with flaps to rectify the air flow. McCormick et al. (1992) states that the main problem with these turbines was the risk of the valves not operating correctly and sticking in one or other of the extreme positions. In addition, if the valves failed in an intermediate position, the result would be a pressure leakage which would cause a reduction in the power captured.

2.3.2 Bidirectional Turbines

A number of novel bidirectional turbines have been designed, many with OWCs devices in mind, and have been extensively developed to increase their efficiency. The following is a list of bidirectional turbines designed for OWCs: the Wells turbine (Thakker & Abdulhadi 2008), Impulse turbines (Banks 2009) including the McCormick turbine (McCormick 1981a) and the Biradial turbine (Falcão & Nunes

2013a), the Denniss-Auld turbine (Alcorn & Finnigan 2004) and the Savonius turbine (Dorrell et al. 2010b).

The performance of the turbines are usually given as the efficiency, η, against the flow coefficient, Φ. The flow coefficient is defined as

$$\Phi = \frac{V_a}{U} \tag{2.1}$$

where V_a is the axial velocity and U is the radial rotational velocity at the mid point of the blade. The ideal turbine has a high peak efficiency and broad operating width i.e. the efficiency does not decrease rapidly for flow coefficients either side of the peak efficiency point.

2.3.3 Wells Turbine

Alan Wells designed and developed the Wells turbine in 1976 (Thakker & Abdulhadi 2008). It is a turbine based on the aerodynamic lift principle and its basic design is a symmetrical blade mounted perpendicular to the flow direction (Wells 1981). There are many variations on the initial design which have been described extensively by Setoguchi & Takao (2006) and Pereiras et al. (2011). The Wells turbine is known to have high peak efficiency but a narrow operating range. It is not self-starting and is reported to be noisy in comparison with other conventional turbines (Thakker & Abdulhadi 2008), particularly at stall conditions (Neumann et al. 2007). Designs have been introduced to mitigate some of the design weaknesses of the turbine. Numerous designs have been proposed as described by Setoguchi & Takao (2006). These turbines include: Wells Turbine with Guide Vanes (WTGV), Turbine Self-pitching Controlled Blades (TSCB), Self-pitch controlled guide vanes, Biplane Wells Turbine with Guide Vanes (BWGV), Variable pitch angle blades and Contra Rotating Wells Turbine (CRWT). Four of these turbines are shown in Figure

2.8. The turbine characteristics for the WTGV, TSCB and the BWGV are shown in Figure 2.9. It can be seen that the torque falls off quickly, as the blade stalls, for the WTGV at low flow coefficients. The BWGV has lower peak torque coefficient and also suffers from stall at low flow coefficient. However, the TSCB has both high peak torque coefficient and the blades stall at a much higher flow coefficient. The Wells designs with pitching components, are more mechanical complex and potentially less reliable and as a result are unfavorable for device developers Falcão & Nunes (2013a).

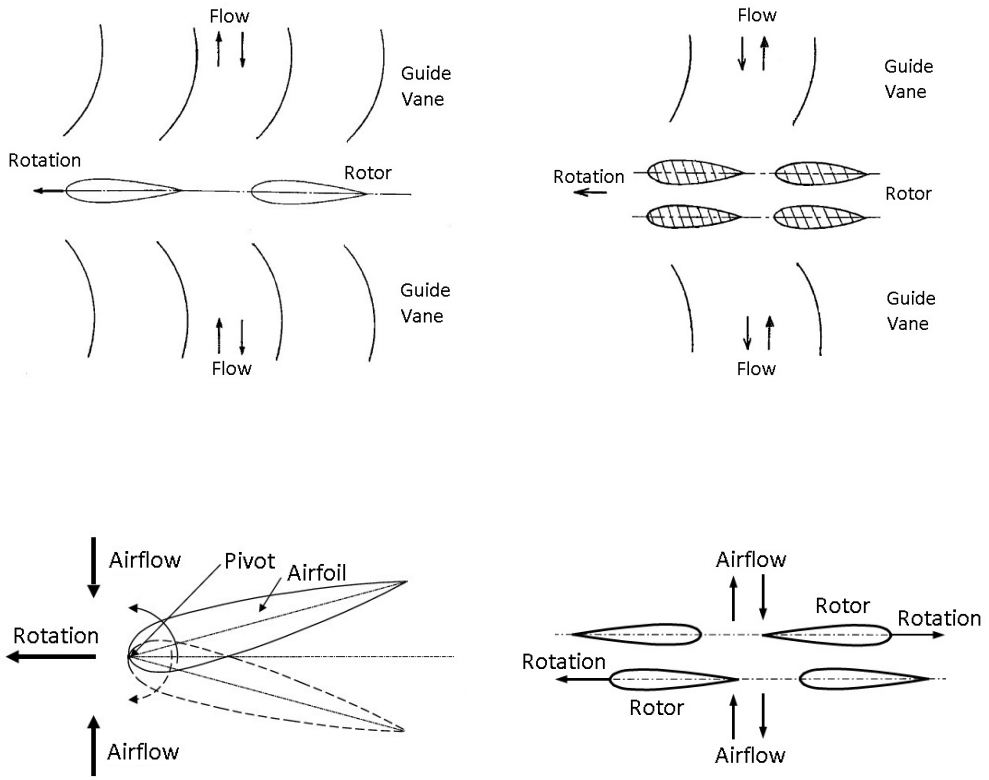

Figure 2.8: Different Wells turbine designs going from left to right, top to bottom: WTGV, BWGV, TSCB and lastly the CRWT (Setoguchi & Takao 2006)

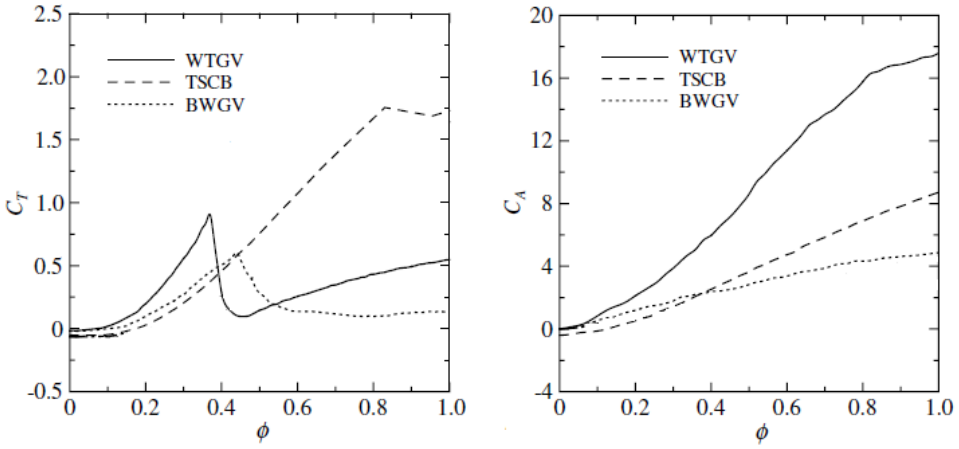

Figure 2.9: Wells turbine characteristics (Setoguchi & Takao 2006)

2.3.4 Denniss-Auld Turbine

The Denniss-Auld turbine was developed as a joint effort between the company Energetech (subsequently Oceanlinx) and Sydney University to overcome the performance limitations of the Wells turbine over the range of expected flows as a result of the Wells design's tendency to stall at flow coefficients above 0.3 (Alcorn & Finnigan 2004, Polinder & Scutto 2005).

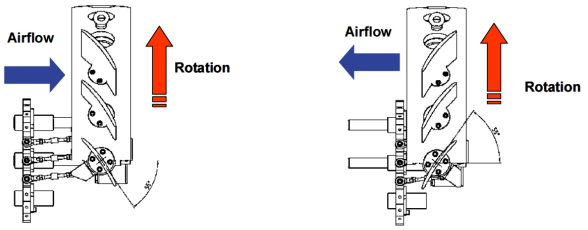

Figure 2.10: Energetech turbine pitching mechanism (Alcorn & Finnigan 2004)

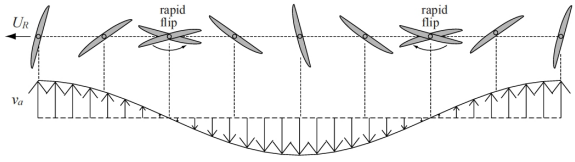

Figure 2.11: Blade pitching sequence in oscillating flow (Finnigan & Auld 2003)

The rotor blades are mounted parallel to the axis rather than perpendicular; as is the case with the impulse and the Wells turbine, there are also symmetrical tangentially

and axially. The rotor blades are pitched through a much greater angle than for a Wells turbine, and the blades have to turn as quickly as physically possible every half wave, Falcão (2010). Figures 2.10 and 2.11 show the angles that the blades traverse every cycle and the direction of air travel relative to the direction of rotation of the shaft. The efficiency curve of the Denniss-Auld turbine can be seen in Figure 2.12, which shows that the turbine has relatively high peak efficiency but, like the Wells turbine, this falls off relatively quickly either side of the peak. This graph also shows the relationship between the non-dimensional pressure, p^*, and the flow coefficient. It can be argued (De Miguel 2010), that the Denniss-Auld turbine, which has a complicated mechanism with several moving parts is potentially unreliable.

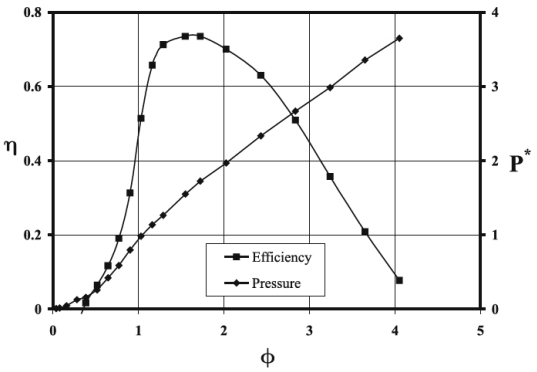

Figure 2.12: Efficiency and non-dimensional pressure drop against flow coefficient for the Denniss-Auld turbine (Curran & Folley 2008)

2.3.5 Savonius Turbine

The Savonius turbine which is more usually associated with wind turbines has been proposed by Dorrell et al. (2010a) for use with OWCs. A schematic of the turbine can be seen in Figure 2.13. Dorrell et al. (2010a) states that the turbine is simple, robust, has good starting characteristics but poor peak efficiency. It was proposed that it would be suitable for smaller OWC applications where the flow coefficient

would be large and hence a Wells turbine would be operating away from its peak efficiency point. In addition, Dorrell et al. (2010a) stated that the turbine could be mechanically cascaded between adjoining chambers.

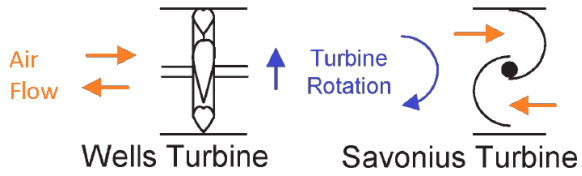

Figure 2.13: Savonius wind turbine (Dorrell et al. 2010a)

2.3.6 Impulse Turbine

Impulse Axial Turbine

A few variants of the impulse turbine design have been suggested for use on OWCs. The design of two, the Impulse turbine with Fixed Guide Vanes (IFGV) and the Impulse turbine with Self-pitching linked Guide Vanes (ISGV), are axial designs and can be seen in Figure 2.14. Guide Vanes (GVs) on bidirectional turbines act as Inlet Guide Vanes (IGV) for half the time and Outlet Guide Vanes (OGV) for the other half.

As its name suggests, the GV on a IFGV are fixed (i.e. the IFGV is not a variable geometry machine). The exit angle from an optimized IGV is not aligned with the incident flow when its operating as an OGV. As a result there are large losses associated with the OGV. However this type of turbine, as it has no moving parts besides the rotor, is considered to tradeoff robustness against a lower peak efficiency than the variable geometry designs.

The ISGV, on the other hand, has GVs that self-pitch and align with the incident flow in both the IGV and OGV operation mode. In comparison with the IFGV,

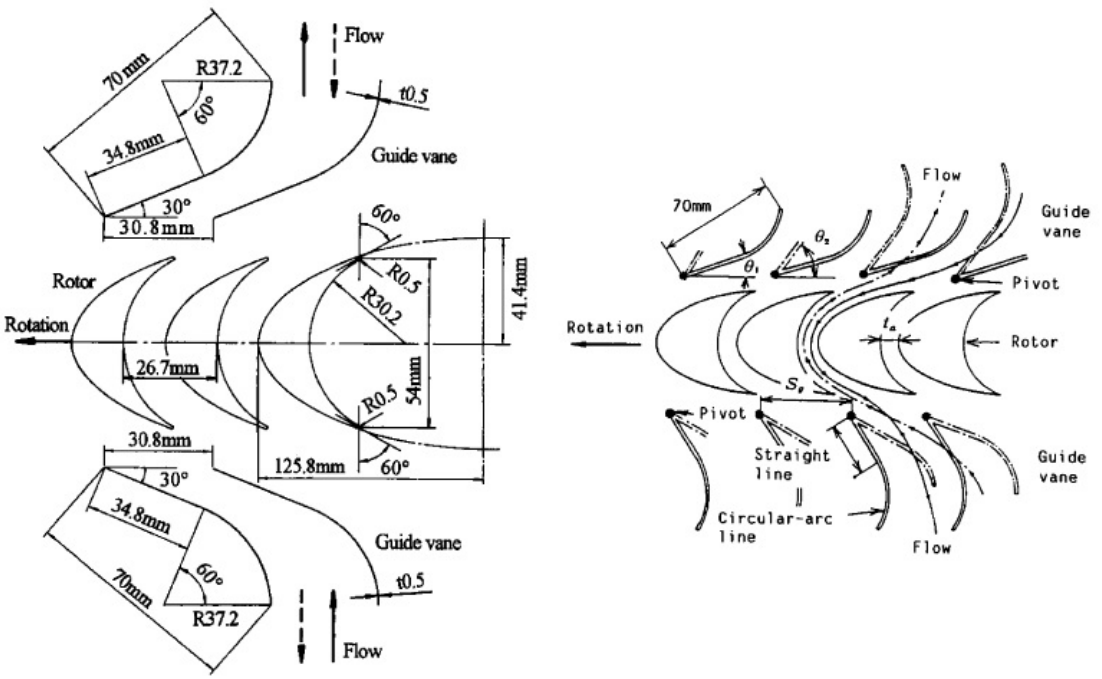

Figure 2.14: IFGV and ISGV turbines (Setoguchi & Takao 2006)

the efficiency is generally higher but the reliability is considered to be a potential problem, resulting in increased maintenance and operation costs (Pereiras et al. 2011).

Variable Radius Turbine

The Variable Radius Turbine (VRT) design, was patented in 2008 (Freeman et al. 2008) and the patent holders are now Dresser-Rand (Dresser-Rand Company Ltd 2015). The IGV and OGV are positioned at a larger radius (relative to the main turbine axis) than the rotor blades, see Figure 2.15, which reduces the velocity through the GV. The viscous losses are proportional to the square of the local velocity and therefore by decreasing the velocity the efficiency of the turbine can be increased (Banks 2009). In addition, the VRT is a variant of the IFGV class of machines and as such has no moving parts other than the rotor, and in such a harsh environment will likely be more robust and require less maintenance (Dresser-Rand

Company Ltd 2015). This turbine is the subject of this body of research.

Figure 2.15: HydroAir prototype VRT (Dresser-Rand Company Ltd 2015)

McCormick Counter-Rotating Turbine

The McCormick turbine has two rotor rows and two stator rows (McCormick 1981a). Though the rotors turn in opposite directions the shafts are connected through bevel gears and hence rotate at the same speed. The additional complex mechanical arrangement is likely to increase the required maintenance and decrease the reliability in comparison with the IFGV machines (Banks 2009). Each rotor row acts as a moving stator for the other rotor row, McCormick (1981a,b). The design can be seen in Figure 2.16 and 2.17. As far as the author is aware, the McCormick turbine is purely a theoretical design and has not been manufactured. No literature has been found to suggest the efficiency of the turbine. According to Banks (2009) the McCormick turbine is a variant of the impulse turbine.

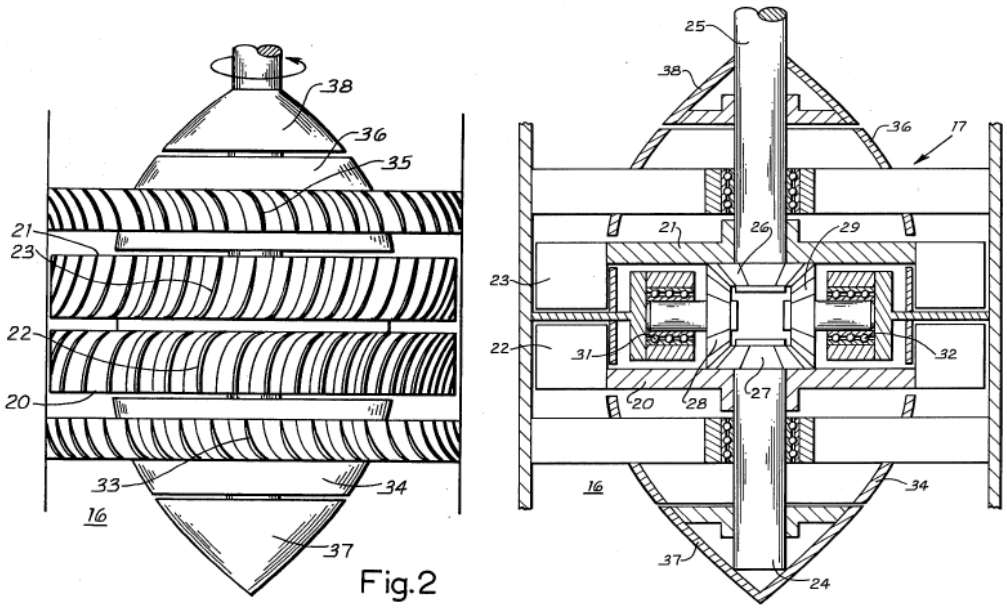

Figure 2.16: McCormick turbine design as shown in the patent (McCormick 1981a)

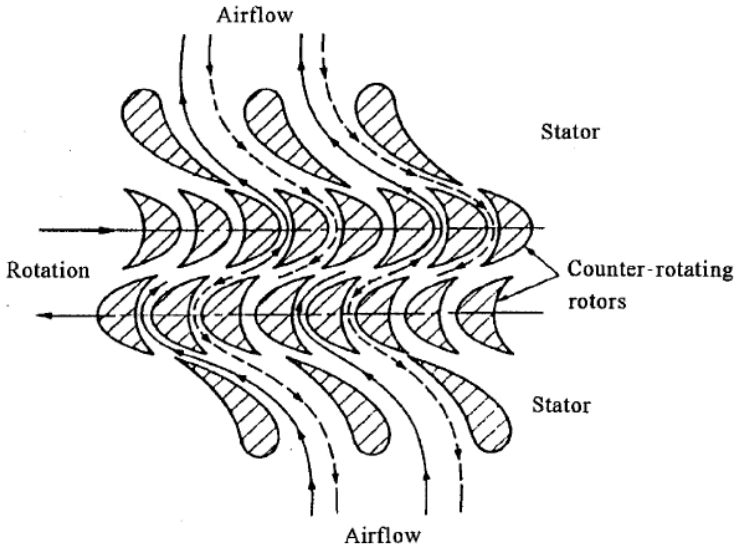

Figure 2.17: McCormick contra-rotating stator and rotor rows (Setoguchi & Takao 2006)

Radial Turbine

McCormick et al. (1992), proposed a radial flow turbine and stated that it had a broader operating range in comparison to the counter-rotating turbine. A literature review conducted by Setoguchi et al. (2002) found that the impulse bladed radial turbines had higher performance than reaction bladed radial turbines. However, detailed performance characteristics were not available and therefore Setoguchi et al. (2002) conducted experiments to obtain the characteristics for a 508.8mm diameter turbine for a range of GV geometries. A diagram of an impulse bladed radial turbine can be seen in Figure 2.18. Pereiras et al. (2011) proposed an improved variation on the radial design by changing the blade and GV profiles and changing the setting angles between them. Pereiras et al. (2011) stated that it subjected the OWC to higher damping, and produced higher torque at a lower speed than axial turbines.

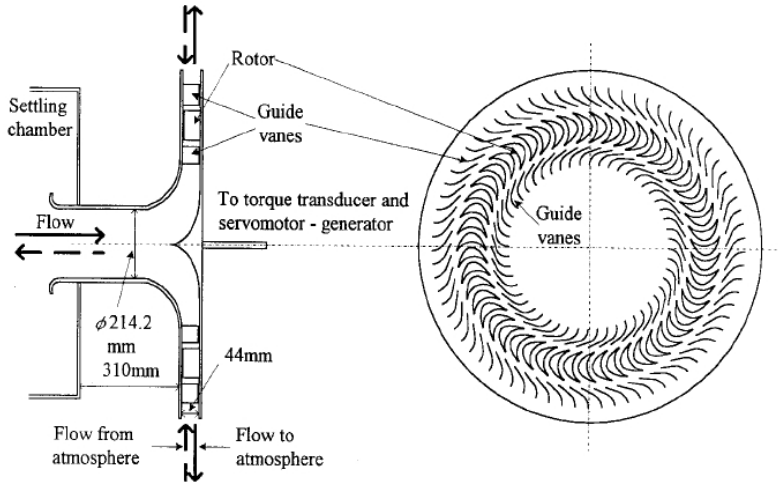

Figure 2.18: Diagrammatic representation of a radial turbine (Setoguchi et al. 2002)

The advantages of the biradial turbine as proposed by Falcão & Nunes (2013a), see Figure 2.19(a), is the compactness of the design, where the ratio of the duct radius to the rotor radius is 3.1. Falcão & Nunes (2013b) proposed a modified version of the biradial turbine which moves the GVs so that there is only an IGV and no OGV, see Figure 2.19(b). The main disadvantages of this design variant, are the moving

GVs, which may pose a potential reliability issue, and determining exactly when to switch the GV position, for optimum efficiency in polychromatic seas. In an infinite response system this issue would be eliminated as the GVs could be directly coupled to the pressure sensors; however, since the response is finite there is a risk of phasing issues in the control of the GVs.

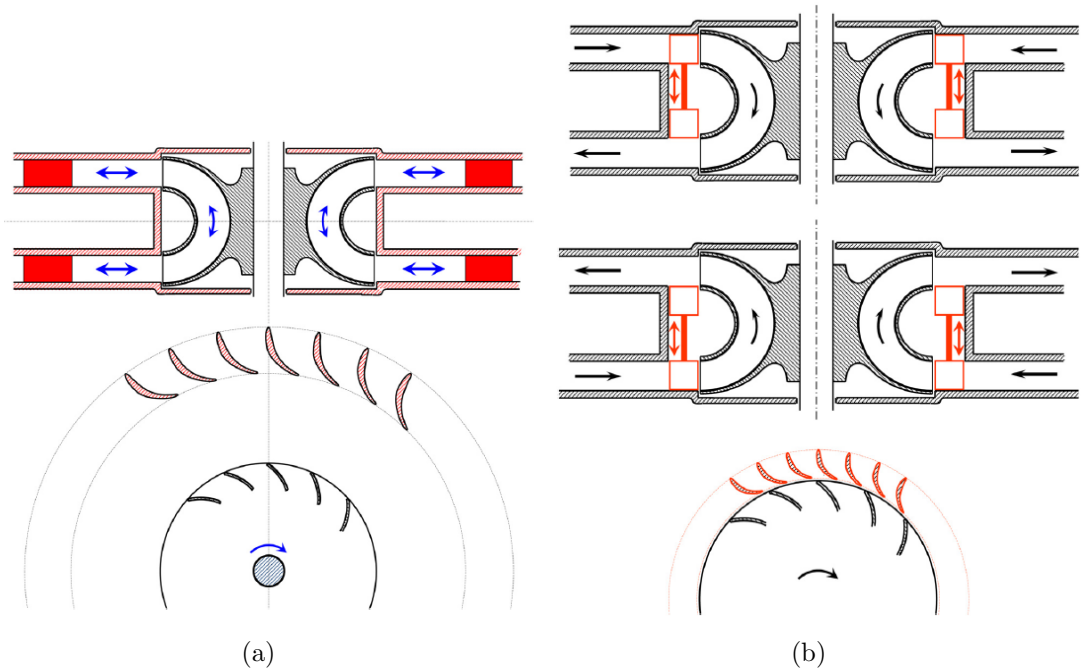

(a) (b)

Figure 2.19: Diagrammatic representation of a biradial turbine with a) fixed guide vanes and b) moving guide vanes (Falcão & Nunes 2013a)

2.4 OWC Electrical PTO System

The power take-off system attached to the turbine consists of a generator and an Integrated Gate Bipolar Transistor (IGBT) regenerative back-to-back inverter drive. The selection of both is a balance between efficiency, operating range and cost. In addition, there are problems to consider such as harmonics, maintenance requirements, reliability etc. A brief discussion will therefore follow on directly as to the technology that could be considered during the design of the power take-off package.

The power take-off system attached to the turbine consists of a generator and an IGBT regenerative back-to-back inverter drive. The selection of both is a question of efficiency, operating range and cost. In addition, there are problems to consider such as harmonics, maintenance requirements, reliability etc. A brief discussion will therefore follow on directly as to the technology that could be considered during the design of the power take-off package.

2.4.1 Generator Selection

There are four main types of generator that will be briefly discussed within this section. These are: Synchronous Generator (SG), Doubly Fed Induction Generator (DFIG) otherwise known as Wound Rotor Induction Generator (WRIG), Squirrel Cage Induction Generator (SCIG) and Permanent Magnet Generator (PMG). O'Sullivan & Lewis (2008) provide a good review of selection criteria for generators to be used on wave devices. A summary of the advantages and disadvantages is provided in Table 2.1. PMGs have a significant initial cost (O'Sullivan & Lewis 2008) though this is mitigated by reduced lifetime costs in comparison with DFIGs. Special attention is required for the PMG system design when considering grid faults which cause island operation, as additional equipment may be required (Hodgins 2010) to prevent machine over speed as the magnetic field can not be switched off. SGs are not suitable for VRT due to the fixed speed which leave the option of DFIGs and SCIGs. The SCIG has a wider speed operating range than the DFIG but requires a fully-fed inverter which is more costly than the third rated inverter that the DFIG machine requires. As a result, the decision depends on the particulars of the OWC. Both the SCIG and the DFIG have been considered for this study.

Table 2.1: Generator selection advantages and disadvantages (O'Sullivan & Lewis 2008)

Generator	Advantages	Disadvantages
DFIG	a) variable speed, b) requires only 1/3 rated inverter for rotor control	a) susceptible to shock loadings as directly connected to the grid, b) brushes need to be changed twice a year
SCIG	a) variable speed	a) several percent less efficient than the PMG and SG
SG		a) fixed speed, b) experience high shock loadings from the grid, c) unable to use the inertia of the system to reduce power fluctuations
PMG	a) variable speed, b) higher efficiency than SG, SCIG and DFIG	a) not currently manufactured in large volume between 100kW and 1MW, b) susceptible to corrosion more than alternative generators in saline environment

2.4.2 Inverter Selection

Variable speed motors output variable frequency voltage which needs to be converted to the fixed frequency of the grid connection point. In Europe this is 50Hz and in North America this is 60Hz. For a SCIG, all the power is transferred through the stator windings to the inverter and so it has to be rated to the maximum power capability of the device. Conversely the DFIG connects the inverter to the rotor windings and transfers only a third of power and hence the inverter unit is cheaper. IGBT inverters are quoted as having an efficiency as high as 98%. However the power consumed is approximately the same under part load as it is full load and hence for a variable power device such as an OWC it may be considered useful to use a modular system e.g. five 200kW power modules or power slices to provide a 1MW system where only the necessary number of modules are switched on at any given moment. Control Techniques offer a product, (Control Techniques - Emerson Group 2015),

which uses a master power module to control additional power modules, electrical arranged in parallel with each other. By switching these parallel modules in only when needed the part load efficiency of the IGBT system may be improved. An additional benefit of such a strategy is that if there is a failure of one module or if one of the modules requires maintenance then the device can continue operating at a reduced capacity. Drury (2009) presents a useful comparison of the IGBT drive with some of the alternatives such as a Thyristor drive. The Thyristor drive has higher switching losses; however, it has a capability up to 30MVA in comparison with a limit of 4MVA with the IGBT drives. It is the high switching frequency of the IGBT drive that makes it so efficient. Although the use of a back-to-back IGBT inverter topology causes extra losses in the power conversion system, it is this component that allows the Wave Energy Converter (WEC) to operate in a variable speed mode, allowing more of the energy of the wave to be captured. It enables more flexibility in the turbine operation and therefore greater wave-to-wire efficiency.

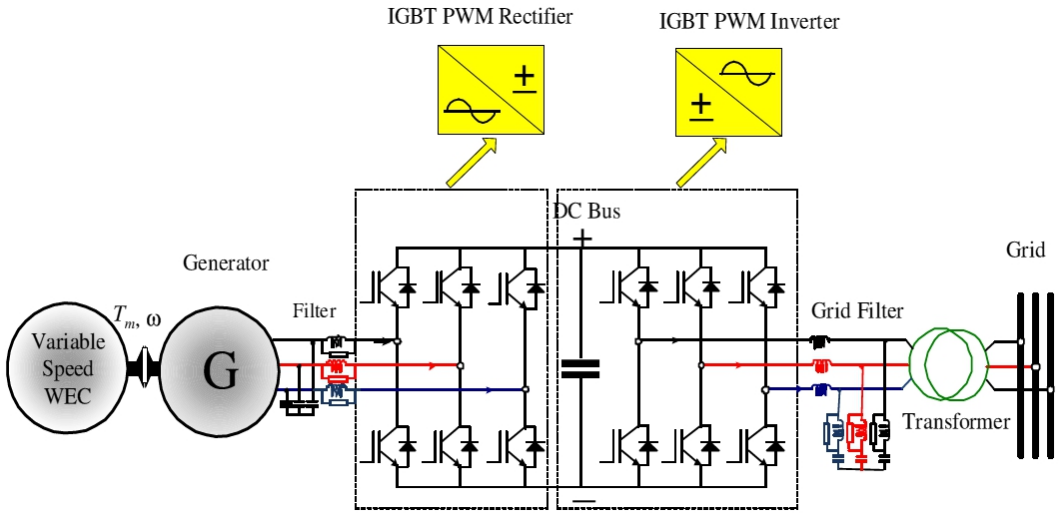

Figure 2.20: Back-to-back rectifiers for generator power rectification for non-synchronous speeds (Ahmed & Zobaa 2009)

2.4.3 Power Conditioning

Grid standards are different from country to country; however, similarities do exist. ENA ER G59/2 and G81 are two of the relevant standards for the UK that are dependent on the voltage and power rating. The grid standards are very complex and cover a large number of topics. For the moment, only the following will be discussed:

The Power Factor (PF) is basically the ratio of real power to the apparent power. PF correction, to reduce cable losses, is easily achievable in a fully-rated converter. PF is a tunable parameter depending on site requirements. It is possible for the grid to request a certain power factor to be delivered from the power generation unit in order to help compensate for others on the local distribution network.

Voltage harmonics occur when the voltage signal does not represent a truly sinusoidal output. When a fully-rated IGBT converter is used, harmonics should not be a problem as long as the equipment meets the relevant standards (Control Techniques Ltd 2009b). Flicker pertains to voltage fluctuations at lower frequencies as the human eye can detect flicker between 5-20Hz. Drury (2009). According to Alcorn & Beattie (2001) the problem relating to flicker and the quantification, measurement and control to minimize the same is more difficult than complying with the voltage and harmonic regulations.

Electro-Magnetic Interference (EMI), on the other hand, can be a problem locally, corrupting instrumentation and control signals, but as EMI is not transferred through transformers, it is not considered a problem as far as the grid is concerned, unless there is no dedicated transformer for the wave device/farm. Complying with the recommendations from the power module suppliers should prevent problems with EMI, but selecting resilient and highly immune electronics is always advisable (Control Techniques Ltd 2009a). EMI can be problematic if installation recom-

mendations are not followed for example is the power cables are unscreened or insufficiently screened.

Appropriate selection and installation of the power conditioning equipment along with appropriate switch gear (e.g. circuit breakers and isolators), filters and transformers goes a long way to preventing issues with the aforementioned grid requirements. For example, solving EMI problems on an installed unit can be a minefield. Appropriate attention to detail is essential.

Chapter 3

Analytical Model of an OWC Wave-to-Wire System

3.1 Modeling Introduction

This chapter discusses the development of dynamic models of four subsystems (hydrodynamic, pneumatic, mechanical and electrical) for an Oscillating Water Column (OWC) system and the integration of those subsystem models. The next section, 3.2, introduces the concepts of energy-based modeling, applying Euler-Lagrangian mechanics, port-Hamiltonian mechanics, Brayton-Moser systems and a brief discussion on bond graph methodology. These energy based modeling techniques will be extremely useful in designing a control strategy to manipulate the flow of energy within the system. However, for clarity, the present chapter progresses through the energy conversion from the incident wave to the electrical connection. Section 3.3 details the use of wave spectra in the creation of wave time series which are used as the input to the system model.

Section 3.4 focuses on the modeling of the hydrodynamics of an OWC using two

approaches. The first approach is a development of the work completed by Gervelas et al. (2011), which assumes frequency independent added mass and has been modified using Euler-Lagrangian mechanics to improve the model to take into account the force which is imposed on the system due to the rate of change of mass and the force that is applied on the system from mass leaving the system at non-null velocity. The second approach applies port-Hamiltonian mechanics in conjunction with hydrodynamic coefficients calculated using numerical Boundary Element Method (BEM) codes (such as WAMIT or, in this case, Nemoh) and are dependent on the wave frequency. The frequency independent method is simpler and less computationally expensive and has fewer system states. It is much less accurate than the frequency dependent method, however it can be argued, with its simplicity, has its place for initial design purposes, including control system design.

The pneumatic model is then discussed in Section 3.5; this model utilizes the non-dimensional flow rate and non-dimensional pressure drop relationship derived from Computational Fluid Dynamics (CFD) numerical simulations (conducted by Banks (2009), Natanzi (2010a), Tarver (2013) and the author of this thesis) to calculate the dimensionless turbine characteristics. The mechanical model is described in Section 3.6 and accounts for the windage, bearing and other losses of the turbine and generator. An electrical model for the generator is described in Section 3.7 for both Squirrel Cage Induction Generators (SCIGs) and Doubly Fed Induction Generators (DFIGs). The power converter/inverter was out of scope for this study. The fully system state equations are then given in Section 3.8. The contribution of this work is then detailed in Section 3.9 with a discussion of potential future improvements.

3.2 Energy Based Modeling

The present section provides a high-level overview of Euler-Lagrangian mechanics, port-Hamiltonian mechanics and Brayton-Moser system methods as presented in the literature of energy-based modeling, together with a description of the differences between the methods. For a more in-depth discussion please see the work by Jeltsema & Scherpen (2009). This is accompanied by a brief description of bond-graph for completeness.

3.2.1 Euler-Lagrangian Mechanics

For a detailed explanation of Lagrangian mechanics, see the work of Banerjee (2005). Presented here is merely a brief overview.

The Lagrangian function, $\mathscr{L}$, is the difference in energy between the kinetic energy, $\mathscr{T}$, and the potential energy, $\mathscr{V}$:

$$\mathscr{L} \triangleq \mathscr{T} - \mathscr{V} \tag{3.1}$$

The system equations are given by the Lagrangian equation in its general form,

$$\frac{d}{dt}\left(\frac{\partial \mathscr{L}}{\partial \dot{q}_i}\right) - \frac{\partial \mathscr{L}}{\partial q_i} + \frac{\partial \mathscr{R}}{\partial \dot{q}_i} = 0 \tag{3.2}$$

described in terms of the generalized positions, q_i, generalized velocities, $\dot{q}_i$ and the Rayleigh dissipation function, $\mathscr{R}$. The general form assumes that the potential energy is independent of the velocity. Dissipation is taken into account by the Rayleigh power dissipation function $\mathscr{R}$. In such cases, where the potential energy is a function of the velocity, it is necessary to use the modified Euler-Lagrangian

equation where

$$\frac{d}{dt}\left(\frac{\partial \mathscr{T}}{\partial \dot{q}_i}\right) - \frac{\partial(\mathscr{T} - \mathscr{V})}{\partial q_i} + \frac{\partial \mathscr{R}}{\partial \dot{q}_i} = 0 \tag{3.3}$$

It should be noted that the externally applied force is defined within the potential energy term. This is not the case for the port-Hamiltonian method which follows later in this chapter.

One of the benefits of using Lagrangian mechanics is that, in some cases, it can significantly reduce the number of system equations by enabling the use of alternative coordinate systems. For example, in the case of an inverted pendulum, the Cartesian coordinates can be replaced by an angle. Lagrangian mechanics also make it possible to integrate systems of different types (e.g. mechanical and electrical), where it can sometimes be difficult to identify how the systems are interlinked. In addition, the Lagrangian approach, when defining the system equations, reduces the complexity of interaction forces between different sub-elements.

3.2.2 Port-Hamiltonian Mechanics

The fundamental concept of port-Hamiltonian system is the flow of energy (i.e. power) in and out of a system through ports. The ports are defined by the product of effort and flow through interconnections to the outside world. A seminal book was written by Duindam et al. (2009) on the modeling and control of complex physical systems using the port-Hamiltonian approach. The Hamiltonian, $\mathscr{H}$, is defined as the total energy within the system, specifically the sum of the kinetic and the total energy

$$\mathscr{H} \triangleq \mathscr{T} + \mathscr{V} \tag{3.4}$$

The derivation of the system equations from the Hamiltonian equation is applicable to many systems and derives the first order equations directly rather than first

deriving the second order equations as per the Euler-Lagrangian method (Banerjee 2005).

In contrast to the Euler-Lagrange equations, the system is defined in terms of the momentum, Y_i, and position, q_i, variables rather than the velocity, $\dot{q}_i$, and position, q_i, variables, where the generalized momentum is defined as

$$Y_i = m\dot{q}_i \tag{3.5}$$

The generic form of the port-Hamiltonian system equations are given as

$$\dot{s} = (\mathscr{J} - \mathscr{R})\frac{\partial \mathscr{H}}{\partial s} + g_s u_c \tag{3.6}$$

where s is the state vector, $\mathscr{J}$ is the inertial matrix (which is skew symmetric) and $\mathscr{R}$ is the dissipation matrix (which is a diagonal matrix). The port-Hamiltonian system, as it name suggests, is centered around the concept of ports and the multiplication of the inputs by the outputs gives the power into the system. The outputs, y, are defined as the port flow variables, the complements to the effort variables.

$$y = {g_s}^T \frac{\partial \mathscr{H}}{\partial s} \tag{3.7}$$

where the input matrix g_s relates the externally applied efforts u_c to the state equations.

The rate of change of energy within the system is equal to the power through the ports which is the product of the effort, u_c, and flow, y, variables defined as

$$\frac{d\mathscr{H}}{dt} = {u_c}^T y \tag{3.8}$$

The power through the ports is not defined by the Hamiltonian and therefore, unlike

the Euler-Lagrangian case, the externally applied efforts are not defined as part of the potential energy.

3.2.3 Port-Hamiltonian Mechanics and Momentum Dependent Potential Energy

As stated in Section 3.2, the standard definition of the Euler-Lagrange equation is

$$\frac{d}{dt}\left(\frac{\partial \mathscr{L}}{\partial \dot{q}_i}\right) - \frac{\partial \mathscr{L}}{\partial q_i} + \frac{\partial \mathscr{R}}{\partial \dot{q}_i} = 0 \tag{3.9}$$

but this is a simplification which is incorrect when the potential energy is a function of the generalized velocities $\dot{q}_i$. Under these conditions the more accurate definition should be used (Banerjee 2005) which is

$$\frac{d}{dt}\left(\frac{\partial \mathscr{T}}{\partial \dot{q}_i}\right) - \frac{\partial (\mathscr{T} - \mathscr{V})}{\partial q_i} + \frac{\partial \mathscr{R}}{\partial \dot{q}_i} = 0 \tag{3.10}$$

It is proposed by the author of this thesis that the Hamiltonian equation can be adjusted in the same way taking into account that the Hamiltonian function is defined in terms of the momentum variables and the position coordinates rather than the flow variables and position coordinates, resulting in the formulation of the port-Hamiltonian system equations as

$$\dot{s} = (\mathscr{J} - \mathscr{R}) \begin{bmatrix} \frac{\partial \mathscr{H}}{\partial q_i} \\ \frac{\partial \mathscr{T}}{\partial Y_i} \end{bmatrix} + g_s u_c \tag{3.11}$$

in comparison with the standard equation

$$\dot{s} = (\mathscr{J} - \mathscr{R}) \frac{\partial \mathscr{H}}{s} + g_s u_c \tag{3.12}$$

An example of a DC motor and mechanical load, Figure 3.1, will be used to illustrate the modification suggested in Equation (3.11). The DC motor and mechanical load was presented by Banerjee (2005) for illustrating the same point with the Euler-Lagrangian system. The system is defined in terms of the armature winding inductance, L_w, the generator inertia, J_g, the load inertia, J_l, the electrical armature resistance, R_w, the mechanical resistances, B_g and B_l, the electrical charge, q_w, generator position θ_g and load position θ_l. The kinetic energy of the system is defined as

$$\mathscr{T} = \frac{1}{2}\frac{1}{L_w}\psi_w{}^2 + \frac{1}{2}\frac{1}{J_g}Y_g{}^2 + \frac{1}{2}\frac{1}{J_l}Y_l{}^2 \tag{3.13}$$

the potential energy of the system is defined as

$$\mathscr{V} = K_f\psi_f\frac{Y_g}{J_g}q_w + \frac{1}{2}k_s(\theta_g - \theta_l)^2 - K_f\psi_f\frac{\psi_w}{L_w}\theta_g \tag{3.14}$$

and the Rayleigh dissipation function is defined as

$$\mathscr{R} = \frac{1}{2}R_w\dot{q_w}{}^2 + \frac{1}{2}B_g\dot{\theta_g}{}^2 + \frac{1}{2}B_l\dot{\theta_l}{}^2 \tag{3.15}$$

Applying the standard port-Hamiltonian Equation, (3.12), gives the following par-

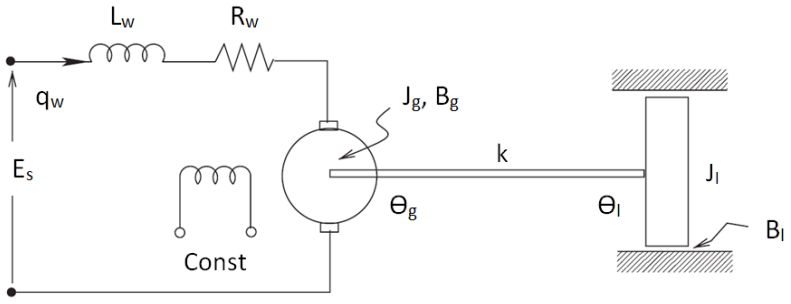

Figure 3.1: DC motor and mechanical load (Banerjee 2005)

tial differential equations

$$\frac{\partial \mathscr{H}}{\partial q_i} = \left[K_f \psi_f \frac{Y_g}{J_g}, \quad k_s(\theta_g - \theta_l) - K_f \psi_f \frac{\psi_w}{L_w}, \quad -k_s(\theta_g - \theta_l) \right]^T \tag{3.16}$$

$$\frac{\partial \mathscr{H}}{\partial Y_i} = \left[\frac{\psi_w}{L_w} - K_f \psi_f \frac{\theta_g}{L_w}, \quad \frac{Y_g}{J_g} + K_f \psi_f \frac{q_w}{J_g}, \quad \frac{Y_l}{J_l} \right]^T \tag{3.17}$$

$$\frac{\partial \mathscr{R}}{\partial \dot{q}_i} = \left[R_w \dot{q_w}, \quad B_g \dot{\theta}_g, \quad B_l \dot{\theta}_l \right]^T \tag{3.18}$$

These partial equations will not form the correct system equations. For example the state equation for the charge q_w will be defined as

$$\dot{q_w} = \frac{\psi_w}{L_w} - K_f \psi_f \frac{\theta_g}{L_w} \tag{3.19}$$

rather than

$$\dot{q_w} = \frac{\psi_w}{L_w} \tag{3.20}$$

Alternatively using the proposed modification for the port-Hamiltonian equation, the following partial differential is calculated from the kinetic energy,

$$\frac{\partial \mathscr{T}}{\partial Y_i} = \left[\frac{\psi_w}{L_w}, \quad \frac{Y_g}{J_g}, \quad \frac{Y_l}{J_l} \right]^T \tag{3.21}$$

From Equations (3.16), (3.18) and (3.21) the system equations are defined as

$$\begin{bmatrix} \dot{q_w} \\ \dot{\theta_g} \\ \dot{\theta_l} \\ \dot{\psi_w} \\ \dot{Y_g} \\ \dot{Y_l} \end{bmatrix} = \begin{bmatrix} 0 & 0 & 0 & 1 & 0 & 0 \\ 0 & 0 & 0 & 0 & 1 & 0 \\ 0 & 0 & 0 & 0 & 0 & 1 \\ -1 & 0 & 0 & -R_w & 0 & 0 \\ 0 & -1 & 0 & 0 & -B_g & 0 \\ 0 & 0 & -1 & 0 & 0 & -B_l \end{bmatrix} \begin{bmatrix} K_f \psi_f \dfrac{Y_g}{J_g} \\ k_s(\theta_g - \theta_l) - K_f \psi_f \dfrac{\psi_w}{L_w} \\ -k_s(\theta_g - \theta_l) \\ \dfrac{\psi_w}{L_w} \\ \dfrac{Y_g}{J_g} \\ \dfrac{Y_l}{J_l} \end{bmatrix} + \begin{bmatrix} 0 \\ 0 \\ 0 \\ 1 \\ 0 \\ 0 \end{bmatrix} \begin{bmatrix} E_s \end{bmatrix} \tag{3.22}$$

The modification to the formulation of the port-Hamiltonian system, given in Equation (3.11), will be used later for the induction generator equation formulation where the potential energy is a function of the velocities.

3.2.4 Brayton-Moser Systems

Where the Hamiltonian, $\mathscr{H}$, is defined in terms of the momentum and the position variables, the Brayton-Moser equation is defined in terms of the efforts, $\mathscr{E}$, and flows, $\mathscr{F}$. Examples of effort variables include voltage, torque, force and pressure and examples of flow variables are current, speed, velocity and flow rate. The efforts and flows are defined for each subsystem component rather than merely being defined for the external interface. The work by Jeltsema & Scherpen (2009) highlights that all components can be considered as either inductors, capacitors, resistors and mem-resistors irrespective of their domain type: translational mechanical, rotational mechanical, electrical, electromechanical, fluid etc. The definition of

the port-Hamiltonian system seems to limit itself in its usual form to systems that contain inductors. For an electrical system this would be a magnetic inductor, for a translational mechanical system this would correspond to mass, for a rotational mechanical system this would be the inertial component. However certain systems have no inertial component such as a current source circuit with no magnetic inductors. In these systems with no inertial component, the Brayton-Moser equation demonstrates its effectiveness.

The mixed potential function, which can be thought of as the definition of power in and out of the system, either through dissipation or port connections or from one component to another, is defined as

$$\mathscr{P} = \mathscr{R}(\mathscr{F}) - \mathscr{R}^*(\mathscr{E}) + \mathscr{E}^T \mathscr{N} \mathscr{F} \tag{3.23}$$

where the resistive content of the flow-controlled components is $\mathscr{R}(\mathscr{F})$ and the resistive co-content of the effort-controlled components is $\mathscr{R}^*(\mathscr{E})$. $\mathscr{N}$ is the interconnection matrix which connects the effort and flow variables. This definition enables the definition of dissipative power in terms of the effort and the flow variables unlike the Euler-Lagrange and port-Hamiltonian systems which define the dissipative energy in terms of purely the flow variables. The resistive co-content function incorporates the external forces applied to the flow variables whereas the resistive content function incorporates the external forces applied to the effort variables.

The system equations are defined as the rate of change of the partial differential of the Hamiltonian with respect to the flow variables:

$$-\frac{d}{dt}\left(\frac{\partial \mathscr{H}}{\partial \mathscr{F}}\right) = \frac{\partial \mathscr{P}}{\partial \mathscr{F}} \tag{3.24}$$

$$\frac{d}{dt}\left(\frac{\partial \mathscr{H}}{\partial \mathscr{E}}\right) = \frac{\partial \mathscr{P}}{\partial \mathscr{E}} \tag{3.25}$$

Note that for the Brayton-Moser systems, the mixed potential function is defined in terms of the flow variables rather than momentum variables. This is in direct contrast to the port-Hamiltonian framework, but aligned with the Euler-Lagrangian framework. Unlike both the port-Hamiltonian and the Euler-Lagrangian framework, the system is defined in terms of the effort variables instead of the position coordinates.

3.2.5 Port-Hamiltonian Mechanics and a Change of Reference Frame

In an effort to apply the Brayton-Moser approach (where the dissipation energy is defined either in terms of flow or effort) to a port-Hamiltonian framework one of the key challenges is the definition of the variables. This challenge arises as the port-Hamiltonian framework has generally only been applied to systems with an inertial component. Consider the two examples in Figure 3.2. The left hand figure is easily defined in the port-Hamiltonian framework where the effort variable is voltage, the momentum variable is flux, the flow variable is current and the position variable is charge.

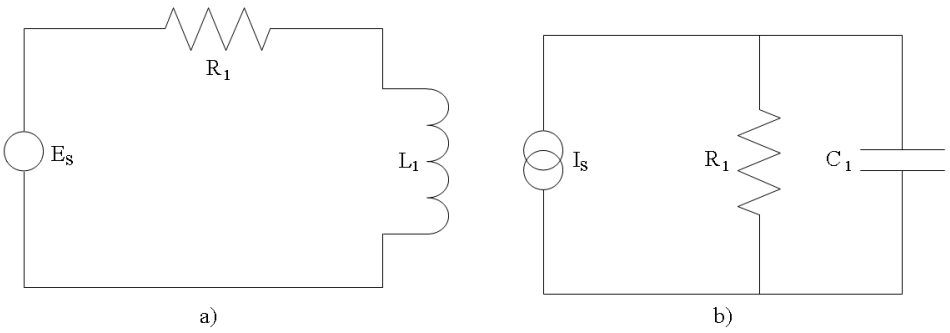

Figure 3.2: Voltage source and current source electrical systems

$$\begin{bmatrix} \dot{q_1} \\ \dot{\psi_1} \end{bmatrix} = \left(\begin{bmatrix} 0 & 1 \\ -1 & 0 \end{bmatrix} - \begin{bmatrix} 0 & 0 \\ 0 & R_1 \end{bmatrix} \right) \begin{bmatrix} 0 \\ \\ \frac{\psi_1}{L_1} \end{bmatrix} + \begin{bmatrix} 0 \\ 1 \end{bmatrix} \begin{bmatrix} E_s \end{bmatrix} \tag{3.26}$$

The right hand circuit contains no inertial component; however, this can be resolved by questioning the traditional assignment of voltage as the effort variable and current as the flow variable. By defining the current as the effort, the voltage as the flow variable, the capacitor charge as the momentum variable and the flux as the position variable one then arrives at a Rayleigh dissipation function defined in terms of the voltage rather than the current.

$$\mathscr{R} = \frac{1}{2}\frac{1}{R_1}{E_r}^2 \tag{3.27}$$

The resulting port-Hamiltonian system is therefore

$$\begin{bmatrix} \dot{\psi} \\ \dot{q_1} \end{bmatrix} = \left(\begin{bmatrix} 0 & 1 \\ -1 & 0 \end{bmatrix} - \begin{bmatrix} 0 & 0 \\ 0 & \frac{1}{R_1} \end{bmatrix} \right) \begin{bmatrix} 0 \\ \frac{q_1}{C} \end{bmatrix} + \begin{bmatrix} 0 \\ 1 \end{bmatrix} \begin{bmatrix} I_s \end{bmatrix} \tag{3.28}$$

It is nevertheless accepted that an extensive proof of the generalized scope of this method would involve significant further work.

3.2.6 Bond Graphs

Bond Graphs are an alternative energy based modeling technique using pictorial representation. The bond graph methodology has not been used in this body of work, however for completeness, it should be noted that an analytical model of an OWC, derived from a bond graph, has been developed by Kurniawan et al. (2011). Bond graphs are constructed from elements and junctions. Similar to the port-

Hamiltonian framework, the one-port elements consist of inductors (I), capacitors (C), resistors (R), and sources (SE). A 0-junction represents a parallel connection whereas a 1-junction represents a series connection. The one-port elements connected in series and in parallel can be seen in Figure 3.3. Additional junction types exist including transformers (TF) and gyrators (GY). The book by Banerjee (2005) gives a good introduction to Bond Graphs.

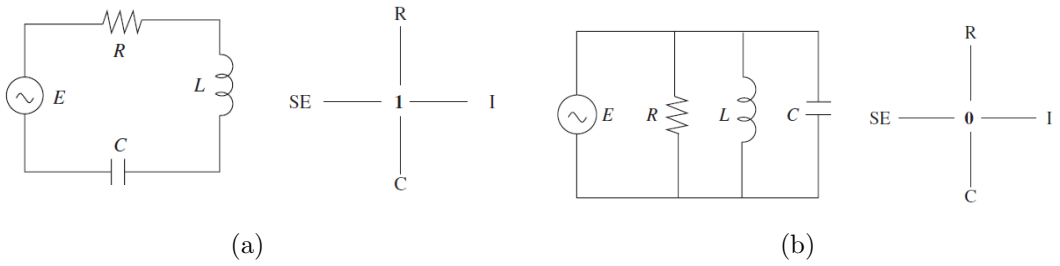

Figure 3.3: Bond Graph for Series and Parallel (Banerjee 2005)

3.2.7 Energy-Based Modeling Summary

As can easily be seen for the earlier examples, the three methods (Euler-Lagrangian, Port-Hamiltonian and Brayton-Moser) result in the same system equations. However, certain systems lend themselves to one or other of these energy-based modeling methods. The Brayton-Moser method deals well with systems without inertial components. However, a method has been introduced to adapt the port-Hamiltonian method for these systems with no inertial component. The port-Hamiltonian and Brayton-Moser method directly calculate first order equations whereas the Euler-Lagrangian method calculates second order equations which then may need to be converted to first order equations for model implementation purposes. The methods detailed in this section will be used extensively in modeling the various subcomponents of the wave-to-wire model.

3.3 Incident Waves

3.3.1 Wave Spectra

A traditional coal or gas power plant can control the input power to the system. Renewable energy plants do not have this luxury and have to be able to cope with whatever the weather systems generate. As a result, an understanding of wave spectra is critical to optimizing the power capture from wave energy devices.

Water wave theory is an involved field in its own right, with many books written solely on this topic. Two excellent books in this field are by McCormick (2010) and Holthuijsen (2007). Waves are usually characterized by their wave height, period, and wave length. Figure 3.4 shows these parameters pictorially.

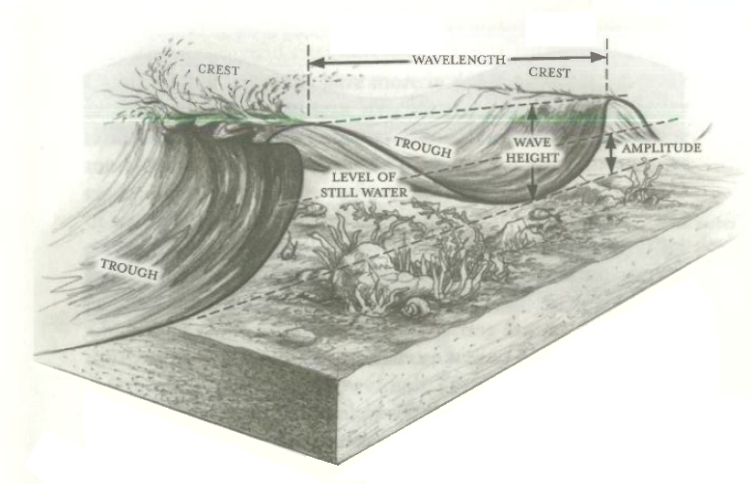

Figure 3.4: Common wave terminology (Pretor-Pinney 2010)

A common misconception is that waves are the movement of water in the direction of the wave direction of travel. This is not the case, with the exception of waves that are breaking. One of the reasons wave theory becomes complicated is that the movement of the water particles is actually elliptical/circular with energy transfer between adjacent particles. The water particles in deep water take on a circular path of motion, and as the water depth becomes shallower, the motion of the particles

tends to an ellipse (see Figure 3.5). Equations have been developed to approximate waves in different water depths, those given by McCormick (2010) can be found in Appendix A.

Linear Wave Theory (LWT) can be used for most engineering applications in deep water. As the depth becomes shallower, it may become necessary to apply another approximation such as Stokes' 2nd order theory (Amundarain, Alberdi, Garrido, Garrido & Maseda 2010).

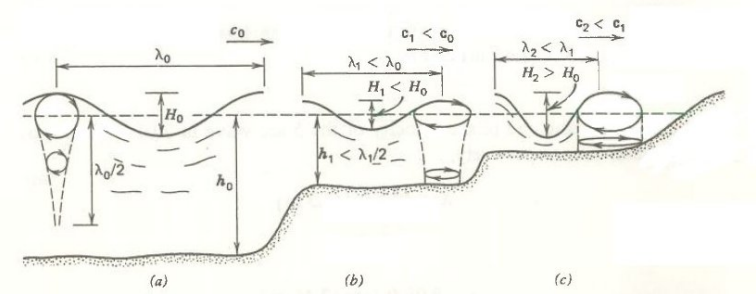

Figure 3.5: Properties of waves under various depth conditions a) deep water; b) intermediate water; and c) shallow water (McCormick 1981b)

Ocean waves are generated by the wind and can travel for many miles as they dissipate very little energy if they do not collide with another object such as a shore-line or off-shore structure. Two of the main factors affecting the size of waves that are generated are a) the fetch (the distance over which the wind is blowing) and b) the wind duration. There is a minimum fetch, F_{DS}, over which the wind needs to blow before a sea is considered to be fully developed McCormick (2010) which is defined as

$$F_{DS} = 2.32{U_{10}}^2 \tag{3.29}$$

where U_{10} is the wind speed measured at 10m above sea level and the constant has the units s^2m^{-1}. In addition there is a minimum time, t_{DS}, over which the wind can blow before the sea is considered to be developed which is defined as

$$t_{DS} = 2.10U_{10} \tag{3.30}$$

where the constant has the units s^2m^{-1}.

Various equations have been developed to approximate wave spectra in different locations, which include, among others, the Pierson-Moskowitz; Joint North Sea Wave Project (JONSWAP); and Bretschneider spectra (Holthuijsen 2007, McCormick 2010, Det Norske Veritas 2011). The selection of one over another depends on the specific location and its distance to another land mass and whether the sea is full developed or developing (McCormick 2010). JONSWAP is valid for fetch limited seas while Brentschneider and Pierson-Moskowitz are for fully developed sea.. The wave climate on the west coast of Ireland is considered to be modeled well by the Pierson-Moskowitz spectrum due to the long distance between Ireland and the Americas. The European Marine Energy Center (EMEC) wave energy testing site, in the North-East coast of Scotland, is more likely to be accurately approximated by the JONSWAP spectrum due to the short distance between Scandinavia and Scotland, limiting the possible fetch.

Figure 3.6 shows good agreement between the data collected by Mollison, several hundred kilometres west of Ireland at the Porcupine station, and which has been averaged over a year, plotted alongside the prediction using the Long Term Energy spectrum as proposed and presented by McCormick (2010). This highlights the importance of understanding which spectrum is appropriate for a specific location.

It can be seen in Figure 3.6 that for waves a long way out to sea averaged over a year, the "Long-term energy spectrum" is a better approximation of the data collected by Mollision (McCormick 2010). McCormick (2010) also highlights that for structural design one needs to look at the peak waves in storm conditions, whereas for control design one needs to design the system around the most likely sea state over a year.

There is, unfortunately, a lack of consistency in the terms or variables used to define the various spectra. For example, the original JONSWAP spectrum is calculated

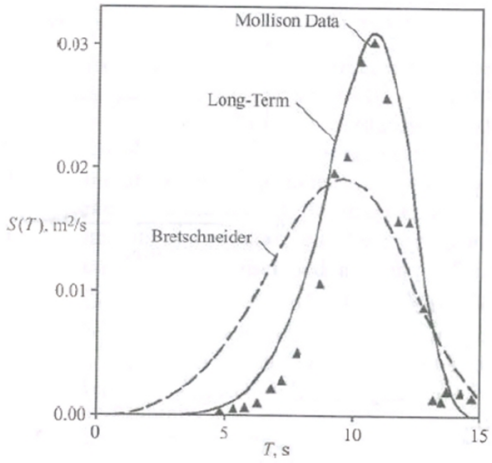

Figure 3.6: Comparison of long term energy spectrum and real data collected by Mollison (McCormick 2010)

from the fetch, the wind speed at 10m above sea level, and the duration of the wind; the Pierson-Moskowitz spectrum is calculated from the wind speed at 19.5m above sea level. According to research by Valério et al. (2007) the Pierson-Moskowitz spectrum is an accurate representation of a sea state. A function exists relating the wind speed at 19.5m and at 10m above sea level (McCormick 2010) defined as

$$U_{19.5} = U_{10}(1 + 0.0528\sqrt{0.80 + 0.114U_{10}}) \approx 1.075U_{10} \tag{3.31}$$

This enables easier comparison between the JONSWAP and Pierson-Moskowitz spectra in their original forms. The Bretschneider spectrum is calculated from the average wave height and average period. In contrast the "Long-term energy spectrum" is calculated from the Root Mean Square (RMS) wave height and the shaping function (McCormick 2010). Det Norske Veritas (2011) gives a redefined version of the Pierson-Moskowitz and JONSWAP spectra in terms of wave frequency, f, significant wave height, H_s, peak frequencies, ω_p, and peak enhancement factor, Γ.

The Pierson-Moskowitz spectrum is redefined as

$$S_{PM}(\omega) = \frac{5}{6}{H_s}^2\frac{{\omega_p}^4}{(2\pi f)^5}\exp\left(-\frac{5}{4}\left(\frac{2\pi f}{\omega_p}\right)^{-4}\right) \tag{3.32}$$

whereas the JONSWAP spectrum is redefined as

$$S_{JON}(\omega) = A_y S_{PM} \Gamma^{\exp\left(-0.5\left(\frac{2\pi f - \omega_p}{\sigma\omega_p}\right)^2\right)} \tag{3.33}$$

where

$$A_y = 1 - 0.287 \ln(\Gamma) \tag{3.34}$$

The peak frequency is related to the peak period, T_p, defined as $\omega_p = 2\pi/T_p$.

The peak enhancement factor can be adjusted to use the JONSWAP spectrum to represent other spectra such as the Bretschneider. The peak enhancement factor, Γ, was identified to be equal to 3.3 for North Sea locations, but is 1 for Bretschneider spectra and 7 for long swells (University of Edinburgh & FP7 partners 2011). The peak enhancement factor can be used to match a spectrum to empirical sea data (Cruz 2008). The associated spectra for a wave height of 3m and peak period of 8s is shown in Figure 3.7, for these three peak enhancement factors.

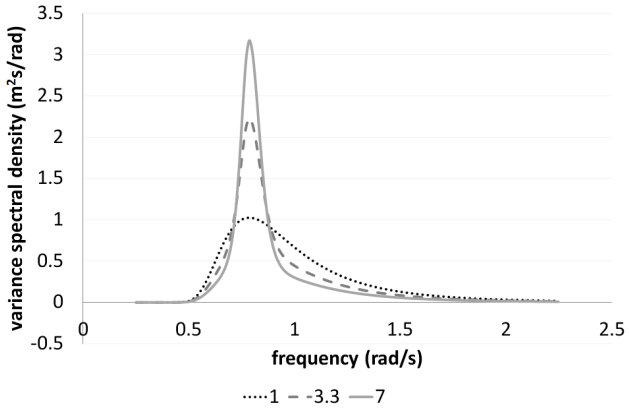

Figure 3.7: JONSWAP spectra for three peak enhancement factors.

The JONSWAP spectrum as a function of wave height, period and the peak enhancement factor is employed in order to simulate seas when a wave scatter diagram is provided, such as that in Figure 3.8. The wave scatter diagram may be given for a site that shows the likelihood of a particular sea spectra (Figure 3.8). A location

can be described using a certain type of spectra such as the Bretschneider, Pierson-Moskowitz or that developed by the JONSWAP. This, combined with data obtained from the wave scatter diagrams, can be used to generate a set of wave time series.

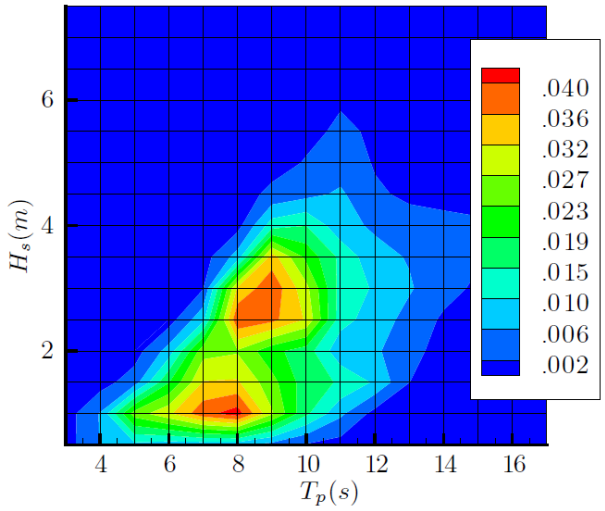

Figure 3.8: Wave scatter diagram (Borgarino et al. 2011)

Brito-Melo et al. (2002) used sea states (each of a 15 minute duration) to represent a specific wave climate at the Pico power plant, in the Azores. These time series have been used to validate their proposed control strategy.

As waves travel for long distances without significant decay unless colliding with an obstacle, seas are rarely purely unidirectional. Bimodal seas are those which have two distinct frequency peaks in the spectrum and are often dealt with, where LWT can be applied, by computing a linear combination of two unimodal spectra (Cruz 2008).

The directional spreading function, $S_D(\Theta)$, can be thought of as the probability that a wave is approaching a point from a given angle, Θ, and has the property

$$\int_0^{2\pi} S_D(\Theta) d\Theta = 1 \tag{3.35}$$

As a result, the sum of all the probabilities is equal to one. For an axisymmetric point

absorber, the directional spreading function can be considered negligible; however, if simulating a device that is directional, this must be taken into account.

The site spectra can be decomposed into the frequency dependent spectra and the angle dependent spreading function:

$$S(f, \Theta) = S(f)S_D(\Theta) \tag{3.36}$$

Bimodal seas could also be represented using the same decomposition and can be treated as a linear combination of unimodal spectra (Mackay 2011). The equations describing the different unimodal spectra given by McCormick (2010) can be found in Appendix B. These spectra along with those provided in Equations (3.32), 3.33 and 3.36 will be used in creating time series as the input for the analytical model and for simulating waves at the turbine test facility. The conversion of the spectra to a time series is detailed in the next sub-section.

3.3.2 Wave Time Series

Traditional LWT can be applied if the assumption of deep water holds true for the oceanic gravity waves under study (Fantini 2007, Guerrini 2009, Krogstad & Arntsen 2000). Under this assumption, a potential wave series can be generated from the spectrum either by applying an Inverse Fast Fourier Transform (IFFT) or by summing a series of sine waves. The latter method is employed here. If one considers the inverse problem of generating a spectrum from a time series (when only one time series exists), then the spectral variance density must be estimated from one amplitude (Holthuijsen 2007) and as such is equal to:

$$S(f) \approx \frac{1}{\Delta f} E\{\frac{1}{2}a_i^2\} \rightarrow \frac{1}{\Delta f}(\frac{1}{2}a_i^2) \tag{3.37}$$

The amplitude of each wave frequency can therefore be calculated as

$$a_i = \sqrt{2S(f)\Delta f} \tag{3.38}$$

The wave elevation time series, η, at a given position, x, can be calculated as the sum of each frequency component, f, with amplitude, a, wavelength λ and random phase ϕ between 2π and zero:

$$\eta = \sum_{i=1}^{N} a_i \sin(2\pi f_i t - \frac{2\pi}{\lambda_i} x + \phi_i) \tag{3.39}$$

The vertical velocity of the water surface, also known as the heave velocity of the wave is therefore

$$\dot{\eta} = \sum_{i=1}^{N} 2\pi f_i a_i \cos(2\pi f_i t - \frac{2\pi}{\lambda_i} x + \phi_i) \tag{3.40}$$

and the acceleration is

$$\ddot{\eta} = -\sum_{i=1}^{N} (2\pi f_i)^2 a_i \sin(2\pi f_i t - \frac{2\pi}{\lambda_i} x + \phi_i) \tag{3.41}$$

The equations for the water movement at a certain depth, h_d, under the mean sea water level, due to the approaching wave, are a function of the water depth of the sea floor, h_w (Gervelas et al. 2011, Krogstad & Arntsen 2000). For deep water:

$$\eta_d(t, x) = \sum_{i=1}^{N} \eta_i e^{-k_i h_d} \tag{3.42}$$

where

$$k = \frac{(2\pi)^2}{gT^2} \tag{3.43}$$

3.4 Hydrodynamic OWC Modeling

This section will first review the existing models that can be found in literature and then two contrasting models will be presented. The first develops upon the work by Gervelas et al. (2011) but adds an additional term previously not considered which accounts for mass leaving the system at non-null velocity. The second model employs the weightless piston model. Additional terms are proposed to account for the coupling radiation force between the two bodies (OWC and piston). A brief comparison of the two methods will be given.

There are two main interfaces when modeling an OWC. Firstly, there is the structural-hydrodynamic interface and secondly, there is the hydrodynamic-pneumatic interface. A wide variety of numerical models have been developed for quantifying the efficiency and the forced vertical response of fixed and floating OWCs. These have mostly been developed using results from BEM codes with a few from computationally expensive CFD codes. The computational expense of the CFD codes arises from their ability to compute the velocities and pressures through out the working fluid whereas the BEM code is limited to computing these values on the surface of the submerged body. As a result, the BEM code is less accurate, but is significantly less computationally expensive. The CFD codes can be used to compute the velocities and pressure values within two interfacing working fluids such as the water surface boundary of the air chamber within an OWC. This adds significantly to the case for using CFD; however, its computational cost is prohibitive. However, simulation models have been developed that assume that the added mass and damping coefficients are frequency independent and hence do not rely on CFD or BEM computational expensive codes (Gervelas et al. 2011). It is intended that the full OWC system model, developed as part of this work, is able to run in real-time for model-based control strategies. The model can therefore make use of the BEM coefficients but these need to be computed in advance; this is also the case for

parameters calculated using CFD codes.

Guerrini (2009) presented a quasi-2D CFD model to represent a forward, backward and bottom opened OWC device. However, the device was fixed and did not take into account any floating behavior; as a result comparisons with sea data from the "Mighty Whale" device did not show good agreement when the wavelength was longer than the device (Guerrini 2009). Baudry et al. (2013) suggests that while CFD can be significantly more accurate than BEM predictions, the additional computational overhead makes it ill-suited for calculating the potential yearly energy yield of a device. CFD is, however, often employed for characterizing the turbine such as the work presented by Banks (2009) and Tarver (2013).

Iturrioz et al. (2013) compared experimental data for an OWC described as "fixed detached" against results from a time domain model employing the equations originally presented by Cummins (1962) and then against results obtained from a BEM code (WADAM) and results from a 2D and 3D CFD simulation as a step towards modeling a floating device. The accuracy was best for the 3D CFD simulation and worst for the time domain model as one would expect. However, the time domain model was sufficiently accurate to be useful for the initial design and sizing process. The time domain model ran four times faster than real-time (a ratio of 1:0.25), however both the 2D code and the 3D code were significantly slower than real-time (with ratios of 1:691 and 1:4320 respectively). This work omitted a turbine from the model; the flow resistance was instead modeled as an orifice slot in the top of the chamber.

Baudry et al. (2013) reviewed analytical, numerical and experimental methods for modeling OWCs. In their work, the authors commented on the inaccuracy of the rigid weightless piston model as it does not account for the sloshing modes that can significantly affect the efficiency of an OWC. Baudry et al. (2013) therefore recommended using pressure distribution models, and in particular using an extended

BEM code to model the pressure distribution oscillation. The author of this thesis suggests that the main disadvantage of the pressure distribution models is added computational expense for a model that ideally should be run in real-time. However this could be reviewed as a potential extension to the port-Hamiltonian model that will be presented as part of this body of work. Another benefit that was suggested by Baudry et al. (2013) was the potential complex structures that can be modeled using BEM codes in direct contrast to purely analytical models.

The work by Brito-Melo et al. (2002) models an OWC using the continuity of mass equation given as

$$\frac{p(t)}{K} + q_v(t) = q_d(t) + q_r(t) - \frac{V_{c0}}{\gamma p_{atm}} \frac{dp(t)}{dt} \tag{3.44}$$

where q_r, q_d and q_v are the flow rates due to radiation, diffraction and the flow through the valve. V_{c0} is the initial volume of air in the chamber and K is the applied damping of the turbine. The radiation flow rate

$$q_r(t) = \int_{-\infty}^{t} h_r(t-\tau) \frac{dp_c}{dt}(\tau) d\tau \tag{3.45}$$

is computed from the impulse response function h_r which is derived from a numerical model utilizing tools such as AQUADYN-OWC, WAMIT or alternative via tank testing. The diffraction flow rate is derived by conducting experimental tank tests, and then using the data from the instrumentation in Equation (3.44) to derive q_d. The turbine power, P_m, is calculated from the constant mechanical speed, ω_m, and derived torque from the turbine flow rate, q_v, in Equation (3.46).

$$P_m = \frac{\omega_m}{T} \int_{0}^{T} [T_t(\omega_m, q_r(t)) - T_b(\omega_m)] dt \tag{3.46}$$

The torque due to mechanical losses is given by T_b and will be function of speed. The

turbine torque, T_t is approximated with a second order polynomial function. The Brito-Melo et al. (2002) model assumes that the turbine never goes into stall because the blow-off-valve will always operate at the appropriate time and will be sufficiently large. It is assumed that due to the large inertia of the system the speed will remain constant over the duration of a particular sea-state, which is given approximately as 15 minutes. The turbine is also approximated by a linear relationship between the flow rate and the pressure, given by K.

A weakness of the Brito-Melo et al. (2002) model is that it is static and therefore cannot validate the dynamic aspects of any control system. The inertia of the rotating machinery is assumed to be significantly large and hence the speed will be constant. For the HydroAir turbine this is thought not to be the case based on the current design and experimental testing. This type of model would be unsuitable for the purposes of validating the dynamic behavior of the control strategy and therefore will not be considered.

The work by Amundarain et al. (2011) neglected the hydrodynamic interface to the turbine and employed a sinusoidal pressure input to the Power Take-Off (PTO) system. This neglects the coupling effect between the two sub-systems (that of the pneumatics and the hydrodynamics) which directly affects the resulting energy absorption of the device.

Hoskin et al. (1986) modeled the OWC as a simple mass-spring-damper system, whose equation of motion is

$$\ddot{z_2} = \frac{1}{M}\Big(F_{di} - \int_0^t K_a(t-\tau)\dot{z_2}(\tau)d\tau - \rho_w g A_c z_2 - (p_c - p_{atm})A_c\Big) \tag{3.47}$$

where A_c is the cross-sectional area of the water column, F_{di} is the wave diffraction force and K_a is the added damping and is determined by the geometry of the device

and is frequency dependent. The mass flow of the turbine can be calculated as

$$\dot{m} \equiv \frac{d(\rho_a V_c)}{dt} \equiv \dot{\rho_a}(V_{c0} - A_c z_2) - \rho_a A_c \dot{z_2} = -u_c \mathscr{G}(p_c - p_{atm})\rho_a \tag{3.48}$$

where $\mathscr{G}$ is a function of the pressure drop across the turbine, V_c is the water column volume and u_c is the control function representing the opening of the valve. The system is governed by the adiabatic gas law which is stated as

$$\frac{p_c}{p_{atm}} = \left(\frac{\rho_a}{\rho_{a0}}\right)^{\gamma} \tag{3.49}$$

This model does not incorporate the mechanical or electrical dynamics and losses. It is not made clear how the added damping and turbine discharge would be computed. As such implementation of these equations within a model without further information would not be possible, and no information is given as to the validation of this derivation.

3.4.1 OWC Model with Frequency Independent Added Mass

As part of this body of work two models of the hydrodynamic subsystem have been developed. The first expands on the work by Gervelas et al. (2011), which uses a frequency independent added mass term and the second, detailed in Section 3.4.2, expands on the work by Evans (1976) which uses the weightless piston approach and computes the frequency dependent added mass.

A diagram of a simplified fixed OWC device is shown in Figure 3.9, with a radius of the cylindrical column, r_c; an orifice of diameter, D_o; mean water depth, h_w; a water draft, h_d; an air draft, h_{a0}; an incident wave height, η; and the water elevation within the column measured from the mean Sea Water Level (SWL),z_2. The model is for a fixed OWC and therefore does not take into account surge, sway, heave, roll,

pitch or yaw of the device; therefore, z_1 is zero. Further, the OWC is modeled as a cylindrical geometry with a uniform distribution of flow. The same assumptions as given by Gervelas et al. (2011) have been made; hence, diffraction, viscous and turbulence effects are ignored. Also, the added mass and damping coefficient of the water column are assumed to be independent of the frequency. Wave linear theory with the principle of superposition is applied under the assumption of deep water.

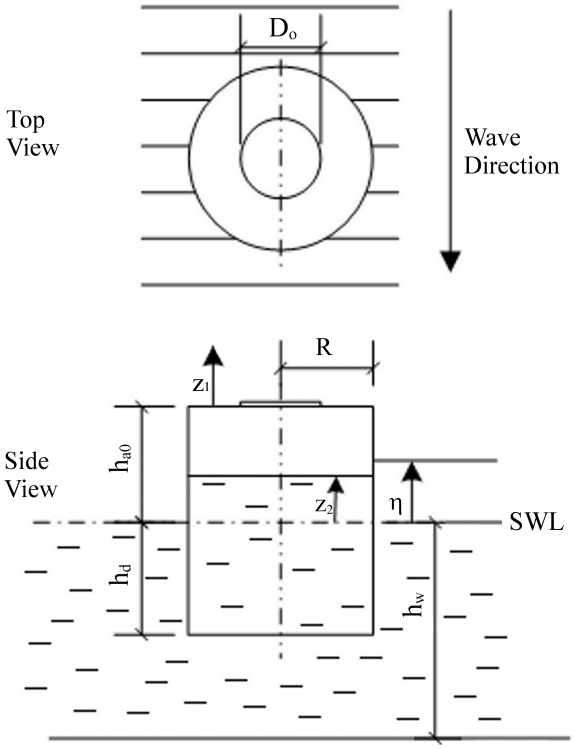

Figure 3.9: Key OWC parameters

Newton-Euler method

The initial model developed by Gervelas et al. (2011) used Newtonian mechanics. It described the dynamics of a fixed OWC device without the need for BEM or CFD numerical results. The main system equation of the model of an OWC with

an orifice plate is given as

$$M_{wc}\,\ddot{z_2} + B\,\dot{z_2} + C\,z_2 = F_n(t) \tag{3.50}$$

where B, the spring constant, C, the damping coefficient, M_{wc}, the water column mass, and M_a, the added mass are defined as

$$B = 0.2\sqrt{C(M_{wc} + M_a)} \tag{3.51}$$

$$C = \pi\rho_w g\,{r_c}^2 \tag{3.52}$$

$$M_{wc} = \pi\rho_w\,{r_c}^2\,(h_d + z_2) \tag{3.53}$$

$$M_a = 2/3\,\pi\rho_w {r_c}^3 \tag{3.54}$$

where ρ_w is the density of the sea water and g is acceleration due to gravity. In addition the mass of the displaced water at the surface within the OWC chamber is defined as

$$M_d = \pi\rho_w {r_c}^2 z_2 \tag{3.55}$$

The generalized force, F_n, or in other words the sum of the externally applied forces,

$$F_n(t) = F_a(t) + F_{FK}(t) + F_{\Delta p}(t) \tag{3.56}$$

is equal to the sum of the forces due to the pressure applied by the air within the chamber, due to the pressure applied by the wave and the force caused by the difference in velocity between the water column and the wave. The forces $F_{\Delta p}$, F_a and F_{FK} are defined below.

The force due to the air pressure within the air chamber is a product of the water surface area and the air pressure, given as

$$F_{\Delta p}(t) = -\pi \Delta p(t)\, {r_c}^2 \tag{3.57}$$

The rate of change of air pressure in the model was calculated based on the aforementioned mass flow,

$$\Delta \dot{p} = \frac{{c_s}^2 \dot{m}_o}{\pi {r_c}^2 (h_{a0} - z_2)} + \gamma \frac{(\Delta p + p_{atm})\dot{z_2}}{h_{a0} - z_2} \tag{3.58}$$

where the mass flow through the orifice plate is,

$$\dot{m}_o = -C_d A_o \sqrt{2 \rho_a \Delta p} \tag{3.59}$$

which is calculated from the orifice coefficient of discharge, C_d, the density of air, ρ_a, the area of the orifice, A_o, and the pressure drop across it.

The added mass force is proportional to the difference in velocity between the heave of the water within the column and the velocity of the wave at a depth equal to the draft of the column,

$$F_a(t) = M_a(\ddot{\eta}_d - \ddot{z_2}) \tag{3.60}$$

The added mass itself is dependent on the geometry of the column (Patel 1989). The added mass for a vertical cylindrical column has already been given in Equation (3.54). Water, within a wave, moves in a circular or oval path, dependent on water depth, with both horizontal and vertical movement. However, for this model, only the vertical component is taken into account, which influences only the heave of the water and air column. The free surface vertical velocity at a certain depth, d, is

given by

$$\ddot{\eta}_{di} = -4\pi^2 f_i^2 a_i \sin(2\pi f_i t + \phi_i) \frac{\sinh k_i(h_w - h_d)}{\sinh k_i h_w} \tag{3.61}$$

The Froude-Krylov force, is proportional to the hydrodynamic pressure of the wave and also to the surface area of the column,

$$F_{FK}(t) = \pi p_w(t)\, {r_c}^2 \tag{3.62}$$

where the pressure head due to the wave is a function of the wave height at the draft entry, gravity and the density of water,

$$p_w = \rho_w g a_i \sin(2\pi f_i t + \phi_i) \frac{\sinh k_i(h_w - h_d)}{\sinh k_i h_w} \tag{3.63}$$

The equations presented so far are the work of Gervelas et al. (2011) and will be used for comparison purposes.

Euler-Lagrangian method

The modeling of an OWC as a mass spring damper and then resolving the external forces applied to the system can be derived using the Lagrange equations developed by Joseph-Louis Lagrange. This example is used to present the method prior to considering any additional terms.

As discussed in Section 3.2.1, the Lagrangian function, $\mathscr{L}$, is the difference in energy between the kinetic energy, $\mathscr{T}$, and the potential energy, $\mathscr{V}$:

$$\mathscr{L} = \mathscr{T} - \mathscr{V} \tag{3.64}$$

The Lagrangian equation in its general form,

$$\frac{d}{dt}\left(\frac{\partial \mathscr{L}}{\partial \dot{q}_i}\right) - \frac{\partial \mathscr{L}}{\partial q_i} + \frac{\partial \mathscr{R}}{\partial \dot{q}_i} = 0 \tag{3.65}$$

assumes that the potential energy is not a function of the velocity. In such cases, where this is not true, it is necessary to use the modified equation where

$$\frac{d}{dt}\left(\frac{\partial \mathscr{T}}{\partial \dot{q}_i}\right) - \frac{\partial (\mathscr{T} - \mathscr{V})}{\partial q_i} + \frac{\partial \mathscr{R}}{\partial \dot{q}_i} = 0 \tag{3.66}$$

A derivation of the model is now presented using the standard Lagrangian model assuming that masses within the system, M_{wc} and M_d, are not functions of position.

The kinetic energy of the system is

$$\mathscr{T} = \frac{1}{2} M_{wc}\, \dot{z_2}^2 \tag{3.67}$$

and the potential energy of the system is

$$\mathscr{V} = M_d\, g z_2 - F_n z_2 \tag{3.68}$$

where M_d is the water surface displaced mass, already given in Equation (3.55). The Rayleigh function is calculated as

$$\mathscr{R} = \frac{1}{2} B \dot{z_2}^2 \tag{3.69}$$

There is only one generalized coordinate considered, which is the water column elevation, z_2.

The rate of change of the kinetic energy with respect to the generalized coordinate

is

$$\frac{\partial \mathscr{T}}{\partial z_2} = 0 \tag{3.70}$$

Whereas the rate of change of the kinetic energy with respect to the generalized velocity is

$$\frac{\partial \mathscr{T}}{\partial \dot{z}_2} = M_{wc}\, \dot{z}_2 \tag{3.71}$$

The rate of change with respect to time is then calculated from the rate of change of the kinetic energy with respect to the generalized velocity,

$$\frac{d}{dt}\left(\frac{\partial \mathscr{T}}{\partial \dot{z}_2}\right) = M_{wc}\, \ddot{z}_2 \tag{3.72}$$

The rate of change of the potential energy with respect to the generalized coordinate is

$$\frac{\partial \mathscr{V}}{\partial z_2} = M_d\, g - \Sigma F_n \tag{3.73}$$

$$= C z_2 - \Sigma F_n \tag{3.74}$$

The rate of change of the dissipation function with respect to the generalized velocity is

$$\frac{\partial \mathscr{R}}{\partial \dot{z}_2} = B \dot{z}_2 \tag{3.75}$$

Combining Equations (3.70), (3.72), (3.74), and (3.75) into the Euler-Lagrangian system equation (3.65) gives the following,

$$M_{wc}\ddot{z}_2 + B\dot{z}_2 + C z_2 - F_n = 0 \tag{3.76}$$

which it can be seen is the same as Equation (3.50), the Newton-Euler equation, confirming the applicability of the method. Equation 3.76 can be rearranged into

the port-Hamiltonian form using Equation 3.11 which gives

$$\begin{bmatrix} \dot{z}_2 \\ \dot{Y}_2 \end{bmatrix} = \left(\begin{bmatrix} 0 & 1 \\ -1 & 0 \end{bmatrix} - \begin{bmatrix} 0 & 0 \\ 0 & B \end{bmatrix} \right) \begin{bmatrix} Cz_2 \\ \frac{Y_2}{M_{wc}} \end{bmatrix} + \begin{bmatrix} 0 \\ 1 \end{bmatrix} F_n \tag{3.77}$$

Pesce (2003) and Pesce et al. (2006) published work on the application of Euler-Lagrange equations to mechanical systems with mass explicitly dependent on position. This modeling technique is applicable to OWCs as the volume of water within the column is dependent on the height of water, z_2, and therefore the assumption made in Equations (3.70) through (3.75) is questionable. In Newtonian mechanics, a simplification is often made that the force is proportional to the product of the mass and the acceleration,

$$F = M\,a \tag{3.78}$$

based on an assumption of constant mass. However force is proportional to the rate of change of momentum,

$$F = \frac{d(Mv)}{dt} \tag{3.79}$$

which is important when mass is varying, as is the case in the system presented here.

A recalculation of the Lagrangian equations shows that the partial derivative of the kinetic energy with respect to the generalized coordinate changes to

$$\frac{\partial \mathscr{T}}{\partial z_2} = \frac{1}{2}\frac{\partial M_{wc}}{\partial z_2}\dot{z}_2{}^2 \tag{3.80}$$

The time derivative of the partial derivative of the kinetic energy with respect to

the generalized velocity also requires amending,

$$\frac{d}{dt}\left(\frac{\partial \mathscr{T}}{\partial \dot{z}_2}\right) = M_{wc}\,\ddot{z}_2 + \frac{\partial M_{wc}}{\partial t}\,\dot{z}_2 \tag{3.81}$$

$$= M_{wc}\,\ddot{z}_2 + \frac{\partial M_{wc}}{\partial z_2}\,\frac{\partial z_2}{\partial t}\dot{z}_2 \tag{3.82}$$

$$= M_{wc}\,\ddot{z}_2 + \frac{\partial M_{wc}}{\partial z_2}\,{\dot{z}_2}^2 \tag{3.83}$$

Additionally, the partial derivative of the potential energy with respect to the generalized coordinate results in

$$\frac{\partial \mathscr{V}}{\partial z_2} = \frac{\partial M_d}{\partial z_2} g z_2 + M_d\, g - F_n \tag{3.84}$$

The remaining equation for the Rayleigh dissipation function is unchanged. However the Lagrangian equation is for conservative systems and as mass is expelled from the system at non-null velocity this also needs to be taken into account (Pesce et al. 2006) as it applies a force onto the system.

$$F_{em} = -\frac{1}{2}\frac{\partial M_{wc}}{\partial z_2}\,{\dot{z}_2}^2 \tag{3.85}$$

If Equations (3.80), (3.83), (3.84) and (3.85), are now incorporated into Equation (3.66), then the following system equation is found:

$$M_{wc}\ddot{z}_2 + \frac{\partial M_{wc}}{\partial z_2}\,{\dot{z}_2}^2 - \frac{1}{2}\frac{\partial M_{wc}}{\partial z_2}\,{\dot{z}_2}^2 + B\dot{z}_2 + \frac{\partial M_d}{\partial z_2} g z_2 + C z_2 - F_n - F_{em} = 0 \tag{3.86}$$

This simplifies to:

$$M_{wc}\ddot{z}_2 + \frac{\partial M_{wc}}{\partial z_2}\,{\dot{z}_2}^2 + B\dot{z}_2 + \frac{\partial M_d}{\partial z_2} g z_2 + C z_2 - F_n = 0 \tag{3.87}$$

It can be seen comparing Equation (3.87) to (3.76) that there are an additional two

terms which will affect the system response.

The frequency independent OWC system can be represented in the port-Hamiltonian framework given by

$$\dot{s} = (\mathscr{J} - \mathscr{D})\mathscr{H} + gu_c \tag{3.88}$$

as

$$\begin{bmatrix} \dot{z}_2 \\ \dot{Y}_2 \end{bmatrix} = \left(\begin{bmatrix} 0 & 1 \\ -1 & 0 \end{bmatrix} - \begin{bmatrix} 0 & 0 \\ 0 & B + \frac{\partial M_{wc}}{\partial z_2} \end{bmatrix} \right) \begin{bmatrix} Cz_2 + \frac{\partial M_d}{\partial z_2} g z_2 \\ \frac{Y_2}{M_{wc}} \end{bmatrix} + \begin{bmatrix} 0 \\ 1 \end{bmatrix} F_n \tag{3.89}$$

3.4.2 OWC Model with Frequency Dependent Added Mass

The main issue with the Euler-Lagrange model is that the added mass and damping coefficients are taken to be frequency independent. This subsection will now address this and present an alternative model that takes into account the frequency dependent added mass. The first time domain model which utilized the frequency dependent coefficients was presented by Cummins (1962).

Assessment work on the performance of OWCs is sometimes conducted in the frequency domain such as the work presented by Gomes et al. (2012); however, due to the non-linear components such as the turbine and any Blow-Off Valve (BOV) or Shut-Off Valve (SOV) the time domain will be considered here.

The coefficients required to compute these forces are obtained through the use of a commercial BEM code (e.g. WAMIT (Vas 2013)). However, open-source alternatives such as Nemoh, published by Delhommeau et al. (2014), are available. BEM codes compute the solution to the Navier-Stokes equation using potential flow theory only on the surface of the submerged bodies as discussed by Baudry et al. (2013). This contrasts with conventional CFD, which solves the Navier-Stokes equations throughout the working fluid.

The mesh density on the surface is critical in order to obtain convergence of the results. The BEM code Nemoh assumes the applicability of LWT and computes the relevant coefficients in the six degrees of freedom: surge, sway, heave, roll, pitch, and yaw. This method enables the simulation of floating OWCs as well as fixed OWCs.

Figure 3.10 shows a simple cylindrical geometry OWC geometry with a draft length of 5m and a diameter of 24m. This basic shape will be employed for the purposes of this body of work and the movement of the device will be assumed to be purely heave motion. A second device will also be modeled with a 12m diameter.

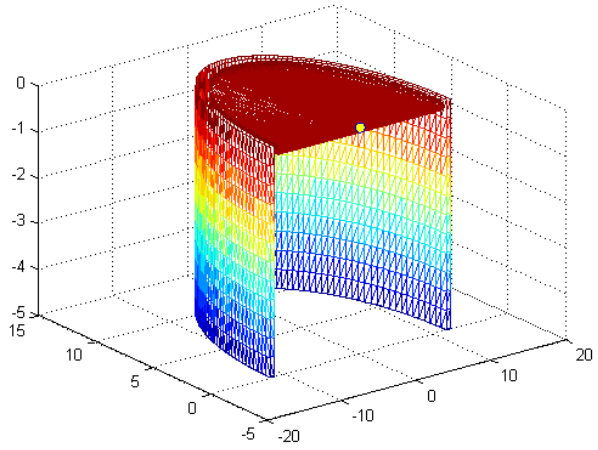

Figure 3.10: Nemoh mesh for a 24m cylindrical OWC device

The frequency domain can be used to assess the performance of the device. The Response Amplitude Operator (RAO) shows the movement of the device in a particular direction when subjected to a unit wave as a function of frequency. It highlights the particular wave frequency to which the device is tuned and therefore the frequency at which the power absorption is likely to be at a maximum. The equation for heave motion for a single device is defined as

$$z(\omega_w) = \frac{F_e(\omega_w)}{-{\omega_w}^2(M_b + \mathscr{A}(\omega_w)) + (k_h + k_m) + i\omega_w(\mathscr{B}(\omega_w) + B_{pto})} \tag{3.90}$$

where F_e is the excitation force, ω_w is the wave angular frequency, M_b is the mass of

the body, k_m is the mooring stiffness, k_h is the Hydrostatic stiffness, z is the vertical position of the body, $\mathscr{A}$ is the added mass coefficient, $\mathscr{B}$ is the damping coefficient, and B_{pto} is the applied damping on the body by the PTO unit.

It is proposed that the RAOs can be calculated from the BEM coefficients for the coupled motion of two devices. In this case, only heave motion will be considered and the two bodies are defined as the OWC structure and the oscillating body of water whose surface is modeled as a piston. The equation of motion in the frequency domain for the first device is

$$z_1(i^2{\omega_w}^2(M_{b1}+\mathscr{A}_1)+i\omega_w(B_{pto1}+\mathscr{B}_1)+(k_{h1}+k_{m1}))+z_2(i^2{\omega_w}^2\mathscr{A}_{12}+i\omega_w\mathscr{B}_{12})=F_{e1} \tag{3.91}$$

where the suffix 1 refers to the first body, the suffix 2 refers to the second body, the suffix 12 refers to the effect of the second body on the first body and the suffix 21 refers to the effect of the first body on the second body due to coupling effects.

The equation of motion for the second device is therefore

$$z_2(i^2{\omega_w}^2(M_{b2}+\mathscr{A}_2)+i\omega_w(B_{pto2}+\mathscr{B}_2)+(k_{h2}+k_{m2}))+z_1(i^2{\omega_w}^2\mathscr{A}_{21}+i\omega_w\mathscr{B}_{21})=F_{e2} \tag{3.92}$$

Rearranging this latter equation in terms of z_2

$$z_2=\frac{F_{e2}-(i^2{\omega_w}^2\mathscr{A}_{21}+i\omega_w\mathscr{B}_{21})z_1}{i^2{\omega_w}^2(M_{b2}+\mathscr{A}_2)+i\omega_w(B_{pto2}+\mathscr{B}_2)} \tag{3.93}$$

substituting into the equation of motion for the first device,

$$\begin{aligned} &z_1(i^2{\omega_w}^2(M_{b1}+\mathscr{A}_1)+i\omega_w(B_{pto1}+\mathscr{B}_1)+(k_{h1}+k_{m1})) \\ &\quad+\frac{F_{e2}-(i^2{\omega_w}^2\mathscr{A}_{21}+i\omega_w\mathscr{B}_{21})z_1}{i^2{\omega_w}^2(M_{b2}+\mathscr{A}_2)+i\omega_w(B_{pto2}+\mathscr{B}_2)}(i^2{\omega_w}^2\mathscr{A}_{12}+i\omega_w\mathscr{B}_{12})=F_{e1} \end{aligned} \tag{3.94}$$

and then rearranging in terms of z_1 results in the heave motion as a function of

frequency as

$$z_1 = \frac{F_{e1}(i^2{\omega_w}^2(M_{b2}+\mathscr{A}_2)+i\omega_w(B_{pto2}+\mathscr{B}_2))-F_{e2}(i^2{\omega_w}^2\mathscr{A}_{12}+i\omega_w\mathscr{B}_{12})}{((i^2{\omega_w}^2(M_{b1}+\mathscr{A}_1)+i\omega_w(B_{pto1}+\mathscr{B}_1)+(k_{h1}+k_{m1}))(i^2{\omega_w}^2(M_{b2}+\mathscr{A}_2) + i\omega_w(B_{pto2}+\mathscr{B}_2))-(i^2{\omega_w}^2\mathscr{A}_{21}+i\omega_w\mathscr{B}_{21})(i^2{\omega_w}^2\mathscr{A}_{12}+i\omega_w\mathscr{B}_{12}))} \tag{3.95}$$

Figure 3.11 shows the added mass, damping and excitation force coefficients that have been calculated for the 12m diameter cylindrical device. These coefficients were determined using the open source BEM code Nemoh. The results are refined by adjusting the panel density until convergence of results is achieved.

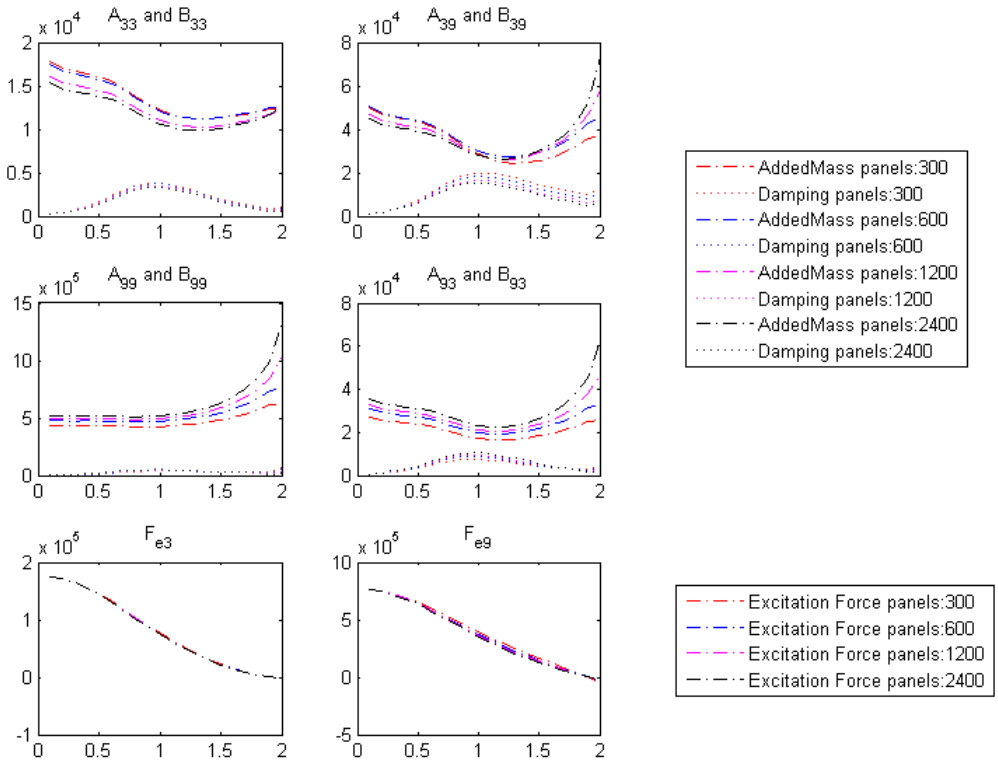

Figure 3.11: BEM calculated coefficients for added mass, damping and excitation force for a cylindrical OWC with a 12m diameter for a range of panel densities

Modeling the pressures on the free surface of the chamber as a piston uses the force

balance equation,

$$F_g(t) = F_e(t) + F_r(t) + F_h(t) + F_{di}(t) + F_P(t) + F_m(t) + F_f(t) \tag{3.96}$$

The definition of each of these forces will now be discussed.

The BEM code computes the hydrostatic stiffness, k_h, where the hydrostatic stiffness is related to the hydrostatic force via

$$F_h = k_h z \tag{3.97}$$

However, the hydrostatic stiffness can be calculated manually

$$k_h = \rho_w g A_s \tag{3.98}$$

This can be used as an additional check that the BEM model has been set-up appropriately.

The excitation force is composed of two components: the Froude-Krylov force due to the incident wave diffraction force due to the diffracted wave (Price 2009). There are two definitions for the excitation force dependent on whether the incident wave data is spectral form or a time domain series. Bhinder et al. (2011) defines the excitation for regular waves as:

$$F_{ej}(t) = \Im\Big(\sum_{i=1}^{N} a_i F_{eij}(\omega_w \exp^{i(\omega_w t + \phi)}\Big) \tag{3.99}$$

where j=1..6, and defines the Degree Of Freedom (DOF) under consideration. Conversely Falnes (1995) defines the excitation force as

$$F_{ej}(t) = \int_{-\infty}^{\infty} \kappa_{ej}(t-\tau)\eta(\tau)d\tau \tag{3.100}$$

As it is non-causal, it is not simply a matter of multiplying the excitation force coefficient by the incident wave height.

It should be noted that drag forces are neglected in this model due to the requirement for experimental testing to obtain the coefficients in order to calculate the diffraction force which is outside the scope of this project but could be encompassed as an extension to this body of work. The Morison equation is used to calculate the diffraction force using coefficients that are derived in a semi empirical manner (Bhinder et al. 2011).

The radiation force for a single body (Gomes et al. 2011) is defined as

$$F_r(t) = \mu_\infty \ddot{z} + \int_0^t \kappa_r(t-\tau)\dot{z}(\tau)d\tau \tag{3.101}$$

which requires the convolution of the impulse response function with the velocity of the body. For a two body system such as an OWC modeled as a device and a piston there is a radiation force due to the movement of the other body.

$$\begin{aligned} F_{r1} &= F_{r1} + F_{r12} && (3.102)\\ &= \mu_{\infty 1}\ddot{z_1} + \int_0^t \kappa_{r1}(t-\tau)\dot{z_1}(\tau)d\tau + \mu_{\infty 12}\ddot{z_2} + \int_0^t \kappa_{r12}(t-\tau)\dot{z_2}(\tau)d\tau && (3.103)\\ F_{r2} &= F_{r2} + F_{r21} && (3.104)\\ &= \mu_{\infty 2}\ddot{z_2} + \int_0^t \kappa_{r2}(t-\tau)\dot{z_2}(\tau)d\tau + \mu_{\infty 21}\ddot{z_1} + \int_0^t \kappa_{r21}(t-\tau)\dot{z_1}(\tau)d\tau && (3.105) \end{aligned}$$

where κ_r is the impulse response function

$$\kappa_r = \frac{2}{\pi}\int_0^\infty [\mathscr{B}(\omega_w]\cos(\omega_w\tau)d\omega_w \tag{3.106}$$

and μ_∞ is the added mass as the frequency tends to infinity

$$\mu_\infty = [\mathscr{A}(\omega_w)] + \frac{1}{\omega_w}\int_0^\infty \kappa_r(\tau)\sin(\omega_w\tau)d\tau \tag{3.107}$$

The added mass and damping coefficients, $\mathscr{A}$ and $\mathscr{B}$, are computed by the BEM code.

The method introduced by Prony and further detailed by Bhinder et al. (2011) gives an approximation to the convolution integral reducing the computational overhead.

A number of states are introduced the sum of which are approximately equal to the convolution

$$\chi = \int_0^t \kappa_r(t-\tau)\dot{z}(\tau)d\tau \tag{3.108}$$

Each state derivative is defined as

$$\dot{\chi}_i = \beta_{pi}\chi_i + \alpha_{pi}\dot{z} \tag{3.109}$$

where the constants α_{pi} and β_{pi} are found using the Prony method. The approximated impulse response function can be calculated as

$$\kappa_r(t) \approx \sum_{i=1}^{l} \alpha_{pi} \exp^{\beta_{pi}t} \tag{3.110}$$

Figure 3.12 shows the impulse response function and the approximation using the Prony method for the cylindrical device already under discussion. The radiation force can therefore be calculated as

$$\begin{aligned} F_{r1} &= F_{r1} + F_{r12} && (3.111)\\ &= \mu_{\infty 1}\ddot{z}_1 + \sum_{i=1}^{l}\chi_{1i} + \mu_{\infty 12}\ddot{z}_2 + \sum_{i=1}^{l}\chi_{12i} && (3.112)\\ F_{r2} &= F_{r2} + F_{r21} && (3.113)\\ &= \mu_{\infty 2}\ddot{z}_2 + \sum_{i=1}^{l}\chi_{2i} + \mu_{\infty 21}\ddot{z}_1 + \sum_{i=1}^{l}\chi_{21i} && (3.114) \end{aligned}$$

The OWC is usually tethered to the sea bed using mooring lines. The mooring lines can be modeled as a simple spring system however there is also non-linear

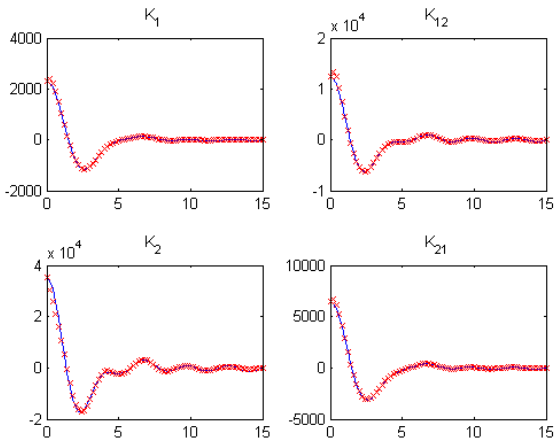

Figure 3.12: Impulse response of a 24m cylindrical OWC

dissipation. For a floating Backward Bent Duct Buoy (BBDB) the movement of the device needs to be considered in multiple degrees of freedom; however, for the simple cylindrical OWC the only motion that will be considered is heave and therefore the mooring force is considered to be zero as the device is not intended to be constrained in this direction.

The motion of the OWC in heave is defined as

$$M_{b1}\ddot{z_1} + \mu_{\infty 1}\ddot{z_1} + \sum_{i=1}^{l} \chi_{1i} + \mu_{\infty 12}\ddot{z_2} + \sum_{i=1}^{l} \chi_{12i} + \rho_w g A_{s1} z_1 = F_{e1} + A_{s2}\Delta p \quad (3.115)$$

and the motion of the piston in heave is defined as

$$M_{b2}\ddot{z_2} + \mu_{\infty 2}\ddot{z_2} + \sum_{i=1}^{l} \chi_{2i} + \mu_{\infty 21}\ddot{z_1} + \sum_{i=1}^{l} \chi_{21i} + \rho_w g A_{s2} z_2 = F_{e2} - A_{s2}\Delta p \quad (3.116)$$

Note that the equations are coupled.

Rearranging Equation (3.116) in terms of the acceleration, $\ddot{z}_2$, gives

$$\ddot{z}_2 = \left(\frac{1}{M_{b2} + \mu_{\infty 2}}\right)\left(F_{e2} - A_{s2}\Delta p - \sum_{i=1}^{l} \chi_{2i} - \sum_{i=1}^{l} \chi_{21i} - \mu_{\infty 21}\ddot{z}_1 - \rho_w g A_{s2} z_2\right) \quad (3.117)$$

Then substituting Equation (3.117) into (3.115) results in

$$(M_{b1}+\mu_{\infty 1})\ddot{z}_1 = F_{e1} + A_{s2}\Delta p - \sum_{i=1}^{l}\chi_{1i} - \sum_{i=1}^{l}\chi_{12i} - \rho_w g A_{s1} z_1 - \Big(\frac{\mu_{\infty 12}}{M_{b2}+\mu_{\infty 2}}\Big)\Big(F_{e2} - A_{s2}\Delta p - \sum_{i=1}^{l}\chi_{2i} - \sum_{i=1}^{l}\chi_{21i} - \mu_{\infty 21}\ddot{z}_1 - \rho_w g A_{s2} z_2\Big) \tag{3.118}$$

Rearranging the equation in terms of the OWC position, z_1, gives

$$\ddot{z}_1 = \frac{1}{\Big(M_{b1}+\mu_{\infty 1} - \frac{\mu_{\infty 12}\mu_{\infty 21}}{M_{b2}+\mu_{\infty 2}}\Big)}\Bigg[F_{e1} + A_{s2}\Delta p - \sum_{i=1}^{l}\chi_{1i} - \sum_{i=1}^{l}\chi_{12i} - \rho_w g A_{s1} z_1 - \Big(\frac{\mu_{\infty 12}}{M_{b2}+\mu_{\infty 2}}\Big)\Big(F_{e2} - A_{s2}\Delta p - \sum_{i=1}^{l}\chi_{2i} - \sum_{i=1}^{l}\chi_{21i} - \rho_w g A_{s2} z_2\Big)\Bigg] \tag{3.119}$$

The equivalent equation for the motion of the piston, z_2, is

$$\ddot{z}_2 = \frac{1}{\Big(M_{b2}+\mu_{\infty 2} - \frac{\mu_{\infty 21}\mu_{\infty 12}}{M_{1}+\mu_{\infty 1}}\Big)}\Bigg[F_{e} - A_{s2}\Delta p - \sum_{i=1}^{l}\chi_{2i} - \sum_{i=1}^{l}\chi_{21i} - \rho_w g A_{s2} z_2 - \Big(\frac{\mu_{\infty 21}}{M_{b1}+\mu_{\infty 1}}\Big)\Big(F_{e} + A_{s2}\Delta p - \sum_{i=1}^{l}\chi_{1i} - \sum_{i=1}^{l}\chi_{12i} - \rho_w g A_{s1} z_1\Big)\Bigg] \tag{3.120}$$

The term

$$\frac{\mu_{\infty 21}}{M_{b1}+\mu_{\infty 1}} \tag{3.121}$$

and its counterpart in the equation for the first body dynamics is so small, as $\mu_{\infty 2}$ is much larger than $\mu_{\infty 12}$, that it is believed that the term can be neglected. No references have been found that incorporate this term and instead the radiation force is defined as

$$F_{r1} = \mu_{\infty 1}\ddot{z}_1 + \sum_{i=1}^{l}\chi_{1i} + \sum_{i=1}^{l}\chi_{12i} \tag{3.122}$$

It has not been investigated how one would implement the OWC system into the

port-Hamiltonian framework without this simplification. Using this simplification, the system equation can be rearranged in the port-Hamiltonian framework to enable power-based control. The total energy within the system is equal to

$$\mathscr{H} = \mathscr{T} + \mathscr{V} \tag{3.123}$$

where the kinetic energy is defined as

$$\mathscr{T} = \frac{1}{2}\Big(\frac{1}{M_{b1} + \mu_{\infty 1}}\Big){Y_1}^2 + \frac{1}{2}\Big(\frac{1}{M_{b2} + \mu_{\infty 2}}\Big){Y_2}^2 \tag{3.124}$$

and the potential energy equates to

$$\mathscr{V} = \frac{1}{2}(k_{m1} + k_{h1})z_1^2 + \frac{1}{2}(k_{m2} + k_{h2})z_2^2 + \mu_{\infty 12}\ddot{z}_2 z_1 + \mu_{\infty 12}\ddot{z}_2 z_1 \tag{3.125}$$

The Rayleigh dissipation equation is defined as

$$\mathscr{R} = \frac{1}{2}B_1 z_1^2 + \frac{1}{2}B_2 z_1^2 \tag{3.126}$$

The states are z_1, z_2, Y_1, Y_2, χ_{1i}, χ_{2i}, χ_{12i} and χ_{21i}.

For uncoupled motion the resulting state equations are

$$\begin{bmatrix} \dot{s} \\ \dot{\chi} \end{bmatrix} = \left(\begin{bmatrix} \mathscr{J}_s & \mathscr{J}_{s\chi} \\ \mathscr{J}_{\chi s} & \mathscr{J}_{\chi} \end{bmatrix} - \begin{bmatrix} \mathscr{D}_s & 0 \\ 0 & \mathscr{D}_{\chi} \end{bmatrix} \right) \begin{bmatrix} \frac{\partial \mathscr{H}}{\partial s} \\ \frac{\partial \mathscr{H}}{\partial \chi} \end{bmatrix} + \begin{bmatrix} g_s \\ 0 \end{bmatrix} u_s \tag{3.127}$$

where the interconnection matrices are defined as

$$\mathscr{J}_s = \begin{bmatrix} 0 & 0 & 1 & 0 \\ 0 & 0 & 0 & 1 \\ -1 & 0 & 0 & 0 \\ 0 & -1 & 0 & 0 \end{bmatrix} \tag{3.128}$$

$$\mathscr{J}_\chi = \begin{bmatrix} 0_{ixi} & 0_{ixi} & 0_{ixi} & 0_{ixi} \\ 0_{ixi} & 0_{ixi} & 0_{ixi} & 0_{ixi} \\ 0_{ixi} & 0_{ixi} & 0_{ixi} & 0_{ixi} \\ 0_{ixi} & 0_{ixi} & 0_{ixi} & 0_{ixi} \end{bmatrix} \tag{3.129}$$

$$\mathscr{J}_{\chi s} = \begin{bmatrix} 0 & 0 & 0 & 0 \\ 0 & 0 & 0 & 0 \\ -\alpha_{p1i}^T & -\alpha_{p12i}^T & 0 & 0 \\ 0 & 0 & -\alpha_{p2i}^T & -\alpha_{p21i}^T \end{bmatrix} \tag{3.130}$$

$$\mathscr{J}_{s\chi} = -\mathscr{J}_{\chi s}^T \tag{3.131}$$

The dissipation matrices are defined as

$$\mathscr{D}_s = \begin{bmatrix} 0 & 0 & 0 & 0 \\ 0 & 0 & 0 & 0 \\ 0 & 0 & B_1 & 0 \\ 0 & 0 & 0 & B_2 \end{bmatrix} \tag{3.132}$$

$$\mathscr{D}_\chi = -\text{diag}\begin{bmatrix} \alpha_{p1i}\beta_{p1i} & \alpha_{p12i}\beta_{p12i} & \alpha_{p2i}\beta_{p2i} & \alpha_{p21i}\beta_{p21i} \end{bmatrix} \tag{3.133}$$

The rate of change of the energy with respect to the state variables s is defined as

$$\frac{\partial \mathscr{H}}{\partial s} = \begin{bmatrix} (k_{m1} + k_{h1})z_1 & (k_{m2} + k_{h2})z_2 & \frac{Y_1}{M_{b1}+\mu_{\infty 1}} & \frac{Y_2}{M_{b2}+\mu_{\infty 2}} \end{bmatrix}^T \tag{3.134}$$

whereas the rate of change of the energy with respect to the state variables χ is defined as

$$\frac{\partial \mathscr{H}}{\partial \chi} = \begin{bmatrix} \frac{\chi_{1i}}{\alpha_{p1i}} & \frac{\chi_{12i}}{\alpha_{p12i}} & \frac{\chi_{2i}}{\alpha_{p2i}} & \frac{\chi_{21i}}{\alpha_{p21i}} \end{bmatrix}^T \tag{3.135}$$

The system input matrix, g_s, is defined as

$$g_s = \begin{bmatrix} 0 & 0 & 0 \\ 0 & 0 & 0 \\ 1 & 0 & 1 \\ 0 & 1 & -1 \end{bmatrix} \tag{3.136}$$

The system inputs are defined as

$$u_s = \begin{bmatrix} F_{e1} & F_{e2} & A_{s2}\Delta p \end{bmatrix}^T \tag{3.137}$$

It is important to check to confirm the skew symmetric property of the $\mathscr{J}$ matrix has been preserved.

3.5 Pneumatic OWC Model

The OWC chamber is a critical component in the energy conversion process. It couples the resulting OWC motion and that of the oscillating body of water to the turbine. Taking into account only the heave motion, the relative height of the water within the chamber and the position of the device results in a volume change directly

affecting the pressure within the chamber. This pressure imposes a force on both the water surface and the OWC itself. It is useful to implement simulations of a completely closed air chamber (i.e. no turbine or valve) and of a completely open chamber (i.e. no pressure build up within the air chamber as it is connected directly to the atmosphere). All other simulations lie in between these two extremes. The air chamber interfaces to the bidirectional turbine by providing a pressure difference across the turbine. The resulting flow rate through the turbine directly affects the mass of air within the chamber, impacting the pressure. As it can be seen, the system is highly coupled and therefore a unidirectional implementation of power flow is far from ideal.

Work published by Amundarain et al. (2011) describes a model of a turbine and generator, with the input to the system being the pressure drop across the turbine, Δp, simulated with a sinusoidal input of $|7000\sin(0.1\pi t)|$. The model was tested with irregular waves but no information is given as to how these waves were developed and if they are associated with any particular spectrum. The OWC pneumatics were not modeled.

The pressure drop across the turbine was related to the power coefficient C_a, the axial velocity of the air, V_a, the rotational speed, U, the cross sectional area of the annulus at the rotor blades, A_R, and was defined as

$$\Delta p = C_a K_x (1/A_R)[{V_a}^2 + U^2] \tag{3.138}$$

where the constant K_x was defined as

$$K_x = \rho_a h_b n l_b / 2 \tag{3.139}$$

The mechanical torque was related to the torque coefficient, C_t, the axial and rota-

tional speed, as well as the radius of the mid-span of the rotor blades, r_m. It was defined as

$$T_m = C_t K_x r_m [{V_a}^2 + U^2] \tag{3.140}$$

The power and torque coefficients can be obtained either though experimental testing or CFD numerical simulations.

These CFD studies concentrate on the turbine performance and do not include the air chamber, such as the work by Banks (2009), Torresi et al. (2011) and Liu et al. (2011). Paixão Conde & Gato (2008), however, employed the CFD code Fluent to model the air chamber and assess the performance of two asymmetrically placed vertical-axis turbines under maximum flow conditions and concluded that the flow distribution is fairly uniform and that steady simulations provide sufficient accuracy. The focus of their study was on air jets impacting the water surface which could cause water spray to be ingested by the air turbines and hence a recommendation was put forward suggesting employing a baffle to prevent this. It would be interesting to see what impact this phenomenon has on the performance of the device as well as considering the potential structural issues.

In summary there are a range of models for the pneumatic subsystem; however, the air chamber is a neglected component since a lot of research focusses either on the hydrodynamics of the OWC or on the pneumatics of the turbine.

3.5.1 Inter-Component Volume Method

The pneumatic model, used in this work, has been derived using two separate methods for comparison purposes. The first method, presented in this section, uses the inter-component volume method as used by Rahman & Whidborne (2008). This

method breaks the subsystem down so that, between each component, there is a volume of air and, for each volume, the properties (e.g. pressure, temperature) are calculated. The simplest interpretation of the OWC pneumatic system is shown in Figure 3.13, with a single volume which has mass exiting through the turbine and potentially a BOV. This is suitable when the turbine needs to be treated as a single entity such as when CFD derived turbine characteristics are being used. In theory if CFD derived characteristics were available for each component (e.g. guide vanes, rotor blades) then the turbine could be modeled using the inter-component volume method to its full extent, see Figure 3.14.

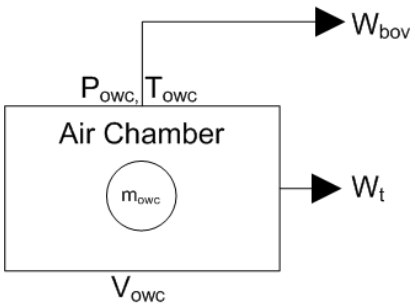

Figure 3.13: Basic inter-component volume method for OWC air chamber and turbine

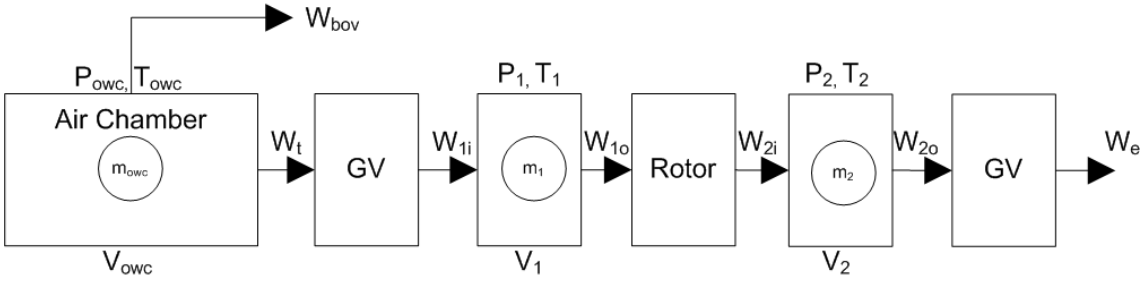

Figure 3.14: Extended inter-component volume method for OWC air chamber and turbine

Assuming that the temperature difference is negligible, the rate of change of pressure can be calculated by applying the following method.

The ideal gas law is critical to the inter-component method; by differentiating the

ideal gas law,

$$p_c V_c = m_c R_a T_c \tag{3.141}$$

the relationship for the rate of change of static pressure, p_c, can be related to the rate of change of the volume, V_c, the mass, m_c, and the temperature T_c as

$$V_c \dot{p_c} + p_c \dot{V_c} = R_a T_c \dot{m_c} + R_a m_c \dot{T_c} \tag{3.142}$$

The temperature derivative, if considered negligible in comparison to the mass derivative as shown by Rahman & Whidborne (2009), can be neglected. If this is the case, the above equation can then be simplified to give

$$\dot{p_c} = \frac{R_a T_c}{V_c} \dot{m_c} - \frac{p_c}{V_c} \dot{V_c} \tag{3.143}$$

The volume within the air chamber is

$$V_c \;\; = \;\; A_c(h_{a0} + z_1 - z_2) \tag{3.144}$$

where h_{a0} is the draft (initial height) of the air chamber, A_c is the cross-sectional area of the OWC, z_1 is the vertical movement of the buoy and z_2 is the wave height within the chamber (as opposed to the incident wave elevation, η). Differentiating the volume with respect to time results in

$$\dot{V_c} \;\; = \;\; A_c(\dot{z_1} - \dot{z_2}) \tag{3.145}$$

Substituting the rate of change of volume into the equation for rate of change of pressure gives

$$\dot{p_c} = \frac{R_a T_c}{V_c} \dot{m_c} - \frac{p_c}{(h_{a0} + z_1 - z_2)} (\dot{z_1} - \dot{z_2}) \tag{3.146}$$

To reduce the number of variables the ideal gas law will be substituted back into the above equation

$$\frac{p_c}{m_c} = \frac{R_a T_c}{V_c} \tag{3.147}$$

The rate of change of pressure is now only a function of the mass, wave height, pressure and the initial height of the air chamber,

$$\dot{p_c} = p_c \left(\frac{1}{m_c} \dot{m_c} - \frac{1}{(h_{a0} + z_1 - z_2)} (\dot{z_1} - \dot{z_2}) \right) \tag{3.148}$$

In the case where the temperature difference cannot be considered negligible, but instead it is considered to be adiabatic (no transfer of heat to the surroundings), then the following equation Gervelas et al. (2011) can be applied

$$p_c{}^{(1-\gamma)} T_c{}^{\gamma} = const \tag{3.149}$$

and hence by applying a logarithm and differentiating, the following equation is derived

$$\frac{\partial T_c}{\partial t} = \frac{T_c}{p_c} \frac{\gamma - 1}{\gamma} \frac{\partial p_c}{\partial t} \tag{3.150}$$

This can be substituted into Equation (3.142) to give

$$V_c \dot{p_c} + p_c \dot{V_c} = R_a T_c \dot{m_c} + R_a m_c \left(\frac{T_c}{p_c} \frac{\gamma - 1}{\gamma} \frac{\partial p_c}{\partial t} \right) \tag{3.151}$$

Rearranging to group the pressure derivatives together results in

$$\frac{\partial p_c}{\partial t} \left(1 - \frac{\gamma - 1}{\gamma}\right) = \frac{R_a T_c}{V_c} \frac{\partial m_c}{\partial t} - \frac{p_c}{V_c} \frac{\partial V_c}{\partial t} \tag{3.152}$$

The equation for the speed of sound in air is

$$c_s = \sqrt{\gamma R_a T_c} \tag{3.153}$$

The pressure in the chamber can be calculated as

$$p_c = p_{atm} + \Delta p \tag{3.154}$$

Substituting both of these into Equation (3.152) results in a simplification of the pressure equation to

$$\frac{\partial \Delta p}{\partial t} = \frac{{c_s}^2}{V_c}\frac{\partial m_c}{\partial t} - \frac{\gamma(\Delta p + p_{atm})}{V_c}\frac{\partial V_c}{\partial t} \tag{3.155}$$

The equations for the volume and the rate of change of volume are unchanged which gives the equation for the rate of change of pressure across the turbine as

$$\frac{\partial \Delta p}{\partial t} = \frac{{c_s}^2}{A_c(h_{a0} + z_1 - z_2)}\frac{\partial m_c}{\partial t} - \frac{\gamma(\Delta p + p_{atm})}{(h_{a0} + z_1 - z_2)}(\dot{z_1} - \dot{z_2}) \tag{3.156}$$

Equation (3.148) can be compared against (3.156) for a comparison of the temperature effect. This second model taking into account the temperature will be used for the remainder of this work.

3.5.2 Turbine Mass Flow

The mass flow through the turbine, w_t can be calculated using the non-dimensional pressure and flow rate relationship derived either through CFD numerical simulations or experimental testing. In this instance non-dimensional turbine characteristics have been derived from CFD numerical results (derived by Banks (2009), Natanzi (2010a), Tarver (2013) and the author of this thesis) and hence the non-dimensional flow rate through the turbine, Q^*, and the non-dimensional turbine torque, T^* are a function of the non-dimensional pressure drop across the turbine,

p^*, the density of air, ρ_a, the diameter of the turbine, D_t, and the rotational speed of the turbine, ω_m. The non-dimensional parameters are calculated using the standard method as given by White (1999).

Non-dimensional pressure is defined as

$$p^* = \frac{\Delta p}{\rho_a {D_t}^2 {\omega_m}^2} \tag{3.157}$$

Non-dimensional torque is defined as

$$T^* = \frac{T_t}{\rho_a {D_t}^5 {\omega_m}^2} \tag{3.158}$$

Non-dimensional flow rate is defined as

$$Q^* = \frac{Q_t}{{D_t}^3 \omega_m} \tag{3.159}$$

where mass flow is subsequently derived from the non-dimensional flow rate, and is defined as

$$w_t = \rho_a Q_t \tag{3.160}$$

The non-dimensional curves enable easy scaling of a system for different power ratings. There are various ways to model a turbine, either with empirical relationships, model equations based on fundamental equations or complex numerical algorithms requiring extensive computational capacity. A trade-off needs to be made to meet the requirements for real-time control (Ray 1980).

The model described by Ray (1980) is very interesting, and suggests a compromise between the two contradicting design criteria of computational speed and fidelity. However, the assumption for steam turbines of constant efficiency across the different

stages and for part load conditions does not carry across the extremely low pressure variable geometry impulse or alternative low pressure single stage turbine.

Various OWC models incorporate empirical relationships of the power coefficient, C_a versus the flow coefficient, Φ, and the torque coefficient, C_t, also against Φ, including the work by Anand et al. (2007). The equations for C_t and C_a given by Herring (2007) are defined as

$$C_t = \frac{T_t}{\rho_a({V_a}^2 + U_R^2) h_b l_b n r_m / 2} \tag{3.161}$$

$$C_a = \frac{\Delta p Q_t}{\rho_a({V_a}^2 + U_R^2) h_b l_b n V_a / 2} \tag{3.162}$$

where T_t is the turbine torque, ρ_a is the air density, h_b is the height of the blade, l_b is the chord length, n is the number of rotor blades and r_m is the mean radius.

Figure 3.15 shows a turbine model using these relationships. CFD numerical simulation results can be used to model the turbine. There are a variety of ways to apply the results into a system model either using look-up tables, alternatively curves can be fit to the data. One of the limitations however to using CFD numerical simulation results is that they are accurate over a finite flow coefficient range.

The turbine characteristics can be linearized around an operating point. In order to do this the equations approximating the data need to be twice differentiable to ensure no discontinuities. Initially, it was decided to fit a least squared fit curve to the data, but this drove a high degree polynomial with large oscillations between the known values. To avoid this issue it was decided to investigate the use of a spline fit and limit the spline to a 3rd order polynomial. It was found that if the end points were not bound by a maximum rate of change they required additional data points adding, otherwise the quality of the fit deteriorated significantly.

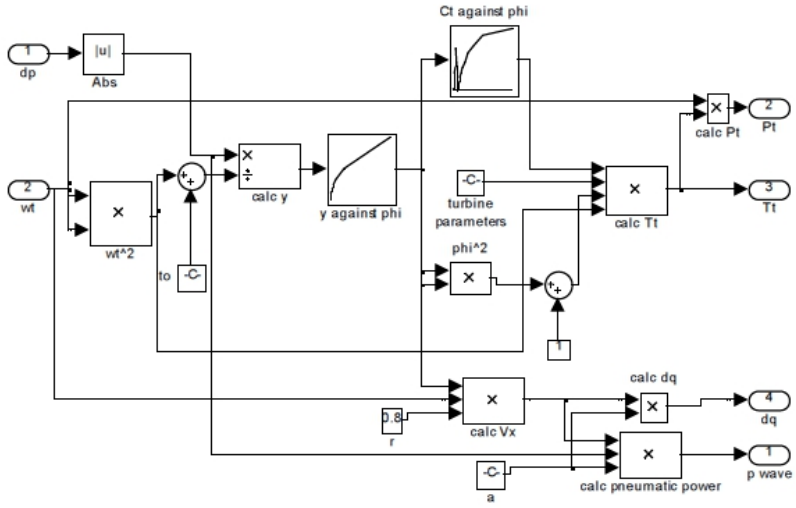

Figure 3.15: Simulink model of the turbine (Anand et al. 2007)

The equation for the non-dimensional turbine flow rate spline of third degree is

$$Q^* = a_{Qi}(p^* - {p^*}_i)^3 + b_{Qi}(p^* - {p^*}_i)^2 + c_{Qi}(p^* - {p^*}_i) + d_{Qi} \tag{3.163}$$

If necessary analysis can be carried out to see which data points can be removed to reduce the size of the coefficients table without significantly deteriorating the fit to the data. For this study it was deemed unnecessary.

Substituting in the spline equations into the non-dimensional turbine equation results in

$$Q_t = \rho_a {\omega_m}{D_t}^3 \Big[a_{Qi}(\frac{\Delta p}{\rho_a {\omega_m}^2 {D_t}^2} - {p^*}_i)^3 + b_{Qi}(\frac{\Delta p}{\rho_a {\omega_m}^2 {D_t}^2} - {p^*}_i)^2 + c_{Qi}(\frac{\Delta p}{\rho_a {\omega_m}^2 {D_t}^2} - {p^*}_i) + d_{Qi} \Big] \tag{3.164}$$

3.5.3 Blow-Off Valve Mass Flow

Another component of the system is the BOV, which can be used to relieve pressure for extreme or freak waves. The BOV is modeled as a simple orifice; the standard

orifice equation is applied. The mass flow through an orifice,

$$w_o = C_d A_o \sqrt{2\rho_a \Delta p} \tag{3.165}$$

is given by Gervelas et al. (2011) as a function of the orifice area, A_o, the coefficient of discharge of the orifice, C_d, the pressure drop across the orifice which in this case is the same as the pressure drop across the turbine, Δp, and the density of air. The BOV is either open or closed, for simulation purposes there is no intermediate position. This is implemented using a gain, G_b which takes only binary values of open, one, or closed, zero. As a result no transient dynamics of the valve are taken into account.

$$w_b = G_b C_d A_b \sqrt{2\rho_a \Delta p} \tag{3.166}$$

3.5.4 Rate of Change of Mass within Air Chamber

The pneumatic system is assumed to be incompressible owing to the low pressure ratios involved in agreement with Herring (2007) and Banks (2009).

The rate of change of mass of air within the OWC therefore has a negative linear relationship to the sum of mass exiting through the BOV, w_b and the turbine w_t,

$$\dot{m}_c = -w_t - w_b \tag{3.167}$$

The dynamics of the pneumatic system are defined by this equation.

3.5.5 Port-Hamiltonian Equations

As will be discussed in Chapter 5, power shaping control offers a potential means of improved system level efficiency. To support the implementation of power shaping

control, the pneumatic system equations discussed in Sections 3.5.1 to 3.5.4 need to be applied into the port-Hamiltonian framework.

The turbine CFD curves are given as a relationship of non-dimensional pressure to non-dimensional flow rate and also non-dimensional pressure to non-dimensional torque. The four fundamental system components of any system, independent of domain, are inductor, capacitor, resistor and mem-resistor (Jeltsema & Scherpen 2009). The inductor is defined in terms of the relationship between momentum and flow, the capacitor in terms of effort and position, the resistor in terms of effort and flow and the mem-resistor in terms of momentum and position. Taking these definitions into account, one potential way to consider the turbine pressure drop and flow rate relationship is as a resistor. The pressure to torque relationship can be thought of as a gyrator where the effort at one side of the component is related to the flow at the other side and vice versa. It should be noted that in a turbine these relationships are non-linear.

The definition for the gyrator ratio, N_t is

$$N_t = \frac{T_t}{p_c} = \frac{Q_{tg}}{\omega_m} \tag{3.168}$$

Section 3.2.5 proposed an amendment to the port-Hamiltonian framework to change the reference frame for systems with potential energy but no kinetic energy or in other words flow source systems rather than effort source. This modification has been applied to the pneumatic system in order to couple it with the hydrodynamic and mechanical systems. The pressure has therefore been defined as the flow variable and the rate of change of volume as the effort variable. As a result the position variable is defined as

$$q_i = \int \Delta p dt \tag{3.169}$$

and the momentum variable is defined as

$$Y_i = V_e \tag{3.170}$$

A simplified version of the OWC dynamics will be considered here in order to illustrate the coupling between the hydrodynamic and mechanical systems through the pneumatic system. As a result the energy function is defined as

$$\mathscr{H} = \frac{1}{2}\frac{1}{M_{11}}{Y_1}^2 + \frac{1}{2}\frac{1}{M_2}{Y_2}^2 + \frac{1}{2}k_1 z_1 + \frac{1}{2}k_2 z_2 + m_c R_a (T_{atm} V_{e0}^{\gamma-1})\frac{1}{1-\gamma}{V_e}^{1-\gamma} + \frac{1}{2}\frac{1}{J_m}{Y_m}^2 \tag{3.171}$$

and the dissipation function is defined as

$$\mathscr{R} = \frac{1}{2}B_1{\dot{z}_1}^2 + \frac{1}{2}B_2{\dot{z}_2}^2 + \frac{1}{2}Q_{tr}{p_c}^2 + \frac{1}{2}B_t{\omega_m}^2 \tag{3.172}$$

where

$$Q_{tr} = Q_t - Q_{tg} \tag{3.173}$$

and

$$Q_t = \rho_a \omega_m {D_t}^3 \Bigg[a_{Qi}\left(\frac{\Delta p}{\rho_a {\omega_m}^2 {D_t}^2} - {p^*}_i\right)^3 + b_{Qi}\left(\frac{\Delta p}{\rho_a {\omega_m}^2 {D_t}^2} - {p^*}_i\right)^2 + c_{Qi}\left(\frac{\Delta p}{\rho_a {\omega_m}^2 {D_t}^2} - {p^*}_i\right) + d_{Qi}\Bigg] \tag{3.174}$$

The resulting system equations are

$$\begin{bmatrix} \dot{z_1} \\ \dot{z_2} \\ \dot{Y_1} \\ \dot{Y_2} \\ \dot{V_e} \\ \dot{\theta}_m \\ \dot{Y_m} \end{bmatrix} = \begin{bmatrix} 0 & 0 & 1 & 0 & 0 & 0 & 0 \\ 0 & 0 & 0 & 1 & 0 & 0 & 0 \\ -1 & 0 & -B_1 & 0 & -A & 0 & 0 \\ 0 & -1 & 0 & -B_2 & A & 0 & 0 \\ 0 & 0 & A & -A & -B_q & 0 & -K \\ 0 & 0 & 0 & 0 & 0 & 0 & 1 \\ 0 & 0 & 0 & 0 & K & -1 & -B_t \end{bmatrix} \begin{bmatrix} k_1 z_1 \\ k_2 z_2 \\ \frac{Y_1}{M_1} \\ \frac{Y_1}{M_2} \\ p_c \\ \frac{\partial \mathscr{H}}{\partial \theta_m} \\ \frac{\partial Y_m}{\partial J_m} \end{bmatrix} + \begin{bmatrix} 0 & 0 \\ 0 & 0 \\ 1 & 0 \\ 0 & 1 \\ 0 & 0 \\ 0 & 0 \\ 0 & 0 \end{bmatrix} \begin{bmatrix} F_{e1} \\ F_{e2} \end{bmatrix} \tag{3.175}$$

where

$$p_c = m_c R_a (T_{atm} V_{e0}^{\gamma-1}) V_e^{-\gamma} \tag{3.176}$$

and

$$B_q = \frac{\partial \mathscr{R}}{\partial p_c} \frac{1}{p_c} \tag{3.177}$$

The turbine relationship between non-dimensional pressure drop and flow rate and that between non-dimensional pressure drop and torque have been successfully integrated into the port-Hamiltonian framework as part of the pneumatic subsystem.

3.6 Mechanical Drive-Train Model

One of the big issues with OWCs is the existence of only a few control variables, especially in the case of a fixed geometry single turbine as presented here. The reduced number of control variables make it harder to control the system to a desired operating condition. As a result a number of proposals have been made to address this issue, one of which is to use a variable inertia flywheel. O'Sullivan & Lewis (2008) stated that, in certain sea states, fixed speed (and high inertia) is preferred while in others it is variable speed. Tuning the inertia of the system is a balance between smoothing of power and dynamic response to fluctuations. As a consequence of this, the next two subsections detail the model for both a fixed inertia and variable inertia system.

3.6.1 Fixed Inertia Turbine Model

The resultant torque, T_n, on the turbine-generator shaft is

$$T_n = T_t + T_e + T_b \tag{3.178}$$

where T_e is the electrical torque applied by the generator; T_b is the losses in the drive train due to bearings and windage in both the turbine and generator and is usually negative unless the turbine is spinning in reverse; and T_t is the torque applied to the turbine from the air flow and is a function of the non-dimensional pressure, density, rotor diameter and speed as calculated in the previous section. The resultant torque is used to calculate the acceleration of the rotating assembly,

$$\ddot{\theta}_m = \frac{T_n}{J_d} \tag{3.179}$$

where J_d is the sum of the moments of inertia of all rotating components in the drive-train.

Alternatively the equations can be calculated using one of the energy-based modeling methods, for example Euler-Lagrange mechanics. First the kinetic energy, $\mathscr{T}$, potential energy, $\mathscr{V}$ and the Rayleigh dissipation function, $\mathscr{R}$ are equal to

$$\mathscr{T} = \frac{1}{2} J_d \dot{\theta}_m^2 \tag{3.180}$$

$$\mathscr{V} = -(T_t + T_e)\theta_m \tag{3.181}$$

$$\mathscr{R} = \frac{1}{2}(B_t + B_b)\dot{\theta}_m^2 \tag{3.182}$$

where the mechanical resistance due to windage and bearings losses is B_t and B_b respectively. Note that the losses are not included in the potential term but rather in the Rayleigh dissipation function. From these equations, the partial derivative with respect to the generalized coordinate and velocity are calculated, in this case the coordinate is θ_m and the generalized velocity is $\dot{\theta}_m$.

$$\frac{\partial \mathscr{T}}{\partial \theta_m} = 0 \tag{3.183}$$

$$\frac{d}{dt}\left(\frac{\partial \mathscr{T}}{\partial \dot{\theta}_m}\right) = J_d \ddot{\theta}_m \tag{3.184}$$

$$\frac{\partial \mathscr{V}}{\partial \theta_m} = -(T_t + T_e) \tag{3.185}$$

$$\frac{\partial \mathscr{R}}{\partial \dot{\theta}_m} = (B_t + B_b)\dot{\theta}_m \tag{3.186}$$

The partial derivatives are substituted into the Euler-Lagrange equation, Equation (3.64), which results in

$$J_d \ddot{\theta}_m - (T_t + T_e) + (B_t + B_b)\dot{\theta}_m = 0 \tag{3.187}$$

Rearranged, this produces the derivative of the system variable speed.

$$\ddot{\theta}_m = \frac{1}{J_d}\Big[\big(T_t + T_e\big) - \big(B_t + B_b\big)\dot{\theta}_m\Big] \tag{3.188}$$

3.6.2 Variable Inertia Turbine Model

A potential variable inertia system is presented here. The kinetic energy, potential energy and Rayleigh dissipation function are the same as that calculated for the fixed inertia turbine and are given in Equations (3.180) to (3.182). As the inertia is now a function of time, the time derivative of the partial derivative of the kinetic energy with respect to the generalized velocity is now

$$\frac{d}{dt}\left(\frac{\partial \mathscr{T}}{\partial \dot{\theta}_m}\right) \;=\; \dot{J}_d\dot{\theta}_m + J_d\ddot{\theta}_m \tag{3.189}$$

The time derivative is then substituted back into the Euler-Lagrange equation, resulting in

$$\ddot{\theta}_m = \frac{1}{J_d}\big[T_m + T_e - \dot{J}_d\theta_m - (B_t + B_b)\dot{\theta}_m\big] \tag{3.190}$$

This will only be true for the variable inertia system assuming that mass is expelled at null velocity. Under this condition both the fixed inertia and variable inertia systems can be represented in the port-Hamiltonian framework as

$$\begin{bmatrix} \frac{d\theta_m}{dt} \\ \frac{dY_m}{dt} \end{bmatrix} = \left(\begin{bmatrix} 0 & 1 \\ -1 & 0 \end{bmatrix} - \begin{bmatrix} 0 & 0 \\ 0 & B_t + B_b \end{bmatrix} \right) \begin{bmatrix} 0 \\ -1 \end{bmatrix} + \begin{bmatrix} 0 \\ 1 \end{bmatrix} \begin{bmatrix} T_m \end{bmatrix} \tag{3.191}$$

However whether this condition is true or not will depend on the specific mechanical design of the variable inertia flywheel. Modifications to the system equation of motion can be made to account for a change in mass at non-null velocity, however this is not presented here.

3.7 Electrical Generator Model

There is an absence of system level models that incorporate one of the accepted electrical generator models such as that presented by Krause (1986). Various different approaches have been developed to model the electrical system for marine energy devices. Some of these completely neglect the effect of generator efficiency under part load conditions and the resulting power factor (ratio of useful power to total power). Other models neglect the dynamic components.

Hodgins (2010) provides a good description of the losses that are associated with a wide variety of generator types including both squirrel cage and doubly fed induction generators. These include the friction, windage, stator copper and rotor copper losses. The resulting efficiencies at part load can be see in Figure 3.16. Note that the per unit (p.u.) value is calculated as the actual value divided by the nominal rated value. This is a common way to normalize electrical parameters. However, the state equations are not given; instead, the power output of the machine is given as

$$P_{out} = P_{in} - P_{loss} \tag{3.192}$$

As a result the generator has no effect back along the power chain and hence has no effect on the turbine or the OWC itself. This same methodology is applied by Curran et al. (1997). In direct contrast, Gonzalez et al. (2013) states the importance of simulating both the steady and transient operation and employs the synchronous generator model as per Sauer & Pai (1998). Approximations based on empirical results were used by Brito-Melo et al. (2002) to simulate the generator.

A permanent magnet model is presented by Ceballos et al. (2013) and a wound rotor induction machine is presented by Enferad & Nazarpour (2013). A direct-quadrature model of a doubly fed induction generator was presented by Amundarain et al. (2011).

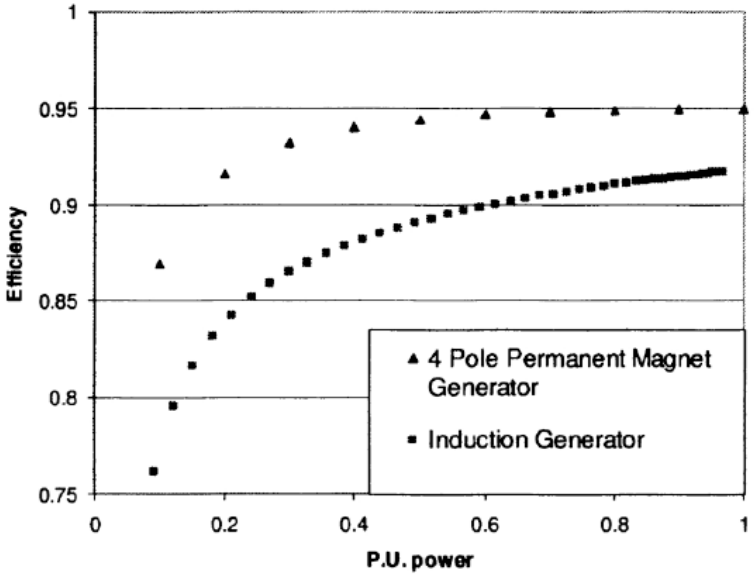

Figure 3.16: Per unit power for induction generator vs permanent magnet (Hodgins 2010)

The system equations for the DFIG and the SCIG are the same; however, the applied voltages are different. The rotor voltage on SCIG is zero and the stator voltage is that of the voltage converter. The voltage on a DFIG is that of the voltage converter and the stator voltage is that of the grid connection. As a result, the control input on the SCIG and the DFIG is the stator and rotor voltages respectively. Krause (1986) is a useful source for a detailed derivation of these well-known equations. Section 3.7.1 will review the derivation of the induction generator equations as presented by Krause (1986) as this will be employed in the generation of the port-Hamiltonian model in Section 3.7.2.

3.7.1 Induction Generator System Equations

The standard three phase reference frame is called the abc reference frame. These are the values that can be measured directly using a volt meter and current clamps on the windings and have sinusoidal oscillating values.

The state variables in the abc frame are the stator and rotor fluxes, ψ_{abcs} and ψ_{abcr} respectively, and the mechanical speed. The rate of change of the stator flux is defined as

$$\frac{d\psi_{abcs}}{dt} = v_{abcs} - R_s i_{abcs} \tag{3.193}$$

where v_{abcs} is the abc stator voltage, R_s is the stator resistance and i_{abcs} is the abc stator current. Whereas the rate of change of the rotor flux is defined as

$$\frac{d\psi_{abcr}}{dt} = v_{abcr} - R_r i_{abcr} \tag{3.194}$$

where v_{abcr} is the abc rotor voltage, R_r is the rotor resistance and i_{abcr} is the abc rotor current. The acceleration of the mechanical shaft is given by

$$\frac{d\omega_m}{dt} = \frac{1}{(J_m)}(T_t + T_e) \tag{3.195}$$

where J_m is the mechanical inertia, is the turbine T_t is the load torque and T_e is the electrical torque, given as

$$T_e = \frac{n_p}{2} {i_{abcs}}^T \frac{\partial L_{srx}}{\partial \theta_r} i_{abcr} \tag{3.196}$$

The inductance matrix is

$$L_{srx} = L_{sr} \begin{bmatrix} \cos(\theta_r) & \cos(\theta_r + \frac{2\pi}{3}) & \cos(\theta_r - \frac{2\pi}{3}) \\ \cos(\theta_r - \frac{2\pi}{3}) & \cos(\theta_r) & \cos(\theta_r + \frac{2\pi}{3}) \\ \cos(\theta_r + \frac{2\pi}{3}) & \cos(\theta_r - \frac{2\pi}{3}) & \cos(\theta_r) \end{bmatrix} \tag{3.197}$$

where θ_r is the rotor position.

The qd0 stator flux is given as

$$\frac{\psi_{qd0s}}{dt} = v_{qd0s} - R_s i_{qd0s} - \omega_e \begin{bmatrix} 0 & 1 & 0 \\ -1 & 0 & 0 \\ 0 & 0 & 0 \end{bmatrix} \psi_{qd0s} \tag{3.198}$$

where v_{qd0s} is the dq0 stator voltage, i_{qd0s} is the qd0 stator current, and ω_e is the electrical speed of the stator.

The qd0 rotor flux is given as

$$\frac{\psi_{qd0r}}{dt} = v_{qd0r} - R_r i_{qd0r} - (\omega_e - \omega_r) \begin{bmatrix} 0 & 1 & 0 \\ -1 & 0 & 0 \\ 0 & 0 & 0 \end{bmatrix} \psi_{qd0r} \tag{3.199}$$

where v_{qd0r} is the dq0 rotor voltage, i_{qd0r} is the qd0 rotor current and ω_r is the electrical speed of the rotor which is defined as

$$\omega_r = \frac{n_p}{2}\omega_m \tag{3.200}$$

The qd0 electrical torque is calculated as

$$T_e = \frac{3}{2}\frac{n_p}{2} L_{ms}(i_{qs} i_{dr} - i_{ds} i_{qr}) \tag{3.201}$$

where the Park transform is used to convert from the abc reference frame to the direct-quadrature-zero (dq0) reference frame and is defined by

$$v_d = \frac{2}{3}(v_a \sin(\omega_x t) + v_b \sin(\omega_x t - \frac{2\pi}{3}) + v_c \sin(\omega_x t + \frac{2\pi}{3})) \tag{3.202}$$

$$v_q = \frac{2}{3}(v_a \cos(\omega_x t) + v_b \cos(\omega_x t - \frac{2\pi}{3}) + v_c \cos(\omega_x t + \frac{2\pi}{3})) \tag{3.203}$$

$$v_0 = \frac{1}{3}(v_a + v_b + v_c) \tag{3.204}$$

The reverse transform is defined as

$$v_a = v_d \sin(\omega_x t) + v_q \cos(\omega_x t) + v_0 \tag{3.205}$$

$$v_b = v_d \sin(\omega_x t - \frac{2\pi}{3}) + v_q \cos(\omega_x t - \frac{2\pi}{3}) + v_0 \tag{3.206}$$

$$v_c = v_d \sin(\omega_x t + \frac{2\pi}{3}) + v_q \cos(\omega_x t + \frac{2\pi}{3}) + v_0 \tag{3.207}$$

For load balanced systems this can result in a minimization of the number of states as the zero component can be disregarded. A load balanced system is quite simply where the voltage and current in each abc phase are of the same magnitude but out of phase by 120°. An example of an unbalanced load in a distribution system is where houses connected to one phase are consuming more power than houses connected to another phase. This can also happen is the resistance is higher on one phase of a generator. It is always advisable to design for balanced load and an additional benefit, as previously stated, is that the number of states within the model can then be reduced.

An alternate definition of the transform is given by Krause (1986) where the transform of the stator and rotor currents in the qd0 reference frame is calculated from the three phase systems using the following equations

$$i_{qd0s} = K_s(\theta_s) i_{abcs} \tag{3.208}$$

$$i_{qd0r} = K_r(\theta_s, \theta_r) i_{abcr} \tag{3.209}$$

The transform matrices have multiple definitions (Krause 1986), however, as it is an arbitrary reference frame it has been decided to use one of the definitions given by Krause (1986) where the matrices are orthogonal so that the inverse of the matrix is equal to the transpose, i.e.

$$(K_s)^T = (K_s)^{-1} \tag{3.210}$$

$$(K_r)^T = (K_r)^{-1} \tag{3.211}$$

as it simplifies the port-Hamiltonian model that will be derived in the next section.

This being the case the stator transform is defined as

$$K_s(\theta_s) = \sqrt{\frac{2}{3}} \begin{bmatrix} \cos(\theta_s) & \cos(\theta_s - \frac{2\pi}{3}) & \cos(\theta_s + \frac{2\pi}{3}) \\ \sin(\theta_s) & \sin(\theta_s - \frac{2\pi}{3}) & \sin(\theta_s + \frac{2\pi}{3}) \\ \frac{1}{\sqrt{2}} & \frac{1}{\sqrt{2}} & \frac{1}{\sqrt{2}} \end{bmatrix} \tag{3.212}$$

whereas the rotor transform is defined as

$$K_r(\beta_x) = \sqrt{\frac{2}{3}} \begin{bmatrix} \cos(\beta_x) & \cos(\beta_x - \frac{2\pi}{3}) & \cos(\beta_x + \frac{2\pi}{3}) \\ \sin(\beta_x) & \sin(\beta_x - \frac{2\pi}{3}) & \sin(\beta_x + \frac{2\pi}{3}) \\ \frac{1}{\sqrt{2}} & \frac{1}{\sqrt{2}} & \frac{1}{\sqrt{2}} \end{bmatrix} \tag{3.213}$$

where

$$\beta_x = \theta_s - \theta_r \tag{3.214}$$

where θ_s is the reference position.

It should be noted that the order of the direct-, quadrature- and zero-components depends on the specific reference. The order of quadrature-direct-zero will be used throughout this work to align with the work by Krause (1986).

3.7.2 Port-Hamiltonian Induction Generator Model

A port-Hamiltonian model of an induction generator model was presented by Dòria-Cerezo (2006).

The state variables are defined as

$$s = \begin{bmatrix} \psi_{dqs} & \psi_{dqr} & Y_m \end{bmatrix}^T \tag{3.215}$$

The state equation in the form of

$$\dot{s} = (\mathscr{J} - \mathscr{D})\frac{\partial \mathscr{H}}{\partial s} + g_s u_s \tag{3.216}$$

is given by

$$\begin{aligned} \dot{s} = \left(\begin{bmatrix} -\omega_s L_s J_2 & -\omega_s L_{sr} J_2 & 0_{2x1} \\ -\omega_s L_{sr} J_2 & -(\omega_s - \omega_r) L_r J_2 & L_{sr} J_2 i_{dqs} \\ 0_{1x2} & L_{sr} {i_{dqs}}^T J_2 & 0 \end{bmatrix} - \begin{bmatrix} R_s I_2 & 0_{2x2} & 0_{2x1} \\ 0_{2x2} & R_r I_2 & 0_{2x1} \\ 0_{1x2} & 0_{1x2} & B_b \end{bmatrix} \right) \begin{bmatrix} i_{dqs} \\ i_{dqr} \\ \omega_m \end{bmatrix} \\ + \begin{bmatrix} I_2 & 0_{2x2} & 0_{2x1} \\ 0_{2x2} & I_2 & 0_{2x1} \\ 0_{2x1} & 0_{2x1} & 1 \end{bmatrix} \begin{bmatrix} v_{dqs} \\ v_{dqr} \\ T_l \end{bmatrix} \end{aligned} \tag{3.217}$$

where

$$J_2 = \begin{bmatrix} 0 & 1 \\ -1 & 0 \end{bmatrix} \tag{3.218}$$

and

$$I_2 = \begin{bmatrix} 1 & 0 \\ 0 & 1 \end{bmatrix} \tag{3.219}$$

The model as presented by Dòria-Cerezo (2006) is merely for a 2 pole generator

which is insufficient for the needs of the OWC system which often requires lower speed machines. Proposed by the author of this thesis is an alternative derivation of the port-Hamiltonian induction generator model which results in the same equations as those given by Krause (1986), and also extends the port-Hamiltonian model for any number of defined poles, n_p. The number of poles is directly coupled to the speed range of the generator. This port-Hamiltonian generator model will enable the use of the power-based control strategies.

The port-Hamiltonian model for the induction generator is derived from the total energy of the system, which is defined in terms of the generalized momentum variables (i.e. flux and mechanical momentum) as

$$\mathscr{H} = \frac{1}{2}{\psi_{abcs}}^T {L_s}^{-1} \psi_{abcs} + \frac{1}{2}{\psi_{abcr}}^T {L_r}^{-1} \psi_{abcr} + \psi_{abcs} {L_{srx}}^{-1} \psi_{abcr} + \frac{1}{2}\frac{{Y_m}^2}{J_m} \tag{3.220}$$

where the stator inductance matrix is

$$L_s = \begin{bmatrix} L_{ls} + L_{ms} & -\frac{1}{2}L_{ms} & -\frac{1}{2}L_{ms} \\ -\frac{1}{2}L_{ms} & L_{ls} + L_{ms} & -\frac{1}{2}L_{ms} \\ -\frac{1}{2}L_{ms} & -\frac{1}{2}L_{ms} & L_{ls} + L_{ms} \end{bmatrix} \tag{3.221}$$

the rotor inductance matrix is

$$L_r = \begin{bmatrix} L_{lr} + L_{mr} & -\frac{1}{2}L_{mr} & -\frac{1}{2}L_{mr} \\ -\frac{1}{2}L_{mr} & L_{lr} + L_{mr} & -\frac{1}{2}L_{mr} \\ -\frac{1}{2}L_{mr} & -\frac{1}{2}L_{mr} & L_{lr} + L_{mr} \end{bmatrix} \tag{3.222}$$

and the mutual inductance matrix is

$$L_{srx} = L_{sr} \begin{bmatrix} \cos(\theta_r) & \cos(\theta_r + \frac{2\pi}{3}) & \cos(\theta_r - \frac{2\pi}{3}) \\ \cos(\theta_r - \frac{2\pi}{3}) & \cos(\theta_r) & \cos(\theta_r + \frac{2\pi}{3}) \\ \cos(\theta_r + \frac{2\pi}{3}) & \cos(\theta_r - \frac{2\pi}{3}) & \cos(\theta_r) \end{bmatrix} \tag{3.223}$$

Applying the park transform to the energy equation results in

$$\mathscr{H} = \frac{1}{2} {i_{qd0s}}^T K_s L_s {K_s}^{-1} i_{qd0s} + \frac{1}{2} {i_{qd0r}}^T K_r L_r {K_r}^{-1} i_{qd0r} + i_{qd0s} K_s L_{srx} K_r i_{qd0r} + \frac{1}{2} J_m {\omega_m}^2 \quad (3.224)$$

$$\mathscr{H} = \frac{1}{2} \begin{bmatrix} i_{qd0s} \\ i_{qd0r} \end{bmatrix}^T \begin{bmatrix} K_s L_s {K_s}^{-1} & K_s L_{sr} {K_r}^{-1} \\ K_r {L_{sr}}^T {K_s}^{-1} & K_r L_r {K_r}^{-1} \end{bmatrix} \begin{bmatrix} i_{qd0s} \\ i_{qd0r} \end{bmatrix} + \frac{1}{2} J_m {\omega_m}^2 \quad (3.225)$$

where the fluxes are related to the currents by

$$\begin{bmatrix} \psi_{qd0s} \\ \psi_{qd0r} \end{bmatrix} = \begin{bmatrix} K_s L_s {K_s}^{-1} & K_s L_{sr} {K_r}^{-1} \\ K_r {L_{sr}}^T {K_s}^{-1} & K_r L_r {K_r}^{-1} \end{bmatrix} \begin{bmatrix} i_{qd0s} \\ i_{qd0r} \end{bmatrix} \quad (3.226)$$

The Rayleigh dissipation function is defined as

$$\mathscr{R} = \frac{1}{2} {i_{qd0s}}^T K_s R_s {K_s}^{-1} i_{qd0s} + \frac{1}{2} {i_{qd0r}}^T K_r R_r {K_r}^{-1} i_{qd0r} + \frac{1}{2} B_b {\omega_m}^2 \quad (3.227)$$

$$\mathscr{R} = \frac{1}{2} \begin{bmatrix} i_{qd0s} \\ i_{qd0r} \end{bmatrix}^T \begin{bmatrix} K_s R_s {K_s}^{-1} & 0_{3x3} \\ 0_{3x3} & K_r R_r {K_r}^{-1} \end{bmatrix} \begin{bmatrix} i_{qd0s} \\ i_{qd0r} \end{bmatrix} + \frac{1}{2} B_b {\omega_m}^2 \quad (3.228)$$

The state variables are

$$s = \begin{bmatrix} q_{qd0s} & q_{qd0r} & \theta_m & \psi_{qd0s} & \psi_{qd0r} & Y_m \end{bmatrix}^T \quad (3.229)$$

The state equations in matrix form are

$$\dot{s} = (\mathscr{J} - \mathscr{D}) \frac{\partial \mathscr{H}}{\partial s} + g_s u_s \quad (3.230)$$

where the vector of the derivatives of the Hamiltonian with respect to the state variables is

$$\frac{\partial \mathscr{H}}{\partial s} = \left[\frac{\partial \mathscr{H}}{\partial q_{qd0s}} \quad \frac{\partial \mathscr{H}}{\partial q_{qd0r}} \quad \frac{\partial \mathscr{H}}{\partial \theta_m} \quad \frac{\partial \mathscr{H}}{\partial \psi_{qd0s}} \quad \frac{\partial \mathscr{H}}{\partial \psi_{qd0r}} \quad \frac{\partial \mathscr{H}}{\partial Y_m} \right]^T \tag{3.231}$$

The derivative of the Hamiltonian with respect to the shaft position, θ_m, is

$$\frac{\partial \mathscr{H}}{\partial \theta_m} = \frac{\partial \mathscr{H}}{\partial \theta_r} \frac{\partial \theta_r}{\partial \theta_m} \tag{3.232}$$

which expands to

$$\frac{\partial \mathscr{H}}{\partial \theta_m} = \frac{n_p}{2} \left(\frac{1}{2} {i_{qd0s}}^T \frac{\partial K_s L_s {K_s}^{-1}}{\partial \theta_r} i_{qd0s} + \frac{1}{2} {i_{qd0r}}^T \frac{\partial K_r L_r {K_r}^{-1}}{\partial \theta_r} i_{qd0r} + {i_{qd0s}}^T \frac{\partial K_s L_{srx} {K_r}^{-1}}{\partial \theta_r} i_{qd0r} \right) \tag{3.233}$$

The equations are calculated in terms of the currents rather than the fluxes due to the simplification of the matrix manipulations. The derivatives of some of the matrices with respect to the shaft position are equal to zero

$$\frac{\partial K_s}{\partial \theta_r} = \frac{\partial L_s}{\partial \theta_r} = \frac{\partial L_r}{\partial \theta_r} = 0 \tag{3.234}$$

some of the other terms cancel

$$\frac{\partial K_r}{\partial \theta_r} L_r {K_r}^{-1} + K_r L_r \frac{\partial {K_r}^{-1}}{\partial \theta_r} = 0 \tag{3.235}$$

$$K_s \frac{\partial L_{srx}}{\partial \theta_r} {K_r}^{-1} + K_s L_{srx} \frac{{K_r}^{-1}}{\partial \theta_r} = -K_s \frac{\partial L_{srx}}{\partial \theta_r} {K_r}^{-1} \tag{3.236}$$

which reduces the equation to

$$\frac{\partial \mathscr{H}}{\partial \theta_m} = -\frac{n_p}{2}({i_{qd0s}}^T K_s \frac{\partial L_{srx}}{\partial \theta_r} {K_r}^{-1} i_{qd0r}) \tag{3.237}$$

The partial derivative of the Hamiltonian with respective to the momentum of the shaft is

$$\frac{\partial \mathscr{H}}{\partial Y_m} = \frac{Y_m}{J_m} \tag{3.238}$$

The partial derivative of the Hamiltonian with respective to the charge is

$$\frac{\partial \mathscr{H}}{\partial q_{qd0s}} = \frac{\partial \mathscr{H}}{\partial q_{qd0r}} = 0 \tag{3.239}$$

However it should be noted that

$$\frac{d\psi_{abcs}}{dt} \neq K_s \frac{d\psi_{qd0s}}{dt} \tag{3.240}$$

in fact

$$\frac{d\psi_{abcs}}{dt} = \frac{dK_s \psi_{qd0s}}{dt} = K_s \frac{d\psi_{qd0s}}{dt} + \frac{dK_s}{dt}\psi_{qd0s} \tag{3.241}$$

and as a result a modification to the energy definition is required to take account for the effect the change of reference frame has made.

An extra term is added into the potential energy equation to take into account the induced voltage

$$\mathscr{V} = K_s \frac{d{K_s}^{-1}}{dt} \psi_{qd0s} q_{qd0s} + K_r \frac{d{K_r}^{-1}}{dt} \psi_{qd0r} q_{qd0r} \tag{3.242}$$

which results in the partial derivative of the Hamiltonian with respect to the stator

charge vector as

$$\frac{\partial \mathscr{H}}{\partial q_{qd0s}} = K_s \frac{dK_s{}^{-1}}{dt} \psi_{qd0s} \tag{3.243}$$

and the rotor charge vector as

$$\frac{\partial \mathscr{H}}{\partial q_{qd0r}} = K_r \frac{dK_r{}^{-1}}{dt} \psi_{qd0r} \tag{3.244}$$

If the standard definition of the port-Hamiltonian equations is used this addition of energy in the total energy term would result in a change to the partial derivative with respect to the fluxes

$$\begin{bmatrix} \frac{\partial \mathscr{H}}{\partial \psi_{qd0s}} \\ \frac{\partial \mathscr{H}}{\partial \psi_{qd0r}} \end{bmatrix} = \begin{bmatrix} K_s L_s K_s{}^{-1} & K_s L_{sr} K_r{}^{-1} \\ (K_s L_{sr} K_r{}^{-1})^T & K_r L_r K_r{}^{-1} \end{bmatrix} \begin{bmatrix} \psi_{qd0s} \\ \psi_{qd0r} \end{bmatrix} + \begin{bmatrix} K_s \frac{dK_s{}^{-1}}{dt} q_{qd0s} \\ K_r \frac{dK_r{}^{-1}}{dt} q_{qd0r} \end{bmatrix} \tag{3.245}$$

However, as discussed in Section 3.2.2 which introduces the proposed modification to the port-Hamiltonian framework in cases where where the potential energy is a function of the generalized velocities, the partial derivative with respect to the rotor and stator fluxes should be defined as

$$\begin{bmatrix} \frac{\partial \mathscr{T}}{\partial \psi_{qd0s}} \\ \frac{\partial \mathscr{T}}{\partial \psi_{qd0r}} \end{bmatrix} = \begin{bmatrix} K_s L_s K_s{}^{-1} & K_s L_{sr} K_r{}^{-1} \\ (K_s L_{sr} K_r{}^{-1})^T & K_r L_r K_r{}^{-1} \end{bmatrix} \begin{bmatrix} \psi_{qd0s} \\ \psi_{qd0r} \end{bmatrix} \tag{3.246}$$

The full system for the induction generator is therefore described by

$$\dot{s} = \left(\begin{bmatrix} O_{7x7} & I_{7x7} \\ -I_{7x7} & O_{7x7} \end{bmatrix} - \begin{bmatrix} O_{7x7} & O_{7x7} \\ O_{7x7} & R_{7x7} \end{bmatrix} \right) \begin{bmatrix} \frac{\partial \mathscr{H}}{\partial q_i} \\ \frac{\partial \mathscr{T}}{\partial Y_i} \end{bmatrix} + \begin{bmatrix} O_{7x6} \\ I_{6x6} \\ O_{1x6} \end{bmatrix} \begin{bmatrix} v_{qd0s} \\ v_{qd0r} \end{bmatrix} \tag{3.247}$$

In such a way, the accepted generator equations have been applied into the port-Hamiltonian framework successfully which enables the use of power-based control

strategies.

3.8 OWC System State Equations

The previous sections have detailed the derivation of the equations for the various OWC subsystems. The present section amalgamates them into a single wave-to-wire model. This is the first port-Hamiltonian model in existence of a wave energy device of which the author is aware.

The state variables, s, are grouped into subgroups for ease of notation, and are defined as

$$s = \begin{bmatrix} {s_x}^T & {s_e}^T & {s_\chi}^T \end{bmatrix}^T \tag{3.248}$$

where the main OWC state parameters are denoted by s_x, the electrical state variables are denoted by s_e and the additional states for the radiation force are s_χ.

The main OWC states are

$$s_x = \begin{bmatrix} z_1 & z_2 & Y_1 & Y_2 & V_e \end{bmatrix}^T \tag{3.249}$$

The electrical states are

$$s_e = \begin{bmatrix} {q_{qd0s}}^T & {q_{qd0r}}^T & \theta_m & {\psi_{qd0s}}^T & {\psi_{qd0r}}^T & Y_m \end{bmatrix}^T \tag{3.250}$$

The additional states are

$$s_\chi = \begin{bmatrix} {\chi_1}^T & {\chi_{12}}^T & {\chi_2}^T & {\chi_{21}}^T \end{bmatrix}^T \tag{3.251}$$

As per the process described in previous sections, the derivative of the system energy

with respect to the state variables is required to define the system state equations. The derivative of the system energy with respect to the OWC state parameters is

$$\frac{\partial \mathscr{H}}{\partial s_x} = \begin{bmatrix} (k_{h1} + k_{m1})z_1 & (k_{h2} + k_{m2})z_2 & \dfrac{Y_1}{(M_1 + \mu_{\infty 1})} & \dfrac{Y_2}{(M_2 + \mu_{\infty 2})} & p_c \end{bmatrix} \tag{3.252}$$

where the chamber pressure is

$$p_c = m_c R_a (T_o V_o^{\gamma - 1})(A_c(h_{a0} + z_1 - z_2))^{-\gamma} \tag{3.253}$$

The partial derivative of the system energy with respect to the electrical states is

$$\frac{\partial \mathscr{H}}{\partial s_e} = \begin{bmatrix} K_s \dfrac{\partial {K_s}^{-1}}{\partial t}\psi_{qs} & K_r \dfrac{\partial {K_r}^{-1}}{\partial t}\psi_{qr} & \dfrac{\partial \mathscr{H}}{\partial \theta_m} & i_{qd0s} & i_{qd0r} & \dfrac{Y_m}{J_d} \end{bmatrix}^T \tag{3.254}$$

and finally the partial derivative of the system energy with respect to the additional radiation force states is

$$\frac{\partial \mathscr{H}}{\partial s_\chi} = \begin{bmatrix} \dfrac{\chi_1}{\alpha_{p1}} & \dfrac{\chi_{12}}{\alpha_{p12}} & \dfrac{\chi_1}{\alpha_{p2}} & \dfrac{\chi_{12}}{\alpha_{p21}} \end{bmatrix}^T \tag{3.255}$$

The interconnection state matrix for the full system still needs to meet the skew symmetric condition. For ease of notation the matrix has been split into sub-matrices in the following manner

$$\mathscr{J} = \begin{bmatrix} \mathscr{J}_x & \mathscr{J}_{xe} & \mathscr{J}_{x\chi} \\ \mathscr{J}_{ex} & \mathscr{J}_e & \mathscr{J}_{e\chi} \\ \mathscr{J}_{\chi x} & \mathscr{J}_{\chi e} & \mathscr{J}_\chi \end{bmatrix} \tag{3.256}$$

The OWC state interconnection matrix is

$$\mathscr{J}_x = \begin{bmatrix} 0 & 0 & 1 & 0 & 0 \\ 0 & 0 & 0 & 1 & 0 \\ -1 & 0 & 0 & 0 & A \\ 0 & -1 & 0 & 0 & -A \\ 0 & 0 & -A & A & 0 \end{bmatrix} \tag{3.257}$$

The interconnection matrix between the OWC states and the electrical states is

$$\mathscr{J}_{xe} = \begin{bmatrix} 0_{(1x3)} & 0_{(1x3)} & 0 & 0_{(1x3)} & 0_{(1x3)} & 0 \\ 0_{(1x3)} & 0_{(1x3)} & 0 & 0_{(1x3)} & 0_{(1x3)} & 0 \\ 0_{(1x3)} & 0_{(1x3)} & 0 & 0_{(1x3)} & 0_{(1x3)} & 0 \\ 0_{(1x3)} & 0_{(1x3)} & 0 & 0_{(1x3)} & 0_{(1x3)} & 0 \\ 0_{(1x3)} & 0_{(1x3)} & 0 & 0_{(1x3)} & 0_{(1x3)} & -N_t \end{bmatrix} \tag{3.258}$$

and due to the skew symmetric property the interconnection matrix between the electrical states and the OWC states is

$$\mathscr{J}_{ex} = -\mathscr{J}_{xe}{}^T \tag{3.259}$$

The interconnection matrix between the OWC states and the additional radiation force states is

$$\mathscr{J}_{x\chi} = \begin{bmatrix} 0_{(1x6)} & 0_{(1x6)} & 0_{(1x6)} & 0_{(1x6)} \\ 0_{(1x6)} & 0_{(1x6)} & 0_{(1x6)} & 0_{(1x6)} \\ \frac{\chi_1}{\alpha_{p1}} & \frac{\chi_{12}}{\alpha_{p12}} & 0_{(1x6)} & 0_{(1x6)} \\ 0_{(1x6)} & 0_{(1x6)} & \frac{\chi_2}{\alpha_{p2}} & \frac{\chi_{21}}{\alpha_{p21}} \\ 0_{(1x6)} & 0_{(1x6)} & 0_{(1x6)} & 0_{(1x6)} \end{bmatrix} \tag{3.260}$$

and the skew symmetric condition requires

$$\mathscr{J}_{\chi x} = -\mathscr{J}_{x\chi}{}^{T} \tag{3.261}$$

The electrical state interconnection matrix is

$$\mathscr{J}_{e} = \begin{bmatrix} 0_{(3x3)} & 0_{(3x3)} & 0_{(3x1)} & I_3 & 0_{(3x3)} & 0_{(3x1)} \\ 0_{(3x3)} & 0_{(3x3)} & 0_{(3x1)} & 0_{(3x3)} & I_3 & 0_{(3x1)} \\ 0_{(1x3)} & 0_{(1x3)} & 0_{(1x1)} & 0_{(1x3)} & 0_{(1x3)} & 1 \\ -I_3 & 0_{(3x3)} & 0_{(3x1)} & 0_{(3x3)} & 0_{(3x3)} & 0_{(3x1)} \\ 0_{(3x3)} & -I_3 & 0_{(3x1)} & 0_{(3x3)} & 0_{(3x3)} & 0_{(3x1)} \\ 0_{(1x3)} & 0_{(1x3)} & -1 & 0_{(1x3)} & 0_{(1x3)} & 0_{(1x1)} \end{bmatrix} \tag{3.262}$$

There is no interconnection between the electrical subsystems and the radiation forces

$$\mathscr{J}_{e\chi} = 0_{(14x24)} \tag{3.263}$$

and the skew symmetric condition requires

$$\mathscr{J}_{\chi e} = \mathscr{J}_{e\chi}{}^{T} \tag{3.264}$$

The radiation force interconnect matrix is

$$\mathscr{J}_{\chi} = 0_{(24x24)} \tag{3.265}$$

In a similar method to that applied to the interconnection matrix, the dissipation

matrix is also split into sub-matrices defined as

$$\mathscr{D} = \begin{bmatrix} \mathscr{D}_x & 0 & 0 \\ 0 & \mathscr{D}_e & 0 \\ 0 & 0 & \mathscr{D}_\chi \end{bmatrix} \tag{3.266}$$

The OWC state dissipation matrix is

$$\mathscr{D}_x = \begin{bmatrix} 0 & 0 & 0 & 0 & 0 \\ 0 & 0 & 0 & 0 & 0 \\ 0 & 0 & B_1 & 0 & 0 \\ 0 & 0 & 0 & B_2 & 0 \\ 0 & 0 & 0 & 0 & B_t \end{bmatrix} \tag{3.267}$$

The electrical state dissipation matrix is

$$\mathscr{D}_e = \begin{bmatrix} 0_{(3x3)} & 0_{(3x3)} & 0_{(3x1)} & 0_{(3x3)} & 0_{(3x3)} & 0_{(3x1)} \\ 0_{(3x3)} & 0_{(3x3)} & 0_{(3x1)} & 0_{(3x3)} & 0_{(3x3)} & 0_{(3x1)} \\ 0_{(1x3)} & 0_{(1x3)} & 0 & 0_{(1x3)} & 0_{(1x3)} & 0 \\ 0_{(3x3)} & 0_{(3x3)} & 0_{(3x1)} & R_s I_3 & 0_{(3x3)} & 0_{(3x1)} \\ 0_{(3x3)} & 0_{(3x3)} & 0_{(3x1)} & 0_{(3x3)} & R_r I_3 & 0_{(3x1)} \\ 0_{(1x3)} & 0_{(1x3)} & 0 & 0_{(1x3)} & 0_{(1x3)} & B_b \end{bmatrix} \tag{3.268}$$

The radiation force dissipation matrix is

$$\mathscr{D}_\chi = \begin{bmatrix} \mathrm{diag}(\alpha_{p1}\beta_{p1}) & 0_{(6x6)} & 0_{(6x6)} & 0_{(6x6)} \\ 0_{(6x6)} & \mathrm{diag}(\alpha_{p12}\beta_{p12}) & 0_{(6x6)} & 0_{(6x6)} \\ 0_{(6x6)} & 0_{(6x6)} & \mathrm{diag}(\alpha_{p2}\beta_{p2}) & 0_{(6x6)} \\ 0_{(6x6)} & 0_{(6x6)} & 0_{(6x6)} & \mathrm{diag}(\alpha_{p21}\beta_{p21}) \end{bmatrix} \tag{3.269}$$

The system inputs, u_s, are split between the disturbance inputs, u_d, and the control inputs, u_c,

$$u_s = \begin{bmatrix} {u_d}^T {u_c}^T \end{bmatrix}^T \tag{3.270}$$

The disturbance inputs are

$$u_d = \begin{bmatrix} F_{e1} & F_{e2} & p_{atm} & {v_{qd0s}}^T \end{bmatrix}^T \tag{3.271}$$

and the control inputs are

$$u_c = \begin{bmatrix} v_{qd0r} \end{bmatrix} \tag{3.272}$$

The input matrix has also been split into sub-matrices

$$g_s = \begin{bmatrix} g_x & 0_{(5\text{x}6)} \\ 0_{(14\text{x}3)} & g_e \\ 0_{(24\text{x}3)} & 0_{(24\text{x}6)} \end{bmatrix} \tag{3.273}$$

The OWC system input matrix is given as

$$g_x = \begin{bmatrix} 0 & 0 & 0 \\ 0 & 0 & 0 \\ 1 & 0 & -A_c \\ 0 & 1 & A_c \\ 0 & 0 & 0 \end{bmatrix} \tag{3.274}$$

and the electrical system input matrix is given as

$$g_e = \begin{bmatrix} 0_{(7x3)} & 0_{(7x3)} \\ I_3 & 0_{(3x3)} \\ 0_{(3x3)} & I_3 \\ 0_{(1x3)} & 0_{(1x3)} \end{bmatrix} \tag{3.275}$$

3.9 Summary of Contribution and Future Work

The existing models of each component of the OWC system are discussed in the relevant sections of this chapter. In order to facilitate the use of energy based modeling control strategies a new model has been derived that applies energy based modeling techniques. In order to achieve this aim two modifications to the port-Hamiltonian equations have been proposed. The first proposes that the system equation for port-Hamiltonian systems is adjusted when the potential energy is a function of the velocities. This modification brings it in-line with the Euler-Lagrangian framework for energy based modeling. The second modification proposes a change of reference in order to model systems with no inertial component. Examples have been given to demonstrate these modifications.

A port-Hamiltonian model has then been derived for each of the subsystems of the OWC system. The incident waves are the input to the system. However as the excitation force is independent of the state variables it is treated as the input.

Initial work concentrated on the development of a frequency independent model that was not reliant on access to BEM and CFD codes. Two additional terms were found to take into account the mass exiting the water column at non-null velocity. On the release of an open source BEM code, Nemoh, focus transferred to this more accurate method. The BEM code was used to compute the hydrodynamic

coefficients for a frequency dependent system model, including the added mass, damping and excitation force coefficients. The radiation force has been integrated using the Prony approximation. The novelty of the hydrodynamic model is its adaption to the port-Hamiltonian framework.

Two subsystem models have been developed for the pneumatic system. The first assumes that the temperature change within the air chamber is negligible. It was decided to implement the second model, which does not make this assumption. The turbine characteristics are derived from CFD numerical results (obtained by Banks (2009), Tarver (2013), Natanzi (2010a) and the author of this thesis) are utilized in the port-Hamiltonian framework using spline equations fitted to the points.

Finally, a novel model of an induction generator model was developed and incorporated into the port-Hamiltonian framework. This addressed the need for a generator model with multiple pole-pairs which was not dealt with in the induction generator model presented by Dòria-Cerezo (2006).

In summary a full system model in the port-Hamiltonian framework has been generated for the OWC system. This model will employed in the Passivity Based Control (PBC) strategy as discussed in Chapter 5.

Any future development of the model would ideally include a dynamic model of the turbine rather than the quasi-steady model which would enable it to be more easily integrated into the port-Hamiltonian framework, as well as increasing the accuracy of the model. The inter-component volume method could be used as a first step towards this end goal. A model of a back-to-back inverter would also be added to the full system model. The OWC hydrodynamic model could be improved by taking into account the sloshing modes within the OWC chamber as well as using the Morrison equation to model the diffraction force. Time limitations did not allow for these components to be added at this stage but the current model enables the

development of either an energy- or power-based control strategy which would be improved by the integration of these components.

Chapter 4

Power Smoothing

4.1 Objectives

Oscillating Water Column (OWC) devices utilize the energy of the rising and falling of an ocean wave to generate electricity. The majority of, if not all, bidirectional turbines employed on OWCs spin in the same direction irrespective of whether the pressure drop across the turbine is positive or negative. Nevertheless the electrical current output rises and falls twice every wave period, as well as varying due to the fluctuations between one wave and the next and due to variations in the prevailing sea state.

In a strong grid connection, any fluctuation in the power output of a wave energy device with a low power rating can be absorbed by the rest of the grid. As the power ratings increase, however, fluctuations become a larger issue, and balancing the load and demand across a farm or multiple farms of devices becomes critical. In theory, when a gust affects wind turbines in one farm, wind turbines at other locations may be able to respond in a short time scale to balance the supply and demand. In other words the fluctuation of one wind turbine is mitigated by other wind turbines.

On a longer time scale, the more traditional thermal power plants (e.g. coal and gas) can also balance the supply and demand. There are expectations from the National Grid (NG) and the Distribution Network Operators (DNOs) that current fluctuations are minimized as much as possible though this is currently not governed by the grid standards. There are, however, strict limits on the voltage fluctuation governed by the grid standards. In the proposed Variable Radius Turbine (VRT) system, voltage fluctuations are controlled by the back-to-back inverter that is used as part of the Power Take-Off (PTO) package.

The problem arises however when one considers a weaker grid connection, either at the extremities of a large grid network, or more significantly on a small grid network such as an island that is self supporting with regards to power generation. In such scenarios it is harder to balance the power fluctuations, and as a result the voltage can fluctuate, which would affect the end user with brown- or black- outs. In addition it is expected that tighter restrictions will be mandated by future grid codes for even the stronger grid networks.

The aim of this chapter is to quantify the potential for power smoothing and to size an energy storage system, then finally identify the different means by which the short-term (wave to wave) power fluctuations could be reduced and possibly eliminated. Fluctuations, on an hourly time-scale can be controlled by dumping power or through long-term energy storage such as a pumped storage scheme (e.g. Dinorwig in Wales). This chapter will not address this latter scenario. The details of this chapter have already been presented in an internal company report by Farman & Hall (2012). All simulations were conducted by the author of this thesis. Research into the various hardware options was a collaborative venture between the two authors.

The magnitude of wave power fluctuations through the year can vary greatly. On one particular site on the Cornish Coast, in England, [50.39°, -5.58°], the monthly

average ranges from 4.17 to 37.3 kW/m and on another site nearby, [50.35°, -5.67°], there is a range of 6.98 kW/m to 52.67 kW/m (Pitt 2006). This will affect the rating of any device deployed to aid the smoothing process.

It is important to understand what is a practical level of smoothing, how it should be defined, and the reasons behind selecting the target. There are approximately 1 million peaks to be smoothed per year (Murray et al. 2012). Another consideration is what to do when there is too little power being generated by the sea, when there is too much power or alternatively what to do when there are large fluctuations on a wave-to-wave basis. According to Murray et al. (2012) there are four main considerations when designing a control strategy to optimize and smooth power a) remaining within system limits, b) efficiency of the system, c) power quality to the grid and d) a realistic strategy that uses measurable data. It is important that all four elements are considered during the design process.

4.2 Modeling

This section will introduce the equations used for assessing the effect of the size and shape of an OWC on smoothing power, the effect of multiple chambers on an OWC (spacing of < 10 m), the effect of a number of OWCs (spacing of >10 m) and finally the addition of an ideal (100 % efficient) energy storage system. In these initial assessment stages the OWC and turbine PTO are assumed to have no losses and no effect on the bandwidth of the power absorbed. The assumption of piston mode operation is used and the sloshing modes are neglected.

The potential power that can be absorbed is calculated from the relevant spectrum and differs depending on how the spectrum has been defined (McCormick 2010).

The power equation for the Bretscheider spectrum is

$$P_{BS} = \sum \overline{\eta}^2 \rho_w g b \tag{4.1}$$

whereas for the Pierson Moskowitz spectrum it is

$$P_{PM} = \sum \frac{\overline{\eta}^2 \rho_w g b}{8} \tag{4.2}$$

4.2.1 Individual Chambers

The equations for the average wave height within an OWC are given for a point absorber, a square device and an approximation of a circular device.

Point Absorber

A point absorber by definition does not smooth the incident wave and so this is used as the baseline for comparison purposes. The wave elevation, η, which acts on the device at position, x, is then a time series generated from a sum of frequency components, f_i, with an amplitude, a_i, a wavelength λ_i and a random phase ϕ_i between 2π and zero:

$$\eta = \sum_{i=1}^{N} a_i \sin(2\pi f_i t - \frac{2\pi}{\lambda_i} x + \phi_i) \tag{4.3}$$

The wavelength, λ, is defined for deep water as

$$\lambda = \frac{g}{2\pi f^2} \tag{4.4}$$

where deep water, h_w, is defined as:

$$h_w \geqslant \frac{\lambda}{2} \tag{4.5}$$

Rectangular OWC Device

The average water height within a square chamber OWC in which one face of the chamber is perpendicular to the wave direction is dependent on the side length of the device, l_c, and is equal to

$$\overline{\eta} = \frac{1}{l_c}\int_{x}^{x+l_c} \eta\, dx \tag{4.6}$$

$$= \frac{\lambda_i}{2\pi l_c} a_i \left(\cos(2\pi f_i t - \frac{2\pi}{\lambda_i}(x+l_c) - \phi_i) - \cos(2\pi f_i t - \frac{2\pi}{\lambda_i}x + \phi_i) \right) \tag{4.7}$$

This assumes that there is no sloshing within the chamber.

Circular OWC Device

A circular OWC device is dependent on the radius, r_c, and can be calculated as

$$\overline{\eta} = \frac{2}{\pi {r_c}^2}\int_{x}^{x+2r_c} \eta\sqrt{{r_c}^2 - (r_c - x)^2}dx \tag{4.8}$$

The analytical solution to this is rather complex and so an approximation is made using the equation for a square chamber, with an equivalent area to that of the circular chamber, with the waves approaching from a direction which is perpendicular to the leading edge of the chamber. The average wave height over the length of the device can be given as

$$\overline{\eta} \;=\; \frac{1}{2r_c}\int_{x}^{x+2r_c} \eta dx \tag{4.9}$$

which results in the following equation:

$$\overline{\eta} = \sum_{i=1}^{N} -\frac{a_i\lambda_i}{4\pi r_c}\left(\cos(2\pi f_i t - \frac{2\pi}{\lambda_i}(x+2r_c)+\phi_i) - \cos(2\pi f_i t - \frac{2\pi}{\lambda_i}x+\phi_i)\right) \tag{4.10}$$

Figure 4.1 shows the comparison of the various devices.

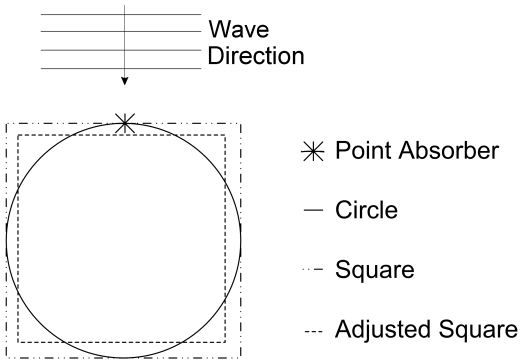

Figure 4.1: Comparison of the device shapes under consideration

4.2.2 Energy Storage

The energy storage system could be positioned either before or after the back-to-back inverter. A single energy storage system could be provided per OWC system, or with each OWC farm. The latter storage system would smooth some of the undulations that have not already been eliminated by combining the power from each device. Figure 4.2 shows a decision matrix for the on-shore energy system with the back-to-back inverter positioned prior to the energy storage system. Five OWCs are at different positions relative to the incident wave, and power is limited to the maximum capability of the inverter by the appropriate control of the turbine, use of a Blow-Off

Valve (BOV) and/or power dissipation through a load bank. The energy storage system is controlled to absorb power when the export power from the OWCs farm is above the storage reference limit. This reference limit could be a fixed value tuned and optimized based on the specific hardware used in the system. However, initial simulations indicated that this drove a larger energy storage capacity, implying that a fixed reference value is not ideal. This is discussed in more depth in Section 4.3.2. The energy storage system is controlled to release energy when the export power falls below the storage reference limit. For the purposes of the present study, the reference limit is calculated as a percentage (95%) of the running average power calculated over several minutes (e.g. 15 minutes). The reference limited is ramped in from zero over the first 2 minutes to enable the storage system to charge. This is considered only a rudimentary strategy and could be improved further.

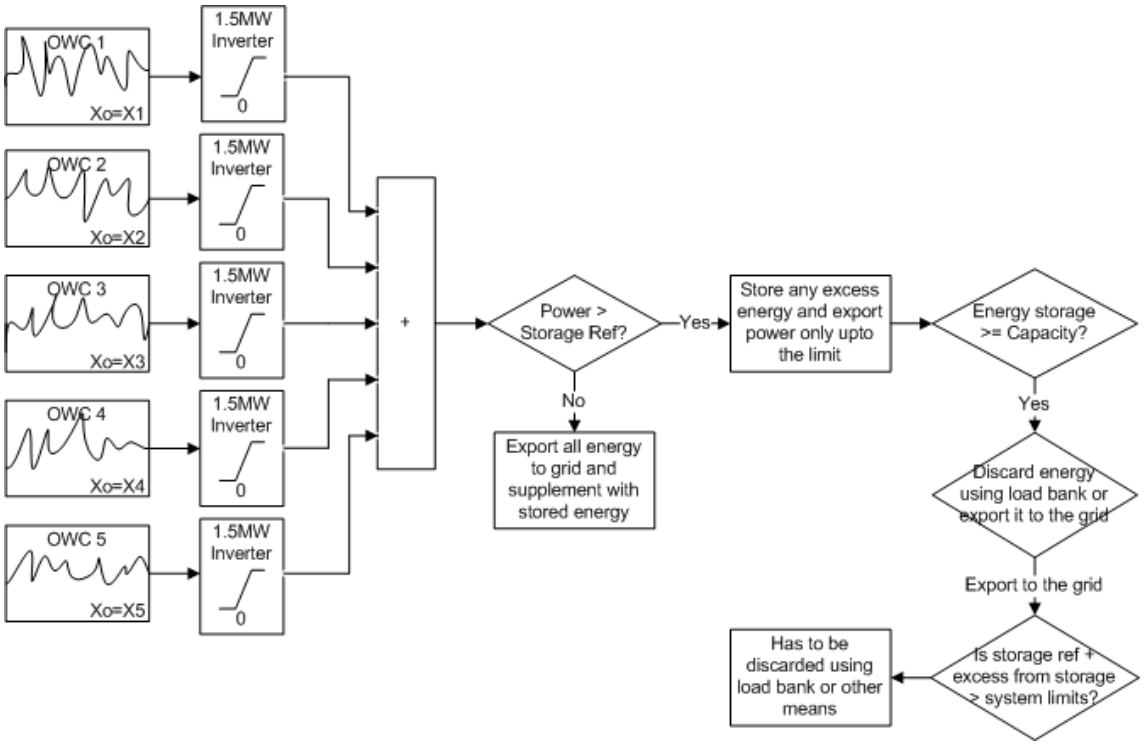

Figure 4.2: Energy storage decision matrix

4.3 Simulation Results

Two sets of simulations were run in Simulink, each investigating different methods of achieving the same goal. The first, described in 4.3.1, was to assess the potential benefit of having farms of OWCs, with multiple individual OWCs smoothing the short-term wave-to-wave fluctuations. The second, described in 4.3.2, was used as a preliminary study to assess the size of the short-term energy storage system required to deliver an acceptable level of power smoothing.

4.3.1 Power Output for Multiple Devices

It was decided to conduct tests for the Wave Hub site due to the readily availability of wave data in the public domain (Halcrow Group Ltd 2010a,b,c). Due to its location on the west coast of Cornwall, a Bretschneider spectra was used to define the climate with a peak period, T_p, of 12 s and a mean significant wave height, H_s, of 2.2 m. An irregular wave was derived by superimposing 256,000 individual sinusoidal monochromatic waves each with a specific phase shift and frequency. This high number of superimposed waves was chosen to ensure that the resulting wave profile had no repeating subsections over the total simulated period of sixty minutes. The resulting power spectra equated to 24 kW/m. Figure 4.3 shows the level of power fluctuations for five 10 m devices spaced at 15 m intervals compared to a single unit.

4.3.2 Energy Storage

Section 4.3.1 showed the effect of five chambers coupled together, this is now extended to include an ideal energy storage system. The system under consideration included five 10 m square devices spaced at 50 m subjected to a Bretshneider spec-

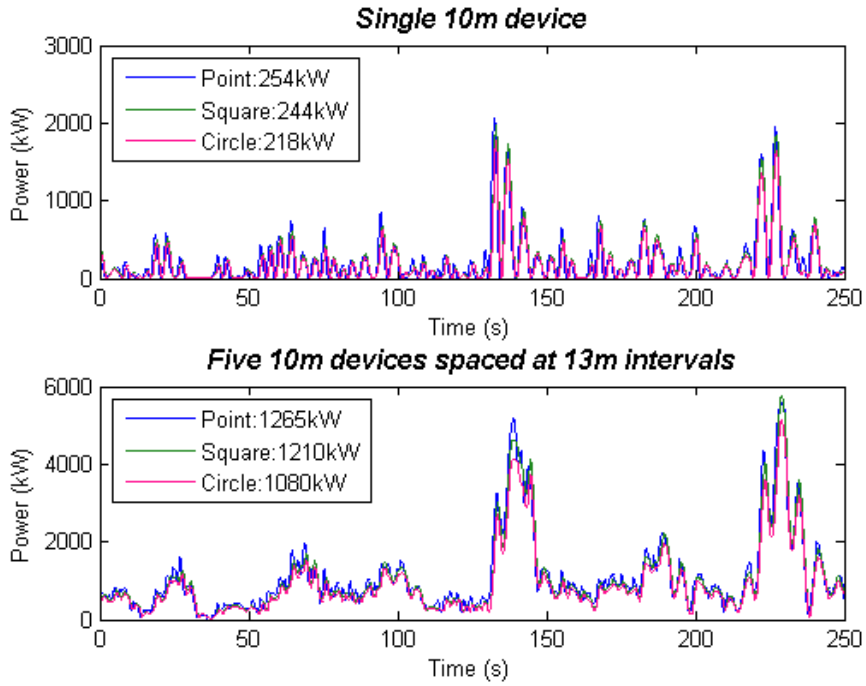

Figure 4.3: Multiple 10 m OWCs spaced at 15 m intervals

trum equating to 24 kW/m. Preliminary simulations showed that a reasonable energy storage capacity would be 20 MJ. The selection of the storage capacity requires a trade-off. A larger storage capacity will enable smoother output power. Conversely a larger storage capacity will increase the losses in the system and have a larger installation cost. One method of defining the selection process is to define an average energy storage capacity and conduct simulations to identify to what total storage capacity this equates. Figure 4.4 shows the results from the five chamber simulation; Figure 4.5 shows the results from the single chamber simulation with the same incident wave as for the five chamber simulation. For the five chamber simulation , the storage capacity ratio (i.e. the average energy stored divided by the total capacity) was 52.4%. This ratio indicates the ability of the storage system to store sufficient power to smooth the peaks and the troughs. This simulation has a relatively high storage capability and does not match the philosophy proposed by Murray et al. (2012) where the energy storage was kept as a minimum. The reduced energy storage capacity affects the capability to smooth the power but with

a capital cost benefit. The decision between the two strategies depends greatly on the priorities of the particular installation.

The output power to the grid, as shown in Figure 4.4(b), follows the reference with an R^2 value of over 0.999 as the model is not considering the dynamic equations of such a energy storage system. The perfect energy storage system would have a flat line power output however the capacity would have to be much greater. The standard deviation of the power divided by the mean can be used as a measure for the smoothness of the power output, this would be 0% for the ideal case. The DNO would be responsible for defining the acceptable variation. In this particular case the individual chamber equates to 133% and the combined chambers to 65% whereas the output to the energy storage system is 13%. Though the output power can not be considered as smooth it is a vast improvement upon the raw power. The power smoothness could be considerably improved with either a reduction in the efficiency or by increasing the energy storage capacity.

In this simulation the energy storage system is located after the back-to-back inverter, as it was deemed to be the most realistic situation when combining multiple devices. Since each inverter was rated to 1.5 MW, any power in excess of this had to be discarded, see Figure 4.4d. This could be achieved either via the turbine control strategy (running the turbine at off-peak efficiency), utilizing a BOV or by utilizing a load bank. The discarded power from the inverter equates to an average of 35 kW in this case. When the energy storage system is full and the available power exceeds the export reference then the energy either needs to be discarded using a technology such as a load bank or it needs to be exported on the grid despite the potential deterioration of the power quality. In the five chamber simulation, the energy storage system exported an average of 1225kW to the grid and discarded an average of 4 kW.

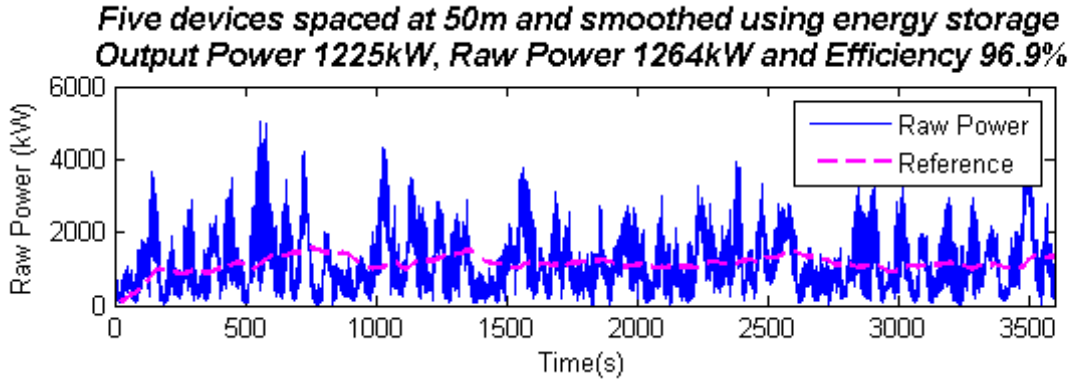

(a)

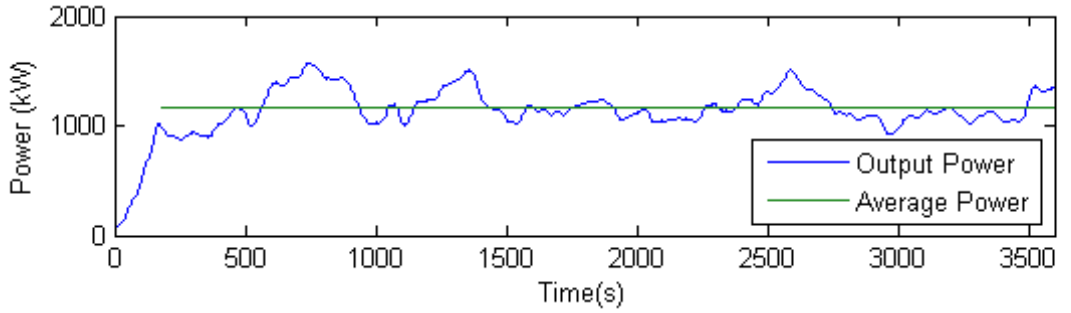

(b)

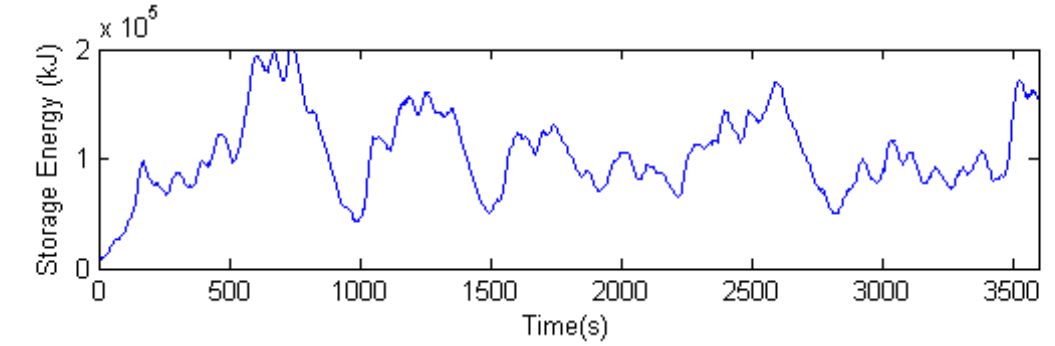

(c)

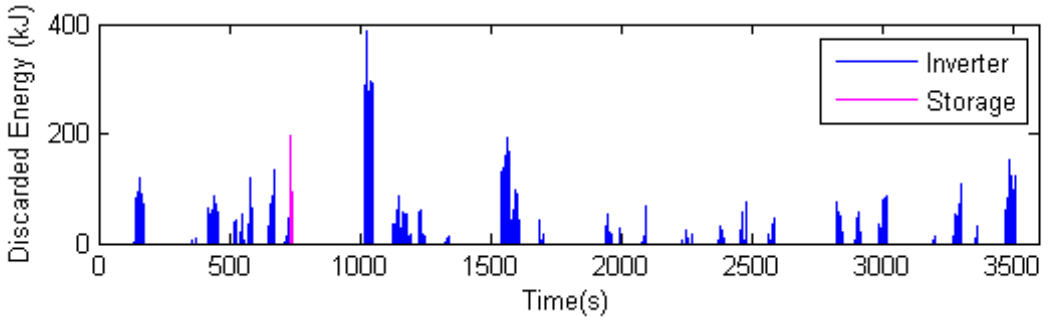

(d)

Figure 4.4: Multiple OWCs with energy storage

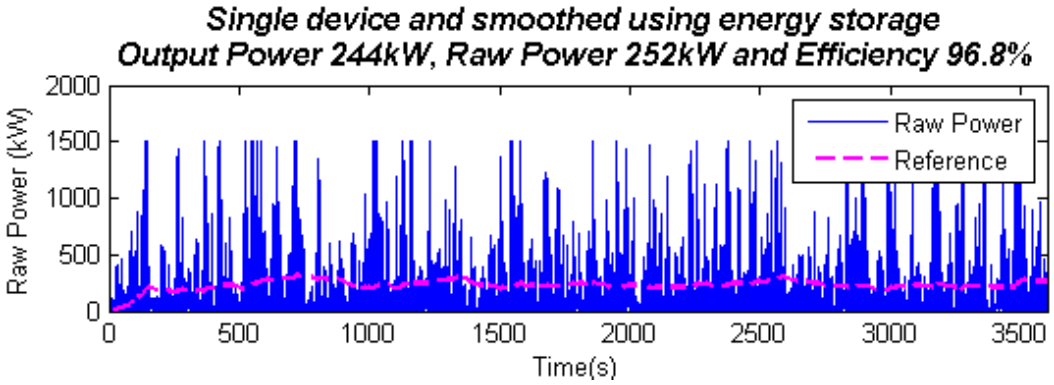

(a)

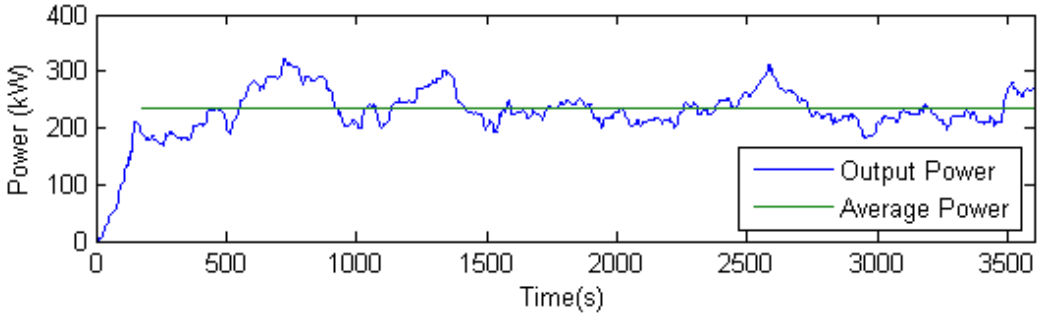

(b)

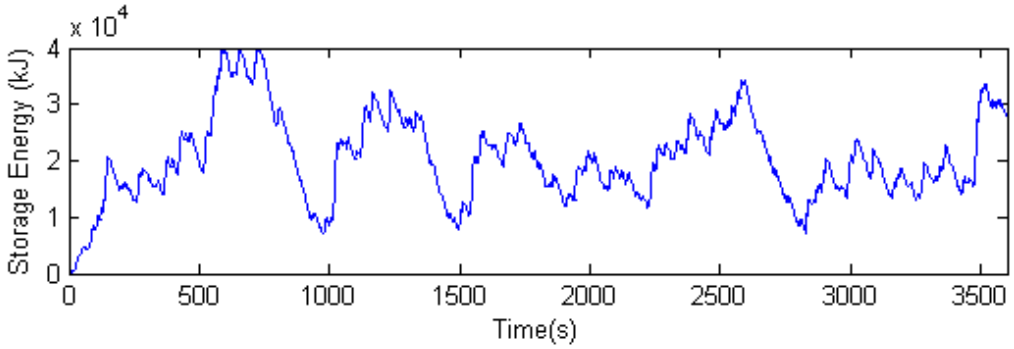

(c)

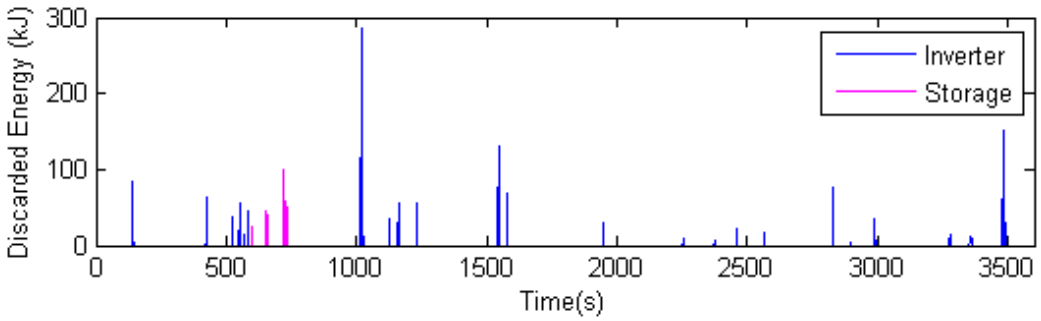

(d)

Figure 4.5: Single OWC with energy storage

4.4 Physical System Design

4.4.1 Baseline Design

In order to assess what system changes can be made to reduce power fluctuations, first the baseline system should be defined. Figure 4.6 shows the baseline turbine PTO system which includes generator, back-to-back inverter, harmonic filter and step-up transformer as well as switchgear.

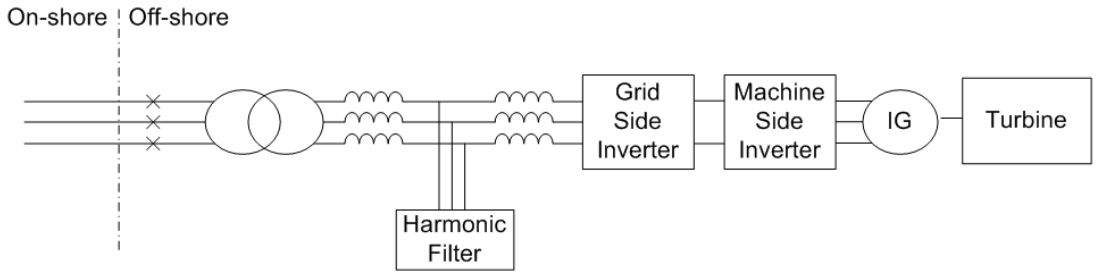

Figure 4.6: Electrical connection for a single OWC

In the standard PTO system the power can be smoothed to a certain extent with the control strategy (i.e. running the turbine off peak efficiency). Whilst this results in an instantaneous reduction in efficiency, when the turbine and generator power is in excess of the capability of the back-to-back inverter action must be taken. The usual methods are to once again run the turbine away from the design conditions, or to close a shut-off-valve which results in a temporary suspension of power generation.

4.4.2 Multiple Units

Currently most demonstration units for OWC devices use individual chambers, each with a single turbine. However the device installed by Oceanlinx in March 2010 consisted of 8 chambers (Oceanlinx Ltd 2010a) and Mutriku consists of 16 chambers also using a single turbine per chamber (Heath 2007, Torre-Enciso et al. 2009). It

is unknown whether any devices exist that utilize more than one turbine for each chamber. Despite this the idea of wave farms is not new, indeed similar to wind farms, it is crucial to enable economies of scale. The additional benefit of utilizing multiple chambers is that they can have a generally positive effect on smoothing the output power for the farm. However it should be noted that at times it is possible that all chambers will be in phase and due to the laws of superposition the power smoothing will be aggravated rather than mitigated. It is proposed that, though utilizing multiple chambers cannot be relied upon, it could potentially enable a reduction in the sizing of any energy storage system. Figure 4.7 shows one potential configuration of multiple turbines to smooth power, though many alternatives are possible including a) the point of coupling could be after the grid side inverter and b) the cable could be Direct Current (D.C.) with the grid side inverter on-shore.

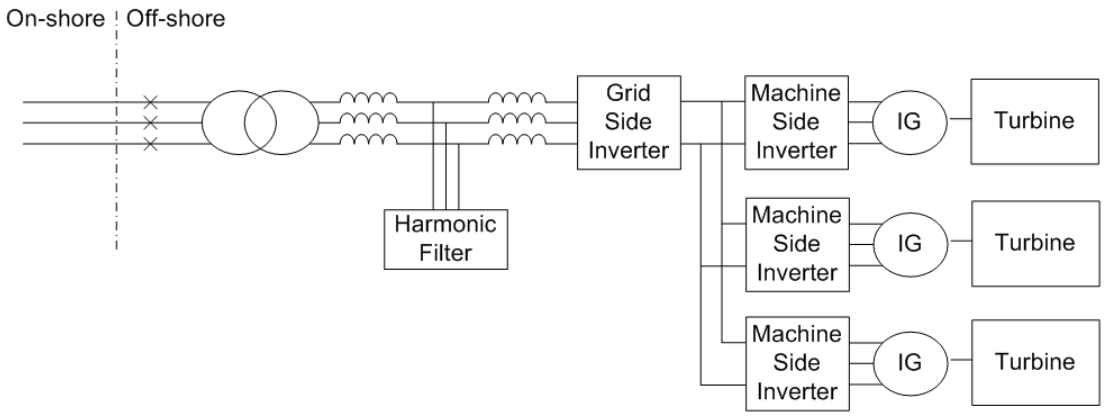

Figure 4.7: Electrical connection for multiple OWCs

4.4.3 Energy Storage

Fixed Inertia Flywheel

One method of storing energy is with a flywheel. The Fixed Inertia Flywheel (FIF) system has to be decoupled from the turbine to enable the turbine to be controlled to the peak efficiency point. This means that the system cannot absorb the peaks of

the wave power as it will be limited to the capability of the turbine inverter. The FIF system could be deployed both on-shore or off-shore. By placing the unit off-shore there is either a reduction in electrical component cost, see Figure 4.8 in comparison with Figure 4.10, or a reduction in cable losses, see Figure 4.9 in comparison with Figure 4.10. However, the additional forces that the flywheel would undergo would result in an increase in the design and build costs that may negate the reduced electrical cost. The advantages of an on-shore system are ease of maintenance and most of the equipment are off-the-shelf components and therefore readily available. This in turn means that they are already proven although in a less harsh environment. There are multiple disadvantages for the off-shore system: maintenance access would be more difficult, it would be harder to control with additional forces on the system, there could be potential vibration issues and increased wear on the bearings. It may not be possible to use off-the-shelf components due to the additional forces. There is no available literature to indicate that this technology has been proven for a marine environment. The main disadvantages of the on-shore system is the increase cable costs, as they will have to be rated for the peak electrical power not the smoothed power, and also the additional cable losses which are proportional to the square of the current.

Variable Inertia Flywheel

A FIF has already been considered but the Variable Inertia Flywheel (VIF) will be considered here. According to Beattie et al. (1995), the fluctuations associated with wave power can be grouped into two categories: the relatively high frequency associated with individual waves, and the relatively low frequency modulation of the wave amplitude (periods of 90 s). The former can be smoothed by the inertia of the system, with energy stored in a peak and released in a trough. One option is to have a VIF attached to the same shaft as the turbine. In this implementation the energy

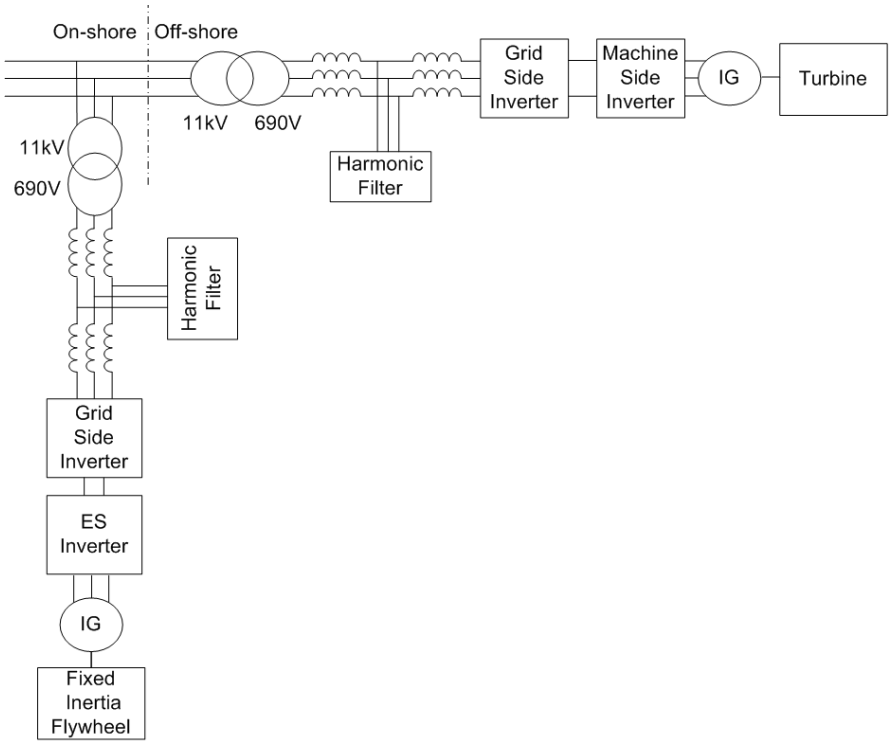

Figure 4.8: Fixed inertia flywheel on-shore with AC transmission lines to shore

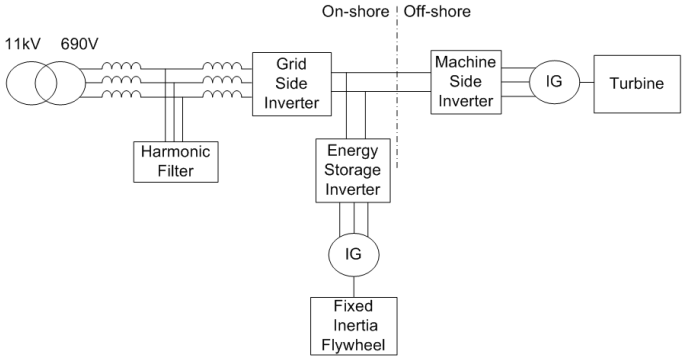

Figure 4.9: Fixed inertia flywheel on-shore with DC transmission lines to shore

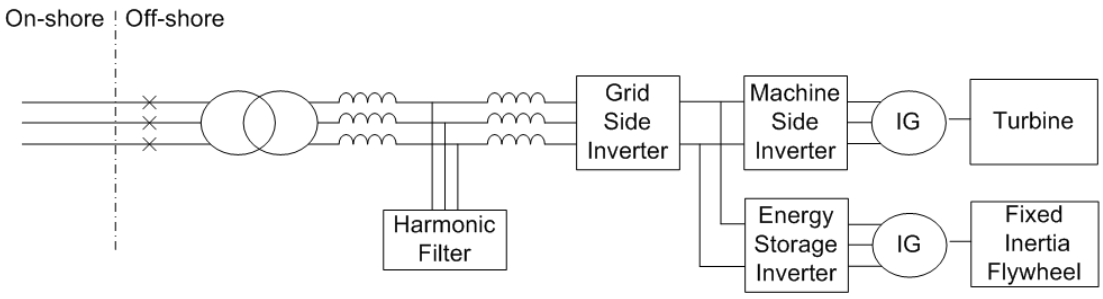

Figure 4.10: Fixed inertia flywheel off-shore with AC transmission lines to shore

storage would be controlled by adjusting the inertia rather than the speed which would be coupled to that of the turbine and hence would be controlled to extract the most energy from the system. This system would require only the acquisition of a VIF whereas most alternatives would require additional electrical equipment.

There are many alternatives but they all require at a least a generator and one half of the back-to-back inverter as shown in Figure 4.11. Both this and the previously mentioned suggestion have the benefit of being highly controllable, especially the flywheel which is decoupled from the shaft as it can be controlled either by changing the inertia or via the speed. However practical VIFs do not currently exist and since the flywheel would have a gyroscopic effect when installed on a floating OWC buoy there is a risk of substantial wear on any bearings. It is anticipated that the control of an off-shore VIF would be more challenging than that of a comparable shore based device due to the external forces applied from the motion of the buoy in the lateral, radial and axial directions. Although patents exist for VIFs, (see Murphy (2012), Dugas (2011)) they are not products that can be bought off-the-shelf and have not been designed for this specific application or environment. Any system would likely be expensive to both design and build. This is not a reason to discard this idea but it should be considered as the wave industry requires cost reduction to become competitive with other energy generation power plants. For the VIF which is decoupled from the turbine, there are limited benefits of the new technology over a standard FIF which could be positioned on-shore where it would be easier to maintain.

The moment of inertia for a 1MW VRT impulse turbine, utilizing an 8 pole generator, is currently estimated to be 150 kgm^2 compared to 595 kgm^2 for a 570 kW Wells turbine Murray et al. (2012). By using a low inertia turbine and generator rotating assembly, it is possible to create an OWC system that is more responsive to the variability in the wave series. This will make it easier to change the speed

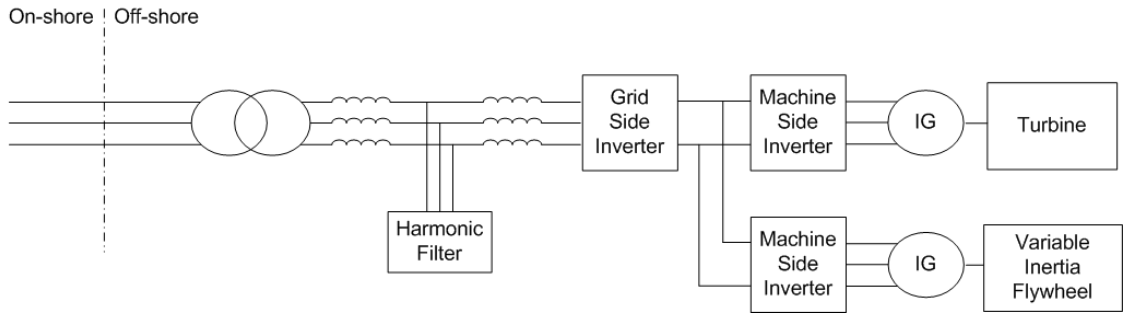

Figure 4.11: Off-shore variable inertia flywheel

and operate at the optimum condition for that instant in time, facilitating higher system efficiency and better power capture, however increasing the need for energy smoothing. According to Brito-Melo et al. (2002) the large inertia of the Wells turbine resulted in the speed remaining constant over a duration of a particular sea state which was given as 15 minutes. However, as the impulse turbine has a lower inertia this conclusion does not necessarily carry over. It has been suggested by Murray et al. (2012) that inertia could be used in conjunction with a variable speed control strategy to smooth the power.

Supercapacitors

Super-Capacitor (SC) technology is developing fast and may be a promising solution for smoothing power in the wave industry. One of the key development challenges facing SCs is the number of charge and discharge cycles the component can support over its life. The end of life conformance is defined as a reduction of capacitance by 30 % and an increase in Equivalent Series Resistance (ESR) of 100 %. There is usually an exponential decrease in capacitance near end of life. Manufacturers of these devices currently quote a lifetime of between 500,000 and 1 million cycles.

The average wave period is between 7 and 14s. For each wave period there are two power peaks, equating to 514 and 257 cycles per hour respectively. Assuming operation 100% of the time and without power smoothing from the device equates

to 4.5 and 2.3 million cycles per year which will result in all capacitors requiring maintenance/replacement after only 3-6 months. This could be considered a harsh critique and all devices are likely to have some smoothing inherent in their design. In addition it is important to understand what is meant by a power cycle as each wave would not completely discharge nor charge the SCs. Murray et al. (2012) have published test results that contradict the manufacturers measurements and have stated that they could potentially be used for more cycles. In addition they stated that there are approximately 1 million peaks to be smoothed per year. They extrapolated their current results and estimated that the SCs would reach the end of their useful life after 4.25 million cycles; they also made the statement that this would correspond to over 20 years of operation at sea. It is stated that desired typical maintenance intervals are between 5 to 10 years. However an ambient temperature increase of only 10 deg can halve the SCs lifetime and hence the control rooms would have to be cooled appropriately, resulting in increased cost. Further research is needed to back up the claims that 20 years is achievable.

The control strategy adopted by Murray et al. (2012) kept the SCs at the lowest operation voltage which enables smoothing of the power peaks, however as the SCs are positioned after the machine side inverter, the peaks are limited to the capability of the inverter.

If budget was not an issue an on-shore installation could be trialled but maintenance (or replacement) off-shore every six months is deemed infeasible. In addition, research is needed to understand the effect of the vibration levels experienced on a device.

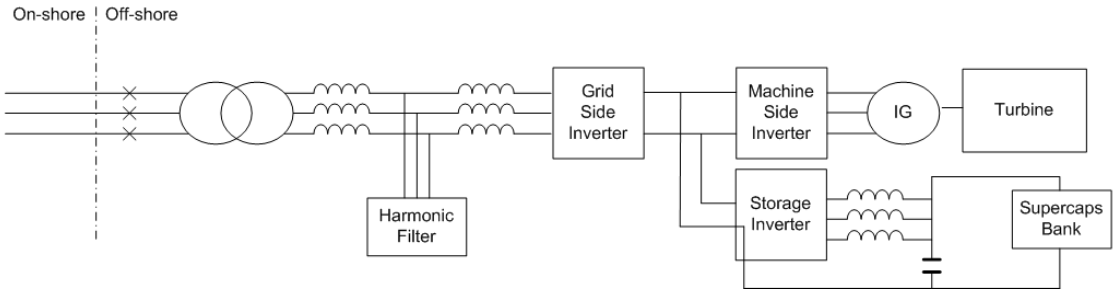

Figure 4.12: Off-shore SC system

Summary

There are other potential power smoothing technologies that have not been mentioned, however, those covered here are perceived to be the most realistic based on the current levels of development. The SC technology is promising, but with manufacturers' stated lifetimes being so low, it would be difficult to obtain support for installation into a commercial project. A VIF would be highly controllable and has a reduced associated electrical cost; however in the absence of a commercially available design it can be considered to be an under-developed technology. It is thought at this time that the lowest risk and cheapest option (though potentially not the most efficient) is the FIF. Based on-shore, it would meet the smoothing requirements while remaining easy to maintain in a benign environment. Therefore to promote greater reliability it is proposed that the FIF is the best option. However, as competitor technologies develop there may be a move to those technologies in pursuit of improved efficiency and/or lower cost.

4.5 Summary of Contribution

Through the simulations of a OWC wave farm it had been shown that the inherent smoothing of power from multiple devices may be a reality but may not necessarily offer sufficient smoothing in order to meet the requirements of the grid. There are

two solutions to this challenge. First is the application of a control strategy to deliberately run off the peak efficiency point in extreme power conditions and limit the peak to trough variations. The second is to implement a short-term energy storage system. However, it has been shown that, without a control strategy to reduce the power fluctuations direct from the OWC, the energy storage systems are likely to be prohibitively large and costly.

Chapter 5

Power Shaping Control

5.1 Literature Review of Control Strategies for OWCs

A significant variety of control strategies have been investigated for use on Oscillating Water Columns (OWCs) and other wave devices (Nunes et al. 2011). Within the field of OWC control, some of these strategies have been developed for use in conjunction with specific turbine types such as a Wells (Valério et al. 2008, Tease et al. 2007) or Denniss-Auld turbine (Alcorn & Finnigan 2004). These may have pitching guide-vanes or rotors, in contrast to the fixed blade impulse turbines such as the HydroAir turbine (Dresser-Rand Company Ltd 2015). Others have not been specified for use with a particular turbine (Salter et al. 2002). Common methods of controlling an OWC device include generator magnetizing current, the pitch of the variable geometry components such as the guide vanes and/or rotor blades, or the actuation of some form of valve arrangement. The Variable Radius Turbine (VRT), with no pitching components, cannot make use of the strategies relevant to the control of

guide vanes and rotor position, such as that proposed by Alcorn & Finnigan (2004), though the general theory may have some relevance. The various control approaches will be detailed in the following sub-sections.

5.1.1 Speed Control

The Energetech variable pitch turbine was simulated in SIMULINK in conjunction with a Squirrel Cage Induction Generator (SCIG) (Alcorn & Finnigan 2004). It was claimed that speed control in isolation reduced the power variability but that it had a marginal but detrimental effect on the power capture efficiency. The control strategy was modeled on maximizing torque rather than specifically aimed at maximizing power, though it is implied that one results in the other.

Fixed speed operation would prevent use of the inherent flywheel nature of the turbine to avoid power output transients. Falcão (2002) discussed the issue that a strong grid connection can absorb power fluctuations, however a weak grid connection has more stringent requirements if voltage swing and Rate Of Change Of Frequency (ROCOF) problems are to be avoided.

According to O'Sullivan & Lewis (2008), the benefits of variable speed operation depend on the sea state. In low power sea states, the efficiency was found to be improved with a variable speed operation, whereas in high power states a fixed speed operation was more efficient. One potential constraint on variable speed operation was highlighted by Neumann et al. (2007), namely that the turbine should be operated away from the natural frequency of the Power Take-Off (PTO) frame and wave device to avoid vibration problems; this could potentially limit the speed range of the turbine. However the structure could potentially be stiffened to shift the natural frequency, if this was indeed a problem.

Two control strategies were presented by Justino & Falcão (1995). The first at-

tempted to keep the speed at a set-point dictated by the sea state, calculated over a reasonably long period of time. However the result was unacceptable because either the speed was out of bounds for the generator or the power did not comply with the grid requirements. The second strategy disregarded the need to match the turbine velocity with the sea condition, and related the rate of change of torque to the rate of change of speed. The initial implementation was found to be highly dependent on the initial conditions so the equation was adjusted to account for deviations from the specific set-point based on the sea state (Justino & Falcão 1999). The electrical torque, T_e was adjusted using the following control law

$$\frac{dT_e}{dt} = G_k T_e \frac{\omega_m - {\omega_m}^d}{{\omega_m}^d} \frac{d\omega_m}{dt} \tag{5.1}$$

where ω_m is the instantaneous speed, ${\omega_m}^d$ is the desired reference speed, and G_k is the control gain.

5.1.2 Valve Control

A Blow-Off Valve (BOV), also called a by-pass pressure-relief valve, can be used to exhaust excess air to reduce the pressure within the OWC chamber and by doing so reduce the flow through the turbine. Essentially, excess energy is being exhausted to atmosphere. A throttle valve, on the other hand, reduces the flow rate and increases the pressure drop.

For a Wells turbine, the size of the turbine can be reduced with the introduction of a BOV, whereas for a non-valved turbine the peak efficiency must be sacrificed for the operating width, no such sacrifice is necessary for the valved turbine (Brito-Melo et al. 2002).

As the impulse turbine is significantly less prone to suffer from the stall problems

that are exhibited by the Wells turbine, the requirement for a BOV is reduced. Nevertheless, under very high sea conditions, a BOV could be employed to keep the device operating rather than activating a Shut-Off Valve (SOV) which results in temporary termination of electrical energy production. A SOV is basically a throttle valve that has only two positions, either completely closed or completely open.

Falcão & Justino (1999) conducted tests on various control strategies using a numerical linearized model of an OWC which took into account the entropy changes within the chamber due to viscous losses. It was concluded that a BOV should be utilized when the damping effect of the turbine on the OWC is too high, and that a throttle valve is necessary when this effect is below the optimum. Falcão & Justino (1999) also concluded that the use of a BOV is crucial under high flow conditions for turbines that are prone to stall. Falcão (2002) states that the correct actuation of a control valve, whether it be in parallel (BOV) or in series (throttle valve) can have the effect of increasing the power captured by 37%.

Figure 5.1, presented by Falcão & Justino (1999), shows the effect of using a BOV or throttle valve in comparison to a valveless system, where Λ is the dimensionless incident wave power and η_t is the efficiency of the turbine. It can be seen that both the peak efficiency and bandwidth are significantly improved. However, implementing a throttle-valve in parallel with the turbine, creates non-linearity in the pressure/flow rate relationship (Falcão 2002). This non-linearity should be taken into account in any model and associated control strategy. Very little quantitative information has been found on the affect of a throttle valve on the full wave-to-wire system efficiency and experimental and numerical analysis would be beneficial.

The SOV is mentioned purely for completeness as to the type of the valves that can be utilized as part of the control strategy. At this stage it is envisaged that a SOV is activated during emergency shut-downs; terminating operation in storm conditions, and facilitating access during maintenance. Dresser-Rand have designed

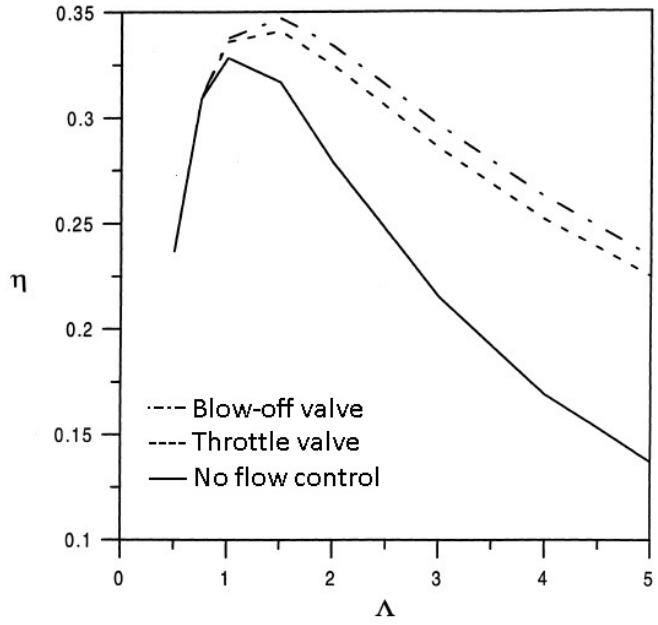

Figure 5.1: Average efficiency, η_t for irregular waves, with air flow control by a throttle-valve, a BOV, and no flow control (Falcão & Justino 1999)

and implemented a unique SOV that was installed and commissioned by the author on a prototype unit in Australia in the first quarter of 2010. It was activated by a hydraulic actuator which was fail-safe in the event of a loss of power. Any trip conditions detected by the control strategy would actuate the SOV.

5.1.3 Latching and Unlatching

Latching is the use of a valve, potentially a SOV or throttle valve, to temporarily prevent flow through the turbine to bring the velocity of the OWC in phase with the exciting force. Latching usually is activated when the heave velocity of the water in the OWC is zero, hence in its extreme position, and released when the velocity is at its maximum. The main challenge, as discussed by Price & Wallace (2007) is the means of detecting the maximum velocity.

A strategy was proposed by Lopes et al. (2009) that does not require wave prediction for latching control optimization, though a measurement of the excitation force (e.g.

wave elevation) is required. It was stated that the pressure measurement within the air chamber cannot be used due to the significant high frequency components in the readings which are a result of the valve actuation. It was concluded, using a mathematical model, that performance improved by 2.5 times (Lopes et al. 2009) in comparison with operation using a passive valve in the open position. In agreement with this, Ringwood (2006) applied the latching principle to a simulation of a heaving buoy and obtained an improved capture efficiency of 2.4 times compared to unlatched operation. The latching control improved the energy captured from 1.94Ws to 4.62Ws.

Summarized briefly by Salter et al. (2002), unlatching is the sister of latching, whereas latching is used with a SOV or latching valve, unlatching utilizes a BOV when applied to an OWC.

5.1.4 Reactive and Complex Conjugate Control

According to Salter et al. (2002), complex conjugate control is difficult to achieve. It is described as being an extreme version of reactive phase control. Across all the frequencies, the inertias and the spring stiffnesses of the system are canceled, in addition the damping coefficient is tuned to match the individual frequency components.

5.1.5 Balast Control

No literature has been found for the use of ballast control on OWCs however it has been suggested for point absorbers as briefly mentioned in Ringwood (2006). By adjusting the Center Of Gravity (COG) and center of buoyancy Center Of Buoyancy (COB) the resonance of the device can be adjusted for different sea states.

5.1.6 Comparison of Control Strategies

A comparison by Salter et al. (2002) stated that there was little to distinguish one control strategy from another when the waves are sinusoidal with fixed amplitude. It is the polychromatic nature of irregular waves that requires the control complexity necessary to encompass the potential range of amplitudes and frequencies. The conclusion from Salter et al. (2002) gives weight to the need to test control strategies with polychromatic waves as well as monochromatic sinusoidal waves.

It was concluded by Amundarain, Alberdi, Garrido & Garrido (2010) that though a speed control strategy captures more energy than the use of an air control valve, the latter better regulates the power output to the requirements of the grid. The improved performance can be seen in Table 5.1 where a) is for the uncontrolled case, b) the neural network rotational speed control and c) the BOV controlled via a Proportional Integral Derivative (PID) controller

$dP = \lvert P_0 \sin(0.1\pi t)\rvert$ P_0 (Pa)	(a) $P_{\text{generator}}$ (kw)	(b) $P_{\text{generator}}$ (kw)	(c) $P_{\text{generator}}$ (kw)
4000	11.920	11.920	11.920
5000	20.060	20.060	20.060
6000	25.202	25.570	25.275
7000	20.053	27.560	22.562
8000	15.012	29.480	18.565
Irregular wave	22.942	27.036	25.328

Table 5.1: Turbine and generator efficiency vs pressure drop (Amundarain, Alberdi, Garrido & Garrido 2010)

In both irregular and regular waves, it was found that both the speed control and valve control methods can avoid the stalling behavior of the Wells turbine. Speed control significantly increased the power capture whereas valve control produced only a marginal increase. In addition, the speed control was faster acting than the valve control (Amundarain, Alberdi, Garrido, Garrido & Maseda 2010).

A brief review of the hardware and control strategies available for wave power devices was given by Salter et al. (2002). It included a discussion on reactive loading and

phase control; latching and unlatching; full complex-conjugate control; and array cooperation. The assessment included no qualitative or quantitative assessment or comparison of the advantages and disadvantages of each design.

According to Price & Wallace (2007), to date the main focus on control design for prototype devices has been to ensure robustness, survivability and reliable operation; however, the focus will move to power optimization as the supporting technologies develop and mature. Though certain control strategies may have performed better in initial testing, as stated by Price & Wallace (2007) it is unwise to conclude that the optimum method has been identified until the alternative methods have been investigated. Furthermore, especially with regards to the Artificial Neural Networks (ANN), alternative networks and training schemes may result in improved performance (Price & Wallace 2007). According to Ringwood (2006), the control needs to have more than one side to it, using phase control, wave ballast control and maximizing the energy capture by adjusting the damping.

5.2 Control Restrictions

With the completion of a dynamic model of the complete OWC system (see Section 3.8), it is possible to commence development of a control strategy. During the development of a control strategy, it is likely that a number of constraints will need to be observed. These would most likely include but would not be limited to, the following:

1. Maximum turbine and generator speed

2. Maximum generator current

3. Maximum rate of change of generator current

4. Maximum water level within the OWC chamber

5. Maximum pressure within the OWC chamber

The grid code mandates the limits for under-voltage, over-voltage, and rate-of-change of frequency at the point of common coupling. In the case of an induction generator connected to a back-to-back inverter, the Sinusoidal Front End (SFE) of the inverter ensures the voltage and frequency meet these requirements. However, as the power and hence current fluctuate greatly this will inevitably affect the voltage on the line, especially on weaker grid connections. To date at least certain grid connected OWCs have had limited restrictions on power variations; however, restrictions will tighten as power ratings increase.

There are various parameters that will need to be monitored as part of an effective and practical control strategy:

1. Grid voltage

2. Grid current

3. Direct Current (D.C.) bus voltage between the grid- and machine-side inverters

4. Generator winding magnetizing current

5. Turbine speed

5.3 Passivity Based Control

As has been discussed in 5.1, there are a range of control strategies available for an OWC the overwhelming majority of which focus on maximizing the efficiency of a particular component in the system. It is proposed herein that developing a control strategy, whose primary focus is to optimize energy across the entire wave-to-wire system, by employing energy shaping techniques in conjunction with a cost function, will result in superior overall performance. This section introduces Passivity Based Control (PBC) which is then employed in the subsequent sections.

As discussed in Section 3.2, a system can be described by the port-Hamiltonian state equations

$$\dot{s} = \left[\mathscr{J} - \mathscr{D} \right] \frac{\partial \mathscr{H}}{\partial s} + g_s u_s \tag{5.2}$$

and the output equation

$$y = {g_s}^T \frac{\partial \mathscr{H}}{\partial s} \tag{5.3}$$

One of the potential control methods is to employ Interconnection and Damping Assignment (IDA)-PBC. A good explanation of IDA-PBC is given by Duindam et al. (2009), according to whom it was originally proposed by Oretga et al. (2002). The key to this control methodology is the solution of the Partial Differential Equation (PDE)

$${g_s}^{\perp} \left[\mathscr{J} - \mathscr{D} \right] \frac{\partial \mathscr{H}}{\partial s} = {g_s}^{\perp} \left[\mathscr{J}^d - \mathscr{D}^d \right] \frac{\partial \mathscr{H}^d}{\partial s} \tag{5.4}$$

where ${g_s}^{\perp}$ is the interconnection matrix full rank left annihilator, $\mathscr{H}^d$ is the closed loop energy, $\mathscr{J}^d$ is the closed loop interconnection matrix and $\mathscr{D}^d$ is the desired dissipation matrix. These variables can be thought of as tuning variables with multiple degrees of freedom. The interconnection matrix needs to meet the skew symmetric condition, $(\mathscr{J}^d)^T = (\mathscr{J}^d)^{-1}$. The dissipation energy should meet the

condition that the minimum energy should be at the desired state condition, i.e.

$$s^d = \arg\min \mathscr{H}^d \tag{5.5}$$

There are at least three different methods (Duindam et al. 2009) for solving the PDE: Non-Parametrized IDA, Parametrized IDA and Algebraic IDA.

Non-Parametrized IDA fixes $\mathscr{J}^d$, $\mathscr{R}^d$ and ${g_s}^{\perp}$, leaving the solution of the PDE, Equation (5.4), to the definition of $\mathscr{H}^d$. Within this family of solutions, the one meeting the condition set in Equation (5.5) should be selected.

Parametrized IDA restricts the class of energy functions. This could mean, for example, restricting the energy function to one which is only equal to the kinetic energy dependent on the generalized coordinates. This places a restriction on the energy function and the interconnection and damping matrices for which the PDE must be solved.

Algebraic IDA fixes the closed loop desired energy function and solves the PDE in terms of $\mathscr{J}^d$ and $\mathscr{D}^d$ and ${g_s}^{\perp}$. The PDE can also be solved in terms of the matching equation

$$\underbrace{\left[\mathscr{J} - \mathscr{D}\right]\frac{\partial \mathscr{H}}{\partial s} + g_s u_s}_{\text{open loop system}} = \underbrace{\left[\mathscr{J}^d - \mathscr{D}^d\right]\frac{\partial \mathscr{H}^d}{\partial s}}_{\text{closed loop system}} \tag{5.6}$$

and can be understood more easily if viewed from the vantage point of closed loop and open systems. The matching equation can be rearranged in terms of the required inputs which gives

$$\begin{bmatrix} u_d \\ u_c \end{bmatrix} = \left[g_s(s)^T g_s(s)\right]^{-1} g_s(s)\left\{\left[\mathscr{J}^d(s) - \mathscr{D}^d(s)\right]\frac{\partial \mathscr{H}^d}{\partial s} - \left[\mathscr{J}(s) - \mathscr{D}(s)\right]\frac{\partial \mathscr{H}}{\partial s}\right\} \tag{5.7}$$

5.4 DFIG Speed Control

As discussed in Section 3.7, the main control input to the OWC system is the generator voltage (the rotor or stator voltages for the Doubly Fed Induction Generator (DFIG) and SCIG respectively). With this in mind it was decided that developing a control strategy for the generator in isolation would aid the process for developing a control strategy for the full wave-to-wire system. The first step in the process of applying algebraic IDA PBC requires finding the solution to the fixed point equations for a specific reference input. The fixed point equation is defined as the equilibrium condition of the state equation,

$$\begin{bmatrix} \dot{q}_i \\ \dot{Y}_i \end{bmatrix} = (\mathscr{J} - \mathscr{D})\frac{\delta \mathscr{H}}{\delta s^d} + g_s {u_s}^d \tag{5.8}$$

While the desired values for the solution of the fixed point equations for the current control reference input is relatively easy to compute (as will be discussed in Section 5.5) a similar solution for a speed controller reference input is more challenging. An alternative approach is to find the solution to the fixed point equations using a numerical method with the view that later development of the strategy could identify an algebraic solution. A Newton-Raphson method is used and a tight convergence criterion applied. The first iteration of the numerical solver, ${s^d}_0$, is set to the current values of the system variables so that the solution found would be close to the current operating conditions, s. For every subsequent loop of the numerical solver the desired value is corrected using the following equation

$${s^d}_{i+1} = {s^d}_i - J^{-1}\mathscr{C} \tag{5.9}$$

where J is the Jacobian matrix and $\mathscr{C}$ is the error function which is calculated as the maximum absolute distance from the steady state solution of the fixed point

equations, i.e.

$$\mathscr{C} = \left\{ \mathscr{J}\left(s^d{}_i\right) - \mathscr{D}_i \right\} \frac{\partial \mathscr{H}}{\partial s^d{}_i} + g_s u_{si} \tag{5.10}$$

The general definition of the Jacobian matrix for each of the fixed point equations is given as

$$J = \begin{bmatrix} \frac{\partial f_1}{\partial s^d{}_1} & \frac{\partial f_1}{\partial s^d{}_2} & \vdots & \frac{\partial f_1}{\partial s^d{}_n} \\ \frac{\partial f_2}{\partial s^d{}_1} & \frac{\partial f_2}{\partial s^d{}_2} & \vdots & \frac{\partial f_2}{\partial s^d{}_n} \\ \cdots & \cdots & \ddots & \cdots \\ \frac{\partial f_n}{\partial s^d{}_1} & \frac{\partial f_n}{\partial s^d{}_2} & \vdots & \frac{\partial f_n}{\partial s^d{}_n} \end{bmatrix} \tag{5.11}$$

There are 14 state equations for the DFIG and three control variables as defined in Equation (3.247). Seven of the state variables relate to the generalized positions and seven to the generalized velocities. The rate of change of the position variables, $\dot{q}_i$, within the system (mechanical velocity and current) cannot be forced to zero. Instead a solution is found for the remaining seven state variables and three control variables. There are more degrees of freedom than the number of equations, it is therefore necessary to fix values for two of these variables if a solution is to be found to determine the desired operating conditions.

The value of the desired quadrature-rotor current, ${i_{qr}}^d$, and the desired zero-rotor voltage, ${v_{0r}}^d$, were chosen to be fixed. Theses variables were chosen after a preliminary parametric study and were set to zero amperes and zero volts respectively. Forcing the zero-rotor voltage, ${v_{0r}}^d$, to zero is preferred in order to minimize the likelihood of imbalance across the phases of the generator. The development of more appropriate values could be the subject of a future more detailed parametric study as a means of minimizing the reactive power and maximizing the real power. The remaining desired state variables to be found are therefore

$$s^d = \begin{bmatrix} {i_{qs}}^d & {i_{ds}}^d & {i_{0s}}^d & {i_{dr}}^d & {i_{0r}}^d & {v_{qr}}^d & {v_{dr}}^d \end{bmatrix} \tag{5.12}$$

As a result the definition of the Jacobian for the DFIG is

$$J = \left[\begin{array}{ccc|cc|cc} X_{a11} & X_{a12} & X_{a13} & X_{b12} & X_{b13} & 0 & 0 \\ X_{a21} & X_{a22} & X_{a23} & X_{b22} & X_{b23} & 0 & 0 \\ X_{a31} & X_{a32} & X_{a33} & X_{b32} & X_{b33} & 0 & 0 \\ \hline X_{c11} & X_{c12} & X_{c13} & X_{d12} & X_{d13} & 1 & 0 \\ X_{c21} & X_{c22} & X_{c23} & X_{d22} & X_{d23} & 0 & 1 \\ X_{c31} & X_{c32} & X_{c33} & X_{d32} & X_{d33} & 0 & 0 \\ \hline X_{e11} & X_{e12} & X_{c13} & X_{f12} & X_{f13} & 0 & 0 \end{array}\right] \tag{5.13}$$

where

$$X_a = -K_s \frac{\partial {K_s}^{-1}}{\partial t}\left(K_s L_s {K_s}^{-1}\right) - R_s I_3 \tag{5.14}$$

$$X_b = -K_s \frac{\partial {K_s}^{-1}}{\partial t}\left(K_s L_{sr} {K_r}^{-1}\right) \tag{5.15}$$

$$X_c = -K_r \frac{\partial {K_r}^{-1}}{\partial t}\left(K_r {L_{sr}}^T {K_s}^{-1}\right) \tag{5.16}$$

$$X_d = -K_r \frac{\partial {K_r}^{-1}}{\partial t}\left(K_r L_r {K_r}^{-1}\right) - R_r I_3 \tag{5.17}$$

$$X_e = \left(\frac{n_p}{2} K_s \frac{\partial L_{sr}}{\partial \theta_r} {K_r}^{-1} {i_{qd0r}}^d\right)^T \tag{5.18}$$

$$X_f = \frac{n_p}{2}\left({i_{qd0s}}^d\right)^T K_s \frac{\partial L_{sr}}{\partial \theta_r} {K_r}^{-1} \tag{5.19}$$

The solution to the Newton-Raphson method derives the instantaneous desired operating conditions for the 7 unknown variables.

The derivative of the desired energy function with respect to each of the state

variables is subsequently calculated. The partial derivative of the desired energy function with respect to the stator charge is

$$\frac{\partial \mathscr{H}^d}{\partial s}_{(1..3)} = K_s \frac{\partial {K_s}^{-1}}{\partial t}\big(\psi_{qd0s} - {\psi_{qd0r}}^d\big) \tag{5.20}$$

with respect to the rotor charge is

$$\frac{\partial \mathscr{H}^d}{\partial s}_{(4..6)} = K_r \frac{\partial {K_r}^{-1}}{\partial t}\psi_{qd0r} - K_r \frac{\partial ({K_r}^{-1})^d}{\partial t}{\psi_{qd0r}}^d \tag{5.21}$$

with respect to the rotor position is

$$\frac{\partial \mathscr{H}^d}{\partial s}_{(7)} = -(i_{qd0s} - {i_{qd0s}}^d)^T K_s \frac{\partial L_{sr}}{\partial \theta_r} {K_r}^{-1}(i_{qd0r} - {i_{qd0r}}^d) \tag{5.22}$$

with respect to the stator flux is

$$\frac{\partial \mathscr{H}^d}{\partial s}_{(8..10)} = i_{qd0s} - {i_{qd0s}}^d \tag{5.23}$$

with respect to the rotor flux is

$$\frac{\partial \mathscr{H}^d}{\partial s}_{(11..13)} = i_{qd0r} - {i_{qd0r}}^d \tag{5.24}$$

and with respect to the mechanical momentum is

$$\frac{\partial \mathscr{H}^d}{\partial s}_{(14)} = \omega_m - {\omega_m}^d \tag{5.25}$$

The next step in the process is to find the solution to the matching equation which is defined as

$$(\mathscr{J}^d - \mathscr{D}^d)\frac{\partial \mathscr{H}^d}{\partial s} = (\mathscr{J} - \mathscr{D})\frac{\partial \mathscr{H}}{\partial s} + g_d u_d + g_c u_c \tag{5.26}$$

where the control input is the rotor voltage, v_{qd0r}, and the disturbance input is the stator voltage, v_{qd0s}, which is outside the control of the algorithm. One potential method for solving the matching equation is to fix the inertial matrix so that

$$\mathscr{J}^d = \mathscr{J} \tag{5.27}$$

This being the case, rows 1 through 7 of the matching equation rearrange to (using MATLAB style notation)

$$\mathscr{D}^d{}_{(1:7,1:7)}\frac{\partial \mathscr{H}^d}{\partial s}(1:7) = -(\mathscr{J}_{(1:7,:)} - \mathscr{D}_{(1:7,:)})\frac{\partial \mathscr{H}}{\partial s} + \mathscr{J}^d{}_{(1:7,:)}\frac{\partial \mathscr{H}^d}{\partial s} \tag{5.28}$$

however as $\mathscr{D}^d$ is a diagonal matrix of terms r^d then it can be rearranged using element wise division to find the desired resistance terms.

$$r^d{}_{(1:7)} = \Big(-(\mathscr{J}_{(1:7,:)} - \mathscr{D}_{(1:7,:)})\frac{\partial \mathscr{H}}{\partial s} + \mathscr{J}^d{}_{(1:7,:)}\frac{\partial \mathscr{H}^d}{\partial s}\Big)./\Big(\frac{\partial \mathscr{H}^d}{\partial s}(1:7)\Big) \tag{5.29}$$

The same method is used for row 14

$$r^d{}_{(14)} = \Big(-(\mathscr{J}_{(14,:)} - \mathscr{D}_{(14,:)})\frac{\partial \mathscr{H}}{\partial s} + \mathscr{J}^d{}_{(14,:)}\frac{\partial \mathscr{H}^d}{\partial s}\Big)./\Big(\frac{\partial \mathscr{H}^d}{\partial s}(14)\Big) \tag{5.30}$$

Rows 8 through 10 can be used in a similar manner but the disturbance inputs needs to be taken into account, as a result

$$r^d{}_{(8:10)} = \Big(-(\mathscr{J}_{(8:10,:)} - \mathscr{D}_{(8:10,:)})\frac{\partial \mathscr{H}}{\partial s} - g_{d(8:10,:)}u_d + \mathscr{J}^d{}_{(8:10,:)}\frac{\partial \mathscr{H}^d}{\partial s}\Big)./\Big(\frac{\partial \mathscr{H}^d}{\partial s}(8:10)\Big) \tag{5.31}$$

The remaining three unknown values, $r^d{}_{(11:13)}$, are tunable parameters. The advantage of this method is that trial and error can be used to obtain the desired speed of response. This requires minimal experience, unlike the tuning of a traditional PID controller.

The control input can then be calculated from the remaining three rows

$$u_c = (g_{c(11:13,:)})^{-1}(\mathscr{J}^{d}{}_{(11:13,:)} - \mathscr{D}^{d}{}_{(11:13,:)})\frac{\partial \mathscr{H}^{d}}{\partial s} - (\mathscr{J}_{(11:13,:)} - \mathscr{D}_{(11:13,:)})\frac{\partial \mathscr{H}}{\partial s} - g_{d(11:13,:)}u_d \quad (5.32)$$

5.4.1 Simulation Results

Simulations have been conducted using the speed controller outlined above. To aid in comparisons with the work by Dòria-Cerezo (2006) the parameters were set as follows: stator voltage was $[0\ 415\ 0]^T$, the stator frequency was 50 Hz, the stator resistance was 0.087 Ω, the rotor resistance 0.0228 Ω, magnetizing inductance 0.041 H, both the stator and rotor inductances were 0.042 H, the mechanical resistance was 0.005 kg m^2 / rad^2 and the rotor inertia was 5.0 kg m^2. The DFIG was a four pole machine.

Time domain results for a series of simulations in which the tuning parameters, $r^{d}{}_{(11:13)}$, were varied are shown in Figure 5.2. These plots show the effect of the value of the tuning parameter on the rate of convergence on the target speed, in addition to the applied direct- and quadrature-rotor voltages (which are the control inputs).

Multiple simulations were run for a range of reference speeds. Figure 5.2 shows the results for the reference speed of 188 rad/s. The tuning parameters, $r^{d}{}_{(11:13)}$, were set to the value R_d and the response in the speed and the control input (the rotor voltage) can be seen. It can be seen that if the tuning parameter value is too high then too much damping is applied and the system is sluggish, however if the damping parameter is too low then the system has an initial fast response but then transitions to oscillatory and sluggish.

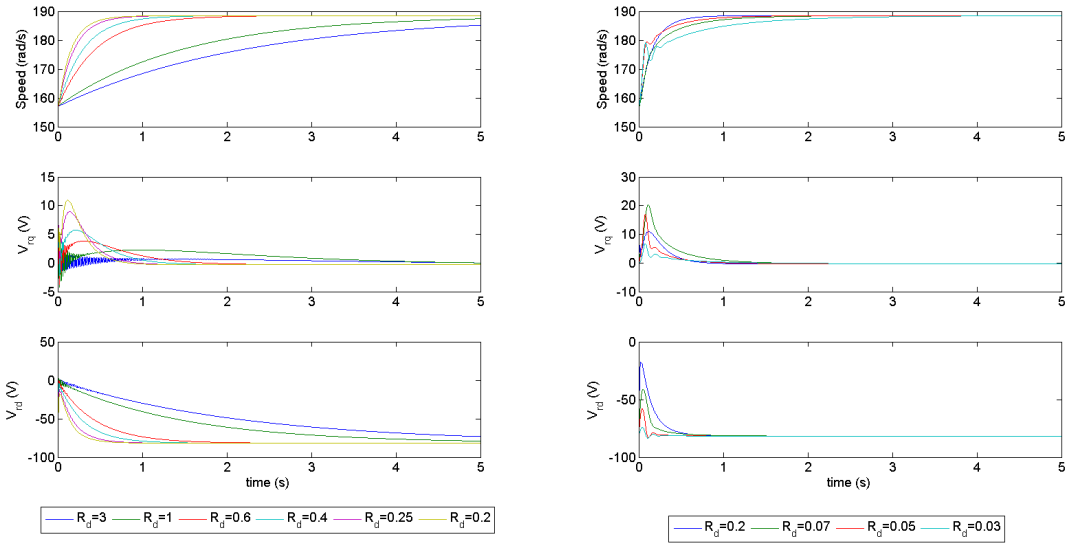

(a) (b)

Figure 5.2: DFIG speed control tuning J_m=5 a) over-damped b) under-damped

The rotor inertia was then increased to 20.0 kg m^2 to investigate the effect of the inertia on the optimum damping coefficients, the results of which can be seen in Figure 5.3. This was investigated in preparation for controlling a Variable Inertia Flywheel (VIF) energy storage system and also for controlling the full wave-to-wire OWC turbine system. In comparison with Figure 5.2, it can be seen that the increase in inertia has had minimal effect as the ideal damping coefficient, which was 0.2 for the lower inertia and 0.25 for the higher inertia.

The development of a port-Hamiltonian speed controller for a multi-pole generator outlined in this subsection was an integral step in the development of the control strategy for the OWC system, which will be expanded upon in Section 5.6.

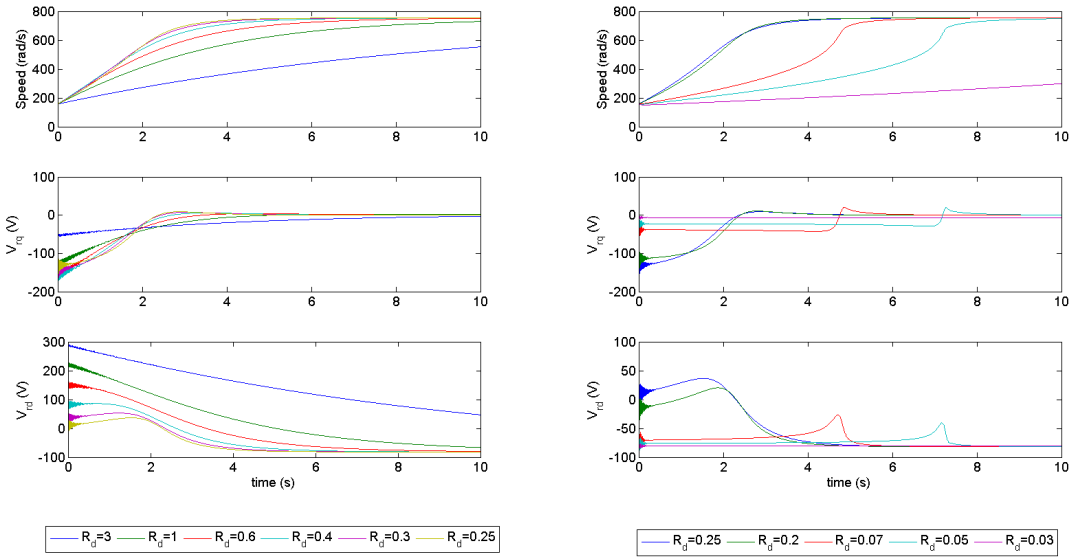

(a) (b)

Figure 5.3: DFIG speed control tuning J_m=10 a) over-damped b) under-damped

5.5 Power Control of an Energy Storage System

In Chapter 4 the potential benefit of using a Fixed Inertia Flywheel (FIF) energy storage system was discussed. As a result, it was decided to create a PBC strategy for a DFIG FIF system. The FIF system would operate in the vicinity of, but independently from the OWC system and would be electrically positioned between the OWC and the grid connection, as seen in Figure 5.4. A demand power reference would be supplied by the local Distribution Network Operator (DNO) both for the real, P_n, and reactive power, Q_n, and hence the power factor.

The real power (Krause 1986) is defined as

$$P_n = \frac{3}{2} {v_{qd0s}}^T \begin{bmatrix} 1 & 0 & 0 \\ 0 & 1 & 0 \\ 0 & 0 & 2 \end{bmatrix} i_{qd0n} \tag{5.33}$$

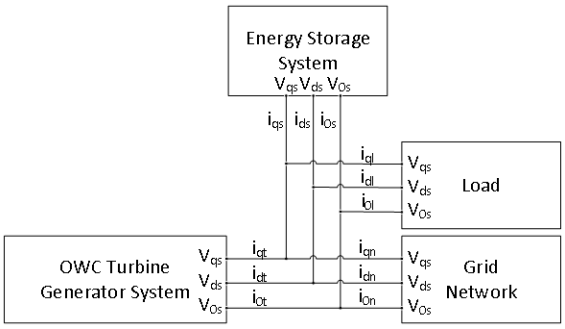

Figure 5.4: Energy storage system is electrically positioned between the OWC system and the national grid

whereas the reactive power is defined as

$$Q_n = \frac{3}{2} {v_{qd0s}}^T \begin{bmatrix} 0 & 1 & 0 \\ -1 & 0 & 0 \\ 0 & 0 & 0 \end{bmatrix} i_{qd0n} \tag{5.34}$$

The desired direct-network current can therefore be defined in terms of the desired quadrature-network current as

$$i_{dn} = \frac{\frac{2}{3} Q_n + v_{ds} i_{qn}}{v_{qs}} \tag{5.35}$$

Substituting this definition into the real power equation results in a definition of the quadrature-network current as

$$i_{qn} = \frac{\frac{2}{3} P_n v_{qs} - \frac{2}{3} Q_n v_{ds}}{{v_{ds}}^2 + {v_{qs}}^2} \tag{5.36}$$

The OWC system output power from the inverter to the grid is treated as a disturbance input to the energy storage system as the two systems are treated independently in this work. The voltage connection of the OWC is also fixed to that of the network hence this disturbance input must be treated as a current input. The method used to calculate the network currents given in Equations (5.33) to (5.36)

can also be applied to calculate the current from the OWC system.

Under certain conditions the FIF energy storage unit may be at full capacity when the OWC power may still be greater than the demand. Under such circumstances a load has been simulated that can dissipate this excess power. It was decided that the load would be used to dissipate power when the speed of the flywheel reached a maximum speed limit ($\omega_m > {\omega_m}^{max}$). In the example presented the maximum was defined as 110% rated speed. The limit depends on the capabilities of the generator as set out by the manufacturers specification sheet. To prevent the load constantly switching at the threshold a hysteresis loop is used. In this case the load was disabled when the FIF mechanical speed reached 100% rated speed. There is a large spike in the current flow if a large load is switched on instantaneously. This can be prevented by bringing the load in steadily. In the simulation this was modelled by applying the change in impedance with a ramp of 0.2s. Practically this could be achieved by using multiple smaller load banks and switching them at staggered intervals.

For a balanced system (i.e. the currents and voltages are equal across each of the abc phases) the impedance of the load is calculated as

$$Z_l = R_l \begin{bmatrix} 1 & 0 & 0 \\ 0 & 1 & 0 \\ 0 & 0 & 1 \end{bmatrix} + \omega_s L_l \begin{bmatrix} 0 & 1 & 0 \\ -1 & 0 & 0 \\ 0 & 0 & 0 \end{bmatrix} \tag{5.37}$$

and therefore the current through the load is

$$i_{qd0l} = {Z_l}^{-1} v_{qd0s} \tag{5.38}$$

For an unbalanced system, the impedance is calculated as

$$Z_l = K_s \begin{bmatrix} R_{l1} & 0 & 0 \\ 0 & R_{l2} & 0 \\ 0 & 0 & R_{l3} \end{bmatrix} {K_s}^{-1} + K_s \frac{\partial {K_s}^{-1}}{\partial t} K_s \begin{bmatrix} 0 & 0 & 0 \\ 0 & 0 & 0 \\ 0 & 0 & 0 \end{bmatrix} {K_s}^{-1} \tag{5.39}$$

The load current can be calculated from the known impedance and voltage. This can then be used, in conjunction with the OWC generator-turbine current and the network current, to calculate the desired stator current,

$${i_{qd0s}}^d = i_{qd0t} - i_{qd0l} - {i_{qd0n}}^d \tag{5.40}$$

By rearranging rows 8 through to 10 of the fixed point operating equations, the desired rotor current can be derived by analytical means. The first part of the rearrangement results in

$$K_s \frac{\partial {K_s}^{-1}}{\partial t} {i_{qd0r}}^d = (K_s L_{sr} {K_r}^{-1})^{-1} (-K_s \frac{\partial {K_s}^{-1}}{\partial t} K_s L_s {K_s}^{-1} {i_{qd0s}}^d - R_s I_3 {i_{qd0s}}^d + v_{qd0s}) \tag{5.41}$$

however the terms in front of i_{qd0r} are not invertible as

$$K_s \frac{\partial {K_s}^{-1}}{\partial t} = \begin{bmatrix} 0 & -\omega_s & 0 \\ \omega_s & 0 & 0 \\ 0 & 0 & 0 \end{bmatrix} \tag{5.42}$$

To solve this equation it was decided that the desired rotor zero component would be set to zero (${i_{0r}}^d = 0$) to prevent imbalance and then the remaining fixed point equation could be used to solve for the first two rows

Rows 1 through to 13 of the fixed point equation are then used for calculating the

desired rotor voltage

$$v_{qd0r}{}^{d} = K_r \frac{\partial K_r{}^{-}1}{\partial t}(K_r L_r K_r{}^{-1} i_{qd0r}{}^{d} + K_r L_{sr} K_s{}^{-1} i_{qd0s}{}^{d}) + R_r I_3 i_{qd0r}{}^{d} \tag{5.43}$$

The rotor speed is then calculated using row 14 of the fixed point equation.

$$\omega_m{}^{d} = \frac{1}{B_b}\left(\frac{n_p}{2}(i_{qd0s}{}^{d})^T K_s \frac{\partial L_{sr}}{\partial \theta_r} K_r{}^{-1} i_{qd0r}{}^{d}\right) \tag{5.44}$$

The calculation of the control input using the matching equation is exactly the same as for the DFIG speed controller as discussed in Section 5.4.

5.5.1 Simulation Results

For the FIF DFIG simulation, the parameters were selected using the per unit values used by Mathworks (2011) in the asynchronous generator model. Krause (1986) presents a derivation of per unit values. These per unit values enabled simulation of a range of generators with different power and voltage ratings. The particular simulation shown in Figures 5.5, 5.6 and 5.7 uses the following System International (SI) values. The generator has been set as a four pole machine, the stator voltage, v_{qd0s} is $[0\ 690\ 0]^T$, the stator resistance, R_s, is 0.0009355 Ω, the rotor resistance is 0.009089 Ω, the mutual magnetizing inductance, L_{sr}, is 0.002052 H, the stator inductance, L_s is 0.002677 H, the rotor inductance, L_r, is 0.002677 H, the mechanical resistance is 0.005 kg m^2 / rad^2 and the rotor inertia J_m is 10 kg m^2.

The results for the simulation can be seen in Figure 5.5. The power flow to the network follows the desired reference from the network for both the real and reactive power with only a slight deviation, when the reference values change. The maximum error, ignoring the error due to the initialization values, is 1.5 kW, which can be

seen in Figure 5.6. This transient lasts less than a thousandth of a second as can be seen in Figure 5.7, which is a zoom-in of the same data set as in Figure 5.6.

The maximum energy storage of this particular FIF system is only 208.5 kJ. This could be increased both by using a two pole generator, which has a higher rated speed, and by increasing the inertia of the FIF during the design process. An increase in the rated FIF speed by a factor of two increases the energy capacity by a factor of four. The inertia only has a linear affect, therefore an increase in the inertia to 20 kg m^2 from 10 kg m^2 would only double the energy storage capability. In addition multiple flywheels could be used in parallel to increase the capability and would enable maintenance of the system without losing the full energy storage capacity.

Chapter 4 highlighted the importance of appropriately sizing the energy storage unit for the prevailing conditions, whereas this study has shown that given the reference conditions the flywheel can follow the demand, however when the energy storage is at a minimum no more energy can be extracted.

The advantage of using a DFIG FIF is the reduced cost in the power electronics since only a one-third rated converter is required as opposed to the fully rated converter required by a SCIG FIF. The relative cost of the generator however is unknown to the author of the thesis. For the DFIG FIF system described in this sub-section the limited operating speed range of 30% either side of the rated speed means that the effective energy storage capacity is 148 kJ. The 60 kJ of energy still present in the flywheel at the lower speed limit is effectively not available for use. A similar four-pole SCIG FIF system has a speed range of 10% and 90% of rated, with a corresponding energy range of 123 kJ. It can therefore be concluded that the DFIG FIF has a higher energy capacity.

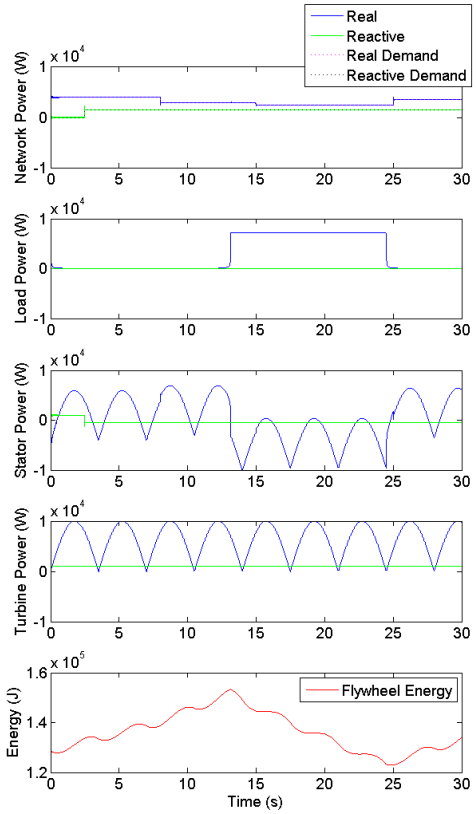

Figure 5.5: DFIG FIF power flow control

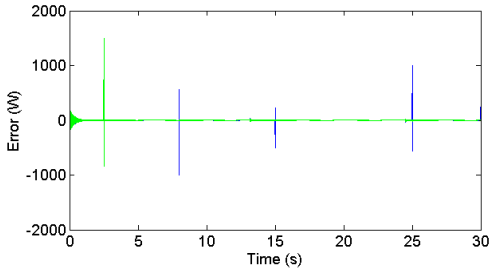

Figure 5.6: DFIG FIF power flow control error

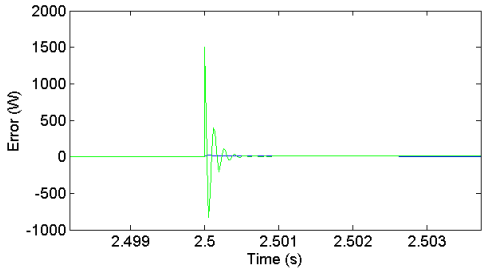

Figure 5.7: DFIG FIF power flow control transient error

5.6 Turbine Damping Control

PBC of a wave energy converter and more specifically an OWC holds a lot of promise and could be an extremely beneficial tool. There is the potential to apply cost optimization techniques to identify the optimum running conditions in order to absorb the maximum energy over a certain time frame or optimization window. However, the PBC problem consists of two tasks. The first task involves identifying the desired operating conditions and the second task involves designing the control strategy for achieving those operating conditions. As a first step towards achieving a control strategy for wave-to-wire optimized efficiency, a speed controller has been designed to control an OWC system to the optimum turbine damping, K^d, as prescribed by the OWC chamber designers. However under some circumstances it may be infeasible to control the device to these optimum conditions based on the limitations of the electrical and mechanical subsystems. This will be discussed further in the simulation results section.

It is advisable to identify the potential range of damping that can be achieved based on the speed limitations of the generator and the instantaneous pressure. The maximum and minimum non-dimensional damping are calculated using

$$p^* = \frac{\Delta p}{\rho_a {\omega_m}^2 {D_t}^2} \tag{5.45}$$

where for the DFIG the speed range is 70% to 130% of rated speed and for the SCIG it is 10% to 100% of rated speed. The minimum and maximum non-dimensional flow rate, Q^*, can then be computed using the non-dimensional curves. The spline curves as discussed in Section 3.5 can be used for this purpose. The minimum and maximum flow rate can then be computed using

$$Q_t = \omega_m {D_t}^3 Q^* \tag{5.46}$$

and from this the minimum and maximum damping can be computed using

$$K = \frac{\Delta p}{Q_t} \tag{5.47}$$

If the desired damping falls outside the minimum and maximum damping then the desired speed should be set to the minimum or maximum, whichever enables the closest possible control to the optimum damping.

For a 1.8m diameter turbine, with a pressure drop across the turbine of 10,000 Pa and a 8 pole pair DFIG, the minimum and maximum damping ratios are 209 and 251 Ns/m^5 respectively. By comparison, a SCIG in the same configuration would have a minimum and maximum damping ratio of 157 and 230 Ns/m^5 respectively. The SCIG has a wider damping ratio and a lower damping range which in general is more suitable for an OWC device, though higher damping OWC devices do exist.

Assuming that the required damping is within the possible range then the next stage is to calculate the desired speed. This has been achieved by calculating the non-dimensional pressure for a range of speeds, between the minimum and maximum, associated with the instantaneous pressure. Each non-dimensional pressure has then been used to calculate a table of non-dimensional flow rates and subsequently dimensionalized flow rates. The damping is then calculated for each value of the dimensional flow rate and instantaneous pressure. Interpolation is then used to identify the desired speed from the table of speed versus damping using the desired damping as the input.

Using the desired speed, the desired value for each of the other state variables can be computed using the fixed point equations. In this first implementation of a port-Hamiltonian control for an OWC system, the hydrodynamic and pneumatic systems will be treated as a torque input to the electrical system and the speed controller developed in Section 5.4 is employed.

5.6.1 Simulation Results

The system state equations are given in Section 3.8. The parameter values are defined in Section 6.4. Tests were initially conducted with a monochromatic wave of 1.5 m amplitude and a frequency of 0.725 rad/s (equivalent to a period of 8.6 s). The turbine diameter and the number of generator poles (and hence speed) dictates the damping range of the device. Fixed speed control (at generator rated speed) was used to find the damping for a variety of turbine diameters and generator poles, the results of which are shown in Figure 5.8.

Damping control was then applied and the results can be seen for a 1m turbine with a single pole pair (two pole) DFIG in Figure 5.9. As it can be seen the damping control is effective within the speed limits of the generator. However the figure also demonstrates the narrower and lower damping range possible with the 4 pole-pair DFIG. Generators with fewer poles have a wider speed range which results in a wider damping range. However a wide range is not strictly necessary as long as the attainable damping aligns with the requirements of the OWC for peak efficiency operation. At this stage, IDA-PBC OWC damping control has not been extended for the SCIG, however it is anticipated that the wider and lower speed range (between 10 and 100% rather than 70% to 130% rated speed) will be preferential for an OWC.

5.7 Summary of Contribution

This chapter has introduced three control strategies. As an initial step an IDA-PBC speed control for a multi-pole DFIG was developed. This approach was a precursor to the subsequent development of both a power-based control strategy for a FIF energy storage system, and an OWC damping control strategy. A Newton-Raphson

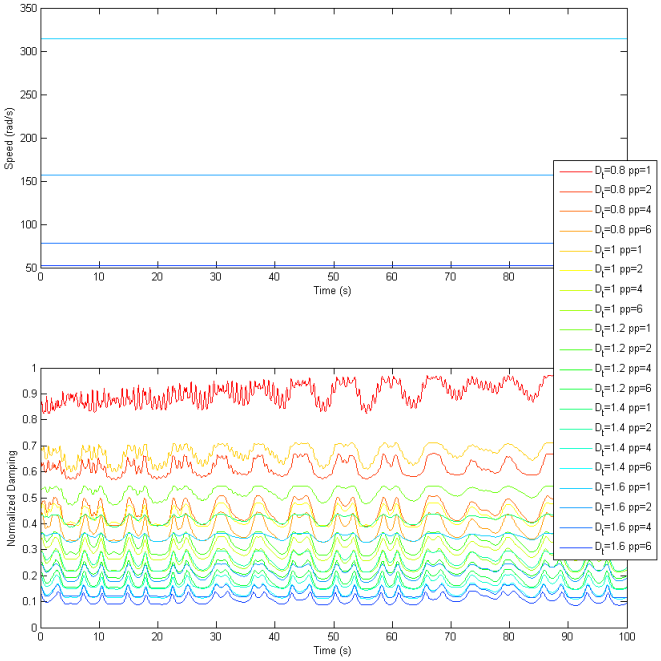

(a)

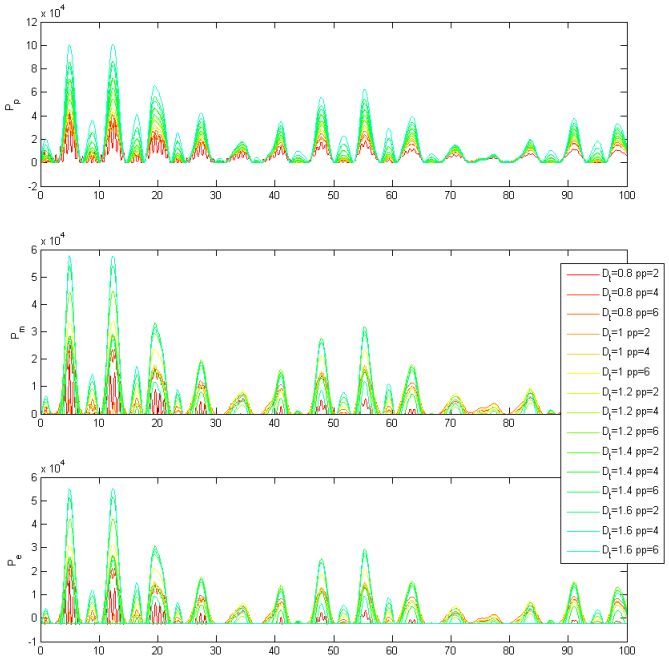

(b)

Figure 5.8: Damping achieved with fixed speed control for a variety of turbine diameters and generators and the associated power extracted

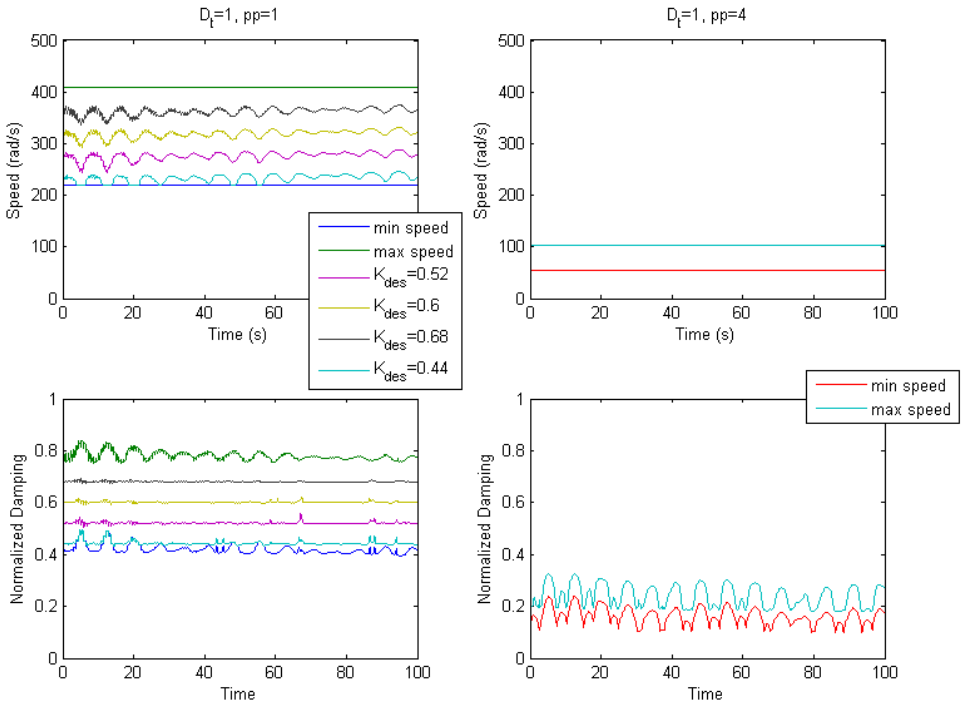

Figure 5.9: DFIG damping control for a 1m turbine diameter in conjunction with a 1 pole-pair and 4 pole-pair generator

numerical solver was used to locate the desired operating condition for the speed control and damping control strategies. An analytical solution was found for the FIF power control strategy. Further work is required to develop an analytical solution to the speed and damping controls. However the successful simulation of the control strategies show promise for further development. This can be expanded upon with more sophisticated PBC strategies, with improved response times and robustness.

It is envisaged that neither an OWC damping control strategy nor a flow coefficient control strategy will obtain optimized power extraction since both strategies focus on the energy extracted from a single component of the energy chain. However, the large benefit of the development of the IDA PBC control strategy proposed herein is the potential for power optimization by employing an energy cost function as a means to calculating the optimized operating conditions.

Chapter 6

Test Facility

The Pneumatic Wave Generator (PWG) test facility discussed in the present chapter was initially built in 2005 and was originally capable of producing monochromatic bidirectional air flows (Herring 2007, Herring & Laird 2007, Natanzi et al. 2011). The planned utilization of the test rig was three-pronged. Firstly, to be used to validate the Computational Fluid Dynamics (CFD) numerical results (obtained by Banks (2009), Natanzi (2010a), Tarver (2013) and the author of this thesis); secondly, to tune an analytical Power Take-Off (PTO) model by identifying the generator windage and bearing losses etc. and validate its accuracy for the pneumatic, mechanical and electrical components, and thirdly to make the test facility suitable for testing potential control strategies.

In order to more accurately represent monochromatic waves and add the ability to generate polychromatic waves the author proposed and undertook an upgrade to the instrumentation, data acquisition software and control software including the algorithm for the wave profiles. The upgraded test facility has been used to validate the numerical results of the turbine which have been generated through CFD numerical simulations.

This chapter includes, in Section 6.1, a review of existing test facilities around the world. The following section, Section 6.2, details the development of the PWG test facility. This includes Section 6.2.1 which details the PWG Hardware. The instrumentation is detailed in Section 6.2.2. The analysis given in Section 6.2.3 introduces the control algorithm including the modifications required for using speed control rather than position control. Section 6.2.4 presents the generated waves for both the monochromatic and polychromatic cases. The work to validate the CFD numerical simulation results is then discussed in Section 6.3.

6.1 Literature Review of Test Facilities

Various test facilities have been developed to allow the characterization of Oscillating Water Column (OWC) turbines and to validate a range of numerical models describing their performance. This review identified six land-based facilities that have been reported as being used for OWC testing employing a range of methods to produce reciprocating flows. Of these test facilities, some examine the performance of the turbines under steady flow conditions and the others under monochromatic bidirectional flow conditions.

The facility described by Dhanasekaran & Govardhan (2005) uses a 4kW variable speed centrifugal blower that can produce a flow rate of $1.1\text{m}^3/\text{s}$ and a pressure drop across the turbine of 2000Pa. Although this test facility could replicate a range of flow rates it does not produce bidirectional flows.

The test rig used by Raghunathan & Ombaka (1985) consisted of an air bellow driven by a ram and hydraulic jack (Figure 6.1). Two 0.2m diameter Wells turbines with different solidities (ratio of blade chord length to pitch) were tested with monochromatic flow oscillation with a frequency range of 0.2 to 1Hz.

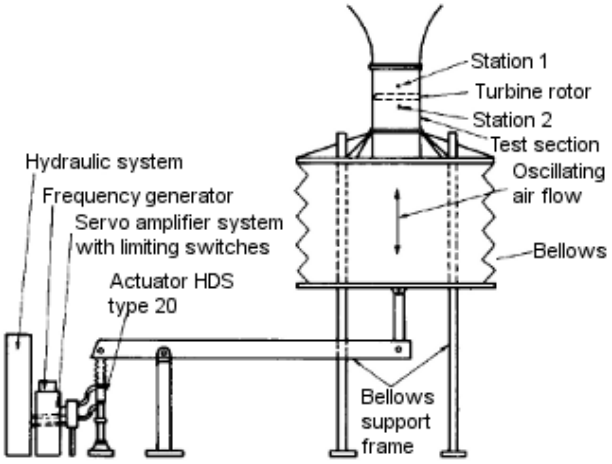

Figure 6.1: Test rig using bellows (Raghunathan & Ombaka 1985).

Maeda, Setoguchi, Takao, Sakurada, Kim & Kaneko (2001) completed unidirectional testing under steady flow conditions and then used numerical simulations to predict the turbine performance under irregular wave conditions, using a test rig consisting of a large piston of diameter 1.4m and stroke of 1.7m. Subsequently Maeda, Takao, Setoguchi, Kaneko & Kim (2001) and Setoguchi et al. (2000), using the same test facility (Figure 6.2) reported a set of experiments using an impulse turbine with a tip radius of 298mm. The tests employed monochromatic waves with a 0.1Hz frequency. The experiments produced pressure drops of up to 1.8kPa with a maximum flow rate of $0.32\text{m}^3/\text{s}$ at a rotational speed of 370rad/s. It was deduced that since sea waves are irregular, it is important to characterize the turbine performance under transient conditions.

Mala et al. (2011) used a piston, with a diameter 1.25m, driven by a crank and rod connected to a disk with a number of holes at different eccentric distances to generate various flow rates. This created simulated sinusoidal waves of 0.404 to $2.46\text{m}^3/\text{s}$. The test rig attained pressures that ranged from 0.77 to 4.3kPa. Although this test rig was used to test a twin unidirectional turbine, it is presumed that it could be used to test bidirectional turbines.

The test facility used by Thakker & Abdulhadi (2008) consists of a plenum chamber

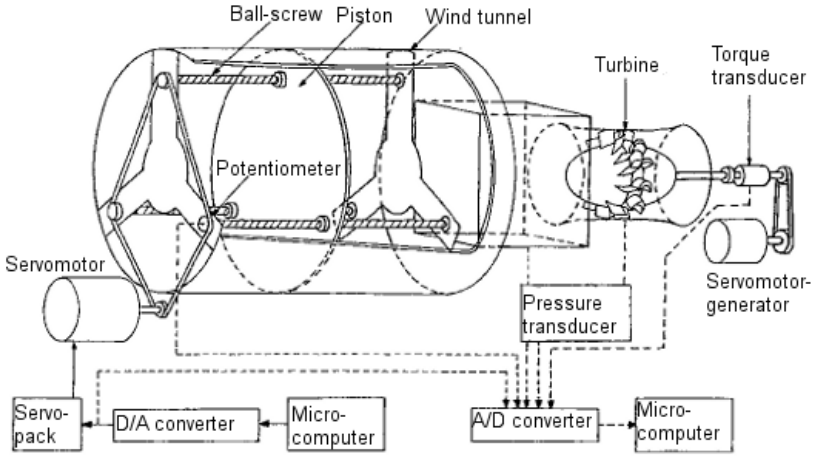

Figure 6.2: Test rig using a piston (Maeda, Takao, Setoguchi, Kaneko & Kim 2001).

with honeycomb section. The air flow rate is generated by a centrifugal fan and then diverted using a bidirectional valve. The tests were conducted on a Wells turbine with turbine speeds ranging from 350 to 1,700rpm with a single period sine wave of period 9.2s and velocity 8.4m/s. The turbine tested had a 597mm diameter.

Liu et al. (2009) present work conducted at a test facility which consists of a large piston-cylinder, a settling chamber and a section to accommodate devices under test with a bell-mouthed end. The sinusoidal motion is created by an A.C. servo-motor driving the piston through mechanical translation, producing more than 1kPa and $0.7\text{m}^3/\text{s}$. The authors reported problems with the test rig which meant the desired and actual frequencies were not perfectly matched. The rig was used to experiment with both turbines and orifice plates.

More recently the author is aware of a test facility that has been commissioned at the University of Siegen although no papers have been published detailing its capabilities.

The Dresser-Rand and Cranfield University PWG test facility, presented initially by Herring (2007) and Herring & Laird (2007), produced a range of monochromatic pressure waves. To compare this test facility with the others, it is common (as

seen above) to quote the capability of the test facility in terms of the flow rate and pressure waves generated. However, both of these values are functions of the turbine geometry, the instantaneous speed of the turbine rotor and the volume of the air chamber and ducting. The current turbine under test is a Variable Radius Turbine (VRT) and has a rotor diameter of 0.6m and can be tested with turbine speeds ranging between 100 to 1,500rpm. Static pressures have been measured up to ± 5kPa. This test facility is grid connected and exports generated power to the grid in compliance with G83/1 engineering recommendations.

Therefore, one may conclude that while a number of dedicated OWC turbine test facilities exist, only some of them can produce monochromatic bidirectional pressure waves. At the time of writing, no turbine testing by employing polychromatic wave conditions at a land-based test facility is reported to have taken place. The test facilities surveyed are stated as producing peak flows of up to 2.46m^3/s and pressure drops of up to 4.3kPa. These figures are comparable with the PWG in its original monochromatic control configuration. The work reported herein develops the test facility to produce polychromatic waves from a variety of wave spectra with a coefficient of determination of better than 0.99 (i.e., better than the measurement system capability). This enables land based testing of control strategies under sea conditions from different potential sites using different spectral types. In addition, seasonal variations can be incorporated by changing the parameters for the selected spectra.

6.2 Pneumatic Wave Generator Test Facility

6.2.1 PWG Hardware

The PWG is composed of a cylindrical air chamber made of Glass Reinforced Plastic (GRP) with a rotary paddle that is controlled to produce oscillating air profiles (see Figure 6.3). The paddle periphery uses a brush seal to reduce leakage. The resulting air profile is then ducted though a square-to-round duct to the device under test. It is used to test the HydroAir^{TM} VRT which uses a variable radius duct profile (Freeman et al. 2008), see Figures 6.3 and 6.4.

Figure 6.3: PWG test facility air chamber

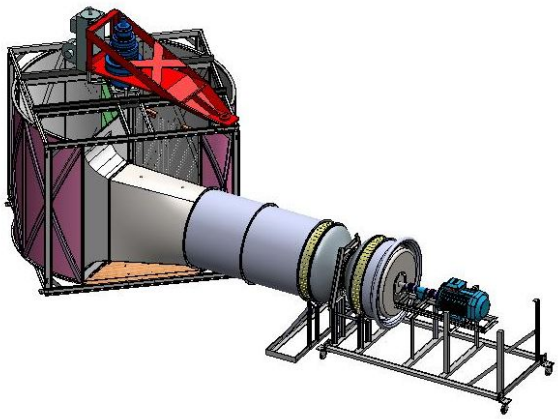

Figure 6.4: CAD drawing of PWG test facility (Dresser-Rand Company Ltd 2014)

The paddle is actuated by an induction motor with an integral position encoder connected via an input card to a back-to-back Integrated Gate Bipolar Transistor

(IGBT) inverter. A diagram of the hardware is shown in Figure 6.5. The PWG inverter is controlled via a Programmable Logic Controller (PLC) on a PROcess FIeld BUS (PROFIBUS) connection. The turbine under test is connected to the National Grid using a back-to-back IGBT inverter decoupling the turbine speed from the frequency of the grid. The inverter (and hence the generator and the turbine) are controlled using an additional PTO PLC.

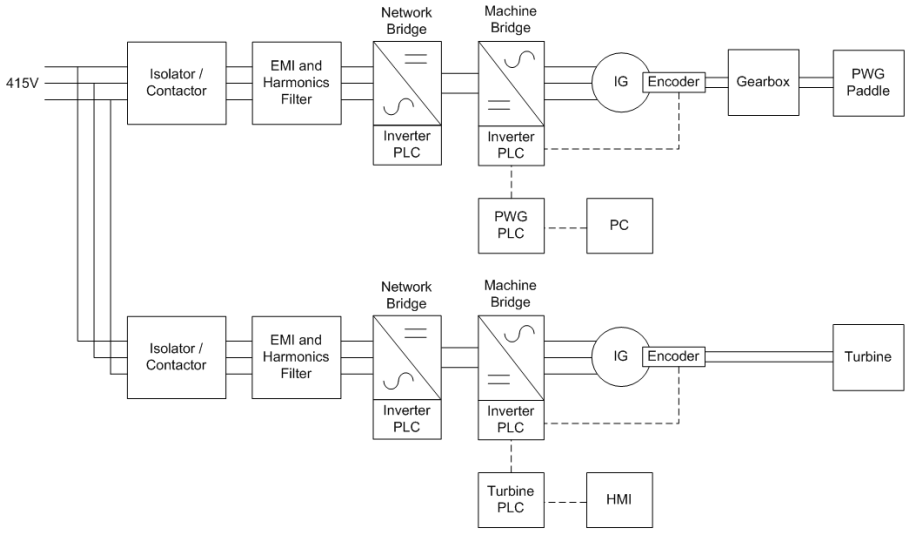

Figure 6.5: Test rig hardware diagram

6.2.2 Instrumentation

As reported in Farman et al. (2013), the PWG test facility was updated to include new measurement equipment. Key changes include the update to the data acquisition software and the creation of polychromatic waves utilizing speed control for the inverter rather than position control. The test rig is currently equipped with the following instrumentation:

1. Two pressure scanners (CANdaq III) each with 32 pressure ports for both static and total pressure measurements

2. Torque and speed transducer (IML RTA200)

3. Temperature probes (K-type thermocouples)
4. Barometer (DPI 142-150)
5. Ambient temperature (RTD)
6. Two 4-20mA channels to communicate information from the inverter to the data acquisition system e.g. grid power, machine power, magnetising torque

The new equipment mandated an update of the data acquisition software. It was decided to use Labview 2009, which utilizes Virtual Instruments (VIs) to interface to the various components. The communication is achieved over Ethernet to the two pressure scanners, and over serial RS232 for the barometer. Processing of the 4-20mA, frequency, voltage and thermocouple sensors is via the inbuilt DAQmx VIs. The data is then logged at the required frequency of 10Hz.

The turbine is fitted with 64 pressure tappings connected to two 32 channel pressure scanners that incorporate digital thermal compensation within a range of ±7kPa. The pressure scanners have a capability of 625 measurements per channel per second with a full scale accuracy of 0.06% (Chell Instruments Ltd 2010). The pressure ports are used to measure both static and total pressures at the guide vanes and static pressure upstream and downstream of the rotor. A number of the turbine guide vanes are fitted with four pressure tappings (see Figure 6.6). The spanwise locations of these tappings were determined from numerical studies of the flow through the guide vanes Natanzi (2010b). The leading edge pressure probes are used to measure the flow rate. The main advantages of their position is their minimal effect on the flow, that the usual area of stagnation pressure behind the probe is reduced and there is an increase in their structural integrity. This latter point is extremely important for using total pressure ports on turbines to be commissioned in the ocean, where redundancy is important. Additional pressure measurements are taken at a number of locations from within the PWG chamber.

A torque speed transducer and generator encoder are used to enable turbine measurements in isolation from the generator. The inverter cubicle has Current Transformers (CTs) and Voltage Transformers (VTs) on the machine and grid side connections in order to calculate the electrical power output. In addition, a power logger and power quality analyzer can be used to monitor the output voltages and the degree of flicker and harmonics in the system. Barometric pressure is measured, as well as atmospheric temperature. A variety of measurements from the back-to-back inverter can be communicated to the data acquisition hardware. An additional encoder is used to measure the position of the PWG flap. The instrumentation data is acquired and processed via a bespoke Human Machine Interface (HMI). IGBT inverters can cause problems with Electro-Magnetic Radiation (EMR); hence all instrumentation cables at the test facility were screened at one end and low voltage signals were avoided wherever possible. The power cables were screened at both ends in accordance with industrial guidelines (Control Techniques Ltd 2009a).

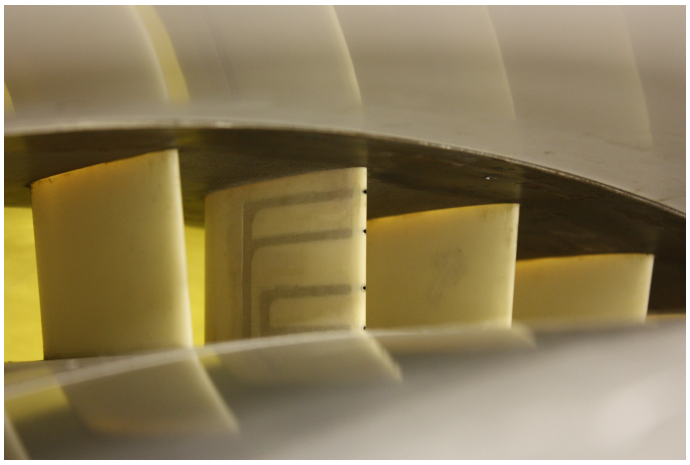

Figure 6.6: Total pressure probes embedded in turbine blades

6.2.3 Test Rig Control Strategy

The work presented here describes the control strategy development to enable the PWG test facility to simulate a range of polychromatic air waves for a variety of

wave spectra. It is believed that this is the first land-based test facility to enable testing of turbines under simulated realistic polychromatic sea conditions (i.e. with polychromatic waves).

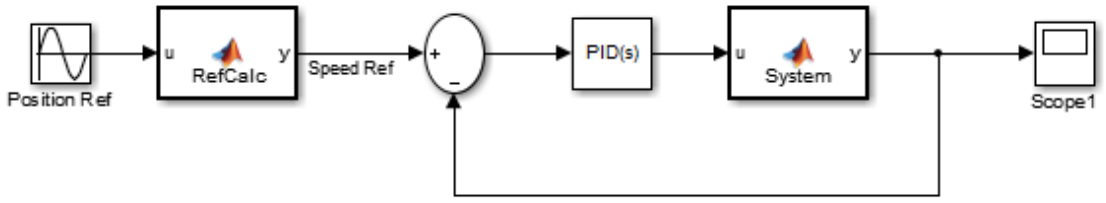

Figure 6.7: PID speed control loop

The PLC calculates the vertical position and velocity using the equations given in Section 3.3 for the wave profile from the required spectrum defined by the operator. The PLC program subsequently determines the speed reference value for the motor which is communicated on a PROFIBUS connection to the inverter drive at an update rate of 50ms and fed into a Proportional Integral Derivative (PID) controller for the speed control loop of the motor. The PID parameters are obtained using the inverter auto-tune function. The control loop can be seen in Figure 6.7. Ideally a position control loop would have been used rather than a speed control loop because the latter is prone to integral errors as well as not being able to limit the range of the paddle. However it was necessary to use the speed control loop due to the limitations of the inverter firmware.

Protection software (i.e. automatic shut-down) has been built into the control strategy to ensure that the paddle does not overshoot the hard limits of the system. The system has been designed to be fail-safe; hence, loss of communication between the PLC and the inverter will result in the motor being controlled to a stationary position. The software has the ability to generate both monochromatic and polychromatic waves. It should be noted that monochromatic waves are an special case of the polychromatic case. The mean Sea Water Level (SWL) is chosen to be the mid-point of the range of paddle sweeping angles. A limit switch positioned at the

maximum swept angle is used to locate the paddle and then position control is used to locate the mid-point.

It was found there were at least three causes of position offset when using a speed control algorithm for generating the wave profiles. One of the causes is that in a realistic test rig, the position and velocity of a wave series are both zero at the start of the test. However, for a sine wave these values are always 90 degrees out of phase (see Figure 6.8). In the case where the position is taken to be zero, the speed needs to ramp up to maximum speed as fast as possible; however, this can activate hardware protection limits. The time taken to bring the speed up to the required value can create an offset in the wave position. The PWG system has a finite sweeping angle; therefore, to maximize the range of waves that can be produced, this offset should be minimized. In addition, this ensures that the mean SWL is constant across all waves irrespective of the flap speed.

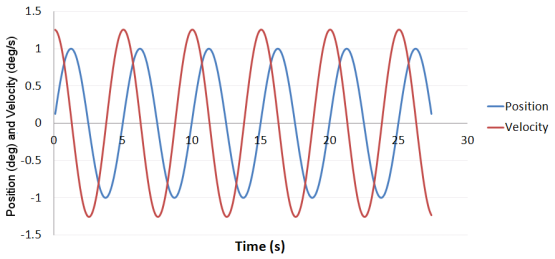

Figure 6.8: Phase relationship between position and velocity

One method to remove the offset is to use a ramp that has the same length as a multiple of the period of the wave in question. For example, a seven-second wave would require a ramp of 7, 14, 21 seconds etc.. If a ramp of a different length is used, then an offset is introduced. This can be carried over to the polychromatic wave scenario by multiplying each frequency component by its own ramp rate. The mathematics behind this are discussed next.

Ramp Mathematical Demonstration

A ramp function is used to remove any position offset that would have been caused by hardware limits in accelerating to maximum velocity at start-up. An offset in the paddle position would result in a change in the air chamber volume, which in turn affects the pressure across the turbine. In addition, an offset limits the range of potential waves that can be generated due to the hard limits of the system and can limit the length of time the paddle can be operated, as it drifts off the mid-point. Therefore, it is imperative that the ramp does not inject any additional position offset.

The equation for one of the frequency components of the wave to be generated is given as:

$$\dot{\eta}_i = 2\pi f_i a_i \cos(2\pi f_i t - \frac{2\pi x}{\lambda_i} + \phi_i) \tag{6.1}$$

The ramp, for the specific frequency component, is described in the following way

$$r_i = \begin{cases} \frac{t}{t_{ri}} & t \leq t_{ri} \\ 1 & t > t_{ri} \end{cases} \tag{6.2}$$

where t_{ri} is the ramp duration; therefore, the equation for the speed of the flap incorporating the ramp is:

$$\eta_{ri} = r_i \dot{\eta}_i \tag{6.3}$$

Thus the instantaneous position of the paddle is calculated as:

$$\eta_{ri} = \int \dot{\eta}_{ri} dt \tag{6.4}$$

Substituting this into Equation (6.1) and calculating the integral results in:

$$\eta_{ri} = \frac{a_i t}{t_{ri}} \sin(2\pi f_i t - \frac{2\pi x}{\lambda_i} + \phi_i) + \frac{a_i}{2\pi f_i t_{ri}} \cos(2\pi f_i t - \frac{2\pi x}{\lambda_i} + \phi_i) + c \qquad (6.5)$$

The integration constant, c, can be found as it is known that the position of the paddle using the ramp is zero at start-up, i.e., the paddle is representing the mean sea water level. Substituting $t = 0$ and $\eta_{ri} = 0$ into the above equation results in:

$$c = \frac{-a_i}{2\pi f_i t_{ri}} \cos(\frac{-2\pi x}{\lambda_i} + \phi_i) \qquad (6.6)$$

This results in the equation for the instantaneous position as:

$$\begin{aligned} \eta_{ri} = \frac{a_i t}{t_{ri}} \sin(2\pi f_i t - \frac{2\pi x}{\lambda_i} + \phi_i) \\ + \frac{a_i}{2\pi f_i t_{ri}} \cos(2\pi f_i t - \frac{2\pi x}{\lambda_i} + \phi_i) \\ - \frac{a_i}{2\pi f_i t_{ri}} \cos(-\frac{2\pi x}{\lambda_i} + \phi_i) \end{aligned} \qquad (6.7)$$

The moment the ramp ends, the speed of the paddle must meet the following criteria:

$$2\pi f_i a_i \cos(2\pi f_i t - \frac{2\pi x}{\lambda_i} + \phi_i) = \frac{t}{t_{ri}} 2\pi f_i a_i \cos(2\pi f_i t - \frac{2\pi x}{\lambda_i} + \phi_i) \qquad (6.8)$$

At $t = t_{ri}$ the ramp for the wave component in question has finished. At this condition, the wave velocity should match that of the unramped wave. Inspection of Equation (6.8) shows that this condition is met. An equivalent requirement is

placed on the position of the paddle:

$$a_i \sin(2\pi f_i t - \frac{2\pi x}{\lambda_i} + \phi_i) = \frac{a_i t}{t_{ri}} \sin(2\pi f_i t - \frac{2\pi x}{\lambda_i} + \phi_i) + \frac{a_i}{2\pi f_i t_{ir}} \cos(2\pi f_i t - \frac{2\pi x}{\lambda_i} + \phi_i) - \frac{a_i}{2\pi f_i t_{ri}} \cos(\frac{-2\pi x}{\lambda_i} + \phi_i) \quad (6.9)$$

substituting $t_{ri} = t$ into the equation and then rearranging gives

$$\cos(-\frac{2\pi x}{\lambda_i} + \phi_i) = \cos(2\pi f_i t - \frac{2\pi x}{\lambda_i} + \phi_i) \quad (6.10)$$

Taking an inverse cosine

$$-\frac{2\pi x}{\lambda_i} + \phi_i = 2\pi f_i t - \frac{2\pi x}{\lambda_i} + \phi_i \pm 2\pi j y \quad , \qquad j = 1, 2, 3... \quad (6.11)$$

Term cancellation reduces this to

$$t_{ri} = \frac{j}{f_i} \quad , \qquad j = 1, 2, 3... \quad (6.12)$$

which is the condition that has to be met in order for there to be no offset introduced into the position of the paddle by using a ramp of the desired speed. Inspection of Equation (6.12) shows that this condition is only satisfied for integer multiples of the wave period.

It can be calculated that the offset that would be introduced if this criteria was not met would be:

$$e_i = \frac{a_i}{2\pi f_i t_{ri}} \left[\cos(\frac{-2\pi x}{\lambda_i} + \phi_i) - \cos(2\pi f_i t_{ri} - \frac{2\pi x}{\lambda_i} + \phi_i) \right] \quad (6.13)$$

For emphasizing this point, a monochromatic wave is considered of amplitude 2.5m and a period of 7s with a phase shift of 0.6 rad, and positioned at the origin; therefore $x = 0$. If a 14s or 21s ramp is used, then it would produce no offset, whereas a 3s wave would produce an offset of 1.68m and a 10s wave would produce an offset of 0.51m. This can be visually inspected in Figure 6.9.

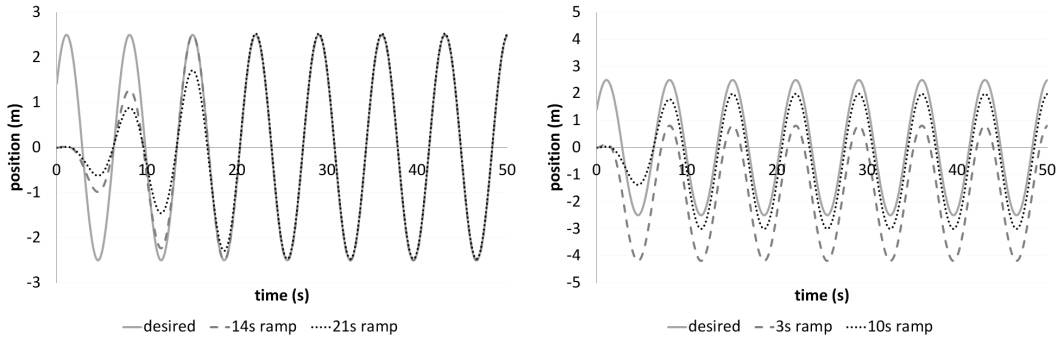

Figure 6.9: a) Monochromatic wave with ramp duration not equal to an integer multiple of the period of the wave which produces no offset. b) Monochromatic wave with ramp duration not equal to an integer multiple of the period and, hence, produces an offset from the desired the position

The total error that would be introduced for a polychromatic wave would be a sum of all the the frequency error components. Therefore, it is necessary to implement a ramp for each individual frequency component. In Figure 6.10, a time series has been generated for three Joint North Sea Wave Project (JONSWAP) spectra with peak enhancement factors of 1, 3.3 and 7. The ramps were employed as discussed. The three different time series were generated with the same phase shifts to emphasize the effect of the peak enhancement factor. The desired and actual position for the aforementioned time series, with a peak enhancement factor of 1, are shown in Figure 6.11 with good accuracy.

A MATLAB simulation, Figure 6.12, demonstrates the raw required polychromatic wave and the wave that uses the ramp for each individual frequency. A generic polychromatic wave is represented though its velocity and amplitude characteristics and where the desired polychromatic series signal is closely represented within 15

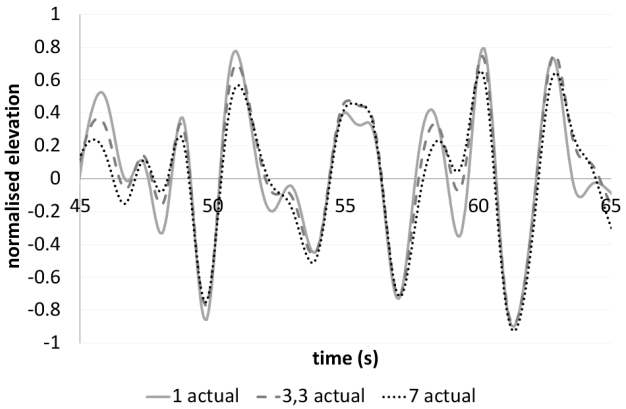

Figure 6.10: Time series generated for three different JONSWAP spectra with the same phase shifts

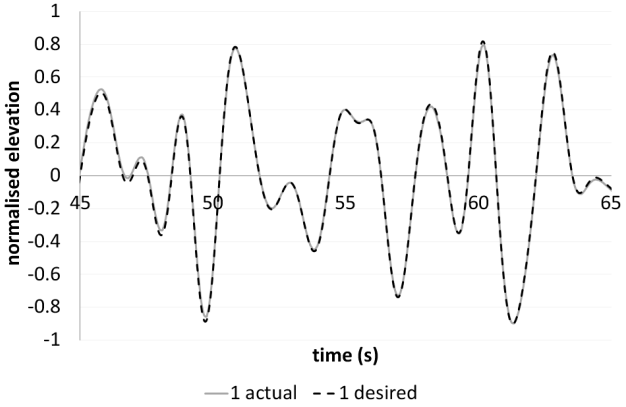

Figure 6.11: Comparison of the desired and actual time series generated for the JONSWAP spectra with a peak enhancement factor of 1

seconds.

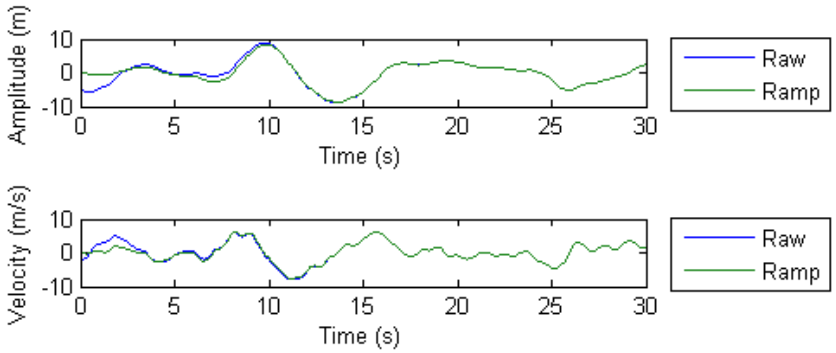

Figure 6.12: Polychromatic wave position and velocity

6.2.4 Generated Waves

Monochromatic Waves

The test facility in its original configuration generated a range of monochromatic waves which are listed in Table 6.1. Initial tests of waves using the speed control method were compared against the original waves using position control.

Linear regression calculations were computed for a range of monochromatic waves for flow rates of 1.2 and 1.77m^3/s and a range of wave periods from 5 up to 12s. The coefficient of determination[1], R^2, between the desired position and actual paddle position for the speed control method is higher than 0.99 for all the monochromatic wave cases, and has a largest error of 2.5%. It can therefore be seen that the velocity set-point approach had no significant detrimental impact on the position accuracy.

The monochromatic waves are used to verify the method for measuring the flow rate indirectly through the total and static pressure measurement through the use of a set of rake-like instrumented guide vanes. Figure 6.13 shows a time history of the

[1] "R^2 is used to describe how well a regression line fits a set of data. An R^2 near 1.0 indicates that a regression line fits the data well, while an R^2 closer to 0 indicates a regression line does not fit the data very well."

Wave No	Design Period	Design RMS Flow Rate	Wave Height (pk-to-trough)	Wave Height (pk-to-trough)
	s	m^3/s	deg	m
wave 1	7	2.3	127	1.92
wave 2	12	1.8	168	2.54
wave 3	9	1.8	126	1.91
wave 4	7	1.8	98	1.48
wave 5	5	1.8	70	1.06
wave 6	12	2.0	190	2.88
wave 7	9	2.0	142	2.15
wave 8	7	2.0	111	1.68
wave 9	5	2.0	79	1.20
wave 10	12	2.3	218	3.30
wave 11	5	2.3	164	2.48
wave 12	9	2.3	91	1.38
wave 13	12	1.5	142	2.15
wave 14	9	1.5	107	1.62
wave 15	7	1.5	83	1.26
wave 16	5	1.5	59	0.89
wave 17	12	1.2	114	1.73
wave 18	9	1.2	85	1.29
wave 19	7	1.2	66	1.00
wave 20	5	1.2	47	0.71

Table 6.1: Scaling of test rig waves for OWC simulation model

dynamic pressure as calculated from the total and static pressure measurements on the chamber side ($P1$) and the atmosphere side ($P2$) of the turbine (see Equation (6.14)). Each total pressure probe is upstream for only half of the wave cycle.

The dynamic pressure is the difference between the total and the static pressure measurements,

$$p_d = p_t - p_s \tag{6.14}$$

It can be observed that the downstream pressure signals follow closely to the corresponding upstream fluctuation. However, the vanes trailing edge pressure shows a fluctuation due to the localized separation near the probe location. The standard deviation of the total pressure measurements at $P1$ as a function of the Root Mean Square (RMS) pressure is shown in Figure 6.14. This quantity is lower than 1% for the pressure probes upstream of the turbine. As the flow changes direction it deteriorates to only 4% at its worst. This indicates that the velocity is relatively uniform across the annulus.

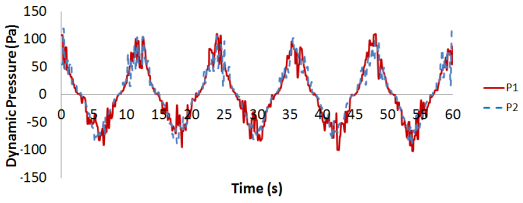

Figure 6.13: Dynamic pressure measurements for a wave of 12s period and $1.8 m^3/s$ flow rate

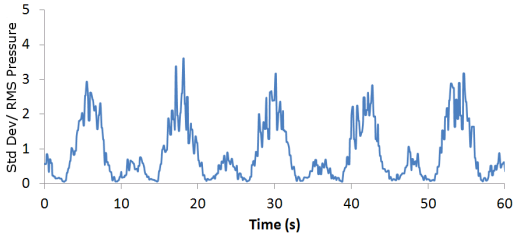

Figure 6.14: Standard deviation of the total pressure measurements divided by the RMS pressure for a wave of 12s period and 1.8 m^3/s flow rate

Polychromatic Waves

Having demonstrated the validity of the speed control method, the test program expanded to demonstrate the feasibility of polychromatic pressure wave generation. The pressure plot for an irregular wave, generated from a Pierson-Moskowitz spectrum with a wind speed of 15.4m/s measured at 19.5m above sea water level, is shown in Figure 6.15. The test was performed three times (V1,V2 and V3) and shows good repeatability. The amplitudes and phase shifts of each individual frequency are calculated via a MATLAB script and then programmed into the PLC. This enables the test facility to repeat a wave series for back-to-back comparison testing. The rig could use a random number generator and calculate the amplitude and phase shift itself; however, this requires more computation and it was decided that this approach offered very little benefit compared to the one described above. The same method was implemented for a Bretschneider spectrum and the resulting pressure wave time series is shown in Figure 6.16. For the results from the Pierson-Moskowitz spectrum testing (Figure 6.17) one can see that there is a strong correlation between the actual and desired position data and the line of best fit (R^2 equals 0.96). The proximity of this line of best fit to $y = x$ demonstrates that the PWG can be relied upon to deliver the required paddle position and, therefore, flow conditions.

6.3 Validation of Numerical CFD Results

As with any new piece of turbo-machinery, much of the initial performance analysis work for the HydroAir VRT was conducted using CFD. Whilst CFD is an established technique it is nevertheless necessary to validate the CFD numerical results using experimental data, wherever possible. To this end, a focused test plan was developed. Initially the turbine speed was kept constant and hence, as the pressure

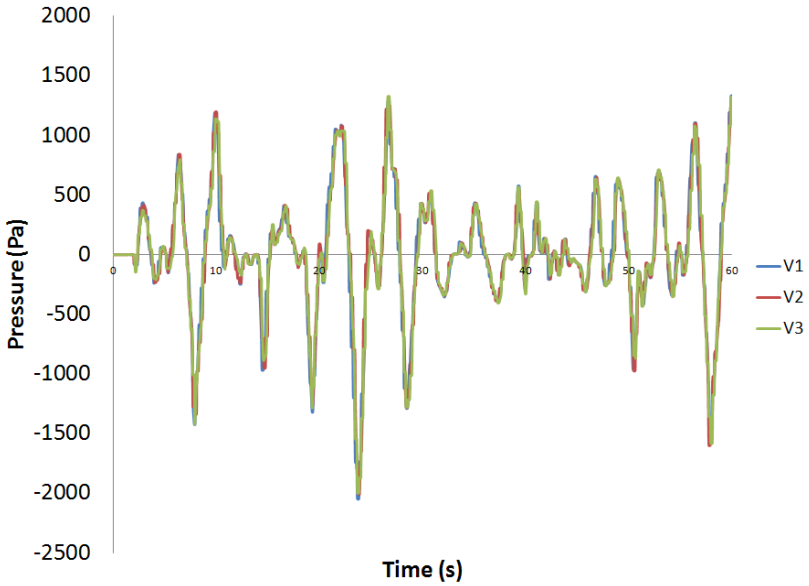

Figure 6.15: Pressure plot for a scaled Pierson-Moskowitz derived irregular wave with a wind speed of 15.4 m/s

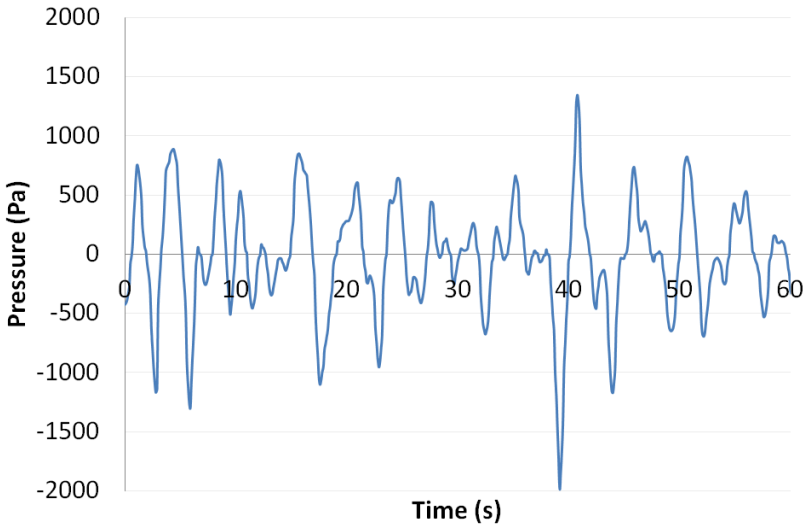

Figure 6.16: Pressure plot for a scaled Bretschneider derived irregular wave with a significant wave height of 4.5m and and a peak period of 12 s

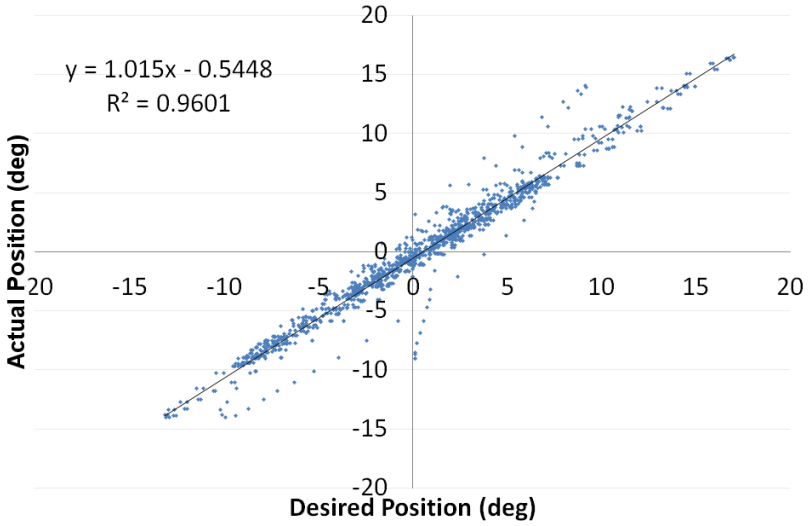

Figure 6.17: Accuracy for a Pierson-Moskowitz wave

varies in an approximately sinusoidal way, the flow coefficient is also varying. It is known that the turbine CFD results are more likely to be accurate on design conditions, i.e. the point of peak efficiency (Denton 2010). As a result, there are additional model matching challenges away from the point of peak efficiency.

Another proposed method of validating the CFD results would be to vary the turbine speed in accordance with the pressure fluctuations and keep the flow coefficient constant. This would result, in reality, with a square wave as the pressure drop across the turbine changes direction every half wave. Maintaining a constant turbine flow coefficient can be achieved by using the control strategy of constant flow coefficient. Multiple tests could be run at various flow coefficients and pressure drops over the full bandwidth of the operating conditions. In order to achieve the constant flow coefficient, additional communication would need to be set up between the Supervisory Control And Data Acquisition (SCADA) system and the Converteam Inverter PLC. This additional communication could be achieved by transmitting the axial velocity from the SCADA to the Converteam PLC over either Ethernet or via an analogue output channel. The PLC used to communicate to the MV3000 Grid and Machine side inverters is an Automatic PC which is connected to a network

hub with spare channels. The protocol employed is Modbus TCP/IP. The software to process the new communication and control the speed to keep constant flow coefficient is a Converteam Tool called P80i.

A third method for validating the CFD results would be to allow the turbine speed to free-wheel. Care is required to ensure that the system does not exceed the over-speed rating of the generator. The variation of the flow coefficient under such conditions is shown in Figure 6.18. This method is not suitable for testing the higher flow coefficients.

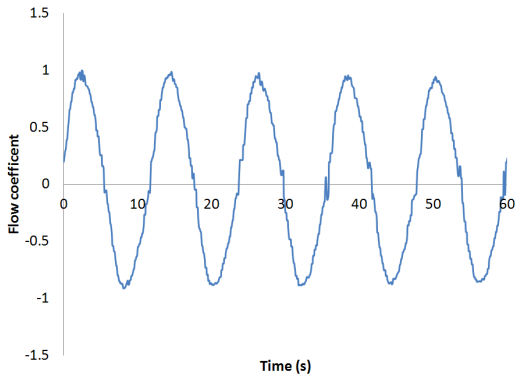

Figure 6.18: Flow coefficient for turbine free-wheeling under a monochromatic wave (wave 17) which has a period of 12s, an amplitude of 114deg and a design flow rate of 1.2m^3/s subject to turbine running conditions

There is little benefit in attempting to achieving a constant flow coefficient and it would be difficult to achieve when the flow changes direction and hence the fixed speed method was selected.

The first test of the CFD results were conducted for a range of monochromatic waves (1, 3, 4, 17 and 19). The monochromatic wave was set-up and then the speed was changed every 60s using the inverter to drive the turbine between 30% and 90% rated speed, see Figure 6.19. Tests were not conducted at lower speeds due to low Reynolds number scaling effects becoming more prevalent at Reynolds numbers less than $2x10^5$ as discussed by Herring (2007). Due to the limited maximum pressure that can be created by the PWG, the higher non-dimensional flow rates and pressure

drops can only be tested by reducing the turbine speed which is in direct conflict with having a high Reynolds number. It can be seen in Figure 6.20a and 6.21a that agreement with the numerical CFD results is very good. The CFD numerical results were obtained by Banks (2009), Natanzi (2010a), Tarver (2013) and the author of this thesis. The instantaneous errors are shown in Figure 6.20b and 6.21b. The standard deviation of the error was calculated as 0.041 Pa.

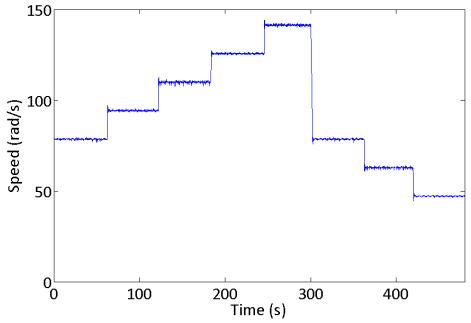

Figure 6.19: Speed for numerical simulation tests

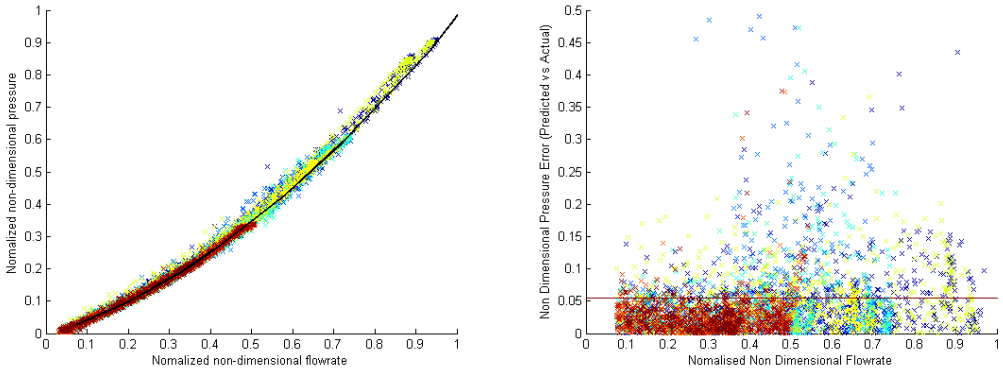

Figure 6.20: Test results and numerical simulation results for non-dimensional pressure flow rate relationship using monochromatic waves

6.4 Simulation Parameters

Simulation of the PWG test rig has been achieved with slight modifications to the analytical model developed in Chapter 3. The internal air chamber wave height, z_2, instead of being a state variable will be forced to follow the applied wave height, η_f.

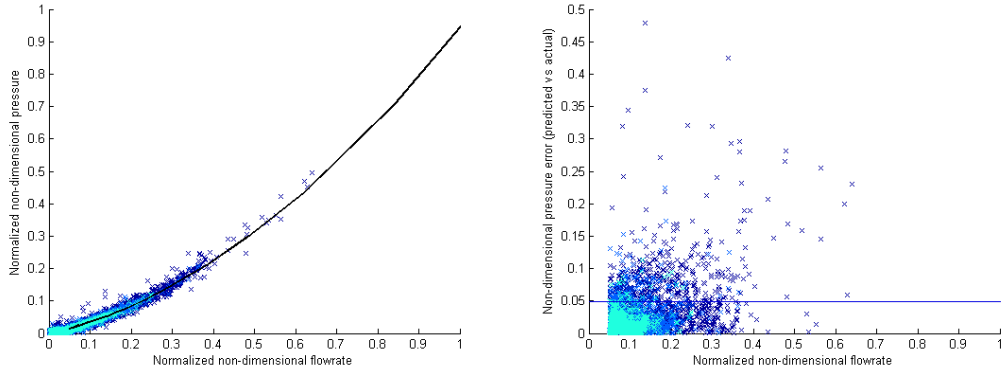

Figure 6.21: Test results and numerical simulation results for non-dimensional pressure flow rate relationship using polychromatic waves

For this work η_f is directly related to the spectra, however future work could apply a transfer function to this input to account for the dynamics of an OWC chamber. The parameters for the test-facility model can be seen in Table 6.2.

The PWG waves are defined in degrees swept rather in meters and so the similarity is realized by ensuring the same volume is shifted using

$$(h_{a0} + z_1 - z_2)A_s \quad = \quad z_p \frac{V_p}{360} \tag{6.15}$$

where z_p is the paddle position in degrees, V_p is the volume within the PWG chamber.

The initial value of system variables are required during the numerical simulation set-up. The initial mass within the air chamber is

$$m_c|_{t=0} = \frac{p_{atm} V_c|_{t=0}}{R_a T_{atm}} \tag{6.16}$$

The mean sea water level is taken at the mid-point paddle movement and is equal to

$$z_p|_{t=0} = 0 \tag{6.17}$$

Parameter	Value (units)	Description
n_p	4	number of generator poles
f_e	50 Hz	frequency
v_{abcs}	415 V	voltage line-to-line
P_{nom}	37 kW	power
R_s	65.5 mΩ	generator stator resistance
R_r	62.4 mΩ	generator rotor resistance
X_m	227 Ω	generator magnetizing reactance
L_{ls}	0.667 mH	generator stator leakage inductance
L_{lr}	1.01 mH	generator rotor impedance
L_m	21.0 mH	generator magnetizing inductance
D_t	0.263 m	turbine rotor tip diameter
J_d	1.47 kgm^2	drive train moment of inertia
A_s	3.76 m^2	water column area
h_d	0 m	water column draft
h_a	3.11 m	air column draft
h_w	35 m	water depth

Table 6.2: Simulation parameter settings

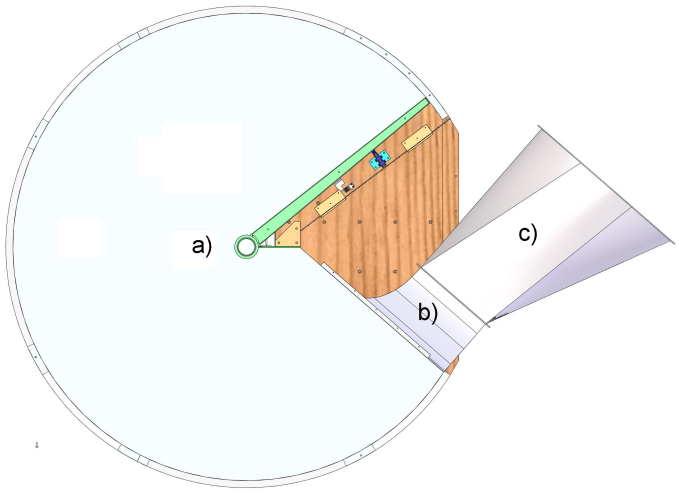

Figure 6.22: Plan view of PWG (Dresser-Rand Company Ltd 2014)

Component	Volume (m^3)
PWG swept volume	16.02
PWG non-swept volume	0.60
McKenzie flare	0.48
Square to round ducting	1.29
Main ducting	1.33
Total	**19.7**
PWG at SWL	8.01
PWG non-swept volume	0.60
McKenzie flare	0.48
Square to round ducting	1.29
Main ducting	1.33
Total	**11.7**

Table 6.3: Air chamber volumes

The enclosed volume within the PWG has changed from that which was reported by Herring (2007) as part of the test facility update conducted in 2011. The physical constraints of the PWG limit the maximum pressure drop that can be generated across the turbine. In a real OWC the water level can, in theory, rise to meet the ceiling of the chamber reducing the air volume to zero. However within the PWG this has not been possible and the minimum volume of the PWG, marked "a" in Figure 6.22, when the paddle is at its maximum position contains a residual volume. In addition to the other components that create the volume of the air chamber which include the McKenzie flare (marked "b" in Figure 6.22), the square to round section (marked "c" in Figure 6.22), and the volume within the ducting prior to the guide vanes, are not shown. The volumes are given in Table 6.3. The volume of the air chamber at mid-sea level is therefore 11.7 m^3.

In order to use the dynamic model to simulate the test rig, the wave height needs to be decoupled from the pressure as the control strategy within the PWG inverter compensates for any forces applied by the wave on the paddle.

6.5 Summary of Contribution

The implementation of polychromatic waves using the PWG rig to test bidirectional turbines was successfully demonstrated. It is thought to be the first test facility with this capability. Pressure waves corresponding to a given free surface elevation can be simulated. The accuracy of the position of the paddle can be controlled to within 2% accuracy and to a high level of repeatability. The method uses speed control rather than position control for the reference due to firmware limitations. However integration errors are minimized by using the appropriate ramp rates for each wave frequency component. This test facility will enable the testing of control strategies as well as the investigation of the performance of self regulating OWC turbines in realistic operating conditions. For the control schemes, this type of testing prior to deployment in the ocean will increase the confidence in and reliability of the strategies employed in maximizing power while seeking to adhere to the quality of grid supply. In addition, the test facility will continue to be used to validate a range of theoretical models.

Chapter 7

Conclusions and Further Work

7.1 Conclusion

The main contributions of this work were

- A generalization of the port-Hamiltonian framework for cases where the potential energy is dependent upon one or more of the momentum variables
- A further development in the field of the port-Hamiltonian framework whereby a change in reference frame allows the modeling of flow sources
- Development of a beyond state-of-the-art port-Hamiltonian model of the complete OWC wave-to-wire analytical model utilizing the aforementioned modifications to the port-Hamiltonian framework
- Development of a power-based control strategy for an energy storage system using a fixed inertia flywheel.
- The development of a power-based control strategy for damping control of an Oscillating Water Column (OWC), using the port-Hamiltonian OWC system model

- An upgrade to the Cranfield University test facility to be the first in the world with bi-directional polychromatic wave capability

- Using the upgraded Cranfield facility, turbine Computational Fluid Dynamics (CFD) results were validated under bi-directional polychromatic flow conditions for the first time

The first of the advances in the port-Hamiltonian framework described in this work is the ability to account for systems where the potential energy is a function of momentum. This new development was arrived at by the process of mathematical inspection, with a series of model-based tests used to prove its validity for the OWC system. By expanding the applicability of port-Hamiltonian modeling the related energy shaping control approaches can also be expanded to new systems. As a consequence, this development is relevant to all fields of study and is not limited to OWCs specifically, or renewable energy in general.

A further new development in the field of the port-Hamiltonian modeling framework is also described. The same approach of mathematical inspection, followed by model-based tests of OWC systems was used to develop a method for modeling systems with flow rather than effort sources. The applicability of this new approach to systems with capacitive (or spring) components and no inductance (or inertial) component is also described. The port-Hamiltonian method has not previously been suitable for modeling systems with these characteristics. The validity of this approach was first demonstrated by modeling electrical systems, including an Resistance Impedance Capacitance (RLC) circuit with a current source, before being applied to a closed pneumatic air volume. As a result of this work, the applicability of the port-Hamiltonian framework has been further expanded.

In support of developing the first energy shaping control strategy (specifically, Interconnection and Damping Assignment (IDA) Passivity Based Control (PBC)) for a

wave energy device, the first step was to develop the first port-Hamiltonian wave-to-wire OWC model. The benefits of employing the port-Hamiltonian framework are the ease of identifying the system equations from the total energy equation, and the ease of connecting multiple subsystems. This system model was derived by developing individual models of each subsystem (hydrodynamic, pneumatic, mechanical and electrical). The port-Hamiltonian multi-pole generator model mandated the use of the updated port-Hamiltonian framework for the scenario when the potential energy is a function of momentum, whilst the pneumatic model required the update to the port-Hamiltonian framework for flow sources. The wave-to-wire OWC port-Hamiltonian model is of particular importance since it has applicability to OWC developers in general, and is not specific to the development of energy based control strategies.

Completion of the development of the OWC wave-to-wire model was followed by investigations into a number of potential control strategies. The first of these was to apply an IDA PBC strategy to control the energy flow into and out of a fixed inertia flywheel energy storage system. The purpose of this study was to demonstrate a means of smoothing the system power output to the grid, thereby removing or reducing the fluctuations in current. This was a development of the work by Batlle et al. (2007) in which a flywheel, connected to a single pole pair generator, was trickle fed prior to delivering a short-duration spike of power for a high energy application. The development work detailed herein includes the significant update to the electrical subsystem model to enable the derivation of the system equations in the port-Hamiltonian framework for multiple pole machines. This electrical system model is applicable for both Squirrel Cage Induction Generator (SCIG) and Doubly Fed Induction Generator (DFIG) designs. Simulation tests conducted on the DFIG and SCIG Fixed Inertia Flywheel (FIF) energy storage systems showed that the larger speed range of the SCIG, in conjunction with the FIF, facilitated a superior

power smoothing effect. The developments arising from this work are applicable to the whole renewable energy system where short-term energy storage and power smoothing are of great importance.

One of the critical areas of investigation to improve the economic viability of OWCs is to increase the overall system-level efficiency. In this work the author proposes that a PBC strategy optimized with a cost function is one potential means of achieving this goal. As a precursor to employing a fully optimized PBC strategy, work has been conducted using the port-Hamiltonian wave-to-wire model to develop a strategy that uses the OWC turbine to control the damping of the chamber. In this way, the system is operated at the peak efficiency point of the OWC chamber. The work herein has shown that controlling an OWC with a PBC is possible.

The practical aspects of this work centered on the OWC test facility at Cranfield University, one of a number of such test facilities at various institutions around the world. Some of these facilities generate unidirectional flows, whilst others generate bidirectional flows. A literature review concluded that all extant bidirectional test facilities were only capable of producing monochromatic sine waves. In the course of the developments described in this work, the Cranfield University test facility has been updated to produce polychromatic waves, and is the first test facility in the world with this capability. The free surface elevation associated with the test facility paddle is derived from a given sea spectra. The importance of developing the capability for polychromatic waves is that such waves gives rise to larger instantaneous accelerations and velocities of the air in chamber. Furthermore, the standard deviation of the flow either side of the mean is greater than for a monochromatic case. As a result of this, unsteady flow is more likely to occur with polychromatic waves than monochromatic waves. The Cranfield test facility now enables the testing of control strategies and identifies turbine characteristics under vastly more realistic flow regimes than those of other known facilities.

Following its upgrade, the polychromatic test facility was used to validate previous CFD results for the turbine characteristics of a small scale prototype of the HydroAir impulse turbine. The turbine was tested under a range of mono- and polychromatic conditions, with the experimental data showing good correlation with the CFD numerical results. This was important as it provides additional credibility to the assumption that turbine characteristics can be derived from steady-state CFD simulations. In addition, the test facility can be used to test alternative bidirectional turbines and (with appropriate ducting and valves) unidirectional turbines to facilitate back-to-back comparisons.

In short, this work has successfully proved that a system model can be developed for an OWC using energy based methods such as the port-Hamiltonian framework. It has also demonstrated that energy- and power-based control strategies can be applied to an OWC system, by implementing one such strategy (IDA-PBC), for a fixed inertia flywheel energy storage system and for damping control of an OWC chamber. This work could be developed further to employ cost functions for energy optimization in both the aforementioned applications. Above all, however, this work has the potential to be applied to many renewable power generation systems where the smoothing of short-term fluctuations in energy input from the environment remains a significant technical challenge.

7.2 Further Work

1. The port-Hamiltonian framework has been extended for systems where the potential energy is a function of one or more velocities in the system. This framework has been tested, within this body of work, for a selection of systems through back-to-back simulations and also by comparing the output state equations for known systems. However, a generalized proof would be benefi-

cial.

2. In a similar way, the proposed modification to the port-Hamiltonian framework to extend its scope for flow sources rather than effort sources has been tested through Simulink simulations, and comparisons of state equations for known systems. This development would also benefit from a generalized proof.

3. It is recommended that future work on the port-Hamiltonian wave-to-wire OWC model focus on further validation of the individual subsystem models. It is intended that the turbine and pneumatic subsystems could be validated using the polychromatic test facility. The generator subsystem could also be experimentally validated at the test facility though additional current and voltage transformers would be required and connected to a fast data acquisition system in order to capture any transient behavior. If it was deemed necessary the subsystems would then need to be further improved for example the generator model could take into account for parameters affected by temperature. Experimental validation of the OWC subsystem would require either small-scale testing in a wave tank facility or preferably a prototype installation in the sea.

4. Further research into a power based control strategy should aim to test the control strategy on a prototype SCIG FIF system. A variety of damping coefficients could be investigated and the associated speed of response of the system to the control reference.

5. Two avenues of future development are recommended for the power based control strategy of the damping control of an OWC. The first avenue would be to test the damping control strategy described in this work at the Cranfield polychromatic wave test facility, and subsequently on an OWC prototype device. As part of the first avenue of work, an analytical solution rather than a numerical solution to the fixed point equations should be found to decrease

the simulation time and facilitate the damping control strategy running in real-time. The second avenue should focus on developing the PBC strategy to employ a cost function to optimize the power captured for the full wave-to-wire system, rather than optimizing for a particular subsystem such as the OWC chamber.

6. Further development of the Pneumatic Wave Generator (PWG) test facility at Cranfield University should aim to cancel the dynamics of the PWG and add the dynamics of specific OWCs. The transfer function of the input-output relationship of the OWC and PWG are defined as G_{owc} and G_{pwg}. In order to cancel the effects of the PWG dynamics and include the effects of the OWC the desired motion of the paddle needs to be adjusted using the following equation

$$u_{pwg} = G_{pwg}^{-1} G_{owc} u_{owc} \tag{7.1}$$

7. Following on from the proposed developments of item 6, future tests at the PWG facility at Cranfield University should aim to verify the pressure and flow-rate relationship for the HydroAir turbine against the CFD derived turbine characteristic curves. Further testing should verify the pressure and torque characteristic. This test facility could also be used to conduct further tests, potentially on other bidirectional turbines and (with appropriate ducting and valves) unidirectional turbines. This would enable back-to-back comparisons.

References

Ahmed, T. & Zobaa, A. F. (2009), Offshore power conditioning system connecting arrays of wave energy converters to the electric power grid, in '8th International Conference on Advances in Power System Control, Operation and Management', Hong Kong, China.

Alcorn, R. & Finnigan, T. (2004), Control strategy development for an inverter controlled wave energy plant, in 'International Conference on Renewable Energies and Power Quality (ICREPQ'04)', Barcelona, Spain.

Alcorn, R. G. & Beattie, W. C. (2001), Power quality assessment from a wave-power station, in 'CIRED 16th International Conference and Exhibition on Electricity-Distribution, 2001 Part I: Contributions', CIRED, Amsterdam, The Netherlands.

Amundarain, M., Alberdi, M., Garrido, A. & Garrido, I. (2010), Control strategies for OWC wave power plants, in 'American Control Conference (ACC)', Baltimore, Maryland, USA, p. 4319.

Amundarain, M., Alberdi, M., Garrido, A., Garrido, I. & Maseda, J. (2010), 'Wave energy plants: Control strategies for avoiding the stalling behaviour in the Wells turbine', Renewable Energy **35**(12), 2639–2648.

Amundarain, M., Alberdi, M., Garrido, A. J. & Garrido, I. (2011), 'Neural rotational speed control for wave energy converters', International Journal of Control **84**(1), 293–309.

Anand, S., Jayashankar, V., Nagata, S., Toyota, K., Takao, M. & Setoguchi, T. (2007), Turbines for wave energy plants, in 'Proceedings of the 8th International Symposium on Experimental and Computational Aerothermodynamics of Internal Flows', Lyon, France.

Banerjee, S. (2005), Dynamics for Engineers, John Wiley & Sons, Chichester, England.

Banks, K. (2009), Optimisation of bidirectional impulse turbines for wave power generation, PhD thesis, Cranfield University, School of Engineering, Cranfield, UK.

Batlle, C., Doria-Cerezo, A. & Fossas, E. (2007), 'Modeling, simulation and control of a doubly-fed induction machine', Proceedings in Applied Mathematics and Mechanics **7**(1), 30300033030004.

Baudry, V., Babarit, A. & Clément, A. (2013), An overview of analytical, numerical and experimental methods for modelling oscillating water columns, in 'Proceedings of the Tenth European Wave Power Conference', Aalborg, Denmark.

Beattie, W., Peters, G. & Alcorn, R. G. (1995), Strategies for the control of a wave power station with a semiconuctor converters, in 'Proceedings of the Second European Wave Power Conference', Lisbon, Portugal, pp. 273–380.

Bhinder, M. A., Babarit, A., Gentaz, L. & Ferrant, P. (2011), Assessment of viscous damping via 3D-CFD modelling of a floating wave energy device, in 'Proceedings of the Ninth European Wave Power Conference', Southampton, UK.

Borgarino, B., Babarit, A. & Ferrant, P. (2011), Impact of the separating distance between interacting wave energy converters on the overall energy extraction of an array, in 'Proceedings of the 9th European Wave and Tidal Energy Conference', EWTEC, Southampton, UK.

Brekken, T. K. A., von Jouanne, A. & Han, H. Y. (2009), Ocean wave energy overview and research at Oregon state university, in 'IEEE Conference on Power Electronics and Machines in Wind Applications', Lincoln, NE, USA.

Brito-Melo, A., Gato, L. M. C. & Sarmento, A. J. N. A. (2002), 'Analysis of Wells turbine design parameters by numerical simulation of the OWC performance', Ocean Engineering **29**(12), 1463–1477.

Ceballos, S., Rea, J., Lopez, I., Pou, J., Robles, E. & O'Sullivan, D. (2013), 'Efficiency optimization in low inertia Wells turbine-oscillating water column devices', IEEE Transactions on Energy Conversions **28**(3), 553–564.

Chell Instruments Ltd (2010), CANdaq III Pressure Scanner Acquisition System Installation and Operating Manual, Chell Instruments Ltd.
URL: *http://www.chell.co.uk*

Control Techniques - Emerson Group (2015), 'Unidrive sp modular - power system flexibility brochure'.
URL: *http://www.emersonindustrial.com/en-EN/controltechniques/products/acdrives/unidrivesp*

Control Techniques Ltd (2009a), Variable speed drives. a guide to electromagnetic compability (EMC), Technical Report P.N 0704-0001-02, Emerson Industrial Automation.
URL: *http://www.emersonindustrial.com*

Control Techniques Ltd (2009b), Variable speed drives. a guide to supply harmonics and other low-frequency disturbances, Technical Report P.N. 0704-0002-02, Emerson Industrial Automation.
URL: *http://www.emersonindustrial.com*

Cruz, J., ed. (2008), Ocean Wave Energy: Current Status and Future Prespectives (Green Energy and Technology), Springer, London.

Cummins, W. E. (1962), The impulse response function and ship motions, Technical report, Hydromechanics Laboratory.

Curran, R. & Folley, M. (2008), Ocean Wave Energy, 1st edn, Spring-Verlag, Berlin Heidelberg, Germany, chapter Power Take-Off System, pp. 189–285.

Curran, R., Stewart, T. P. & Whittaker, T. J. T. (1997), Design synthesis of oscillating water column wave energy converters: performance matching, in 'Proceedings of the Institute of Mechanical Engineers Part A Journal of Power and Energy'.

De Miguel, B. (2010), Investigation of OWC Buoys for Offshore Power Generation, PhD thesis, Cranfield University, School of Engineering, Cranfield, Engineering.

Delhommeau, G., Babarit, A., Singh, J., Guével, P. & Daubisse, J. C. (2014), 'Nemoh - BEM open source code'.
URL: *http://lheea.ec-nantes.fr/doku.php/emo/nemoh/start*

Denton, J. D. (2010), Some limitations of turbomachinery CFD, in 'Proceedings of the ASME Turbo Expo 2010: Power for Land, Sea and Air', Glasgow, UK.

Det Norske Veritas (2011), Modelling and analysis of marine operations recommended practice dnv-rp-h103, Technical report, DNV.

Dhanasekaran, T. & Govardhan, M. (2005), 'Computational analysis of performance and flow investigation on Wells turbine for wave energy conversion', Renewable Energy **30**, 2129–2147.

Dòria-Cerezo, A. (2006), Modelling, Simulation and Control of a Doubly-Fed Induction Machine Controlled By a Back-To-Back Converter, PhD thesis, Universitat Politécnica de Catalunya, Spain.

Dorrell, D. G., Hsieh, M.-F. & Lin, C.-C. (2010a), 'A multichamber oscillating water column using cascaded savonius turbines', IEEE Transactions on Industry Applications **46**(6), 2372–2380.

Dorrell, D. G., Hsieh, M.-F. & Lin, C.-C. (2010b), 'A small segmented oscillating water column using a savonius rotor turbine', IEEE Transactions on Industry Applications **46**(5), 2080–2088.

Dresser-Rand Company Ltd (2014), 'private communication'.

Dresser-Rand Company Ltd (2015), 'Hydroair - variable radius turbine brochure'.
URL: *http://www.dresser-rand.co.uk/products/hydroair/*

Drury, B. (2009), The Control Techniques Drives and Controls Handbook 2nd Edition, The Institution of Engineering and Technology, Stevenage, UK.

Dugas, P. A. (2011), 'Variable inertia flywheel, US Pat. 2011277587A1'.

Duindam, V., Macchelli, A., Stramigioli, S. & Bruyninckx, H., eds (2009), Modeling and Control of Complex Physical Systems: The Port-Hamiltonian Approach, Springer-Verlag, Berlin, Germany.

Earth Techling (2010), 'Clean 'energy islands' planned for australian coast - June 5th 2012'.
URL: *http://earthtechling.com/2012/06/clean-energy-islands-planned-for-australian-coast/*

EMEC Ltd (2009), 'Wave devices'.
URL: *http://www.emec.org.uk*

Enferad, E. & Nazarpour, D. (2013), Implementing double fed induction generator for converting ocean wave power to electrical, in 'Proceedings of the 4th Power Electronics, Drive Systems and Technologies Conference', Tehran, Iran.

Evans, D. V. (1976), 'A theory for wave-power absorption by oscillating bodies', Journal of Fluid Mechanics **77**(1), 1–25.

Falcão, A. F. d. O. (2002), 'Control of an oscillating-water-column wave power plant for maximum energy production', Applied Ocean Research **24**(2), 73–82.

Falcão, A. F. d. O. (2010), 'Wave energy utilization: A review of the technologies', Renewable and Sustainable Reviews **14**(3), 899–918.

Falcão, A. F. d. O. & Justino, P. A. P. (1999), 'OWC wave energy devices with air flow control', Ocean Engineering **26**(12), 1275–1295.

Falcão, A. F. de O., G. L. M. C. & Nunes, E. P. A. S. (2013a), 'A novel radial self-rectifying air turbine for use in wave energy converters', Renewable Energy **50**, 289–298.

Falcão, A. F. de O., G. L. M. C. & Nunes, E. P. A. S. (2013b), 'A novel radial self-rectifying air turbine for use in wave energy converters. part 2. results from model testing', Renewable Energy **50**, 289–298.

Falnes, J. (1995), 'On non-causal impulse response functions related to propagating water waves', Applied Ocean Research **17**(6), 379–389.

Fantini, E. (2007), Free surface flow CFD simulation for developing oscillating water column technology, Master's thesis, Cranfield University, School of Engineering, Cranfield, UK.

Farman, J. R. & Hall, R. (2012), 'Power take-off optimization - internal Dresser-Rand communication'.

Farman, J. R., Teixeira, J., Whidborne, J. F., Mba, D. & Natanzi, S. (2013), Development of polychromatic irregular waves for testing owc bidirectional turbines at a land-based test facility, in 'Proceedings of the Tenth European Wave Power Conference', Aalborg, Denmark.

Finnigan, T. D. & Auld, D. (2003), Model testing of a variable-pitch aerodynamic turbine, in 'Proceedings of the Thirteenth International Offshore an Polar Engineering Conference', The International Society of Offshore and Polar Engineers, Honolulu, Hawaii, USA, p. 357.

Folley, M. & Whittaker, T. J. (2002), Identification of non-linear flow characteristics of the LIMPET shoreline OWC, in 'Proceedings of The Twelfth International Offshore and Polar Engineering Conference', The International Society of Offshore and Polar Engineers (ISOPE), Kitakyushu, Japan.

Freeman, C., Herring, S. & Banks, K. (2008), 'Impulse turbine design, UK Pat. GB2440344A'.

Gervelas, R., Trarieux, T. & Patel, M. (2011), 'A time-domain simulator for an oscillating water column in irregular waves at model scale', Ocean Engineering **38**(8-9), 1007–1013.

Gomes, R. P. F., Henriques, J. C. C., Gato, L. M. C. & Falcão, A. F. d. O. (2011), Design of a floating oscillating water column for wave energy conversion, in 'Proceedings of the 9th European Wave and Tidal Energy Conference', EWTEC, Southampton, UK.

Gomes, R. P. F., Henriques, L. M. C., Gato, L. M. C. & Falcão, A. F. d. O. (2012), 'Hydrodynamic optimization of an axisymmetric floating oscillating water column for wave energy conversion', Renewable Energy **44**, 328–339.

Gonzalez, G., Shahpar, S. & Castro, C. (2013), Non-linear dynamic modelling of oscillating water column power plants, in 'Proceedings of the Tenth European Wave Power Conference', Aalborg, Denmark.

Guerrini, F. (2009), Numerical analysis of OWC devices for offshore applications, Master's thesis, Cranfield University, School of Engineering, Cranfield, UK.

Halcrow Group Ltd (2010a), Wave hub wave monitoring project, interim report number 1, june 2009, Technical Report Doc No 2 Rev 1, South West of England Regional Development Agency.

URL: *http://www.wavehub.co.uk/information-for-developers/*

Halcrow Group Ltd (2010b), Wave hub wave monitoring project, interim report number 2, nov 2009, Technical Report Doc No 2 Rev 1, South West of England Regional Development Agency.
URL: *http://www.wavehub.co.uk/information-for-developers/*

Halcrow Group Ltd (2010c), Wave hub wave monitoring project, interim report number 3, feb 2010, Technical Report Doc No 1 Rev 0, South West of England Regional Development Agency (SW RDA).
URL: *http://www.wavehub.co.uk/information-for-developers/*

Heath, T. V. (2007), The development of a turbo-generation system for application in OWC breakwaters, in 'Proceedings of the 7th European Wave and Tidal Energy Conference', Porto, Portugal.

Herring, S. (2007), Design and evaluation of turbines for use in OWC power plants, PhD thesis, Cranfield University, School of Engineering, Cranfield, UK.

Herring, S. & Laird, G. (2007), A new test facility for evaluating turbines for use in OWC power plants, in 'Proceedings of the 7th European Wave and Tidal Energy Conference', Porto, Portugal.

Hodgins, N. (2010), High speed electrical power takeoff for oscillating water columns, PhD thesis, University of Edinburgh, Edinburgh, UK.

Holthuijsen, L. H. (2007), Waves in Oceanic and Coastal Waters, Cambridge University Press, Cambridge, UK.

Hoskin, R. E., Count, B. M., Nichols, N. K. & Nicol, D. A. C. (1986), Hydrodynamics of Ocean Wave Energy Utilization., Berlin, Springer, chapter Phase control for the oscillating water column, pp. 257–268.

Iturrioz, A., Guanche, R., Armesto, J. A., Vidal, C. & Losada, I. J. (2013), Experimental and numerical development of a floating multi-chamber owc device, in

'Proceedings of the 10th European Wave and Tidal Energy Conference', EWTEC, Aalborg, Denmark.

Jeltsema, D. & Scherpen, J. M. (2009), 'Multidomain modeling of nonlinear networks and systems', IEEE Control Systems Magazine **29**(4), 28–59.

Johnson, F. & Dai, Y. M. (2003), Multi resonant converter wave energy device: proof of concept, Master's thesis, Department of Mechanical and Marine Engineering, University of Plymouth, UK.

Justino, P. A. P. & Falcão, A. F. d. O. (1995), Control simulation of an OWC wave power plant, in G. Elliot & K. Diamantaras, eds, 'The 2nd European Wave Power Conference', Lison, Portugal, p. 268.

Justino, P. A. P. & Falcão, A. F. d. O. (1999), 'Rotational speed control of an OWC wave power plant', Journal of Offshore Mechanics and Arctic Engineering **121**(2), 65–70.

Kelly, T., Dooley, T., Campbell, J. & Ringwood, J. (2013), An overview of analytical, numerical and experimental methods for modelling oscillating water columns, in 'Proceedings of the Tenth European Wave Power Conference', Aalborg, Denmark.

Krause, P. C. (1986), Analysis of Electric Machinery, McGraw-Hill, New York, USA.

Krogstad, H. E. & Arntsen, O. A. (2000), Linear Wave Theory, Norwegian University of Science and Technology, Trondheim, Norway.

Kurniawan, A., Hals, J. & Moan, T. (2011), Modelling and simulation of a floating oscillating water column, in 'Proceedings of the ASME 2011 30th International Conference on Ocean, Offshore and Arctic Engineering', Rotterdam, The Netherlands.

Liu, Z., Hyun, B.-S., Hong, K.-Y. & Lee, Y.-Y. (2009), Investigation on integrated system of chamber and turbine for OWC wave energy convertor, in 'Proceedings of

the Nineteenth (2009) International Offshore and Polar Engineering Conference', Osaka, Japan.

Liu, Z., Jin, J., Hyun, B.-S., Shi, H., Hong, K. & Ma, Z. (2011), Transient calculation of impulse turbine for oscillating water column wave energy convertor, in 'Proceedings of the 9th European Wave and Tidal Energy Conference', EWTEC, Southampton, UK.

Lopes, M. F. P., Hals, J., Gomes, R. P. F., Moan, T., Gato, L. M. C. & Falcão, A. F. d. O. (2009), 'Experimental and numerical investigation of non-predictive phase-control strategies for a point-absorbing wave energy converter', Ocean Engineering **36**(5), 386–402.

Mackay, E. (2011), Modelling and description of omnidirectional wave spectra, in 'Proceedings of the 9th European Wave and Tidal Energy Conference', EWTEC, Southampton, UK.

Maeda, H., Setoguchi, T., Takao, M., Sakurada, K., Kim, T. H. & Kaneko, K. (2001), 'Comparative study of turbines for wave energy conversion', Journal of Thermal Science **10**(1), 27–31.

Maeda, H., Takao, M., Setoguchi, T., Kaneko, K. & Kim, T. H. (2001), Impulse turbine for wave power conversion with air flow rectification system, in 'Proceedings of the Eleventh International Offshore and Polar Engineering Conference', Stavanger, Norway, pp. 646–652.

Mala, K., Jayaraj, J., Jayashankar, V., Muruganandam, T. M., Santhakumar, S., Ravindran, M., Takao, M., Setoguchi, T., Toyota, K. & Nagata, S. (2011), 'A twin unidirectional impulse turbine topology for OWC based wave energy plants - experimental validation and scaling', Renewable Energy **36**, 307 – 314.

Masuda, Y., Kuboki, T., Thakker, A., Lewis, T., Liang, X. & Sun, P. (2002),

Prospect of economical wave power electric generator by the terminator backward bent duct buoy (bbdb), in 'Proceedings of the Twelfth (2002) International Offshore and Polar Engineering Conference', IEEE, New York, NY, USA, Kitakyushu, Japan, pp. 607–613.

Mathworks (2011), Asynchronous machine - model the dynamics of three-phase asynchronous machine - r2011a documentation - sim power systems, Technical report, Mathworks.
URL: *available at http://www.mathworks.com*

McCormick, M. E. (1981a), 'Counter-rotating wave energy conversion turbine, US Pat. US4271668'.

McCormick, M. E. (1981b), Ocean Wave Energy Conversion, Wiley, New York, USA.

McCormick, M. E. (2010), Ocean Engineering Mechanics: with Applications, Cambridge University Press, Cambridge.

McCormick, M. E., Rehak, J. G. & Williams, B. D. (1992), An experimental study of a bidirectional radial turbine for pneumatic wave energy conversion, in 'Proceedings of OCEANs '92 'Mastering the Oceans Through Technology", Vol. 2, Newport, Rhode Island, USA, p. 866.

Murphy, G. (2012), 'An energy storage system, World Pat. 2012127194A2'.

Murray, D. B., Hayes, J. G., O'Sullivan, D. L. & Egan, M. G. (2012), 'Supercapacitor testing for power smoothing in a variable speed offshore wave energy converter', IEEE Journal of Oceanic Engineering **37**(2), 301–308.

Natanzi, S. (2010a), Design and Investigation of Turbines for use in Oscillating Water Columns Power Plants, PhD thesis, Cranfield University, School of Engineering, Cranfield, UK.

Natanzi, S. (2010b), Internal communication - positioning of pressure taps, Technical report, Dresser-Rand. unpublished.

Natanzi, S., Teixeira, J. A. & Laird, G. (2011), A novel high-efficiency impulse turbine for use in oscillating water column devices, in 'Proceedings of the 9th European Wave and Tidal Energy Conference', EWTEC, Southampton, UK.

Neumann, F., Brito-Melo, A., Didier, E. & Sarmento, A. J. N. A. (2007), Pico OWC recovery project: Recent activities and performance data, in 'Proceedings of the 7th European Wave and Tidal Energy Conference', EWTEC, Porto, Portugal.

Nunes, G., Valério, D., Beirão, P. & Sá da Costa, J. (2011), 'Modelling and control of a wave energy converter', Renewable Energy **36**(7), 1913–1921.

Ocean Energy Ltd (2011), 'Ocean Energy a world of power'.
URL: *http://www.oceanenergy.ie/index.html*

Oceanlinx Ltd (2010a), 'MK3PC performs better than expected', website press release. accessed 17th July 2011.
URL: *http://www.oceanlinx.com/latest-news/mk3pc-performs-better-than-expected*

Oceanlinx Ltd (2010b), 'Oceanlinx unveils greenWAVE and blueWAVE', website press release. accessed 15th August 2011.
URL: *http://www.oceanlinx.com/latest-news/oceanlinx-unveils-greenwave-and-bluewave*

Oceanlinx Ltd (2011a), 'Detailed testing confirms the commercian viability of greenWAVE', website press release. accessed 15th August 2011.
URL: *http://www.oceanlinx.com/latest-news/detailed-testing-confirms-the-commercial-viability-of-greenwave*

Oceanlinx Ltd (2011b), 'Products'. accessed 15th Aug 2011.
URL: *http://www.oceanlinx.com/*

Oretga, R., van der Schaft, A., Maschke, B. & Escobar, G. (2002), 'Interconnection and damping assignment passivity based control of port-controlled Hamiltonian systems', Automatica **38**, 585–596.

O'Sullivan, D., Griffiths, J., Egan, M. G. & Lewis, A. W. (2011), 'Development of a an electrical power take off system for a sea-test scaled offshore wave energy device', Renewable Energy (36), 1236 – 1244.

O'Sullivan, D. L. & Lewis, A. W. (2008), Generator selection for offshore oscillating water column wave energy converters, in '13th International Power Electronics and Motion Control Conference (EPM-PEMC)', Poland, p. 1790.

O'Sullivan, D. & Lewis, A. W. (2011), 'Generator selection and comparative performance in offshore oscillating water column ocean wave energy converters', IEEE Transactions of Energy Conversion **26**(2), 603–614.

Paixão Conde, J. M. & Gato, L. M. C. (2008), 'Numerical study of the air-flow in an oscillating water column wave energy converter', Renewable Energy **33**(12), 2637–2644.

Patel, M. H. (1989), Dynamics of Offshore Structures, Butterworth-Heinemann Ltd.

Patel, S., Ram, K., Ahmed, M. R. & Lee, Y.-H. (2011), 'Performance studies on an oscillating water column employing a savonius rotor', Science China Technological Sciences **54**(7), 1674–1679.

Pereiras, B., Castro, F., Marjani, A. E. & Rodriguez, M. A. (2011), 'An improved radial impulse turbine for OWC', Renewable Energy **36**(5), 1477–1484.

Pesce, C. P. (2003), 'The application of Lagrange equations to mechanical systems with mass explicitly dependent on position', Journal of Applied Mechanics **70**(5), 751–756.

Pesce, C. P., Tannuri, E. A. & Casetta, L. (2006), 'The Lagrange equations for systems with mass varying explicitly with postion: Some applications to offshore engineering', Journal of the Brazilian Society of Mechanical Sciences and Engineering **28**(4), 496–504.
URL: *http://dx.doi.org/10.1590/S1678-58782006000400015*

Pitt, E. G. (2006), 'The wave power climate at the Wave Hub site', Applied Wave Research .

Polinder, H. & Scutto, M. (2005), Wave energy converters and their impact on power systems, in 'International Conference on Future Power Systems', Amsterdam, The Netherlands.

Pretor-Pinney, G. (2010), The wavewatcher's companion, Bloomsbury Publishing Plc, London, UK.

Price, A. A. E. (2009), New Perspectives on Wave Energy Converter Control, PhD thesis, The University of Edinburgh, Edinburgh, UK.

Price, A. A. E. & Wallace, A. R. (2007), Non-linear methods for next wave estimation, in 'Proceedings of the 7th European Wave and Tidal Energy Conference', Porto, Portugal.
URL: *http://www.ewtec2007.com.pt*

Raghunathan, S. & Ombaka, O. O. (1985), 'Effect of frequency of air flow on the performance of the Wells turbine', Int. J. Heat and Fluid Flow **6**(2), 127–132.

Rahman, N. U. & Whidborne, J. F. (2008), 'A numerical investigation into the effect of engine bleed on performance of a single-spool turbojet engine', Proceedings of

the Institution of Mechanical Engineers, Part G: Journal of Aerospace Engineering **222**(7), 939–949.

Rahman, N. U. & Whidborne, J. F. (2009), 'Real-time transient three spool turbofan engine simulation: A hybrid approach', Journal of Engingeering for Gas Turbines and Power **131**(5), 1–8.

Ray, A. (1980), 'Dynamic modelling of power plant turbines for controller design', Applied Mathematical Modelling **4**, 109–112.

Renewable Energy Development (2009), 'Wave power: Orecon MRC device to be deployed', webpage.
URL: *http://renewableenergydev.com/red/wave-power-orecon-mrc-device-to-be-deployed/*

Ringwood, J. (2006), The dynamics of wave energy, in 'Irish Signals and Systems Conference', Dublin, Ireland, pp. 23–34.

Salter, S. H., Taylor, J. R. M. & Caldwell, N. J. (2002), Power conversion mechanisms for wave energy, in 'Proceedings of the Institution of Mechanical Engineers, Part M: Journal of Engineering for the Maritime Environment', Vol. 216, pp. 1–27.

Sauer, P. W. & Pai, M. A. (1998), Power System Dynamics and Stability, Prentice Hall, Upper Saddle River, NJ, USA.

Setoguchi, T., Santhakumar, S., Takao, M., Kim, T. H. & Kaneko, K. (2002), A performance study of a radial turbine for wave energy conversion, in 'Proceedings of the Institution of Mechanical Engineers, Part A: Journal of Power and Energy', Vol. 216, pp. 15–22.

Setoguchi, T. & Takao, M. (2006), 'Curent status of self rectifying air turbines for wave energy conversion', Energy Conversion and Management **47**(15-16), 2382–2396.

Setoguchi, T., Takao, M., Kinoue, Y. & Kaneko, K. (2000), 'Study on an impulse turbine for wave energy conversion', International Journal of Offshore and Polar Engineering **10**(2), 145–152.

Tarver, B. (2013), Development of turbines for use in oscillating water columns, PhD thesis, Cranfield University, School of Engineering, Cranfield, Engineering.

Tease, W. K., Lees, J. & Hall, A. (2007), Advances in oscillating water column air turbine development, in 'Proceedings of the 7th European Wave and Tidal Energy Conference', EWTEC, Porto, Portugal.
URL: *http://www.wavegen.co.uk*

Thakker, A. & Abdulhadi, R. (2008), 'The performance of Wells turbine under bidirectional airflow', Renewable Energy **33**(11), 2467–2474.

Thorpe, T. W. (1999), A brief review of wave energy, Technical report, The UK Department of Trade and Industry.

Torre-Enciso, Y., Ortubia, I., López de Aguileta, L. I. & Marqués, J. (2009), Mutriku wave power plant: from the thinking out to the reality, in 'Proceedings of the 8th European Wave and Tidal Energy Conference', EWTEC, Uppsala, Sweden.

Torresi, M., Pranzo, D., Camporeale, S. M. & Pascazio, G. (2011), Improved design of high solidity Wells turbine, in 'Proceedings of the 9th European Wave and Tidal Energy Conference', EWTEC, Southampton, UK.

University of Edinburgh & FP7 partners (2011), Equitable testing and evaluation of marine energy extraction devices in terms of performance, cost and environmental impact, deliverable D2.2 wave and tidal resource characterisation, Technical report, EquiMar.

Valério, D., Beirão, P., Mendes, M. J. G. C. & Sá da Costa, J. (2008), Comparison of control strategies performance for a wave energy converter, in 'Conference Pro-

ceedings 16th Mediterranean Conference on Control and Automation', Ajaccio, Corsica, France, pp. 773–778.

Valério, D., Beirão, P. & Sá da Costa, J. (2007), 'Optimisation of wave energy extraction with the archimedes wave swing', Ocean Engineering **34**(17-18), 2330–2344.

Vas, P. (2013), WAMIT User Manual Version 7.0, WAMIT, Inc., MA, USA.

Washio, Y., Osawa, H. & Ogata, T. (2001), The open sea tests of offshore floating type wave power device "mighty whale" - characteristics of wave energy absorption and power generation, in 'Conference Proceedings MTS/IEEE Oceans 2001', Vol. 1, Honolulu, Hawaii, USA, pp. 579–585.

Wells, A. (1981), 'Fluid driven rotary transducer UK Pat. GB1595700A'.

White, F. M. (1999), Fluid Mechanics, 4th edn, McGraw-Hill, Singapore.

Appendix A

Wave Equations

A.1 Linear Theory - Deep Water

$$h_w = \frac{H}{2}\cos\left(\frac{2\pi x}{\lambda} - \frac{2\pi t}{T}\right) \tag{A.1}$$

$$\lambda = \frac{gT^2}{2\pi} \tag{A.2}$$

$$T = \sqrt{\frac{2\pi\lambda}{g}} \tag{A.3}$$

$$c = \frac{\lambda}{T} \therefore c = \frac{gT}{2\pi} \tag{A.4}$$

$$u = \frac{\pi H}{T} e^{kz}\cos(kx - \omega t) \tag{A.5}$$

$$u_{max} = \frac{\pi H}{T} e^{k\frac{H}{2}} \tag{A.6}$$

$$w = \frac{\pi H}{T} e^{kz} \sin(kx - \omega t) \tag{A.7}$$

$$w_{max} = \frac{\pi H}{T} \tag{A.8}$$

$$c_g = \frac{c}{2} \tag{A.9}$$

$$k = \frac{2\pi}{\lambda} \tag{A.10}$$

A.2 Intermediate Water

$$h_w = \frac{H}{2} \cos\left(\frac{2\pi x}{\lambda} - \frac{2\pi t}{T}\right) \tag{A.11}$$

$$\lambda = \frac{gT^2}{2\pi} \tanh\left(\frac{2\pi h}{\lambda}\right) \tag{A.12}$$

$$T = 2\pi \left(\frac{2\pi g}{\lambda} \tanh\left(\frac{2\pi h}{\lambda}\right)\right)^{-1/2} \tag{A.13}$$

$$c = \frac{\lambda}{T} \therefore c = \frac{gT}{2\pi} \tanh\left(\frac{2\pi h}{\lambda}\right) \tag{A.14}$$

$$u = \frac{\pi H}{T} \frac{\cosh[k(z+h)]}{\sinh(kh)} \cos(kx - \omega t) \tag{A.15}$$

$$u_{max} = \frac{\pi H}{T} \frac{\cosh[k(H/2+h)]}{\sinh(kh)} \tag{A.16}$$

$$w = \frac{\pi H}{T} \frac{\sinh[k(z+h)]}{\sinh(kh)} \sin(kx - \omega t) \tag{A.17}$$

$$w_{max} = \frac{\pi H}{T} \tag{A.18}$$

$$c_g = \frac{c}{2}\{1 + \frac{2kh}{\sinh(2kh)}\} = nc \tag{A.19}$$

$$k = \frac{2\pi}{\lambda} \tag{A.20}$$

A.3 Deep Water

$$h_w = \frac{H}{2} \cos(\frac{2\pi x}{\lambda} - \frac{2\pi t}{T}) \tag{A.21}$$

$$\lambda = \sqrt{gh}T \tag{A.22}$$

$$T = \frac{\lambda}{\sqrt{gh}} \tag{A.23}$$

$$c = \frac{\lambda}{T} \therefore c = \sqrt{gh} \tag{A.24}$$

$$u = \frac{H}{2}\sqrt{\frac{g}{H}}\cos(kx - \omega t) u = \frac{\omega H}{2kh}\cos(kx - \omega t) \tag{A.25}$$

$$u_{max} = \frac{H}{2}\sqrt{\frac{g}{h}} \tag{A.26}$$

$$w = \frac{\pi H}{T}\frac{z+h}{h}\sin(kx - \omega t) \tag{A.27}$$

$$w_{max} = \frac{\pi H}{T} \tag{A.28}$$

$$c_g = c \tag{A.29}$$

$$k = \frac{2\pi}{\lambda} \tag{A.30}$$

$$\frac{E}{b} = \frac{E_p + E_k}{b} = \frac{\rho_w g H^2 \lambda}{8} \tag{A.31}$$

$$\frac{P}{b} = \frac{\rho_w g H^2 c_g}{8} \tag{A.32}$$

Appendix B

Wave Spectra

B.1 Wave Spectra Equations

The equations defining the variance spectral density are sometimes given in terms of the period and other times in terms of the frequency, the spectra are related in the following way:

$$S(f) = \frac{1}{f^2} S(T) \tag{B.1}$$

It is imperative that this relationship is used rather than simply substituting the frequency by its reciprocal as the amplitude of the variance is adjusted by this relationship. The energy contained in the spectra is given by

$$E = \rho_w g \int_0^\infty S(T) dT \tag{B.2}$$

$$= \rho_w g \int_0^\infty S(f) df \tag{B.3}$$

The equations for defining the Pierson-Moskowitz, JONSWAP, Bretschneider and

the Long Term Energy spectra are given by McCormick (2010), in (B.4), (B.8), (B.11) and (B.13).

Pierson-Moskowitz Spectrum

$$S_{\mathrm{PM}} = \frac{0.00810}{(2\pi)^4} g^2 T^3 e^{-\frac{0.74}{(2\pi)^4}\left(\frac{g}{U_{19.5}}T\right)} \tag{B.4}$$

$$t_D < t_{DF} = 1.167\left(\frac{F^{0.7}}{U_{10}^{0.4}}\right) \tag{B.5}$$

$$T_p \approx 2.80\left(\frac{U_{10}}{g}\right)\left(\frac{gF}{U_{10}^2}\right)^{0.3} \tag{B.6}$$

$$T_p \approx 1.99\left(\frac{U_{10}}{g}\right)\left(\frac{gt_D}{U_{10}}\right)^{\frac{3}{7}} \tag{B.7}$$

JONSWAP Spectrum

$$S_{JON}(T) = A_{JON} T^3 e^{-B_{JON}T^4} \chi^{e^{-\left(\frac{1}{2\sigma_{a,b}^2}\right)\left(\frac{T_p}{T}-1\right)^2}} \tag{B.8}$$

where χ, σ_a and σ_b are constants and the coefficients A_{JON} and B_{JON} are given below

$$A_{JON} = \frac{0.076}{(2\pi)^4} g^2 \left(\frac{Fg}{U_{10}^2}\right)^{-0.22} \tag{B.9}$$

$$B_{JON} = \frac{1.25}{T_p^4} \tag{B.10}$$

Bretschneider Spectrum

$$S_B(T) = 3.437 \frac{H_{avg}^2}{T_{avg}^4} T^3 e^{-0.675\left(\frac{T}{T_{avg}}\right)^4} \tag{B.11}$$

Probability density function

$$p_B(T) = \frac{S_B(T)}{1.27 H_{avg}^2} \tag{B.12}$$

Long Term Energy Spectrum

$$S_{LT}(T) = \frac{m_T - 1}{T_0^{m_T}} \frac{H_{rms}^2}{8} T^{(m_T-1)} e^{-\left(\frac{m_T-1}{m_T}\right)\left(\frac{T}{T_0}\right)^{m_T}} \tag{B.13}$$

Explanation: Terminology here can become a stumbling block, the variance density spectrum is often given in lieu of the energy spectrum. E(f) and E(f) with the units m^2/Hz and m^2/s respectively are used, when to be strictly accurate, the energy spectrum per unit area should have units of J/m^2 Hz or J/m^{2}s (Holthuijsen 2007). The energy equation is as follows:

$$E_{energy}(f) = \rho g \overline{h_w^2} \tag{B.14}$$

Checking the units:

$$[kgm^2/s^2]/[m^2] = [kg/m^3][m/s^2][m^2] \tag{B.15}$$

$$\overline{h_w^2} = \int_0^\infty E(f)\Delta f = \int_0^\infty E(t)\partial t \tag{B.16}$$

To transform variance spectral density with respect to frequency to variance spectral density with respect to time, or vice versa, one should use the one-dimensional Jacobian function, J, calculated for every value of t or f respectively.

$$E(f)J = E(t) \tag{B.17}$$

$$J = \frac{df}{dt} \tag{B.18}$$

$$\frac{df}{dt} = -1/t^2 \tag{B.19}$$

$$\frac{dt}{df} = -1/f^2 \tag{B.20}$$

Note the negative sign, this is due to the direction of the integral and the Jacobian function.

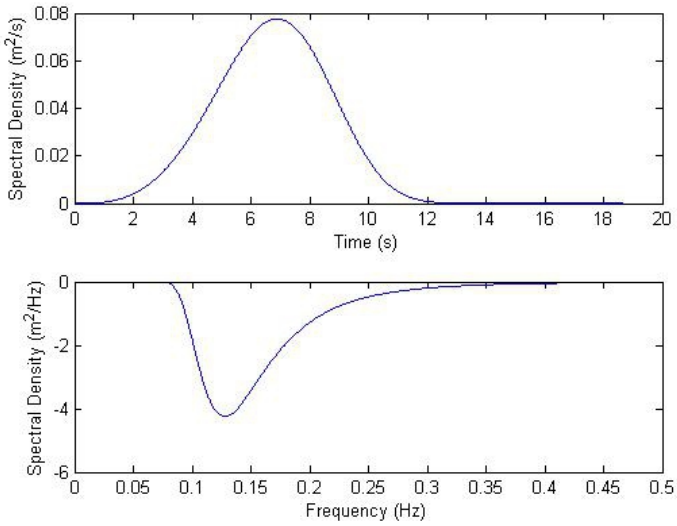

Figure B.1: Variance spectral density for Pierson-Moskowitz spectrum in frequency and time domain

To calculate the total energy for a discrete set it is important to use the appropriate limits as the data is not known for the full range between 0 and ∞.

$$E_{energy} = \rho_w g \int_{\frac{1}{t_{max}}=df}^{\frac{1}{dt}=f_{max}} E(f)\partial f = \rho_w g \int_{dt=\frac{1}{f_{max}}}^{t_{max}=\frac{1}{df}} E(t)\partial t \tag{B.21}$$